Particle Identification by dE/dx with the ILD TPC

–

Prototype Development and Application at the ILC

Dissertation
zur Erlangung des Doktorgrades
an der Fakultät für Mathematik, Informatik und Naturwissenschaften
Fachbereich Physik
der Universität Hamburg

vorgelegt von

Paul Malek

aus Aachen

Hamburg

2021

Gutacher/innen der Dissertation:	Dr. Ties Behnke Prof. Dr. Erika Garutti
Zusammesetzung der Prüfungskommission:	Dr. Ties Behnke Prof. Dr. Erika Garutti Prof. Dr. Ingrid-Maria Gregor Prof. Dr. Gudrid Moortgat-Pick Prof. Dr. Günter H. W. Sigl
Vorsitzender der Prüfungskommission:	Prof. Dr. Günter H. W. Sigl
Datum der Disputation:	11.02.2022
Vorsitzender Fach-Promotionsausschuss PHYSIK:	Prof. Dr. Wolfgang Hansen
Leiter des Fachbereichs PHYSIK:	Prof. Dr. Günter H. W. Sigl
Dekan der Fakultät MIN:	Prof. Dr. Heinrich Graener

Abstract

In this thesis the development of a time projection chamber (TPC) for the International Large Detector (ILD) concept at the International Linear Collider (ILC) is discussed and an analysis is carried out to evaluate the performance of the detector concept. The ILC is a planned linear electron-positron collider. Its first construction stage with a centre-of-mass energy of 250 GeV is primarily intended to perform precision measurements of the Higgs boson that was discovered at the LHC in 2012. In addition, the unprecedented precision that is aimed for also allows to search for indirect signs of new physics that manifest as deviations from the predictions of the standard model. The ILD is one of the detector concepts proposed for the ILC. Its distinctive feature is the large TPC foreseen as its main tracking detector. A TPC provides a large number of measured space points on each track, resulting in an excellent momentum resolution even for low momentum particles. Additionally it allows to measure the specific energy loss ($\mathrm{d}E/\mathrm{d}x$) of the particles and thus perform particle identification.

In the first part of this thesis the development of a modular readout for the ILD TPC is presented. Each module provides avalanche gas amplification of the electron signal via a stack of three gas electron multiplier (GEM) foils, supported by thin ceramic grids. The signal is read out on the anode plane, which is segmented into pads. For this work the production procedure for the modules was reviewed and improved to achieve a higher accuracy and repeatability. Three newly assembled modules were tested in a prototype TPC at the DESY II Test Beam Facility. The acquired data is used to validate the results regarding the spatial resolution acquired in a previous study. Additionally the $\mathrm{d}E/\mathrm{d}x$ resolution of the setup is determined for the first time. An extrapolation of the result to the conditions of the ILD TPC shows that the envisioned relative resolution of 5 % can be achieved.

In the second part of this thesis a measurement of the branching fractions of the Z boson into the light quarks d, u and s is presented. In the standard model the coupling of the Z to the quarks is independent of the flavour. Any deviation from this pattern is a hint of new physics. Due to the difficulty in identifying the flavour of the primary quark in jets originating from light quarks, the respective individual branching fractions are only known with uncertainties of 5 % to 10 %. The analysis presented here uses data from a detailed simulation of the ILD, scaled to the full data set of $L_{\mathrm{int}} = 2\,\mathrm{ab}^{-1}$ of the ILC at $\sqrt{s} = 250\,\mathrm{GeV}$. To tag the flavour of light quark jets, the high momentum leading hadrons in each jet are used since their flavour content is correlated to the flavour of the primary quark. One challenge of this approach is to identify the species of the tagging hadrons in the detector. The $\mathrm{d}E/\mathrm{d}x$ measurement in the TPC is an essential tool for this purpose. The analysis shows that a relative statistical precision of the branching fraction into light down-type quarks of about 1 % can be achieved.

Kurzfassung

Die vorliegende Arbeit behandelt die Entwicklung einer Zeitprojektionskammer (TPC) für den International Large Detector (ILD) am International Linear Collider (ILC). Zudem wird die Leistung des Detektorkonzepts im Rahmen einer Physikanalyse betrachtet. Der ILC ist ein geplanter Linearbeschleuniger zur Kollision von Elektronen mit Positronen. Die erste Ausbaustufe sieht eine Schwerpunktsenergie von 250 GeV vor, um Präzisionsmessungen der Eigenschaften des Higgsbosons durchzuführen, das 2012 am LHC entdeckt wurde. Die angestrebte Genauigkeit erlaubt es außerdem indirekte Anzeichen von unbekannter Physik zu finden, die als Abweichungen von den Vorhersagen des Standardmodells erkennbar sind. Der ILD ist eines der Detektorkonzepte, die für den ILC vorgeschlagen werden. Die Besonderheit des ILD is die TPC, die als zentraler Spurdetektor vorgesehen ist. Durch die hohe Anzahl an Messpunkten entlang jeder Spur erreicht eine TPC eine hervorragende Impulsauflösung selbst für Teilchen mit sehr geringem Impuls. Des Weiteren erlaubt die hohe Messdichte eine Bestimmung des Energieverlusts der Teilchen und so eine Ermittlung der Teilchenart.

Der erste Teil der Arbeit befasst sich mit der Entwicklung einer modularen Auslese für die ILD TPC. Jedes Modul beinhaltet eine Gasverstärkungsstufe bestehend aus drei gas electron multipliers (GEMs), die von schmalen Keramikrahmen gehalten werden. Das elektrische Signal wird auf der segementierten Anode ausgelesen. Im Zuge dieser Arbeit wurde der Fertigungsprozess für die Module überarbeitet, um eine höhere Wiederholgenauigkeit zu erreichen. Drei neu gebaute Module wurden in einem TPC-Prototypen an der DESY II Teststrahl Einrichtung erprobt. Die erhaltenen Daten werden ausgewertet, um die Ergebnisse einer früheren Studie bezüglich der Ortsauflösung zu überprüfen. Zudem wird zum ersten Mal die Messauflösung des Energieverlusts für dieses System bestimmt. Eine Extrapolation des Ergebnisses zu den Bedingungen der ILD TPC zeigt, dass die angestrebte relative Auflösung von 5 % erreicht werden kann.

Der zweite Teil der Arbeit behandelt eine Messung der Verzweigungsverhältnisse des Z-Bosons in die leichten Quarks d, u und s. Im Standardmodell ist die Kopplungsstärke des Z zu den Quarks unabhängig von deren Flavour-Quantenzahl. Jede Abweichung von diesem Schema ist ein Hinweis auf neue Physik. Da es für Jets, die von leichten Quarks erzeugt werden, schwierig ist die Art des ursprünglichen Quarks zu bestimmen, sind die jeweiligen Verzweigungsverhältnisse nur bis auf Unsicherheiten von 5 % bis 10 % bekannt. Die hier vorgestellte Analyse beruht auf simulierten Daten, die mit einem detailierten Modell des ILD erzeugt wurden und auf die Größe von $L_{\text{int}} = 2\,\text{ab}^{-1}$ des vollständigen Datensatzes des ILC bei $\sqrt{s} = 250\,\text{GeV}$ skaliert wurden. Um die Art des Primärquarks zu ermitteln, werden die Teilchen mit der höchsten Energie in jedem Jet betrachtet, da der Quarkinhalt der entsprechenden Hadronen mit dem Flavour des Primärquarks korreliert ist. Eine Herausforderung dieser Methode is die Identifikation dieser Hadronen. Hierfür ist die Messung des

Energieverlusts in der TPC unverzichtbar. Im Ergebnis zeigt die Analyse, dass für die Messung des Verzweigungsverhältnisses in leichte d- und s-Quarks ein relativer stochastischer Fehler von ungefähr 1 % erreicht werden kann.

Contents

Introduction

1. The Standard Model of Particle Physics

The standard model of particle physics (SM) is currently the best description of the fundamental particles and their interactions. The SM is a Yang-Mills gauge theory [1] based on the formalism of quantum field theory (QFT) that combines quantum mechanics with Einstein's special theory of relativity [2], but does not include the general theory of relativity [3]. Therefore from the four known fundamental forces, electromagnetism, the weak and strong interactions and gravity, only the former three are incorporated in the SM. While the electromagnetic (EM) and strong interactions are described in self contained theories, quantum electrodynamics (QED) [4, 5] and quantum chromodynamics (QCD) [6, 7], respectively, the weak interaction is better understood within a unified description of EM and weak forces, the electroweak (EW) model, also called Glashow-Salam-Weinberg (GSW) theory [8–10]. Therefore strictly speaking QED is not part of the SM. The EW model was completed with the introduction of the mechanism of electroweak symmetry breaking [11–14], often called Higgs mechanism.

Quantum mechanics differentiates between particles with integral spin values, i.e. bosons that follow Bose-Einstein statistics [15], and half odd-integral spin, i.e. fermions following Fermi-Dirac statistics [16, 17]. In QFT each elementary particle is understood as an excited state, or a quantum, of an underlying field and bosons and fermions play distinct roles, which are described in the following. Mathematically, the particles and their interactions are described as terms in the Lagrangian density $\mathscr{L}$ involving the corresponding fields. The requirement of local gauge invariance defines the possible terms and thus the existing interactions. The underlying gauge symmetry of the standard model is given by the group structure $\mathrm{SU}(3)_C \times \mathrm{SU}(2)_T \times \mathrm{U}(1)_Y$. For each generator of these gauge groups, a gauge field must be introduced in the Lagrangian to ensure local gauge invariance. The gauge fields of the standard model are vector fields and their quanta are the gauge bosons, which are interpreted as the mediator particles of the respective forces. In addition, the spontaneous breaking of the EW symmetry requires the introduction of a scalar field, the so-called Higgs field, and at least one scalar boson, the Higgs boson. The properties of particles that define their couplings to the mediators are additive quantum numbers called charges. The gauge bosons of the SM are listed in table 1.1.

While the interactions are mediated by bosons, the matter in the universe is comprised of elementary fermions. Protons and neutrons are made up of up- and down-quarks (u and d), which are confined to the hadrons by the strong force. The electrons (e^-) are not affected by the strong force and are bound by electromagnetic Coulomb forces, e.g. to atomic nuclei. Finally, neutrinos (ν), which are for example produced in the neutron β-decay and nuclear fission and fusion, only interact with the weak force. While most visible matter is comprised

Table 1.1.: Summary of the gauge bosons of the three fundamental interactions described by the standard model, including their masses and charges. The experimental photon, weak boson and Higgs masses are taken from ref. [18]. The bound on the gluon mass was estimated in ref. [19]. In their respective theories the gluons and the photon are massless. The charges are explained in the corresponding sections on the interactions.

interaction	boson	mass [GeV]	Q	T_3	Y	colour
strong	gluons (g)	$0(<10^{-3})$	0	0	0	octet
weak	$W^{\pm}$	80.379(12)	±1	±1	0	neutral
	Z	91.1876(21)	0	0	0	neutral
EM	photon (γ)	$0(<10^{-27})$	0	0	0	neutral
—	Higgs (h)	125.10(14)	0	$-1/2$	+1	neutral

Table 1.2.: The elementary fermions of the standard model and their charges. The charges are explained in the corresponding sections on the interactions. The absence of right-chiral neutrinos is discussed in section 1.2.

	generation					left-chiral		right-chiral	
	1	2	3	colour	Q	T_3	Y	T_3	Y
quarks	u	c	t	triplet	$+2/3$	$+1/2$	$+1/3$	0	$+4/3$
	d	s	b		$-1/3$	$-1/2$	$+1/3$	0	$-2/3$
leptons	ν_e	ν_μ	ν_τ	neutral	0	$+1/2$	-1	—	
	e^-	μ^-	τ^-		-1	$-1/2$	-1	0	-2

of these four constituents, there exist two additional, successively more massive, copies of each, for a total of three generations, as displayed in table 1.2. The second generation includes the strange (s) and charm (c) quark as well as the muon (μ^-) and the corresponding neutrino. The third generation quarks are the bottom (b) and top (t) and the charged lepton is designated τ^-. Potential undiscovered heavier generations are constraint by the best fit of the number of light neutrino flavours of $N_\nu = 2.991 \pm 0.007$ [18].

Except for their mass, the particles in higher generations only differ by their so-called flavour quantum number. For the quarks the flavour directly represents their type and generation. By convention, the flavour of a quark has the same sign as its electric charge. As is explained in section 1.2, quark flavour is not conserved by the weak interaction and it can mediate decays between generations. Therefore only the quarks of the first generation are stable. For the leptons instead of six individual quantum numbers, often a single flavour is assigned to both the charged lepton and the neutrino of each generation, i.e. electron number, muon number and tau number. In this picture, the heavier generation charged leptons can decay by transforming into the corresponding neutrino via the weak interaction, without violating flavour conservation. The neutrinos themselves are lighter than all other fermions and thus cannot decay. Since in the SM, the particles in all three generations have the same values of the charges corresponding to the SM forces, their couplings to the SM gauge bo-

sons are expected to be generation independent, this is known as flavour universality.

Each of the fermions also has an antiparticle that has the same properties, such as mass, but all additive quantum numbers, e.g. the standard model charges and the flavour, have the opposite sign, i.e. particles transform into their antiparticles under charge inversion. This is reflected in the solutions of the Dirac equation [20] describing the propagation of fermions. The resulting Dirac spinor exhibits two components with positive energy and two with negative energy. The latter are identified as the antiparticle solutions. The Dirac spinor can be projected into so-called left- and right-chiral components [21], which transform into each other under parity inversion [22], i.e. when going from a left-handed to a right-handed coordinate system and vice versa. The two chiral projections are generally not identical to the particle and antiparticle components, except for Majorana fermions [23]. Therefore Dirac fermions and antifermions both exist as left- as well as right-chiral states. For massless particles chirality is identical to helicity, i.e. the normalised projection of their spin onto their momentum vector. For massive particles there always exists a Lorentz boost that inverts the momentum direction and thus flips the sign of their helicity. Therefore it must be distinguished from chirality, which does not depend on the observer. In experiments only helicity is observed, not chirality directly.

For light particles, such as electrons and positrons, at high momenta helicity is almost equivalent to chirality. This can be utilised in e^+e^--colliders by spin polarising the particle beams, i.e. aligning the spins (anti-)parallel with the momentum vector to a significant degree. This has two effects that can be used to suppress or enhance certain processes. First, since the SM interactions are mediated by vector bosons, many processes are only allowed for configurations where the helicities of the colliding particles have opposite signs. Secondly, as is explained in section 1.2, the weak interactions are sensitive to the chirality of the interacting particles since they only interact with left-chiral particles and right-chiral antiparticles.

The SM has several free parameters, which are not given by the theory. Since some of the parameters depend on each other, different sets of independent parameters can be defined. The set typically used includes the mass of the Higgs boson, the masses of the fermions and the strong coupling constant α_s as well as the mass of the Z, the Fermi constant G_F and the fine structure constant α [18]. These and other parameters have been measured to great precision in past and current experiments, e.g. α_s at LEP [24] and HERA [25], M_Z at LEP and SLC [26], the $\mathrm{W}^\pm$ mass at the Tevatron [27] and the top-quark mass at the LHC [28, 29]. A review of the current experimental status is published regularly by the Particle Data Group [30]. Once the free parameters are known, the model can be used to predict other quantities such as production cross sections and decay branching ratios. Predictions made by the SM have widely been confirmed by experiments, e.g. the production cross sections of a wide range of processes by ATLAS [31] and CMS [32] at the LHC and the decay branching fractions of the Z boson into two fermions at LEP [26]. However, some experiments have produced evidence of discrepancies, e.g. the measured anomalous magnetic moment of the muon deviates by $4.2\,\sigma$ from the SM expectation [33] and certain branching fractions of rare decays of hadrons containing b quarks deviate by more than $3\,\sigma$ [34, 35].

1.1. Quantum Chromodynamics

The gauge field theory that describes the interactions of quarks via the strong force is called quantum chromodynamics (QCD) and its gauge structure is the $SU(3)_C$ component of the standard model of particle physics [18]. The charge of the strong interaction is called colour, as it comes in three states generally denoted as red, green and blue, in reference to the three primary colours in additive colour models. The quarks are in the fundamental representation of $SU(3)_C$, i.e. they exist as colour triplets **3** with one colour degree of freedom. Correspondingly, antiquarks are triplets of anticolour, $\bar{\mathbf{3}}$. The strong gauge bosons are the massless gluons, which were discovered at the e^+e^- colliders DORIS [36] and PETRA [37]. Gluons can be interpreted as carrying both colour and anticolour, i.e. they are in the adjoint representation of $SU(3)_C$ and thus form an octet **8** [7]. Therefore, they not only mediate the interaction but also take part in it themselves via gluon-gluon interactions. From group theory it follows that the nine possible combined colour-anticolour states are arranged into an octet and a singlet: $\mathbf{3} \otimes \bar{\mathbf{3}} = \mathbf{8} \oplus \mathbf{1}$. Since the singlet is colour neutral it could only interact with other colour singlet states, i.e. not with the quarks or the gluon octet but with the colour neutral SM particles [6, 7]. Like the photon, such a gluon would have infinite range. However, no long-range strong interaction has been observed. Therefore the gluon singlet is believed to not be realised in nature and QCD only includes the gluon octet, i.e. it has SU(3) and not U(3) symmetry.

The Lagrangian of QCD is given by [18]

$$\mathscr{L}_{\mathrm{QCD}} = \sum_q \bar{\psi}_{q,a}\left(i\gamma^\mu \partial_\mu \delta_{ab} - g_s \gamma^\mu t^C_{ab} \mathscr{A}^C_\mu - m_q \delta_{ab}\right)\psi_{q,b} - \frac{1}{4} F^A_{\mu\nu} F^{A\,\mu\nu} \quad , \tag{1.1}$$

using Einstein notation, summing over any repeated indices. The Kronecker symbol δ_{ab} is zero for $a \neq b$ and one for $a = b$, where the indices a and b run from 1 to $N_c = 3$, representing the three colour states. The γ^μ, with $\mu = 0, 1, 2, 3$, are the four Dirac γ-matrices. The first term of the Lagrangian describes the propagation of the quarks, represented by the spinors $\psi_{q,a}$, with flavour q and mass m_q as well as their interaction with the gluon octet fields $\mathscr{A}^C$, where C runs from 1 to ${N_c}^2 - 1 = 8$. This quark-antiquark-gluon interaction term is proportional to the QCD coupling constant g_s. The quark masses m_q and the coupling constant g_s are free parameters of QCD. The t^A are related to the Gell-Mann matrices λ^A [38] by $t^A_{ab} = \lambda^A_{ab}/2$. They are eight 3×3 matrices that, as generators of SU(3) transformations, fulfil the commutation relation

$$\left[t^A, t^B\right] = i f_{ABC} t^C \quad , \tag{1.2}$$

where the f_{ABC} are the structure constants of the group. The second term of the Lagrangian, containing the field tensor

$$F^A_{\mu\nu} = \partial_\mu \mathscr{A}^A_\nu - \partial_\nu \mathscr{A}^A_\mu - g_s f_{ABC} \mathscr{A}^B_\mu \mathscr{A}^C_\nu \quad , \tag{1.3}$$

describes the interaction between the gluons. It gives rise to three- and four-gluon interaction terms, proportional to g_s and ${g_s}^2$, respectively.

1.1.1. The Quark-Parton Model of Hadrons

At low energies, colour is believed to be permanently confined due to the gluon self interactions. This reflects the fact that in nature quarks and gluons only appear as colour-singlet bound states, the hadrons. Since gluons carry no intrinsic quantum numbers except colour, the properties of hadrons are defined by their constituent quarks and antiquarks. This description of hadrons is called the quark-parton model [18]. In this model there exist two types of hadrons [39]: Mesons are $q\bar{q}'$ bound states of quarks q and antiquarks $\bar{q}'$, where the flavours of quark and antiquark can be different but their colour charges have to cancel each other, e.g. red and anti-red. Baryons are three-quark bound states with a fully antisymmetric state of the three colours. Also here, the flavours of the three quarks may be different. The quark model only describes the minimal quark content of hadrons, i.e. their so-called valence quarks. In addition however, within each hadron there exists a sea of gluons and virtual quarks. While these sea quarks do not influence the quantum numbers of a hadron, they can partake in interactions with other particles. For the proton the properties of the quark sea have been measured in deep inelastic $e^{\pm}p$ collisions at HERA [40].

All quarks except the top quark have been observed as part of hadrons. Due to its high mass, the lifetime of the top quark is too short to form bound states. The hadronic states can be described as $SU(n)$ multiplets of n quark flavours [38, 39]. Since the u and d quarks have almost equal mass, their $SU(2)$ symmetry is nearly unbroken. Historically, this led to the introduction of the isospin of the nucleons. In the quark model, the isospin I, or rather its third component I_3, is kept as the flavour quantum number of the first generation quarks, with $I_3 = {}^{-1}/_{2}$ for the d quark and $I_3 = {}^{+1}/_{2}$ for the u quark. Including the somewhat heavier s quark with strangeness $S = -1$ results in an only slightly broken $SU(3)$ symmetry. However for $n > 3$, i.e. hadrons containing c or b quarks, the symmetry is badly broken due to the much higher masses of these quarks.

1.1.2. Fragmentation and Hadronisation

For interactions with large momentum transfers the strong coupling constant is greatly reduced [18]. This effect is referred to as asymptotic freedom of QCD [41, 42]. Therefore in sufficiently hard interactions quarks and gluons can often be treated as free particles and the interactions can be calculated using perturbation theory. However, on the scale of experiments and detectors only hadrons may be observed. The transition between the parton state of the hard interaction and the measurable hadronic event is called fragmentation. Describing this process is an important task in Monte Carlo simulations. Since at some point in the transition the average involved momentum transfers become too low and the perturbative approach fails, it can not be described fully analytically but requires phenomenological parametrisations [43]. Different models have been developed, which are mostly grouped in the two classes of string [44, 45] and cluster [46] fragmentation.

Typically the transition is split into three stages [43], the parton shower, hadronisation and the decay of unstable hadrons. Immediately after a hard scattering process, e.g. $e^+e^- \to Z \to q\bar{q}$, the primary partons in the final state are quasi-free colour charges. However, they are still coupled via the colour field between them. Therefore they emit bremsstrahlung in

the form of gluons. The gluons can interact and generate additional $q\bar{q}$ pairs, using energy available in the colour field between the partons. These secondary particles form the parton shower. During this stage the global properties of the event are determined [43], e.g. energy and angular distributions, multiplicities etc. The bremsstrahlung gluons are predominantly emitted with low momentum and at small angles to the primary parton. Therefore, the parton shower develops into a roughly conical jet around the momentum axis of the primary parton. Below a fixed cut-off scale, typically chosen at ~1 GeV [43], the processes can no longer be calculated perturbatively. Here, the phenomenological models are employed to transfer the secondary partons into hadrons. This hadronisation is assumed to be local, since the emitted soft gluons shield the colour charges of the individual higher momentum partons, creating independent colour neutral systems [43]. Finally, any unstable hadrons are decayed into stable particles, hadrons as well as leptons, according to their known decay widths. However, the time scales of decays are often much shorter than that of the hadronisation, so that the two processes cannot be clearly separated in reality.

Since the gluons emitted during formation of the parton shower are mostly soft, the primary parton typically retains a large fraction of its initial momentum, i.e. the total momentum of the jet. Most of this momentum is carried over to the hadron as the hadronisation process happens at low momentum-transfer scales. Therefore the leading hadron in a jet often contains the primary parton [47]. This fact is used in the analysis in part II of this thesis to tag the flavour of jets generated by light u, d and s quarks.

1.2. Electroweak Model and Higgs Mechanism

The theory describing the unified EM and weak interactions of fermions, the electroweak (EW) or Glashow-Salam-Weinberg (GSW) theory [8–10], contributes the gauge structure $\mathrm{SU}(2)_T \times \mathrm{U}(1)_Y$ of the standard model of particle physics. The corresponding charges are the weak isospin T and the weak hypercharge Y, which fulfil the relation

$$Q = T_3 + \frac{1}{2}Y \tag{1.4}$$

with the electric charge Q in units of the elementary charge e and where T_3 is the third component of the weak isospin. The gauge fields form a weak isospin triplet W_i, $i = 0, 1, 2$, with $T = 1$ and $Y = 0$ for the $\mathrm{SU}(2)_T$ component and a singlet B with $T = Y = 0$ for the $\mathrm{U}(1)_Y$ component.

In the original GSW theory the EW gauge bosons were massless since the corresponding mass terms would break the gauge invariance of the Lagrangian. However, in experiments it was shown that the three weak gauge bosons have masses of $\mathcal{O}(100\,\mathrm{GeV})$ [26, 27, 18], which are responsible for the short range of the weak interaction. The mechanism of electroweak symmetry breaking (EWSB) [11–14] was developed to restore gauge invariance in the presence of massive gauge bosons. In the minimal model a new complex $\mathrm{SU}(2)_T$ doublet field $\boldsymbol{\Phi}$ with scalar potential

$$V(\boldsymbol{\Phi}) = \mu^2 \boldsymbol{\Phi}^\dagger \boldsymbol{\Phi} + \frac{\lambda^2}{2}\left(\boldsymbol{\Phi}^\dagger \boldsymbol{\Phi}\right)^2 \tag{1.5}$$

is introduced, which is generally called the Higgs field. With quantum numbers $T = 1/2$ and $Y = 1$ this doublet has an electrically charged component ϕ^+ and a neutral component ϕ^0, following equation (1.4). Since the doublet is complex it has a total of four real degrees of freedom. If $\mu^2 < 0$, the neutral component acquires a non-zero vacuum expectation value v:

$$\phi^0 = H + \langle \phi^0 \rangle \quad , \quad \langle \phi^0 \rangle =: v \approx 246\,\text{GeV} \quad . \tag{1.6}$$

At low energies where the system is in the ground state, this results in the spontaneous breaking of the SM gauge symmetry $\mathrm{SU}(3)_C \times \mathrm{SU}(2)_T \times \mathrm{U}(1)_Y$ into $\mathrm{SU}(3)_C \times \mathrm{U}(1)_{\mathrm{em}}$. This breaking of three of the four generators of the EW gauge symmetry implies the existence of three massless Goldstone bosons [48]. These are identified with three of the four degrees of freedom of the Higgs field. The two charged and one neutral Goldstone degrees of freedom mix with the EW gauge fields, W^i and B. They become the longitudinal components of the now massive gauge bosons, the two charged $W^\pm \equiv (W_1 \mp iW_2)/\sqrt{2}$ and the neutral $Z \equiv -B \sin\theta_{\mathrm{W}} + W_0 \cos\theta_{\mathrm{W}}$, respectively. The fourth EW generator stays unbroken and the corresponding gauge field, the $\mathrm{U}(1)_{\mathrm{em}}$ photon $A \equiv B \cos\theta_{\mathrm{W}} + W_0 \sin\theta_{\mathrm{W}}$, remains massless. The weak mixing or Weinberg angle $\theta_{\mathrm{W}} \coloneqq \arctan(g'/g)$ is defined by the relative strength of the couplings g and g' of $\mathrm{SU}(2)_T$ and $\mathrm{U}(1)_Y$, respectively. The last, neutral degree of freedom H of the Higgs doublet remains as a new scalar particle, the Higgs boson. A candidate for this particle, with a mass of about 125 GeV and properties consistent with the SM predictions, was discovered by the CMS [49] and ATLAS [50] experiments at the LHC.

After EWSB the Lagrangian for the fermion fields ψ_f is [18]

$$\begin{aligned}
\mathscr{L}_F = & \sum_f \bar{\psi}_f \left(i\gamma^\mu \partial_\mu - m_f - \frac{m_f}{v} H \right) \psi_f \\
& - \frac{g}{2\sqrt{2}} \sum_i \left[\bar{\nu}_{L_i} \gamma^\mu \left(1 - \gamma^5\right) e_{L_i} + \bar{u}_{L_i} \gamma^\mu \left(1 - \gamma^5\right) V_{ij} d_{L_j} \right] W_\mu^+ + \text{h.c.} \\
& - \frac{g}{2\cos\theta_{\mathrm{W}}} \sum_f \bar{\psi}_f \gamma^\mu \left[\left(1 - \gamma^5\right) T_{3L}^f - 2Q_f \sin^2\theta_{\mathrm{W}} \right] \psi_f Z_\mu \\
& - g \sin\theta_{\mathrm{W}} \sum_f Q_f \bar{\psi}_f \gamma^\mu \psi_f A_\mu \quad ,
\end{aligned} \tag{1.7}$$

using Einstein notation, summing over any repeated indices. The first term contains the propagation term $i\gamma^\mu \partial_\mu$, where the γ^μ are the Dirac γ-matrices. It also includes the masses m_f of the fermions and their couplings to the Higgs field H, which both appear when diagonalising the Yukawa interactions [51] between the Dirac fermions and the Higgs field once EWSB takes place. The neutrinos were originally thought to be massless and thus have no Yukawa couplings. However, neutrino oscillations [52, 53] are observed in various experiments probing different neutrino sources [54–60]. This shows that their mass eigenstates are misaligned with their weak eigenstates, which implies that they have to possess non-zero masses. Since it is not known whether neutrinos are Dirac or Majorana fermions, it is also unclear whether their masses originate from Yukawa interactions or are acquired through a version of the see-saw mechanism [61].

This distinction of the neutrinos from the other fermions comes from the fact that the $\mathrm{SU}(2)_T$ component of the EW interaction couples only to left-chiral fermions. This is re-

flected in the second term of equation (1.7), which represents the charged current (CC) weak interactions. The left-chiral fermion fields of each generation form weak isospin doublets with $T = 1/2$,

$$\ell_{Li} = \begin{pmatrix} \nu_{Li} \\ e_{Li} \end{pmatrix} \text{ and } q_{Li} = \begin{pmatrix} u_{Li} \\ d'_{Li} \end{pmatrix} , \tag{1.8}$$

while the right-chiral fields, e_{Ri}, u_{Ri} and d_{Ri}, are singlets with $T = 0$. The opposite is true for the antifermions, i.e. right-chiral doublets and left-chiral singlets. Right-chiral neutrinos ν_{Ri}, which need to exist if neutrinos are Dirac fermions, would not interact via any SM force and thus are not part of the current theory.

Similar to neutrino oscillations, the three generations of quarks mix via the charged weak currents since their mass eigenstates are not identical to the weak eigenstates. Per convention the mixing is applied to the down-type states according to $d'_{Li} \coloneqq \sum_j V_{ij} d_{Lj}$, where V is the Cabibbo-Kobayashi-Maskawa (CKM) mixing matrix [62, 63]. The structure of the matrix and its consequences for the decays of quarks are explained in section 1.2.1 below. An analogous mixing of the (charged) leptons through the charged weak currents has not been observed due to the difficulty in detecting the neutrinos in traditional particle physics experiments.

The third term of equation (1.7) describes the neutral current (NC) weak interactions. The field Z couples to both the weak isospin T_3 and the electric charge Q. Here T_{3L} represents the weak isospin operator, which results in $T_3 = \pm 1/2$ for the left-chiral components and $T_3 = 0$ for the right-chiral components of the fermion spinor, according to table 1.2. The interactions can also be expressed in terms of the vector and axial-vector components

$$g_{\mathrm{V}}^f \coloneqq T_{3L}^f - 2Q_f \sin^2\theta_{\mathrm{W}} \text{ and } g_{\mathrm{A}}^f \coloneqq T_{3L}^f , \tag{1.9}$$

respectively, such that the addends of the term become $\bar{\psi}_f \gamma^\mu (g_{\mathrm{V}}^f - \gamma^5 g_{\mathrm{A}}^f) \psi_f Z_\mu$.

The last term in equation (1.7) describes the electromagnetic interactions of QED. As above Q_f is the electric charge in units of the elementary charge $\mathrm{e} \equiv g \sin\theta_{\mathrm{W}}$. As opposed to the weak interactions, the electromagnetic interaction is purely vector like.

1.2.1. The CKM Matrix and Quark Decays

The Cabibbo-Kobayashi-Maskawa (CKM) mixing matrix [62, 63]

$$V = \begin{pmatrix} V_{\mathrm{ud}} & V_{\mathrm{us}} & V_{\mathrm{ub}} \\ V_{\mathrm{cd}} & V_{\mathrm{cs}} & V_{\mathrm{cb}} \\ V_{\mathrm{td}} & V_{\mathrm{ts}} & V_{\mathrm{tb}} \end{pmatrix} \tag{1.10}$$

is a 3×3 unitary matrix, that describes the mixing between the three generations of quarks via the charged weak currents. It can be parametrised by three mixing angles. An additional complex phase can be included without breaking unitarity. A non-zero value of this phase implies a violation of charge-parity (CP) symmetry.

The phases and magnitudes of the matrix elements have been determined using data from experiments employing different methods and probing various processes. These measurements are used in ref. [18] to perform a global fit and achieve the best precision for all values.

The general structure of the matrix in terms of the magnitude of the elements is as follows: The main-diagonal elements, $|V_{ud}|$, $|V_{cs}|$ and $|V_{tb}|$, are just below unity. The first sub- and super-diagonal elements between the first and second generation, $|V_{us}|$ and $|V_{cd}|$, have values of about 0.2, while those between the second and third generation, $|V_{cb}|$ and $|V_{ts}|$, are around 0.04. The elements between first and third generation, $|V_{ub}|$ and $|V_{td}|$, are the smallest with values below 0.01.

In the second term of equation (1.7) the CKM matrix governs the interactions of the different quark flavours via the charged weak currents, i.e. the transformation of up-type quarks into down-type quarks by radiating a (virtual) W^+ boson, e.g. $c \to sW^+$, and vice versa with a W^-. Since the matrix is not diagonal, the quarks can change between generations at these vertices. However, as the off-diagonal elements are successively smaller, such transitions are suppressed compared to transitions within one generation. This has consequences for the decays of quarks and their containing hadrons. For all quarks except the top, the decays are additionally suppressed by their mass difference to the $W^\pm$, which necessitates the creation of an off-shell $W^\pm$. Since the b quark is lighter than the top, it can only decay into a lower generation quark. Therefore its lifetime is increased by the CKM suppression, resulting in values of $c\tau \approx (0.3\text{–}0.5)$ mm for bottom hadrons [18]. In collider experiments this results in the decay vertices of bottom hadrons often being significantly offset from the primary collision vertex, producing a distinct signature. Even though the decay of charm into strange quarks is not CKM suppressed, the large mass difference to the $W^\pm$ increases the lifetime of the charm quark. This results in charmed hadron lifetimes of $c\tau \approx (0.1\text{–}0.3)$ mm [18] and similar experimental decay signatures as for b quarks. For the strange quark, CKM suppression of the decay to u is weaker than for the b quark but the $W^\pm$ is produced much further off shell. This results in even larger hadron lifetimes $c\tau$ of several centimetres to metres [18].

The top quark is special, as it is the only quark more massive than the $W^\pm$. Therefore in its decay it can create an on-shell W boson. This substantially increases its decay width and reduces its lifetime so much that it cannot form bound states before decaying. Being the heaviest quark the top quark can potentially decay into any down-type quark but the decays into s and d are strongly CKM suppressed so that it does actually decay almost exclusively into a b quark.

1.3. Open Questions and Issues

The standard model of particle physics has been thoroughly tested at various energy scales and so far is very successful in explaining even the most precise measurements. However, it is known to be incomplete in several aspects. One such issue arises from astronomical and cosmological observations [64–66]. These imply that a large part of the energy density of the universe is comprised of an unknown type of matter, called dark matter (DM), that is massive but electrically neutral and only interacts faintly with the known, visible particles. The standard model provides no suitable particle to fulfil this role. Therefore many extensions of the SM introduce new particles to resolve this issue [67]. While the SM neutrinos seem like a natural candidate, their potential contribution to dark matter is severely limited by the observations [68, 69, 18].

The existence of neutrino masses and mixing itself raises several questions. For one, the absolute masses of the neutrinos are unknown but the existing upper limits [18] show that the masses must be much smaller than those of the charged leptons. This may be linked to the origin of neutrino masses, i.e. whether they are Dirac or Majorana fermions. In the former case the simplest mechanism to generate the masses would be Yukawa interactions. In the latter case the most attractive option is the see-saw mechanism [61]. The sterile, right-chiral neutrinos introduced by this mechanism could also serve as a dark matter candidate.

Another feature of the see-saw mechanism is that it links the generation and scale of the neutrino masses to another open issue of the standard model, the matter-antimatter asymmetry of the universe. Currently it is unknown which mechanism is responsible for the preferred production of matter over antimatter in the early universe. The see-saw mechanism could provide the violation of CP symmetry that is required in leptogenesis models [70, 71] generating the asymmetry.

Other issues are related to the nature of the Higgs boson. Subsequent measurements of the particle discovered at the LHC find it to be consistent with SM predictions for the Higgs boson of the minimal model described in section 1.2. However, the mass of the Higgs boson is of concern. It receives quantum corrections proportional to the highest energy scale the SM is valid to and therefore should be of the same order of magnitude. If no new physics is introduced below the Planck scale, this implies a fine tuning of $(M_\mathrm{h}/m_\mathrm{P})^2 = \mathcal{O}(10^{-34})$ from the Planck mass $m_\mathrm{P} = \mathcal{O}(10^{19}\,\mathrm{GeV})$ to the measured mass M_h of about 125 GeV, by unrelated parameters. This is called the hierarchy problem [72–74]. Several theories exist to resolve this issue, including more complex models with additional degrees of freedom or the possibility that the Higgs boson is not elementary but a composite particle of a new underlying symmetry.

Additionally some experiments have produced evidence of deviations from the SM, e.g. the measured anomalous magnetic moment of the muon deviates by $4.2\,\sigma$ [33]. Also certain ratios of branching fractions of b-hadrons into different lepton flavours deviate from the SM prediction by more than $3\,\sigma$, e.g. [34, 35]. The latter indicates a violation of lepton-flavour universality. The theories proposed to explain the non-universality include, amongst others, phenomenological models with additional gauge bosons Z' [75–77] or leptoquarks [78, 79], and models of R-parity violating supersymmetry [80–82]. While these models typically only consider new couplings specific to the divergent channels, they could be readily extended to include flavour non-universality in the quark sector. Therefore many of these models may be relevant to part II of this thesis.

To verify the theories above, continued tests by experiments are required. New particles proposed can be either discovered directly, by producing them at high enough energies, or indirectly, by their influence on the couplings of SM particles. In this regard, different types of collider play important, complementary roles. On one hand, hadron colliders like the Large Hadron Collider (LHC) with their high energy reach can discover new heavy particles directly. On the other hand, $\mathrm{e}^+\mathrm{e}^-$ colliders like the proposed International Linear Collider (ILC), introduced in the next chapter, can use their higher precision for indirect searches by looking for deviations from the SM. Of particular interest in this regard are precision measurements of the properties of the Higgs boson.

2. The International Linear Collider

The International Linear Collider (ILC) is a linear electron-positron collider designed to reach centre-of-mass energies of 200 GeV to 500 GeV, with a potential upgrade to 1 TeV. The possibility for operation at the Z-pole is also investigated. After the discovery of a Higgs boson with a mass of 125 GeV at the LHC, the baseline design was changed to an initial stage with a maximum centre-of-mass energy of 250 GeV, a so-called Higgs factory, reducing the initial cost. The technical possibilities for a later stage of 500 GeV and the 1 TeV upgrade are retained with this new design. To study the chiral structure of particles as well as to better differentiate between signal and background processes, both particle beams are foreseen to be spin polarised. The longitudinal polarisation reached in the interaction point (IP) is $|\mathcal{P}_{e^-}| = 80\,\%$ for the electron beam and $|\mathcal{P}_{e^+}| = 30\,\%$ for the positron beam.

The design of the central region provides space for two detectors sharing runtime and integrated luminosity at the same IP. This is achieved by the so-called push-pull concept, where each detector is placed on a movable platform such that either can be moved as a whole into the interaction region while the other is shifted into a parking position. The detector hall is designed such that maintenance can be performed at the parked detector during operation of the collider. Having two separate experiments gives the advantage that results can be cross-checked directly and potential detector biases can be identified.

A detailed description of the ILC with a maximum centre-of-mass energy of 500 GeV, including the machine design, physics programme and detectors, is available in the form of a technical design report (TDR) [83]. With the change of the initial stage to 250 GeV, updates of the baseline design and physics case were published in refs. [84, 85]. A comprehensive overview of the project including the most recent advancements is available in ref. [86]. More details on the detector concept used for this work, the International Large Detector (ILD), are given in ref. [87]. In the following the main components of the accelerator are described in section 2.1. Afterwards the running scenario in terms of beam energy and polarisation is detailed in section 2.2. Finally the design and subdetectors of the ILD are presented in section 2.3.

2.1. The Accelerator Baseline Design

A schematic illustration of the ILC accelerator complex is shown in figure 2.1. The indicated subsystems are briefly described in the following sections. The total footprint of the accelerator complex has a length of about 20 km for the centre-of-mass energy of $\sqrt{s} = 250\,\text{GeV}$. This would need to be extended to 31 km for the potential upgrade to $\sqrt{s} = 500\,\text{GeV}$. Major components of the accelerator, like the damping rings and the central region including the beam delivery system and the beam dumps, as well as the detectors are already designed to

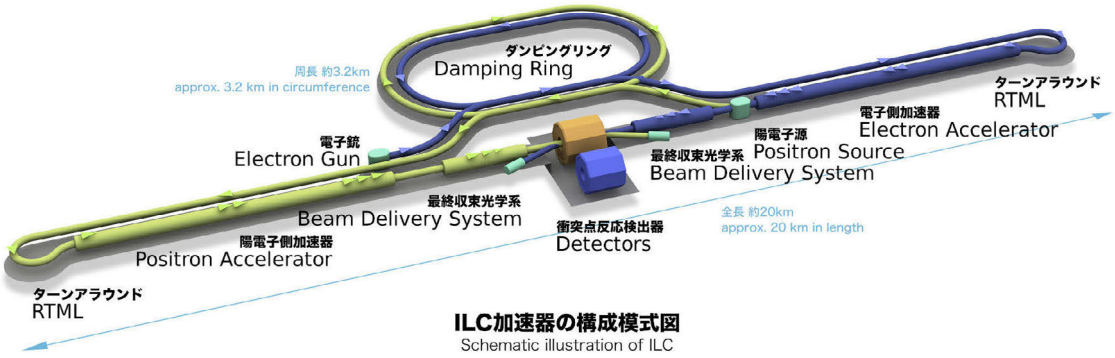

Figure 2.1.: A schematic illustration of the ILC accelerator complex (not to scale). The main subsystems are labelled. © Rey.Hori/KEK [88]

be operated in the upgraded system. A full, detailed description of the machine design can be found in ref. [89, 90] and the design changes made to optimise the machine for 250 GeV operation are described in ref. [84].

2.1.1. Particle Sources

The polarised electron source consists of a semiconductor photocathode that is illuminated by a circularly polarised laser inside a direct current (DC) electron gun. The most promising material for the photocathode are strained superlattices of thin, alternating layers of gallium arsenide (GaAs) and gallium arsenide phosphide (GaAsP), which typically provide electron polarisation of at least 85 % [91]. For illumination, a titanium-sapphire laser with a wavelength of 790 nm, matching the band gap in the semiconductor, is used. The pulses generated by the gun are compressed by a bunching system into ~20 ps long bunches.

The positron source uses the electron beam in the main linear accelerator (linac). Therefore, its performance and design depend on the beam energy. Below, the parameters for the ILC at $\sqrt{s} = 250$ GeV are presented. By passing the electrons through a 231 m long helical undulator, a multi-MeV beam of circularly polarised photons is generated. The photons are directed at a thin titanium-alloy target to produce electromagnetic showers of polarised electrons and positrons. The positrons from these showers are captured and accelerated to 125 MeV before being separated from the remaining photons and shower electrons, which are dumped afterwards. The baseline positron polarisation achieved this way is 30 %. Since for the 500 GeV machine the photon yield in the undulator is higher, this can be increased to 60 % by introducing an additional photon collimator in front of the target to absorb more photons with the wrong polarisation state [90].

Both beams, electrons and positrons, are accelerated to 5 GeV in a superconducting (SC) linac. Afterwards the polarisation vectors are rotated from the longitudinal direction to the vertical to preserve the polarisation in the damping rings.

2.1.2. Damping Rings

The ILC has two damping rings (DRs), one for the electrons and one for the positrons, each with a circumference of 3.2 km. The rings are operated at beam energies of 5 GeV. Their main function is to reduce the large transverse and longitudinal emittances of the electron and positron beams to the level required to reach the intended high luminosity at the IP. This is achieved by a 100 m long system of superconducting wigglers operating at ~2 T, forcing the beam particles to emit synchrotron radiation. The average beam energy lost in this process is recuperated by systems of superconducting radio-frequency (SCRF) cavities. This way the emittances are reduced by up to six orders of magnitude (in case of the positron vertical emittance) [90].

2.1.3. Main Linacs

From the damping rings, located in the central region of the ILC complex, the electron and positron beams are transported to the upstream ends of the respective main linacs by the so-called ring to main linac (RTML) systems. Before injection into the main linac the spin polarisation vectors are rotated from the vertical to any arbitrary angle, i.e. generally to a longitudinal orientation. Additionally the bunches are compressed in length to the size required at the IP. At the same time, the beam energy is increased to 15 GeV.

The main linacs then accelerate the beams to their final collision energy. The length of each linac is defined by the desired centre-of-mass energy and the field gradient of the acceleration structures. The design gradient for the ILC cavities is 31.5 MV/m, resulting in a length of about 5 km for each linac, including an energy margin of 6 %. To recover the energy lost in the undulators of the positron source, the electron beam also passes an extra length of accelerator afterwards. The acceleration structures intended to be used for the ILC are SCRF cavities made of pure niobium, originally developed as part of the TESLA project [92]. Extensive R&D effort has gone into the design of these cavities and the development of an industrial mass production. The technology was first successfully operated at the TESLA Test Facility (TTF), which was later developed into the Free-Electron Laser in Hamburg (FLASH), where now electrons are accelerated up to 1.25 GeV with field gradients exceeding 25 MV/m [93]. A further milestone for the technology was the construction and commissioning of the European X-ray Free-Electron Laser (XFEL) [94]. For the 3.5 km long linac more than 800 nine-cell cavities were produced by industry partners, showing that a mass production on the scale required for the ILC is possible. The XFEL cavities reach an average gradient of 30 MV/m [95] and the full linac is successfully operated at electron beam energies of up to 17.5 GeV [96].

2.1.4. Beam Delivery System

From the end of the main linacs the beams are guided to the interaction point by the beam delivery system (BDS), which also includes the transport lines to the beam dumps. In addition, the BDS fulfils several other tasks. First, it provides beam diagnostics, including emittance measurement and correction, trajectory feedback as well as polarimetry and en-

ergy spectroscopy. The latter two systems determine the polarisation $\mathcal{P}$ and energy E with precisions of $\Delta\mathcal{P}/\mathcal{P} = 0.25\,\%$ and $\Delta E/E = 10^{-4}$ bunch-to-bunch [97]. Furthermore, a collimation system removes beam-halo particles that could create excessive background in the detector. Finally, the BDS contains the final focussing system that focusses the beams at the IP to achieve the beam cross section with a vertical size of a few nanometres and a horizontal size of a few hundred nanometres. The two beams have a crossing angle of 14 mrad in the horizontal plane to provide the space for the separate extraction lines. This reduces the geometric overlap of the two colliding bunches and thus the luminosity. Therefore, so-called crab cavities are used that rotate the bunches in the horizontal plane to effectively create head-on collisions [98, 99].

2.1.5. Beam Parameters and Bunch Structure

The beams at the ILC are accelerated in pulses, so-called bunch trains, with a repetition rate of 5 Hz. Each train contains 1312 bunches, separated by 554 ns, for a total length of ~0.7 ms, leaving over 199 ms without activity in the interaction region between trains. This structure

Table 2.1.: Selected beam parameters at the interaction point of the ILC optimised for 250 GeV [100]. For values that have changed from the TDR the original values are given in brackets.

parameter		unit	value	
bunch population	N	10^{10}	2	
bunch separation	Δt_b	ns	554	
number of bunches per pulse	n_b		1312	
pulse repetition rate	f_rep	Hz	5	
RMS bunch length	σ_z	µm	300	
electron RMS energy spread	$\Delta p/p$	%	0.19	
positron RMS energy spread	$\Delta p/p$	%	0.15	
electron beam polarisation	$\mathcal{P}_-$	%	80	
positron beam polarisation	$\mathcal{P}_+$	%	30	
horizontal emittance	$\gamma\epsilon_x$	µm	5	(10)
vertical emittance	$\gamma\epsilon_y$	µm	35	
RMS horizontal beam size	σ_x	nm	516	(729)
RMS vertical beam size	σ_y	nm	7.66	
horizontal disruption parameter	D_x		0.51	(0.26)
vertical disruption parameter	D_y		34.5	(24.5)
avg. beamstrahlung energy loss	δ_BS	%	2.62	(0.97)
photons per beam particle	n_γ		1.91	(1.21)
e^+e^- pairs per bunch crossing	N_pairs	10^3	n.s.	(62.4)
geometrical luminosity	L_geo	$10^{34}\,\mathrm{cm}^{-2}\,\mathrm{s}^{-1}$	0.53	(0.37)
total instantaneous luminosity	L	$10^{34}\,\mathrm{cm}^{-2}\,\mathrm{s}^{-1}$	1.35	(0.82)

has certain implications for the design of the detectors. These are discussed in section 2.3. The full beam parameters are listed in table 2.1. They are constrained by the capabilities of the various subsystems of the accelerator as well as the goal to maximise the physics performance in the form of luminosity and acceptable beam induced backgrounds. For the updated 250 GeV baseline operation the beam parameters were changed to increase the instantaneous luminosity from $L = 0.82 \cdot 10^{34}\,\mathrm{cm}^{-2}\,\mathrm{s}^{-1}$ in the TDR to $1.35 \cdot 10^{34}\,\mathrm{cm}^{-2}\,\mathrm{s}^{-1}$ [100]. This is achieved by reducing the horizontal size of each beam at the IP. However there are additional consequences of this change due to the interaction between the two bunches just before the collision, including an increased disruption of the beams and a larger background from beamstrahlung. Both effects are explained in the next section.

2.1.6. Pinch Effect and Beamstrahlung

The design of the ILC makes use of the bunch-bunch interaction at the collision point to increase the achievable luminosity. Due to the high charge density within a single bunch, the beams generate strong electromagnetic fields, that have a focussing effect for the oncoming particles of opposite charge. This so-called pinch effect reduces the effective beam size at the IP, which leads to an increased luminosity. The effect only becomes relevant at linear colliders due to the highly focussed beams that are required to reach the desired instantaneous luminosity. The luminosity at a linear collider is given by [101]

$$L = H_D \cdot L_{\mathrm{geo}} \approx H_D \cdot \frac{N}{4\pi\sigma_x\sigma_y} \cdot N n_{\mathrm{b}} f_{\mathrm{rep}} \quad , \tag{2.1}$$

where L_{geo} is the luminosity expected purely from the beam geometry and the beam current. The luminosity enhancement due to beam-beam interaction is described by the factor H_D, which generally grows with the disruption parameters $D_{x/y}$ [101]. The disruption parameters are defined as [102]

$$D_{x/y} = \frac{2Nr_{\mathrm{e}}\sigma_z}{\gamma\sigma_{x/y}(\sigma_x + \sigma_y)} \quad , \tag{2.2}$$

with the classical electron radius r_{e} and the relativistic Lorentz factor γ.

While it may seem desirable to maximise H_D, and therefore $D_{x/y}$, to achieve the highest effective luminosity, there are other effects to consider that arise from the disruption of the beams. Firstly, a stronger disruption of the beams requires a more accurate beam position feedback at the IP. Otherwise, misalignment of the beams can induce the so-called kink instability [101], which leads to a growing displacement of the two beams over time, causing a loss of luminosity. Secondly, when the particles in one bunch are deflected in the strong electromagnetic field generated by the opposing bunch they emit photons in a process similar to synchrotron radiation, as is shown in figure 2.2. This radiation is called beamstrahlung (BS) Each beam particle emits on average $n_\gamma \propto 1/(\sigma_x + \sigma_y)$ photons, which carry away a fraction $\delta_{\mathrm{BS}} = \langle -\Delta E_\gamma / E \rangle \propto 1/(\sigma_x + \sigma_y)^2$ of the particle's energy [101]. Typically, values of $n_\gamma = \mathcal{O}(1)$ and $\delta_{\mathrm{BS}} \leq \mathcal{O}(10\,\%)$ are aimed for. Since the process is non-Gaussian the average energy loss is strongly influenced by the presence of a tail towards higher values in the distribution, while the most probable value is much lower. It is possible to maximise the

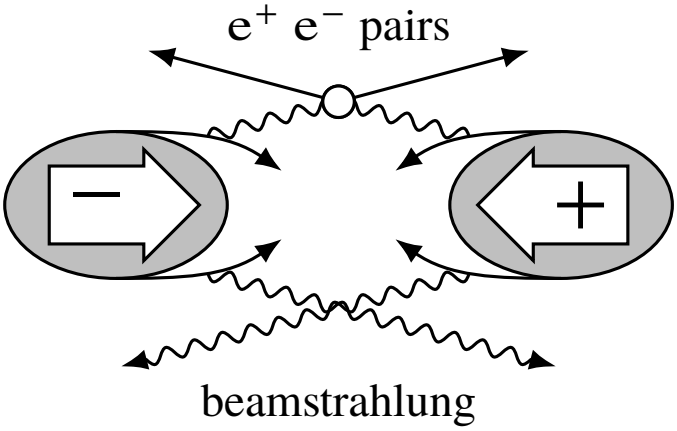

Figure 2.2.: Sketch of the beamstrahlung photon emission and pair production processes. Illustration adapted from ref. [103].

luminosity while keeping the beam disruption and beamstrahlung at an acceptable level by choosing a very flat beam profile with $\sigma_x \gg \sigma_y$. This minimises the product $\sigma_x\sigma_y$ for a high luminosity, while keeping the sum $\sigma_x + \sigma_y$ large to reduce $D_{x/y}$, n_γ and δ_{BS}.

The generated photons can also undergo further interactions with beamstrahlung or virtual photons emitted from the opposing bunch, creating e^+e^- pairs or hadrons. While the number of such pairs is not specified for the updated parameters in ref. [100], for the original ILC parameters typically $\mathcal{O}(10^6)$ pairs are created per bunch crossing [104]. Due to their relatively low transverse momentum the detector solenoid focusses the pair particles tightly around the beam axis and most leave the detector through the beam pipes. However, due to their large number they can cause a significant background in the subdetectors closest to the beam axis, i.e. the vertex detector. This pair background can be mitigated by limiting the number of bunch crossings the detector integrates over during one readout frame [105]. During reconstruction the background can be further reduced by requiring additional matching hits in subdetectors at larger radii in the pattern recognition. The number of hadrons generated is much lower. For most ILC parameter sets $\mathcal{O}(1)$ $\gamma\gamma \rightarrow$ hadrons interaction per bunch crossing takes place on average, each producing a few hadrons [106]. While also these hadrons have low transverse momenta, they are not as tightly forward focussed as the e^+e^- pairs so that they traverse more parts of the detector. Therefore they can present a challenging background to analyses with multi-jet final states, especially at higher centre-of-mass energies. However, dedicated jet clustering algorithms are able to efficiently separate the hard collision event from this background [107].

2.2. The ILC Running Scenario

To best utilise the runtime of the ILC, several scenarios regarding runtime with different beam parameters, including centre-of-mass energy and polarisation, have been proposed by the ILC Parameters Joint Working Group [108]. Based on an evaluation of the evolution of the measurement accuracies of several physics observables one scenario was recommended.

To reflect the change to a first stage at a centre-of-mass energy of 250 GeV, this recommendation has been updated in ref. [85].

The original running scenario recommended for the ILC in ref. [108] assumes an initial centre-of-mass energy of 500 GeV, reflecting the premise of the TDR. Following this plan, in a first running period the ILC would provide integrated luminosities of 500 fb^{-1}, 200 fb^{-1} and 500 fb^{-1} at centre-of-mass energies of 500 GeV, 350 GeV and 250 GeV, respectively, in this order. After an upgrade to increase the instantaneous luminosity, further 3500 fb^{-1} at 500 GeV and 1500 fb^{-1} at 250 GeV would be accumulated, resulting in the total integrated luminosities of 4000 fb^{-1}, 200 fb^{-1} and 2000 fb^{-1} at 500 GeV, 350 GeV and 250 GeV, respectively, within a period of 20 years. Three main reasons led to the decision for a starting energy of 500 GeV:

- The availability of both major Higgs production processes, Higgs-strahlung and vector-boson fusion, to measure the Higgs couplings,
- the accessibility of the top quark couplings, including the top-Yukawa coupling,
- and the ability to utilise the full energy range for the discovery of new particles.

The subsequent, dedicated studies in ref. [85] show that the programme at a centre-of-mass energy of 250 GeV already results in compelling, model-independent constraints on the properties of the Higgs boson. Therefore a staged scheme with a long first stage at 250 GeV is also well motivated from a physics standpoint. In this scenario the same final integrated luminosities are foreseen. First the full integrated luminosity at 250 GeV is accumulated, with an upgrade of the instantaneous luminosity after 500 fb^{-1}. Then the machine is upgraded to higher centre-of-mass energies and the runs at 500 GeV and 350 GeV are performed.

The original scenario assumes a beam repetition rate of 10 Hz during 250 GeV operation instead of the default 5 Hz, utilising the full available cryogenic and radio frequency power of the 500 GeV machine. This option is not available with the initial stage of 250 GeV, which consequently must be stretched over a longer period of time to reach the desired integrated luminosity. With the baseline parameters assumed in the TDR this would require 15 years of operation at 250 GeV and 26 years for the full programme. Yet, by focussing the beams more strongly at the interaction point than foreseen in the TDR, as described in section 2.1.5, the instantaneous luminosity can be increased and the length of the 250 GeV stage can be reduced to 11 years. The required accelerator parameters for this option, including the impact on the beam induced backgrounds described in section 2.1.6, are discussed in ref. [84].

In all scenarios beam polarisations of $\mathcal{P}_{e^-} = \pm 80\,\%$ and $\mathcal{P}_{e^+} = \pm 30\,\%$ are assumed. However, the combination of the different signs of the electron and positron beam polarisation $(-,+)$, $(+,-)$, $(-,-)$ and $(+,+)$, where the first sign applies to the electron beam polarisation and the second to that of the positron beam, can have a significant impact on various physics processes. Therefore the fraction of the total integrated luminosity taken with each of the combinations must be adapted to the physics programme at each centre-of-mass energy. For the 250 GeV data set the original scenario foresees fractions of 67.5 %, 22.5 %, 5 % and 5 %, respectively. The $(-,+)$ configuration is prioritised because it has the largest Higgs production cross section. In ref. [85] the left-right cross-section asymmetry is

emphasised instead. Here, allocations of 45 %, 45 %, 5 % and 5 % are chosen, to optimise the measurement of this parameter. This sharing is also assumed in part II of this work. At 350 GeV both scenarios propose fractions of 67.5 %, 22.5 %, 5 % and 5 % to maximise the production of $t\bar{t}$ -pairs via the s-channel exchange of Z bosons or photons. At 500 GeV the same-sign configurations are allocated larger fractions of the luminosity. This increases the discovery potential for new physics beyond the standard model, as within the standard model only few processes are allowed for same-sign chiralities. Therefore, a sharing of 40 %, 40 %, 10 % and 10 % is chosen.

While not part of the running scenario described above, the option to run the accelerator at the Z-resonance for an integrated luminosity of $100\,\mathrm{fb}^{-1}$, which is equivalent to about $3 \cdot 10^9$ hadronic Z events (*GigaZ*), is also considered [108]. This would allow to perform measurements of the electroweak parameters of the standard model with unprecedented precision. The analysis presented in part II of this thesis could benefit greatly from this data.

2.3. The International Large Detector

The International Large Detector (ILD) is one of the two detector concepts currently proposed for experiments at the ILC. The detector, shown in figure 2.3, has been designed for a wide range of precision measurements at collision energies between 90 GeV and 1 TeV with a focus on the performance at the initial energy of 250 GeV. Geometrically the detector can be separated in a barrel part and two end caps. In the barrel the subdetectors are arranged concentrically around the beam pipe, with a silicon-pixel vertex detector (VTX) located very close to the interaction point, followed by the main tracking detector, consisting of a combination of silicon sensor layers (inner and external silicon tracker; SIT, SET) with a time projection chamber (TPC), and the electromagnetic and hadron calorimeters (ECAL, HCAL). All of these are enclosed in the coil of a superconducting solenoid magnet. Placed on the outside of the coil is an iron yoke that returns the magnetic flux and is instrumented to serve as a tail catcher for the calorimeter system and as a muon system. The forward directions are instrumented similarly, including discs of silicon tracking layers around the beam pipe (forward tracking detector; FTD) and the end caps of the calorimeters, yoke and muon chambers. Additional calorimeters that are intended for measurement of the luminosity (LumiCAL) and the beam parameters (BeamCAL), extend the coverage in the forward directions, very close to the beam axis.

The beam structure at the ILC, described in section 2.1.5, in combination with the small cross section of hard electron-positron collisions, allows to operate the detector in a continuous readout mode without a hardware based trigger. Additionally, several subsystems, in particular the calorimeters and the TPC, are intended to operate in a so-called power-pulsing mode to reduce the required power and cooling [105]. In this mode parts of the front-end electronics are powered down after the data of each bunch train have been read out, until the next train arrives. To fulfil the challenging performance requirements, described in section 2.3.2, the detector has been optimised for application of the particle-flow reconstruction paradigm. Particle flow (PF) describes the approach to precisely reconstruct each individual

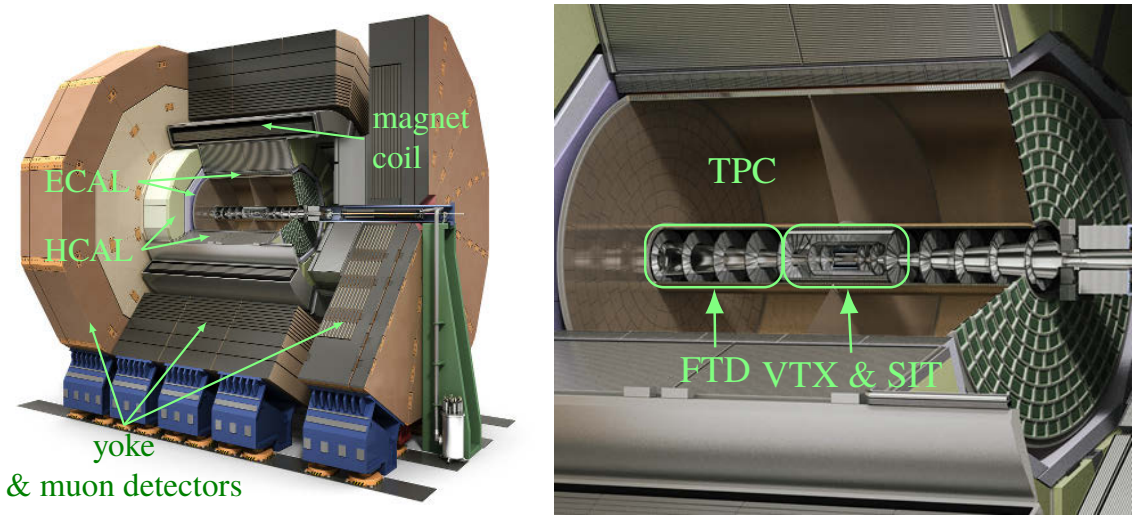

(a) Overview of the detector. **(b)** Detailed view of the inner detector.

Figure 2.3.: Artist's model of the ILD. © Rey.Hori/KEK [88]

Table 2.2.: The dimensions of the subdetectors for the large ILD model [87]. For the small model the outer radius of the TPC is reduced by 343 mm and the number of pad rows (layers) is reduced to 163. The values marked with * are adjusted accordingly. The acronyms are explained in the text.

	system	r_{min} [mm]	r_{max} [mm]	$\lvert z\rvert_{\text{min}}$ [mm]	$\lvert z\rvert_{\text{max}}$ [mm]	layers
barrel	VTX	16	60		125	3×2
	SIT	153	303		644	2×2
	TPC	329	1770*		2350	220*
	SET	1773*	1776*		2300	1×2
	ECAL	1805*	2028*		2350	30
	HCAL	2058*	3345*		2350	48
	coil	3425*	4175*		3872	—
	muon system	4450*	7755*		4047	14
end caps	FTD (pixel)	$\theta \geq 4.8°$	153	220	371	2
	FTD (strip)		300	645	2212	5×2
	ECAL	250	2096*	2411	2635	30
	HCAL	350	3226*	2650	3937	48
	LumiCAL	84	194	2412	2541	30
	LHCAL	130	315	2680	3160	n.s.
	BeamCAL	18	140	3115	3315	30
	muon system	350	7716*	4072	6712	12

particle in an event, using the full available information from all subdetectors. The concept is presented in more detail in section 2.3.3. Afterwards the subdetectors relevant for this thesis are described briefly in sections 2.3.4 to 2.3.6. The focus here lies on the time projection chamber of the main tracking system, to motivate the research presented in part I of this thesis.

The complete ILD concept is described in detail in the ILC TDR [105], also referred to as the detailed baseline document (DBD), and a dedicated interim design report (IDR) [87] that includes updates and development results since the TDR. One such update is a study of the performance impact of scaling down the detector's length or radius to reduce the overall cost. This resulted in a version of the detector with a smaller radius of the main tracker and consequently all external subsystems, e.g. calorimeters, coil, yoke and end caps, while keeping the inner subdetectors and the depth of the calorimeters unchanged. To compensate for the reduced lever arm in the tracking system, the nominal magnetic field of the solenoid is increased from 3.5 T to 4 T. The dimensions of the subdetectors are given in table 2.2. In the rest of this work the baseline, large version is designated ILD-L and the new, smaller one ILD-S. If not specified, the baseline version is implied.

2.3.1. The ILD Coordinate System

The coordinate system used globally for the ILD has its origin at the interaction point. Generally, Cartesian coordinates are used to describe locations, e.g. of vertices. The z-axis is parallel to the beam axis and pointing into the direction of the electron beam, the y-axis is pointing upwards and the x-axis points sideways in the horizontal plane, such that a right-handed coordinate system is formed. To describe directions, e.g. of particle momenta, polar coordinates are used, where the azimuthal angle φ is measured from the x-axis in the xy-plane and the polar angle θ is measured from the z-axis. Locally, many subdetectors use cylindrical coordinates with the radius r measured perpendicular to the z-axis and the azimuth angle φ as above. In this context the coordinate $r\varphi$ describes the distance along the circumference of a circle of a given radius r around the axis corresponding to the angle φ.

2.3.2. Detector Performance Requirements

The performance requirements of the ILD are defined based on the physics goals of the ILC. Therefore both versions of the detector, ILD-S and ILD-L, are designed to fulfil the same requirements.

The goal for the momentum resolution was chosen such that the Higgs mass measurement via the recoil mass in the Higgs-strahlung process $e^+e^- \to Zh,\ Z \to \mu^+\mu^-$ at $\sqrt{s} = 250\,\text{GeV}$ is dominated by the beam energy spread, given in table 2.1, and not the uncertainty of the muon momentum measurement. This results in a requirement of

$$\sigma_{1/p_t} = \frac{\sigma_{p_t}}{{p_t}^2} = 2 \cdot 10^{-5}\,\text{GeV}^{-1} \oplus \frac{10^{-3}}{p_t \sin\theta} \quad , \tag{2.3}$$

where $p_t = p \sin\theta$ is the transverse momentum. The first term describes the resolution for high particle momenta. It is defined by the detector geometry, point resolution in the

transverse plane $\sigma_{r\varphi}$ and magnetic field B via the Gluckstern formula [109]

$$\delta_{1/p_\mathrm{t}} = \frac{\sigma_{r\varphi}}{qBL^2}\sqrt{\frac{720}{N+4}} \ , \tag{2.4}$$

where L is the lever arm of the tracking system, N is the number of (equidistant) measurement points and $q = 1\,\mathrm{e} \approx 0.3\,\mathrm{GeV/(T\,m)}$ is the charge of the particle. The second term of equation (2.3) describes the contribution due to multiple scattering. The constant in the numerator is mainly defined by the radiation length X_0 in the detector material and the total length of the trajectory [18].

Many analyses in the ILC physics programme rely on flavour tagging to identify jets from heavy c or b quarks as well as to separate the two, e.g. for measuring the Higgs branching fraction into c quarks $\mathcal{B}(\mathrm{h} \to \mathrm{c\bar{c}})$. Since the main signature of heavy quark jets are secondary vertices from decays of D and B mesons that are offset from the IP, measuring the impact parameter of tracks is particularly important. Therefore, the resolution of the transverse impact parameter d_0 is required to fulfil

$$\sigma_{d_0} = 5\,\mu\mathrm{m} \oplus \frac{10\,\mu\mathrm{m}}{(p/\mathrm{GeV})\sin^{3/2}\theta} \ . \tag{2.5}$$

Other measurements require the ability to separate the hadronic decays of the massive gauge bosons $\mathrm{W}^\pm$ and Z as well as the Higgs boson h. One example is the measurement of the quartic gauge coupling vertices $\mathrm{W^+W^-} \to \mathrm{W^+W^-}$ and $\mathrm{W^+W^-} \to \mathrm{ZZ}$. These can be probed at $\sqrt{s} = 0.5\,\mathrm{TeV}$ to 1 TeV in the process $\mathrm{e^+e^-} \to \nu\nu VV \to \nu\nu qqqq$, where VV can be either $\mathrm{W^+W^-}$ or ZZ. Therefore the di-jet mass resolution must be smaller than the natural widths of the gauge bosons, i.e. $\sigma_{m_{\mathrm{jj}}}/m_{\mathrm{jj}} < \Gamma_\mathrm{Z}/M_\mathrm{Z} \approx \Gamma_\mathrm{W}/M_\mathrm{W} \approx 2.7\,\%$. This defines the requirement for the jet energy resolution (JER) of

$$\sigma_{E_\mathrm{jet}}/E_\mathrm{jet} \approx 3\,\% \text{ to } 4\,\% \tag{2.6}$$

for the typical jet energies of $\mathcal{O}(100\,\mathrm{GeV})$ in the processes above [110]. This requirement translates into a stochastic term of $\sigma_E/E \sim 30\,\%/\sqrt{E/\mathrm{GeV}}$ in the calorimeter resolution. This is very difficult to achieve with traditional calorimetry approaches, cf. the compensating uranium hadron calorimeter of the ZEUS detector at HERA [111]. Recent collider experiments have typically only reached stochastic terms of 50 % to 100 % [112, 113]. Therefore, a new approach to jet energy reconstruction is necessary.

2.3.3. The Particle Flow Concept

Particle flow is a strategy for jet energy reconstruction that diverges from the traditional, purely calorimetric technique [114]. It is based on the knowledge that on average about 60 % of the jet energy is carried by charged particles, most of which are hadrons, 30 % by photons and 10 % by neutral hadrons. In the traditional approach this means that the jet energy resolution is dominated by the accuracy of the hadron calorimeter, as it is used to measure ~70 % of the jet energy. The particle flow method reduces the impact of the hadronic energy resolution by identifying and separating individual particles and reconstructing their

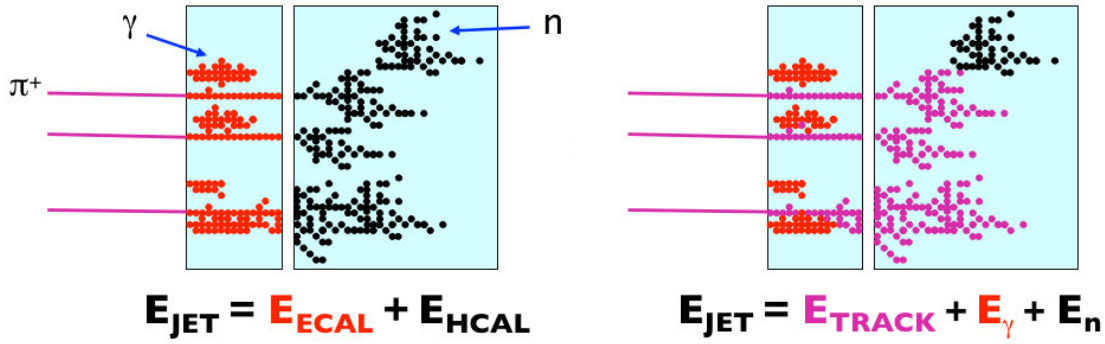

(a) Classical calorimetry approach. **(b)** Particle flow approach.

Figure 2.4.: Sketches comparing (a) the classical calorimetry and (b) the particle flow approaches to measuring the jet energy [115].

four-vectors in the best suited subdetector, i.e. charged particles benefit from the excellent momentum resolution of the tracking system, the electromagnetic calorimeter provides a reasonable photon energy resolution and only the neutral hadrons rely on the relatively poor energy resolution of the hadron calorimeter. Figure 2.4 illustrates the differences between both techniques.

In the particle flow approach the jet energy resolution is limited by the ability to correctly associate energy deposits in the calorimeter to the particles reconstructed in the tracker. This in turn relies on the capability to separate energy deposits from individual particles within the calorimeters. For the case of perfect assignment an energy resolution of $\sigma_E/E \sim 20\,\%/\sqrt{E/\mathrm{GeV}}$ could be achieved for a detector like the ILD [114] but situations where the assignment process fails deteriorate this performance. This so-called confusion can be broadly described in two categories. On the one hand, if energy deposits from a charged particle are not correctly linked to the corresponding track, they can be identified falsely as an additional neutral particle or part of an existing one and the energy is counted twice. On the other hand, it is possible that a shower from a real neutral particle is not fully separated from a charged shower and thus a part of the energy deposit, or all of it, is falsely associated to the charged particle and not counted at all.

The goal to keep the confusion as small as possible strongly influences the design of the ILD calorimeters and the tracking system. An efficient matching of tracks to showers in the calorimeters requires a high tracking efficiency down to very low particle momenta, as well as a minimal amount of material in front of the calorimeters to minimise multiple scattering of these low momentum particles. These requirements contributed to the decision for a TPC as the main tracking device of the ILD. The large number of measurement points results in an excellent pattern recognition, which enables almost perfect tracking efficiency for all particles with transverse momenta $p_\mathrm{t} \geq 0.3\,\mathrm{GeV}$ [87]. Below this momentum they no longer traverse enough of the TPC volume. For the calorimeters the separation of energy deposits relies heavily on topological information and pattern recognition. Thus imaging calorimeters with high readout granularities are needed.

Using a detailed model of the detector described in this section, the performance of the

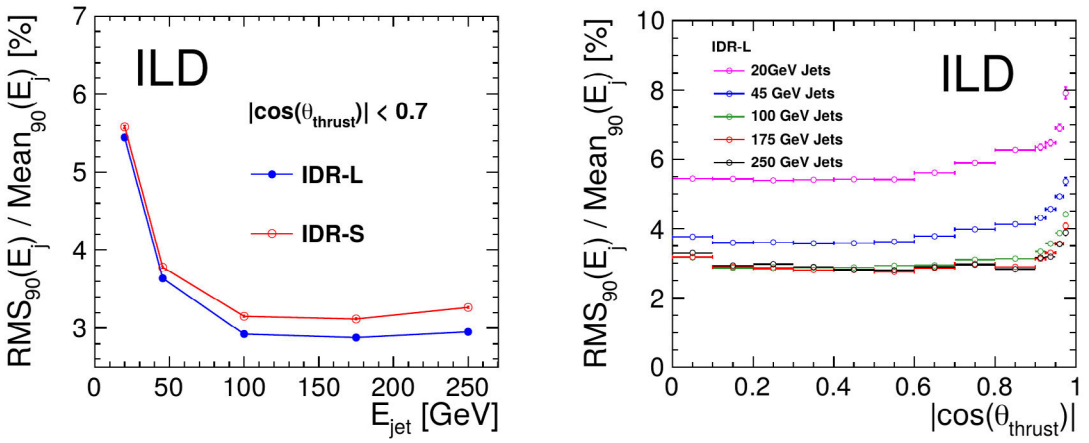

(a) Energy dependence. **(b)** Polar angle dependence.

Figure 2.5.: The jet energy resolution achieved in simulation [87]. (a) Comparison for jets in the barrel region of the large (IDR-L) and small (IDR-S) ILD models at various jet energies. (b) Dependence on the jet polar angle at the different jet energies for the large ILD model.

particle-flow algorithm (PFA) has been evaluated [87]. The simulation employed $Z \to q\bar{q}$ events, $q = u, d, s$, where the Z decayed at rest and its mass was varied to achieve the desired jet energies. This event topology was chosen to separate the pure jet energy resolution from effects arising from other sources that occur in more complex scenarios, e.g. confusion in jet clustering. Results of this simulation are shown in figure 2.5. For jet energies ≥45 GeV the jet energy resolution is better than the required 4 % and approaches 3 % for higher energies. Almost no dependence on the polar angle is observed. Only in the very forward region the resolution visibly deteriorates.

2.3.4. Calorimeter System

The considerations for the design choices of the ILD calorimeter system are given in the TDR [105]. The design is mainly driven by the requirements of the particle flow approach. Separating individual showers originating from different particles in the calorimeters is emphasised over the intrinsic energy resolution. A small radiation length X_0 and Molière radius R_M of the absorber material is needed to keep electromagnetic showers compact to cope with high particle densities. To observe the transverse and longitudinal shower profile as well as substructures of the showers, a high granularity of the readout is required in all three dimensions. It has been shown that it must be of the order of X_0 and R_M. Therefore, sampling calorimeter designs were identified as the optimal choice for all calorimeter subsystems. In addition the system needs to cover close to the full 4π solid angle and be deep enough to minimise leakage of high energy showers. In depth the calorimeter system is divided into an electromagnetic calorimeter (ECAL) in front of a hadron calorimeter (HCAL). In the end caps these are complemented by additional calorimeters at small angles to the beam axis, the LumiCAL, low-angle hadron calorimeter (LHCAL) and BeamCAL.

Electromagnetic Calorimeter

The main task of the ECAL is to identify photons and measure their energy. The baseline design [87] uses 30 layers of tungsten absorber ($X_0 = 3.5\,\text{mm}$, $\lambda_\text{I} = 9.6\,\text{cm}$ [18]). It has a total depth of $24\,X_0$ or 0.85 nuclear interaction lengths λ_I within a space of 20 cm. This large ratio of λ_I/X_0 helps to separate electromagnetic and hadronic showers longitudinally [105]. Alternating with the absorber are the readout layers, for which a transverse size of the readout cells of 5 mm × 5 mm was chosen. Two readout technologies are considered, or a combination of both. The baseline option are silicon sensors, which easily achieve the required granularity. The other option are scintillator strips read out by silicon photomultipliers (SiPMs). The individual scintillator strips have dimensions of 5 mm × 45 mm and are intended to be arranged in alternating layers with orthogonal orientation of the strips to effectively achieve the desired cell size. Tests of prototypes with electron beams reached stochastic terms of the energy resolution of 16.5 % for the silicon option [116] and 12.5 % for the scintillator option [117], while the constant terms are ~1 % in both cases.

Hadron Calorimeter

The HCAL must provide topological separation of hadronic showers in order to identify neutral hadrons and measure their energy. Its design [87] foresees 48 steel absorber layers ($X_0 = 1.8\,\text{cm}$, $\lambda_\text{I} = 16.8\,\text{cm}$ [18]) with a total depth of $6\,\lambda_\text{I}$ within the extent of 1.3 m. Two technologies are considered for the readout layers. One option are scintillator tiles of 3 cm × 3 cm that are read out by SiPMs, providing an analogue measurement of the energy deposition in each cell. The other variant uses resistive plate chambers (RPCs), which enable a higher granularity with cells of 1 cm × 1 cm, but only foresees a 2 bit, so-called semi-digital, energy measurement. A combined system of scintillator based ECAL and HCAL prototypes achieved single particle energy resolutions for pions with momenta between 4 GeV and 32 GeV between about 20 % and 8 %, respectively [118].

Forward Calorimeters

The forward calorimeters, LumiCAL, LHCAL and BeamCAL, need to operate with much higher occupancies than the ECAL and HCAL, due to beamstrahlung and the resulting pair particles [87]. Therefore all three foresee tungsten absorber layers with a thickness of $1\,X_0$, alternating with finely segmented readout layers. While the LHCAL, placed in a cut-out in the HCAL end cap, only serves to extend the hadron calorimeter coverage in the forward directions, the other two are designed to perform specific additional tasks.

The LumiCAL measures the integrated luminosity with high precision by counting the electrons and positrons originating from Bhabha scattering events at the IP [105]. It is positioned in a circular hole in the ECAL end cap. The readout layers consist of silicon sensors with pads in the shape of concentric ring sections covering an angle of $\Delta\varphi = 30°$ and a radial pitch of 1.8 mm.

The BeamCAL provides a bunch-by-bunch estimate of the luminosity by measuring the energy deposited by beamstrahlung pairs [105]. Additionally it can be included in a fast feedback system for beam tuning. It is placed behind the LHCAL, extending the calorimeter

coverage down to 6 mrad to the beam axis [87]. Due to the large particle flux at these small angles, the BeamCAL requires radiation hard sensors. Therefore, several options for the sensor material are investigated, namely GaAs, diamond and sapphire [87]. The size of the readout pads will be in the order of 5 mm × 5 mm.

2.3.5. Main Tracking System

The main tracking device of the ILD is a time projection chamber (TPC), which offers continuous tracking with a large number of three-dimensional space points. This is complemented by layers of silicon sensors in front of and behind the TPC, the so-called silicon envelope. These few precisely measured space points added before and after the TPC greatly improve the overall momentum resolution. Additional silicon tracker discs cover the forward regions at polar angles below the TPC acceptance. A detailed view of the tracking systems within the inner detector is shown in figure 2.3b on page 21.

The track momentum resolution of the ILD models has been evaluated using single muon events [87]. The muons were simulated with fixed momenta between 1 GeV and 100 GeV and polar angles of 10°, 20°, 40° and 85°. In figure 2.6a the resulting transverse momentum resolution σ_{1/p_t} is shown. The goal of $2 \cdot 10^{-5}\,\text{GeV}^{-1}$ for the asymptotic resolution stated in equation (2.3) on page 22 is achieved for central tracks. For the polar angles of 10° and 20° the simulated resolution degrades slightly faster than equation (2.3).

The tracking efficiency was evaluated using simulated $t\bar{t}$-events at $\sqrt{s} = 500\,\text{GeV}$ [87]. As is shown in figure 2.6b, it is close to 100 % for tracks with transverse momenta larger than

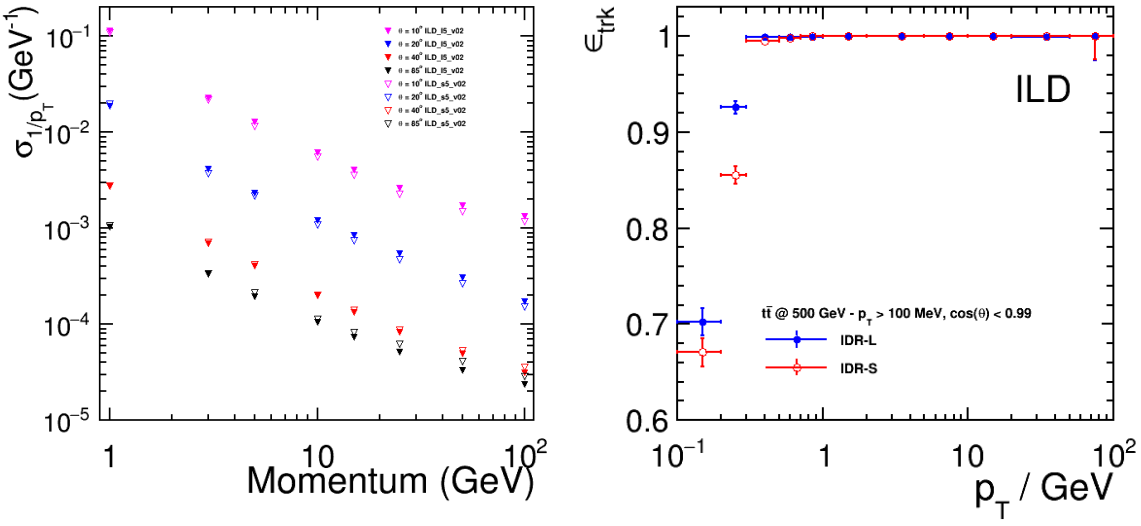

(a) Momentum resolution.

(b) Tracking efficiency.

Figure 2.6.: Performance of the tracking system in the large (IDR-L) and small (IDR-S) ILD models [87]. (a) The dependence of the transverse momentum resolution on the total particle momentum at different polar angles. Full markers represent the large model, open markers the small one. From top to bottom the series are at polar angles of 10°, 20°, 40° and 85°. (b) The tracking efficiency in dependence of the transverse momentum.

~0.3 GeV. The simulation also shows that it is better than 99 % even in the very forward direction, $0.95 < \cos\theta < 0.99$.

Silicon Tracking System

The silicon envelope consists of two subsystems, the inner silicon tracker (SIT), providing two space points between the vertex detector and the TPC, and the external silicon tracker (SET) providing an additional measurement between the TPC and the ECAL barrel. The main tasks of these systems are to help connect the stand-alone tracks found in the vertex detector and the TPC, to contribute additional precisely measured space points at a large lever arm for an improved momentum resolution and to provide time-stamping information. In the TDR [105] double-layers of strip sensors with a small stereo angle were foreseen for both subsystems, achieving a resolution of $\sigma_{r\varphi} = 7\,\mu\text{m}$ in $r\varphi$-direction and $\sigma_z = 50\,\mu\text{m}$ in z-direction. With technological advancements in CMOS technology, the IDR [87] includes the option to use pixel sensors in the SIT. For the SET the option to use sensors with high timing resolution of $\mathcal{O}(10\,\text{ps})$ is considered, to enable time-of-flight (TOF) measurements for particle identification.

The forward tracking detector (FTD) consists of seven discs, providing stand-alone tracking coverage at polar angles between 16° and 4.8°. To retain the momentum resolution for tracks under such shallow angles relative to the magnetic field, the FTD provides a single hit resolution in $r\varphi$ of $\sigma_{r\varphi} \leq 7\,\mu\text{m}$ [105]. The inner two discs are equipped with pixel sensors, to provide an accurate measurement of the radial component as well, which is required for a precise measurement of the longitudinal impact parameter z_0 for very forward directed tracks. Otherwise the measurement of the radial component is more relaxed with a required resolution of several hundred microns. Therefore the outer five discs are equipped with double-layers of strip sensors, arranged under a small stereo angle.

Time Projection Chamber

The main advantage of a TPC as main tracking device is the capability of highly redundant, continuous three-dimensional tracking. In addition to the very good tracking efficiency, the 3D-imaging capability allows to reconstruct non-pointing tracks, which indicate the decay of a charged particle within the tracking volume, e.g. $\pi^+ \to \mu^+\nu_\mu$. Also the decays of long-lived neutral particles, e.g. K^0_S, into charged particles inside the TPC can be identified easily. Additionally, the TPC offers a minimal amount of material in front of the barrel calorimeters. The material budget in this region is dominated by the field cage walls, in particular the outer wall. This limits multiple scattering within the tracking volume, improving momentum resolution and the performance of particle-flow algorithms. The low amount of material also helps to mitigate backgrounds from pair conversions of beamstrahlung photons. Finally, a TPC intrinsically provides particle identification via a measurement of the specific energy loss $\mathrm{d}E/\mathrm{d}x$, which can be a valuable tool for various physics analyses.

To benefit from these advantages, the TPC must satisfy challenging performance requirements that have been specified in the TDR [105]. Most importantly, to achieve the required overall momentum resolution of the tracking system, the stand-alone resolution of the TPC

needs to fulfil $\delta_{1/p_t} \leq 10^{-4}\,\mathrm{GeV}^{-1}$. Following equation (2.4) on page 23, for the baseline number of 220 readout rows, this corresponds to a single point resolution in the transverse plane of $\sigma_{r\varphi} \leq 100\,\mu\mathrm{m}$. In addition a transverse point resolution at zero drift distance of $\sigma_{r\varphi} = 60\,\mu\mathrm{m}$ is specified. The measurement of the longitudinal coordinate is mainly needed to match tracks in the TPC to hits in the silicon envelope. Therefore, the goal for the longitudinal point resolution is more relaxed with $\sigma_z = 0.4\,\mathrm{mm}$ to 1.4 mm at zero to full drift distance, respectively. The corresponding goals for the two-hit resolution are 2 mm and 6 mm in $r\varphi$ and z-direction, respectively. A total material budget of $0.05\,X_0$ including the field cage walls is allowed in the barrel region. The end caps, including the readout electronics, should stay below $0.25\,X_0$. The goal for the $\mathrm{d}E/\mathrm{d}x$ measurement is a relative resolution of 5 %.

The geometrical parameters of the TPC are given in table 2.2. The sensitive volume is divided by the central cathode into two equal drift volumes that are read out at the end caps. The readout is modular and each module is self contained with integrated gas amplification and readout electronics. The design performance cannot be achieved with multi-wire proportional chamber (MWPC) readouts [119]. Therefore, new readouts based on micro-pattern gaseous detectors (MPGDs) have been developed. The investigated options include pad-based readouts with ~1 mm × 6 mm pitch, using gas electron multipliers (GEMs) [120] or micro-mesh gaseous structures (Micromegas) [121] for gas amplification, as well as a pixel-based approach that implements a 55 µm × 55 µm pitch on silicon with an integrated Micromegas gas amplification (GridPix) [122]. The development of the GEM based option is the topic of part I of this thesis.

2.3.6. Vertex Detector

The main task of the vertex detector (VTX) is to resolve tracks and vertices that are offset from the primary interaction point, e.g. from decays of D or B mesons. This is used to identify heavy charm and bottom quarks or tau leptons, which is crucial for many parts of the ILC physics programme, e.g. the measurement of the Higgs branching ratios. Additionally, the vertex detector is capable of stand-alone tracking and thus contributes to the overall tracking performance.

A set of requirements has been formulated to achieve the envisaged impact parameter resolution [105]. The primary requirements are a point resolution better than 3 µm and a material budget below 0.15 % of an X_0 per layer. Additionally, the first layer needs to be at a radius of ~16 mm. Due to the beamstrahlung backgrounds this proximity to the IP makes the vertex detector one of the few subsystems for which radiation hardness is of concern. The backgrounds also dictate a requirement of a pixel occupancy below a few percent.

The baseline design [87] consists of three concentric cylindrical double-layers of silicon pixel sensors, where the two sensor-planes in each double-layer are ~2 mm apart. Three sensor technologies are under investigation, CMOS, depleted field effect transistor (DEPFET) and fine pixel CCD (FPCCD) sensors.

The impact-parameter resolution of the detector model has been evaluated using simulated single-muon events at various momenta and polar angles of 10°, 20°, 40° and 85° [87]. Figure 2.7a shows the resolution of the transverse impact parameter d_0 as a function of the

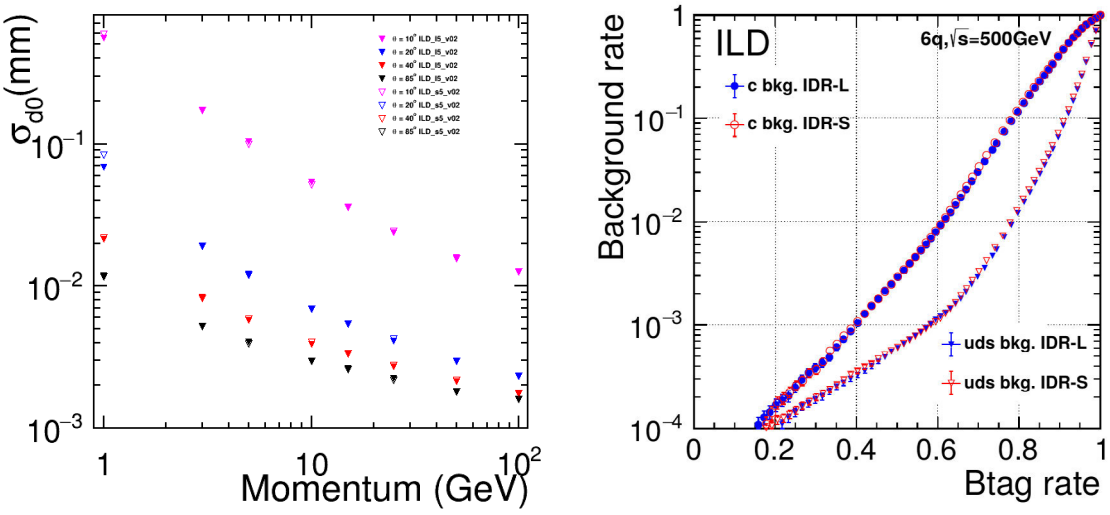

(a) d_0 resolution.

(b) b-tagging performance.

Figure 2.7.: Performance of the vertex detector in the large (IDR-L) and small (IDR-S) ILD models [87]. (a) The resolution of the transverse impact parameter for single muons as a function of the muon momentum. From top to bottom the series are at polar angles of 10°, 20°, 40° and 85°. The the large and small model, represented by full and open markers, respectively, perform almost identically. (b) The background rates for b-tagging as a function of the tagging efficiency in $e^+e^- \to 6q$ events at $\sqrt{s} = 500\,\text{GeV}$.

muon momentum. The resolutions achieved with the large and small ILD model are equal to within a few percent. Only at low momenta in the forward region the ILD-S performs worse since here the higher magnetic field increases the curvature and thus reduces the lever arm for the measurement. At large momenta the resolution is significantly better than the required asymptotic value of 5 µm. Also at low momenta the requirement is fulfilled. The resolution of the longitudinal impact parameter z_0 is similar to d_0 for tracks in the barrel region. In the forward region, where less VTX hits are available, it is significantly worse, e.g. by a factor of ~5 at $\theta = 10°$.

The vertex resolution and flavour-tagging performance was investigated with $e^+e^- \to 6q$ events at $\sqrt{s} = 500\,\text{GeV}$, where all quarks were chosen to have the same flavour [87]. As expected from the impact-parameter resolution, the large and small detector model perform very similarly. In the direction perpendicular to the jet axis the vertex resolution approaches 2 µm for increasing distances from the IP, whereas the resolution of the coordinate along the jet axis approaches 55 µm. The b-tagging performance is shown in figure 2.7b in terms of the background rates of c-quarks and light-flavour quarks, respectively, as functions of the tagging efficiency. The background from light quarks, which becomes important for the analysis in part II of this work, stays below 1 % up to an efficiency of about 0.75. For c-tagging this is the case up to an efficiency of about 0.45.

Part I.

Development of a Modular GEM based Readout for a TPC

3. Working Principles of Time Projection Chambers

A time projection chamber (TPC) is a type of drift chamber. In figure 3.1 the basic working principle is shown. As all tracking detectors, TPCs rely on the ionisation of the detection medium by highly energetic charged particles along their trajectory. For collider physics experiments most often gaseous mixtures with large fractions of noble gases are used as detection and drift medium. The ions and free electrons created by a passing charged particle are separated by applying an electric field across the chamber. This field forces the charges to drift to the respective electrode, where they can be detected. In most experiments only the electrons are detected since their faster drift velocity allows for higher repetition rates. In a TPC the sensitive volume is defined by a single pair of cathode and anode, and surrounded by a field cage of electrode strips creating a homogeneous field. In this way the track of free electrons created along the particle trajectory is projected onto the anode plane. A segmentation of the anode allows to register the two-dimensional position within the plane. A measurement of the drift time together with a known drift velocity provides the possibility to calculate the third coordinate perpendicular to the plane. The initial ionisation density along the trajectory in gases at atmospheric pressure is typically of the order of 10 e^-/cm to 100 e^-/cm, which is too low to be detected directly. Therefore, to create a measurable signal, amplification structures utilising the process of avalanche gas amplification are employed

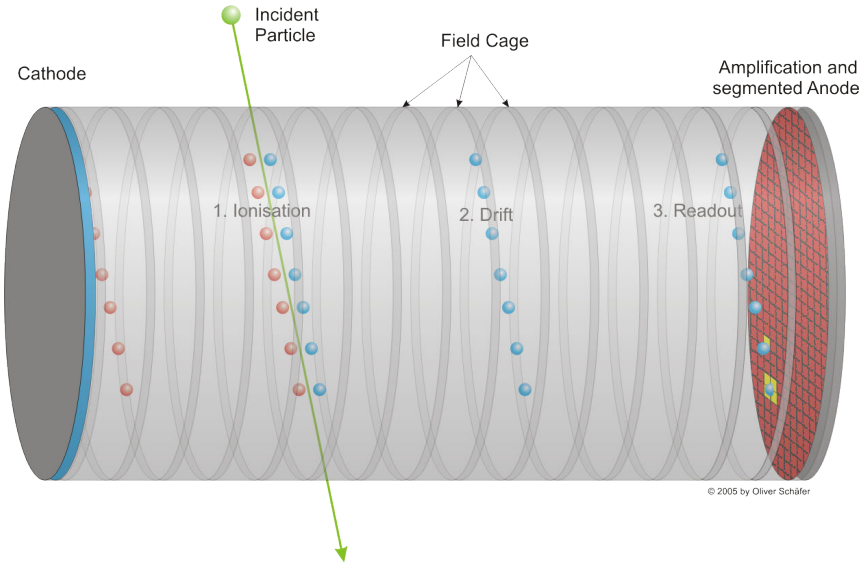

Figure 3.1.: Sketch of the working principle of a TPC. © 2005 Oliver Schäfer [123]

in front of the anode.

In this chapter the physics mechanisms underlying these principles are explained in more detail. Section 3.1 starts with the primary ionisation process, including the potential for particle identification via a measurement of the ionisation density. This is followed by the drift of electrons and ions in the gas in section 3.2. Finally, the gas amplification process and signal creation are described in sections 3.3 and 3.4 and different amplification technologies in section 3.5.

3.1. Gas Ionisation by Charged Particles

Fast moving charged particles ionise the gas along their flight path, thereby leaving a track of electron-ion pairs along their trajectory. The ionising interactions are random and their rate is characterised by the mean free path

$$\lambda = 1/(N\sigma_{\mathrm{I}}) \ , \tag{3.1}$$

defined by the electron density N of the gas and the ionisation cross section σ_{I}. Therefore, the number k of ionisation events per flight length L is Poisson distributed

$$P(L/\lambda, k) = \frac{(L/\lambda)^k}{k!}\, e^{-L/\lambda} \tag{3.2}$$

with a mean of $\langle k \rangle = L/\lambda$ [124]. The cross section σ_{I} and thus also λ depend on the velocity of the travelling particle.

The above only holds true for primary ionisation events, i.e. the direct interaction of the fast particle with the gas atoms or molecules, e.g. for a charged pion π^+ and a gas atom or molecule A

$$\pi^+ A \to \pi^+ A^+ \mathrm{e}^- \ , \quad \pi^+ A \to \pi^+ A^{++} \mathrm{e}^- \mathrm{e}^- \ , \quad \dots \ . \tag{3.3}$$

Primary ionisation needs to be distinguished from secondary ionisation, which includes all ionisation events where the electrons are discharged from atoms or molecules that do not interact directly with the initial, fast particle. Instead, secondary ionisation occurs through collisions with ionisation electrons

$$\mathrm{e}^- A \to \mathrm{e}^- A^+ \mathrm{e}^- \ , \quad \mathrm{e}^- A \to \mathrm{e}^- A^{++} \mathrm{e}^- \mathrm{e}^- \ , \quad \dots \ . \tag{3.4}$$

Alternatively, intermediate excited states A^*, created in a primary collision or from ionisation electrons, can interact with other species of atoms or molecules B, e.g.

$$\pi^+ A \to \pi^+ A^* \ , \quad A^* B \to A B^+ \mathrm{e}^- \ . \tag{3.5}$$

This process requires the excitation energy of A^* to be higher than the ionisation potential of B. In typical drift chamber gases often A^* is a metastable excitation of a noble gas, while B is a molecule of a quencher gas, which are required for stable operation of the gas amplification system (see section 3.3). B may also be a molecule of a contaminant, e.g. nitrogen from air. This type of ionisation process involving metastable states is known as Penning

ionisation [125] and the resulting increase in ionisation in gas mixtures is called Penning effect or Jesse effect [126]. The secondary ionisation created through these effects may be significantly delayed with respect to the primary ionisation, depending on the de-excitation rate of A^*. Retardation times as large as 1 µs have been observed [127]. In fast TPCs with electron drift velocities of $\mathcal{O}(50\,\mathrm{mm/\mu s})$, this spreads the signal significantly and potentially reduces the accuracy of the position measurement in the drift direction.

The fast particle expends part of its kinetic energy in the primary ionisation process. The total amount of ionisation from all processes is proportional to this energy loss. This relation is characterised by the average energy W required to create one free electron [124]:

$$W\langle N_\mathrm{I}\rangle = L\left\langle \frac{\mathrm{d}E}{\mathrm{d}x}\right\rangle \ , \tag{3.6}$$

where $\langle N_\mathrm{I}\rangle$ is the average number of ionisation electrons created along a path of length L and $\langle \mathrm{d}E/\mathrm{d}x\rangle$ is the average energy loss per unit distance of the fast particle. Due to the different contributions from the possible ionisation processes, W depends on the composition of the gas. It is not readily calculable but must be measured for every gas mixture. Considering this, it is an important feature that for sufficiently fast particles, e.g. electrons with momenta above a few keV or α-particles above a few MeV, W is independent of the initial momentum [128, 129]. This allows measurements of W at a certain energy, e.g. using stopped α, β or γ-rays of known momentum, to be used to calibrate a measurement of the energy loss of a particle via equation (3.6) at any sufficiently high energy. Measurements also show that for pure noble gases the value of W does not depend on the type of particle, while for some hydrocarbon vapours, measurements with α and β-sources show ratios of W_α/W_β up to 1.15 [130]. This means no large dependence on the particle type is expected for typical drift chamber gas mixtures that consist mostly of noble gases with only small fractions of molecular additives.

3.1.1. Specific Energy Loss

While there is no direct dependence of the average ionisation energy W of a fast charged particle on the type of particle nor on the initial energy, there is a velocity dependence of the average energy loss $\langle \mathrm{d}E/\mathrm{d}x\rangle$ itself, meaning different types of particles with distinct masses show different ionisation strengths at the same momentum. This velocity dependence was first calculated by Bethe in ref. [131], resulting in what is known today as the Bethe-Bloch equation [132, 18]

$$\left\langle \frac{\mathrm{d}E}{\mathrm{d}x}\right\rangle = K\rho\frac{Z}{A}\frac{z^2}{\beta^2}\left[\frac{1}{2}\ln\left(\frac{2m_\mathrm{e}c^2(\beta\gamma)^2Q_\mathrm{max}}{I^2}\right) - \beta^2 - \frac{\delta(\beta\gamma)}{2}\right] \ , \tag{3.7}$$

with $K = 4\pi N_\mathrm{A} {r_\mathrm{e}}^2 m_\mathrm{e}c^2 \approx 0.3071\,\mathrm{MeV\,mol^{-1}\,cm^2}$ and where

$N_\mathbf{A}$ is Avogadro's constant,

r_e is the classical electron radius,

m_e is the mass of the electron,

ρ is the density of the medium,

Z is the atomic number of the medium,

A is the molar mass of the medium,

I is the mean excitation energy of the atoms of the medium,

z is the charge number of the travelling particle,

$Q_{\mathbf{max}}$ is the maximum energy transfer to an electron in a single collision,

$\beta = v/c$ is the velocity of the fast particle in terms of the speed of light and

$\gamma = 1/\sqrt{1-\beta^2}$ is its relativistic Lorentz factor.

This function describes, with a precision of a few percent, the average energy loss in the region $0.1 \lesssim \beta\gamma \lesssim 1000$ as indicated in figure 3.2. At lower $\beta\gamma$ atomic shell effects of the medium become important, while at higher energies, radiative losses such as bremsstrahlung or Čherenkov radiation become dominant over ionisation. For small values of $\beta\gamma$ in the valid region the energy loss first falls with $1/\beta^2$. Then, after going through a minimum around $\beta\gamma \approx 3$ to 4, it rises again for larger values of $\beta\gamma$. This so-called relativistic rise is described by the logarithmic term. The exact position of the minimum and the strength of the rise are defined by the mean excitation energy I of the medium. The last term, $\delta(\beta\gamma)$, describes the so-called density effect. This effect is a result of the polarisation of the medium, which leads to a shielding of the field created by the travelling particle [133]. Near the minimum δ vanishes while in the limit of $\beta \to 1$ the correction becomes [132]

$$\delta(\beta\gamma) \to \ln\left(\frac{(\hbar\omega_\mathrm{p})^2(\beta\gamma)^2}{I^2}\right) - 1 \quad , \tag{3.8}$$

where $\hbar\omega_\mathrm{p}$ is the energy equivalent to the plasma frequency of the medium. This means that at high energies the density effect cancels the explicit $\beta\gamma$ dependence of the logarithmic term, suppressing the relativistic rise.

As can be seen in figure 3.2, the rise is not eliminated completely. This is due to an increase of the kinematic limit Q_max for the energy transfer between the travelling particle and an electron in a single collision. For particles heavier than electrons, with mass M and energy E [132]

$$Q_\mathrm{max} = \frac{2m_\mathrm{e}\left(E^2 - M^2c^4\right)}{(M^2 + m_\mathrm{e}{}^2)c^2 + 2m_\mathrm{e}E} = \frac{2m_\mathrm{e}c^2(\beta\gamma)^2}{1 + 2\gamma m_\mathrm{e}/M + (m_\mathrm{e}/M)^2} \quad . \tag{3.9}$$

Electrons need to be distinguished since they have different kinematic limits and a different spectrum of transferred energy. This is due to their small mass and because in this case the collisions happen between indistinguishable partners.

For the measurement of the energy loss in a real drift chamber, the kinematic limit is not always relevant, for several reasons. First, collisions with higher energy transfer become

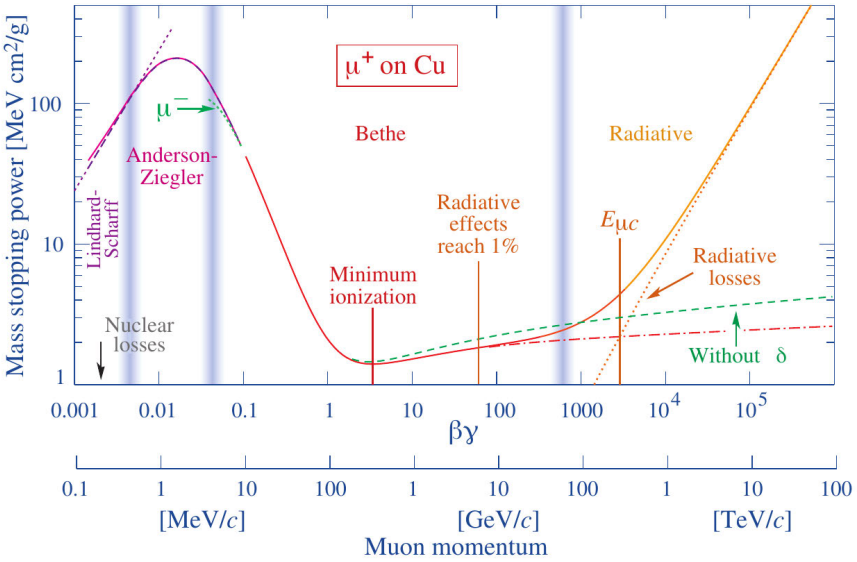

Figure 3.2.: The energy loss of muons in copper [18]. The Bethe-Bloch equation (3.7) is only valid in the indicated *Bethe* region as described in the text.

exceedingly rare. Therefore, in a finite set of measurements, a value of energy transfer may become so improbable that it does not appear in a significant fraction of tracks in a measurement series. This leads to a statistically motivated effective cut-off [124]. More important, especially in detectors with high spacial resolution, is the distance a highly energetic ionisation electron travels away from the incident particle track. Above a certain energy, this distance becomes large enough that it can be resolved from the primary track. These so-called δ-electrons form secondary tracks and no longer contribute their energy to the primary track. The threshold energy above which such a separate track is identified depends on the experimental conditions, in particular the range of the electron in the detection medium, i.e. the average distance they travel before their energy is expended. In a spectrometer with a magnetic field the tracks are curved and some δ-electrons curl up around the track. Here, in addition to the linear range the radius of curvature becomes a relevant scale. However, in this case the situation is more complicated than a single number conveys, since δ-electrons can be emitted under any angle to the magnetic field lines. Depending upon its direction, a δ-electron may travel a significant distance parallel to the magnetic field while curling around the field lines. These so-called micro-curlers leave a distinct signal already at much lower energy transfers than expected purely from the radius of curvature. The effects above lead to an effective cut-off Q_{cut} for the energy transfer Q, the exact value of which depends on the details of the drift chamber but typically lies between 30 keV and 1 MeV [124].

For the range of $\beta\gamma$ where $Q_{\text{cut}} < Q_{\text{max}}$ this results in the restricted Bethe-Bloch equation [132, 18]

$$\left\langle \frac{\mathrm{d}E}{\mathrm{d}x} \right\rangle \Bigg|_{Q<Q_{\text{cut}}} = K\rho \frac{Z}{A} \frac{z^2}{\beta^2} \left[\frac{1}{2} \ln\left(\frac{2m_{\text{e}}c^2(\beta\gamma)^2 Q_{\text{cut}}}{I^2} \right) - \frac{\beta^2}{2} \left(1 + \frac{Q_{\text{cut}}}{Q_{\text{max}}} \right) - \frac{\delta(\beta\gamma)}{2} \right] . \quad (3.10)$$

Since Q_{cut} replaces Q_{max} in the logarithmic term, the value at the minimum becomes smal-

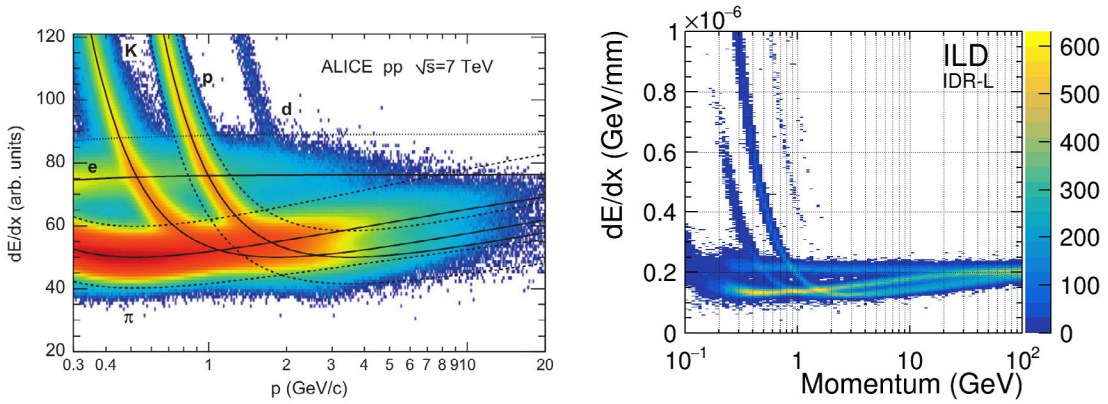

(a) ALICE measurement [135].

(b) ILD simulation [87].

Figure 3.3.: Spectra of $\mathrm{d}E/\mathrm{d}x$ vs. particle momentum (a) measured with the ALICE TPC and (b) simulated with GEANT4 for the large ILD model.

ler and the relativistic rise slower. Additionally, the indirect dependence on $\beta\gamma$, which is responsible for the continued relativistic rise for $\beta \to 1$ in equation (3.7), disappears. Consequently the energy loss now approaches a constant value, the so-called Fermi plateau, as the density effect correction $\delta(\beta\gamma)$ cancels the explicit dependence.

In this form, equation (3.10) becomes applicable also for electrons, if $Q_{\mathrm{cut}}/Q_{\mathrm{max}} \ll 1$, because they are affected the same cut-off. Additionally, it can be shown that electrons travelling with $\gamma^2 \gg Q_{\mathrm{cut}}/m_{\mathrm{e}}c^2$ produce approximately the same spectrum of ionisation as heavier particles with the same velocity [124, 134]. Thus, the average energy loss of a fast particle only depends on its velocity and not separately on its mass or energy. This is an important fact for the identification of particles, when otherwise only their momentum is known, e.g. from a spectrometer measurement. Since $\beta\gamma = p/Mc$, at any fixed momentum p each particle has a specific energy loss, depending only on its mass M. This can be seen in figure 3.3, which shows the $\mathrm{d}E/\mathrm{d}x$ spectrum of different particle species vs. their momentum as measured with the ALICE TPC [135] and simulated with GEANT4 for a model of the ILD TPC [87].

Also visible in the figure is the importance of the statistical fluctuations of the energy loss, as they limit the accuracy of the measurement and thus the discrimination power between different particle species. While the rate of primary interactions is Poisson distributed, as discussed at the start of section 3.1, the total number n of free electrons resulting directly or indirectly from each primary interaction is not. Because the secondary electrons are usually produced in close vicinity of the primary interaction, the distribution of this number is called cluster-size distribution. It is generally not known, as it depends on the details of the different secondary ionisation mechanisms. Simulations based on theoretical assumptions [136] and measurements with several gases [137] show that it falls steeply with the number of electrons. In principle, knowledge of the cluster-size distribution allows to calculate numerically the total ionisation distribution on a track length as the convolution of the primary ionisation distribution and the cluster-size distribution.

In practice often the Landau, or Landau-Vavilov, distribution is used [138, 139] to de-

scribe the total ionisation energy loss $\Delta = nW$. This distribution is asymmetric, with a peak around the most probable value (MPV) Δ_{mp} and a tail proportional to $1/\Delta^2$ towards higher energy losses [124]. Because of this tail, the mean and variance are only well defined if an upper cut-off is introduced. Due to the assumptions made in Landau's calculation for the spectrum of energy transfers in ionising interactions, the Landau distribution is only a good description of the energy loss fluctuations for sampling lengths equivalent to $\mathcal{O}(100\,\mathrm{cm})$ or more of argon gas at standard temperature and pressure (STP) [140, 141]. For thinner samples, as is generally the case in a gaseous TPCs, the width of the peak increases significantly. However, the most probable energy loss is still well described by the Landau distribution. Its velocity dependence takes the form [141]

$$\Delta_{\mathrm{mp}} = \xi\left[\ln\left(\frac{2m_{\mathrm{e}}c^2(\beta\gamma)^2\xi}{I^2}\right) + j - \beta^2 - \delta(\beta\gamma)\right] \ , \tag{3.11}$$

where $\xi = x\rho(K/2)(Z/A)z^2/\beta^2$ for a detector with sampling length x, and $j \approx 0.2$. Similar to the restricted energy loss, the most probable energy loss has a shallow minimum around $\beta\gamma = 4$ and reaches a Fermi plateau for $\beta\gamma \gtrsim 100$.

In a measurement of the energy loss of single particles, the MPV is better defined than the (restricted) mean energy loss, because the latter is weighted by few, rare events in the tail of the distribution and thus subject to large fluctuations and susceptible to cuts. However, a measurement of the MPV in a TPC with $\mathcal{O}(100)$ samples requires detailed knowledge of the shape of the distribution, which is generally not known for thin samples. Therefore, in TPCs often the mean of a fraction of the samples with the smallest signal, typically 50 % to 70 %, is used to estimate the mean. In this way many of the rare events in the tail are eliminated and the fluctuations reduced.

3.2. Drift of Electrons in Gases

The electron-ion pairs created by the travelling charged particle are separated as they are forced to drift along the electric field. In a TPC at a collider experiment this field is usually homogeneous, created between a single pair of anode and cathode, and parallel to the magnetic field $\vec{B}$ used to measure the particle momentum. For a TPC it is essential to know the time it takes the charges to reach the readout electrode. This is possible due to the fact that they drift with a constant velocity $\vec{u}$, the direction and magnitude of which depend on the configuration of electric and magnetic field $\vec{E}$ and $\vec{B}$. The following discussion focuses on drifting electrons since in most experiments, including this work, the ions are not used for particle detection.

Macroscopically, the constant drift velocity can be understood as the result of an equation of motion with friction [124]

$$m\frac{\mathrm{d}\vec{u}}{\mathrm{d}t} = q\vec{E} + q(\vec{u}\times\vec{B}) - K\vec{u} \ , \tag{3.12}$$

where m and q are mass and charge of the drifting particle, respectively, and K is the coefficient of friction. $\tau \coloneqq m/K$ has the dimension of a characteristic time and for times $t \gg \tau$

the solution becomes static, i.e. $\mathrm{d}\vec{u}/\mathrm{d}t = 0$ and

$$\vec{u} = \frac{q}{m}\frac{\tau}{1+(\omega\tau)^2}|\vec{E}|\left[\hat{E} + \omega\tau(\hat{E}\times\hat{B}) + (\omega\tau)^2(\hat{E}\cdot\hat{B})\hat{B}\right] \ , \tag{3.13}$$

where $\hat{E} \coloneqq \vec{E}/|\vec{E}|$ and $\hat{B} \coloneqq \vec{B}/|\vec{B}|$ are the unit field vectors, and $\omega \coloneqq (q/m)|\vec{B}|$ is the cyclotron frequency of the drifting particle in the magnetic field. The second term gives rise to a velocity component perpendicular to the drift field if it is not perfectly parallel to the magnetic field. This so-called $E \times B$ effect can also appear in areas where the fields are not homogeneous, e.g. close to the gas amplification structures. It is generally tried to minimise such areas and other sources of field inhomogeneity in a TPC, since they distort the projection of the tracks of travelling particles and thus deteriorate the reconstruction accuracy. For the case of no magnetic field, $\vec{B} = 0$, or parallel fields, $\vec{B} \parallel \vec{E}$, the solution (3.13) reduces to

$$\vec{u} = \frac{q}{m}\tau\vec{E} \ . \tag{3.14}$$

The time scale τ can be understood in the microscopic picture, where the drifting electrons are scattered in collisions with gas molecules. Between collisions the electrons move with an instantaneous velocity v. They gain kinetic energy from the electric field until an equilibrium is achieved, where they lose on average just as much energy in each collision as they gained since the last one. Since their mass is negligible compared to that of the gas molecules, electrons scatter isotropically and thus their direction of motion immediately after each collision is effectively random. Due to the acceleration by the electric field, the electrons obtain an additional velocity proportional to the time elapsed since the last collision. When averaging the velocity over a large time, the random oriented component does not contribute and this second component emerges as the macroscopic drift velocity, equation (3.14), which is often written as $u = \mu E$, defining the electron mobility $\mu \coloneqq (q/m)\tau$. In this picture, τ is the average time elapsed after the last collision, which is equal to the average time between collisions

$$\tau = \frac{\lambda}{v} = \frac{1}{N\sigma v} \ , \tag{3.15}$$

where λ is the mean free path of the electron, N is the number density of the gas and σ the collision cross section. The latter depends on the kinetic energy $\varepsilon = (m/2)v^2$ of the electron. Some gases show a distinct minimum of σ at low ε, e.g. argon around $\varepsilon \approx 0.2\,\mathrm{eV}$ [142]. This is the so-called Ramsauer minimum [143].

3.2.1. Diffusion

While the random movement of the individual electrons does not contribute to the macroscopic drift velocity, on average it causes them to migrate away from their initial position. This means a cluster of electrons spreads out over time. Motivated by the isotropic scattering of the electrons, originally diffusion was also assumed to be isotropic in the absence of a magnetic field. In this case, after a time $t \gg \tau$ an originally point-like cloud of electrons

will have a Gaussian density distribution [124]

$$n = \left(4\pi\tilde{D}t\right)^{-3/2} \exp\left(-\frac{x^2 + y^2 + (z - ut)^2}{4\tilde{D}t}\right) \ , \tag{3.16}$$

where the drift direction is parallel to the z-axis and the diffusion constant $\tilde{D}$ is defined such that n fulfils the continuity equation for the conserved electron current. The diffusion width σ after the electron cloud has drifted a distance $\Delta z = ut$ is thus given by

$$\sigma^2 \coloneqq 2\tilde{D}t = 2\tilde{D}\frac{\Delta z}{u} = \frac{2\tilde{D}}{\mu E}\Delta z = \frac{4}{3}\frac{\varepsilon}{qE}\Delta z \ . \tag{3.17}$$

In the last step it was used that in terms of the microscopic picture, the diffusion constant is [124]

$$\tilde{D} = \frac{\lambda^2}{3\tau} = \frac{v^2\tau}{3} = \frac{2}{3}\frac{\varepsilon}{m}\tau = \frac{2}{3}\frac{\mu\varepsilon}{q} \ . \tag{3.18}$$

Equation (3.17) implies, that to achieve small diffusion, a gas mixture must provide small electron energies ε at high drift fields E.

This case of isotropic diffusion was assumed to be true until experiments by Wagner et al. [144] showed that the value of the diffusion parallel to the direction of the electric field can be very different from that in the perpendicular direction. Following these measurements, Parker and Lowke developed a model to explain this disparity [145], which represents the following underlying reasoning: If the average collision rate $\nu \coloneqq 1/\tau = N\sigma v$ is a function of the electron energy, i.e. if the change of velocity v and cross section σ do not cancel, then the mobility of the electrons in the centre of the cloud is different from that of those at the leading and the trailing edge. Consequently the drift velocity varies throughout the length of the cloud. This is equivalent to a change of the diffusion in the direction of the electric field, given by

$$\frac{\tilde{D}_{\parallel E}}{\tilde{D}_0} = \frac{1 + \eta}{1 + 2\eta} \ , \tag{3.19}$$

where $\eta \propto \partial\nu/\partial\varepsilon$ and $\tilde{D}_0$ is the diffusion constant without the anisotropy. The diffusion in the direction perpendicular to the field is unaffected, i.e.

$$\tilde{D}_{\perp E} = \tilde{D}_0 \ . \tag{3.20}$$

In the presence of a magnetic field, the situation is again different. Between collisions the electrons are now forced to follow helical paths, curving in the plane perpendicular to the magnetic field. Thus the straight distance travelled in this plane is reduced, which is effectively equivalent to a reduction of the mean free path $\lambda_\perp$ perpendicular to the magnetic field. The resulting change of diffusion is given by [124]

$$\frac{\tilde{D}_{\perp B}(\omega)}{\tilde{D}_{\perp B}(0)} = \left(\frac{\lambda_\perp(\omega)}{\lambda_\perp(0)}\right)^2 = \frac{1}{1 + (\omega\tau)^2} \ , \tag{3.21}$$

where ω is again the cyclotron frequency of the electron. The diffusion parallel to the magnetic field is unchanged, i.e.

$$\tilde{D}_{\parallel B}(\omega) = \tilde{D}_{\parallel B}(0) \ . \tag{3.22}$$

For an arbitrary configuration of electric and magnetic fields, the anisotropies combine and the individual diffusion constants are replaced by a three dimensional diffusion tensor that depends on the angle between the fields. However, in typical TPCs where the electric and magnetic fields are parallel, the combination of the electric and magnetic anisotropies results in two distinct diffusion coefficients for the transverse and longitudinal directions, $\tilde{D}_\mathrm{t}$ and $\tilde{D}_\mathrm{l}$, respectively. Then the electron density distribution is given by

$$n = \left(4\pi\tilde{D}_\mathrm{l}t\right)^{-1/2}\left(4\pi\tilde{D}_\mathrm{t}t\right)^{-3/2}\exp\left(-\frac{x^2+y^2}{4\tilde{D}_\mathrm{t}t} - \frac{(z-ut)^2}{4\tilde{D}_\mathrm{l}t}\right) \ , \tag{3.23}$$

Analogous to equation (3.17) the corresponding diffusion widths are

$$\sigma_\mathrm{t}{}^2 = 2\tilde{D}_\mathrm{t}t = \frac{2\tilde{D}_\mathrm{t}}{\mu E}\Delta z =: D_\mathrm{t}{}^2\Delta z \tag{3.24}$$

$$\sigma_\mathrm{l}{}^2 = 2\tilde{D}_\mathrm{l}t = \frac{2\tilde{D}_\mathrm{l}}{\mu E}\Delta z =: D_\mathrm{l}{}^2\Delta z \ . \tag{3.25}$$

The last step defines the parameters D_t and D_l that characterise the relation between diffusion and drift distance. These are often used instead of the diffusion constants $\tilde{D}_{\mathrm{t/l}}$ to describe the performance of detectors, since the maximum drift distance is fixed while the drift time depends on other parameters.

3.2.2. Electron Attachment

During drift electrons can be absorbed by gas atoms or molecules, forming negative ions. The gases typically used in drift chambers, i.e. noble gases and most organic vapours, require electron energies of several eV to form stable ions, which is much higher than the energies reached during drift. However, some molecules, such as oxygen (O_2) or halides, have much larger electron affinities and are capable of attaching electrons at much lower energies. Therefore it is important to avoid contamination of the drift gas with water or air and outgassing of detector components containing halocarbon polymers.

Attachment mechanisms are classified into two and three-body processes. The simplest mechanism are two-body processes with a molecule M:

$$\mathrm{e}^- + M \rightarrow M^- \ . \tag{3.26}$$

However, quite often the molecule dissociates in the process and one of the components A, B, … forms a negative ion:

$$\mathrm{e}^- + M \rightarrow A^- + B + \ldots \ . \tag{3.27}$$

For these processes the rate $\tilde{A}$ of attachment is given by the electron velocity v, the number density N of the attaching molecule and the cross section σ_A:

$$\tilde{A} = N\sigma_A v \ . \tag{3.28}$$

For the three-body processes, which play an important role in the attachment to O_2 molecules, two mechanisms are distinguished. First, there is the Bloch-Bradbury process [146, 147]. At the typical energies of drifting electrons, the attaching O_2 molecule forms an excited and unstable state O_2^{*-}. Therefore, within the lifetime of $\mathcal{O}(10^{-10}\,\mathrm{s})$ an additional interaction with a third body X is required to carry away the excitation energy. Otherwise the oxygen will lose the additional electron. The effective attachment rate $\tilde{A}$ thus depends on the lifetime as well as the number densities of O_2 and X and the cross sections of the two processes,

$$e^- + O_2 \rightarrow O_2^{*-} \ , \tag{3.29}$$

$$O_2^{*-} + X \rightarrow O_2^- + X \ . \tag{3.30}$$

Secondly, there are processes involving unstable Van der Waals molecules [148]:

$$O_2 + X \leftrightarrow (O_2X) \ . \tag{3.31}$$

In collisions with an electron, these bonds are broken, dissipating the excess energy, and the electron remains attached to the O_2 molecule:

$$e^- + (O_2X) \rightarrow O_2^- + X \ . \tag{3.32}$$

Measurements have shown that for mixtures of oxygen with pure noble gases the Van der Waals mechanism is dominant, while for many hydrocarbons the Bloch-Bradbury process is more important [149]. Because the oxygen attachment rates are generally much larger in mixtures with hydrocarbons, in typical drift chamber gases, containing both noble gases and organic quenchers, the Bloch-Bradbury process plays the bigger role.

For either of the processes above, the number N of free electrons drifting in a gas is reduced over time as given by the attachment rate $\tilde{A}$:

$$N = N_0 \cdot e^{-\tilde{A}t} = N_0 \cdot e^{-A\,\Delta z} \ . \tag{3.33}$$

Instead of $\tilde{A}$, the attachment coefficient $A \coloneqq \tilde{A}/u$ per drifted distance $\Delta z = ut$ is used in this work.

3.3. Gas Amplification

The amount of charge produced by the primary and secondary ionisation processes introduced in section 3.1 is too small to be detected over the electronic noise of most electronic amplifiers and readouts. Therefore gaseous detectors make use of the process of proportional avalanche gas amplification. This mechanism occurs in regions of high enough electric field, typically $\mathcal{O}(10^4\,\mathrm{V/cm})$ for gases at STP [124], where drifting electrons acquire enough energy between individual collisions with gas atoms or molecules, that they can ionise these. The newly liberated electrons then undergo this process themselves and an avalanche forms. The avalanche only stops, when it leaves the high field region or all electrons are collected on the anode.

The production cross sections for photons, e.g. due to bremsstrahlung, are of the same order of magnitude as the ionisation cross sections. Therefore photons are as abundant in the avalanche as electrons. The small fraction of photons that is energetic enough to ionise the gas is an important factor in the amplification process, especially in the presence of gas components with low ionisation potentials. This can become a problem if the mean free path of these photons is larger than the extent of the amplification region, as is typically the case in pure noble gases. In this case the photons may escape the amplification region and give rise to full, independent avalanches somewhere else in the detector. In the best case this only creates a background of spurious, localised signals but in the worst case it can cause the detector to break down. To prevent this scenario, detector gas mixtures typically contain hydrocarbons or other molecules with wide photon absorption spectra due to an abundance of vibrational and rotational degrees of freedom [150, 151]. Already fractions of a few percent of these additives can reduce the mean free path of photons considerably.

One important aspect of the gas amplification process is that the amount of charge created in the avalanche is proportional to the initial number of electrons. This is true as long as the changes of the electric field induced by the avalanche are small compared to the overall field strength, i.e. the charge density of the avalanche is small compared to that of the amplification structure. This fact gave its name to one of the most widely used types of gas amplification structure, the proportional wire and in turn the multi-wire proportional chamber (MWPC). Due to its widespread use, many of the models of gas amplification were developed based on its radial field $E \propto 1/r$. Others make use of the simple geometry of a homogeneous field.

In general the amplification process is described by the first Townsend coefficient

$$\alpha = 1/\lambda_{\text{ion}} = N_{\text{gas}}\sigma_{\text{ion}} \ , \tag{3.34}$$

where λ_{ion} is the average distance between ionising collisions, σ_{ion} is the cross section for these collisions and N_{gas} is the number density of the gas. The amount of additional electrons liberated per path length ds is given by [124]

$$\mathrm{d}N = \alpha N \mathrm{d}s \ . \tag{3.35}$$

No analytical expression exists for the Townsend coefficient α, since the excitation and ionisation cross sections σ_{ion} of the electrons depend on the details of the ionisation mechanisms presented in section 3.1. Therefore α must be measured for every gas mixture. Generally the ionisation cross section increases with larger collision energy ε, which in turn rises with the electric field [152]. Therefore α is often used as a function of E.

The amplification factor, or gain G, is defined as the ratio of the final to initial number of electrons, N and N_0, respectively. From equation (3.35) the gain of an avalanche along a path $\mathscr{C}$ is given by

$$G \coloneqq \frac{N}{N_0} = \exp\Big(\int_{\mathscr{C}} \alpha(\vec{r})\mathrm{d}s\Big) = \exp\left(\int_{E_1}^{E_2} \frac{\alpha(E)}{\mathrm{d}E/\mathrm{d}s}\mathrm{d}E\right) \ , \tag{3.36}$$

where E_1 and E_2 are the corresponding field strengths at the start and end of the path and $\mathrm{d}E/\mathrm{d}s$ is the electric field gradient along the path. The last relation is only strictly true if

there is a bijection between the points of the path and the field strength, i.e. the behaviour of the field along the path is strongly monotonic. Other geometries can be described by piecewise integration, where each segment of the path fulfils this condition.

Since the multiplication process in the avalanche is random, equation (3.36) only describes the average gain. The statistical fluctuations can affect measurements of the initial ionisation and the specific energy loss. Therefore, they were the subject of many studies. For weak electric fields Legler found the gain to follow an exponential distribution [153]. For the general case with strong fields no explicit analytical description of the gain distribution is known. However, Legler calculated distributions for homogeneous fields of various strength [154], which were in good agreement with measurements [155]. For the radial field $E \propto 1/r$ of a proportional wire, Alkhazov [156] calculated the variance and the higher moments of the distribution and found that the fluctuations are approximately described by a Pólya distribution

$$P(G) = \frac{1}{\langle G \rangle} \frac{(\vartheta+1)^{\vartheta+1}}{\Gamma(\vartheta+1)} \left(\frac{G}{\langle G \rangle} \right)^{\vartheta} \exp\left(-(\vartheta+1) \frac{G}{\langle G \rangle} \right) , \tag{3.37}$$

with the average gain $\langle G \rangle$ and the gamma function $\Gamma(x)$. The parameter ϑ depends on the field strength and gas mixture. In ref. [156], typical values of $\vartheta = 0.25$ to 0.67 are reported. While this distribution does not match the measured spectra for the case of homogeneous fields exactly, in practice the difference is often negligible. In particular this applies if one measures avalanches started by a large number of electrons, as then the central limit theorem of statistics applies and the total distribution approaches a Gaussian. This is the case in many drift chambers used for tracking, with typical sampling lengths of $\mathcal{O}(1\,\mathrm{cm})$ and $\mathcal{O}(100)$ initial electrons per sample. Therefore the Pólya distribution is also widely used in calculations for other field geometries.

3.4. Signal Creation

The free charges moving in the gas induce an electric current in all electrodes in the vicinity. This signal can be read out by connecting the relevant electrodes, e.g. the anode wire of an MWPC or dedicated readout strips or pads, to electric amplifiers. The creation of the signal is described in the following for the case of electrodes connected directly to ground. The effect of the impedance of the readout electronics on the induced signal is discussed in ref. [124].

A point charge q at position $\vec{r}_q$ generates an electric field $\vec{E}(\vec{r}; \vec{r}_q)$ at any point $\vec{r}$. In the presence of a grounded electrode, the field is locally perpendicular to the conducting surface. From Gauss' law it follows that the surface charge density σ on the electrode is related to the electric field by $\sigma(\vec{r}; \vec{r}_q) = \epsilon_0 E(\vec{r}; \vec{r}_q)$, with the vacuum permittivity ϵ_0. The total charge Q induced on the electrode surface $\mathcal{S}$ is then

$$Q = \iint_{\mathcal{S}} \sigma(\vec{r}) \mathrm{d}S \ . \tag{3.38}$$

For a closed surface surrounding q or an infinite surface, Q is always equal to $-q$, independent of the position $\vec{r}_q$. Since this is generally not the case for real electrodes, the induced

charge on each electrode depends on $\vec{r}_q$. Therefore, if the charge is moving with velocity $\vec{v} = \mathrm{d}\vec{r}_q/\mathrm{d}t$, the current induced in electrode i is given by

$$I_i^{\mathrm{ind}}(t) = -\frac{\mathrm{d}}{\mathrm{d}t} Q_i\big(\vec{r}_q(t)\big) = -\nabla Q_i\big(\vec{r}_q\big) \cdot \frac{\mathrm{d}}{\mathrm{d}t}\vec{r}_q(t) = -\nabla Q_i\big(\vec{r}_q\big) \cdot \vec{v}(t) \ , \tag{3.39}$$

where ∇ is the gradient with respect to $\vec{r}_q$.

The electrode geometries in real detectors are generally quite complex and the method of signal calculation described above can become difficult to perform. A method to simplify this process was proposed independently by Shockley [157] and Ramo [158]. In this approach the charge on each electrode is given by

$$Q_i = -\frac{q}{V_{\mathrm{w}}} \psi_i\big(\vec{r}_q\big) \ , \tag{3.40}$$

where ψ_i is called the electrodes weighting potential. It is defined as the potential that emerges when the electrode i is set to a voltage $V_i = V_{\mathrm{w}}$, while all other electrodes are grounded, i.e. $\forall j \neq i \ V_j = 0$, and the charge q is absent. For simplicity often $V_{\mathrm{w}} = 1\,\mathrm{V}$ is chosen. Then the current induced on the electrode is given by the Shockley-Ramo theorem, which follows from equations (3.39) and (3.40):

$$I_i^{\mathrm{ind}}(t) = -\nabla Q_i\big(\vec{r}_q\big) \cdot \vec{v}(t) = \frac{q}{V_{\mathrm{w}}} \nabla \psi_i\big(\vec{r}_q\big) \cdot \vec{v}(t) = -\frac{q}{V_{\mathrm{w}}} \vec{E}_i\big(\vec{r}_q\big) \cdot \vec{v}(t) \ , \tag{3.41}$$

defining the weighting field of the electrode

$$\vec{E}_i\big(\vec{r}_q(t)\big) = -\nabla \psi_i\big(\vec{r}_q(t)\big) \ . \tag{3.42}$$

The weighting field can be calculated for each electrode individually from the boundary conditions defined above, either analytically or using numerical simulations. It is important to note that the weighting field is independent of the actual field configuration used during operation of the detector, as well as the position, movement and value of the drifting charges. Therefore, it only needs to be calculated once for each relevant electrode.

For distances much larger than the dimensions of the electrode, the weighting field generally drops rapidly. Therefore, the induced signal is only large for the charges in the vicinity of each electrode, even though each charge induces a signal in every electrode. Once all charges have been collected on the different electrodes, it follows from the definition of the weighting potential that the total charge induced in an electrode is equivalent to the sum of all electrons and ions collected on that electrode, consistent with the conservation of charge. In principle this allows to completely separate the signal induced by the electrons and the positive ions produced in the gas amplification process. However, due to their difference in mass, which causes ions to drift much slower than electrons, they produce signals of vastly different time scales. These aspects need to be considered in the design of the amplification and readout structure, and in particular the readout electronics.

3.5. Gas Amplification Technologies

To achieve the high field strengths required for gas amplification, several technologies have been developed. The earliest solution was the proportional wire, still widely used in the form

of multi-wire proportional chambers (MWPCs), first introduced by Charpak in 1968 [159]. Depending on the detector geometry, MWPCs are realised in various ways. The common structure in all cases is the thin anode wire that creates a strong, radial electric field in its vicinity and collects the electrons, as well as some surrounding cathode arrangement. Planar detectors, such as TPC readout chambers, e.g. in the original ALICE TPC [160], commonly consist of a grid of parallel anode wires placed between two cathode layers. In a TPC, the cathode plane facing the drift volume must be transparent to drifting electrons, and thus is implemented as a parallel wire grid itself. The other cathode plane can be formed by a pad plane, a printed circuit board (PCB) with segmented electrodes that pick up the signal induced by the electron avalanche at the anode wire. While the spatial resolution can be increased this way, compared to measuring the signal on the anode wires, the performance is ultimately limited by the spacing of the wires to each other and to the pad plane. This applies in particular to the multi-track resolution. Additionally, in a strong magnetic field, where the transverse electric field components close to the wire induce $E \times B$ effects, the resolution in the wire direction is deteriorated. Experiments with a TPC prototype in a 4 T magnetic field have shown that even with an optimised wire spacing the performance requirements of the ILD TPC cannot be met [119].

Due to the increasing performance requirements in tracking detectors so-called micro-pattern gaseous detectors (MPGDs) were adopted [161]. Today there are mainly two MPGD technologies in use, micro-mesh gaseous structures (Micromegas) and gas electron multipliers (GEMs). Both technologies have in common that their typical structure size is about an order of magnitude smaller than possible with wires, i.e. $\mathcal{O}(100\,\mu\text{m})$ instead of $\mathcal{O}(1\,\text{mm})$, greatly reducing $E \times B$ effects. Since in most MPGDs the electron avalanche is collected directly on the readout pad plane instead of picking up an induced signal, the position of the avalanche can be measured with high precision. For such devices the spread of the charge cloud on the pad plane is the limiting factor for the spatial resolution measurement. In addition to allowing for higher precision, MPGDs have the advantage of being more robust and easier to handle than an MWPC, potentially containing hundreds or thousands of wires. Therefore, MPGDs are widely used in various applications, also outside of particle physics. Since this work is centred around the development of a GEM-based TPC readout, GEMs are introduced in detail in the following section. Information about Micromegas can be found in various publications, starting with their first introduction in ref. [121].

3.5.1. Gas Electron Multipliers

The gas electron multiplier (GEM) was introduced as a new concept for electron gas amplification by Sauli in 1997 [120]. GEMs consist of a thin insulator coated on both sides with a conductive metal layer. To allow the passage of drifting charges, a dense, regular grid of holes is pierced into this foil, as is displayed in figure 3.4a. By applying a sufficiently high voltage between the two conductive layers compared to the external fields, a field line configuration as sketched in figure 3.4b is created. Electrons in the drift volume at the top of the figure are forced to follow the field lines into the holes. There the field becomes strong enough to initiate gas amplification. Afterwards the field guides the amplified electrons out of the holes to the other side of the foil.

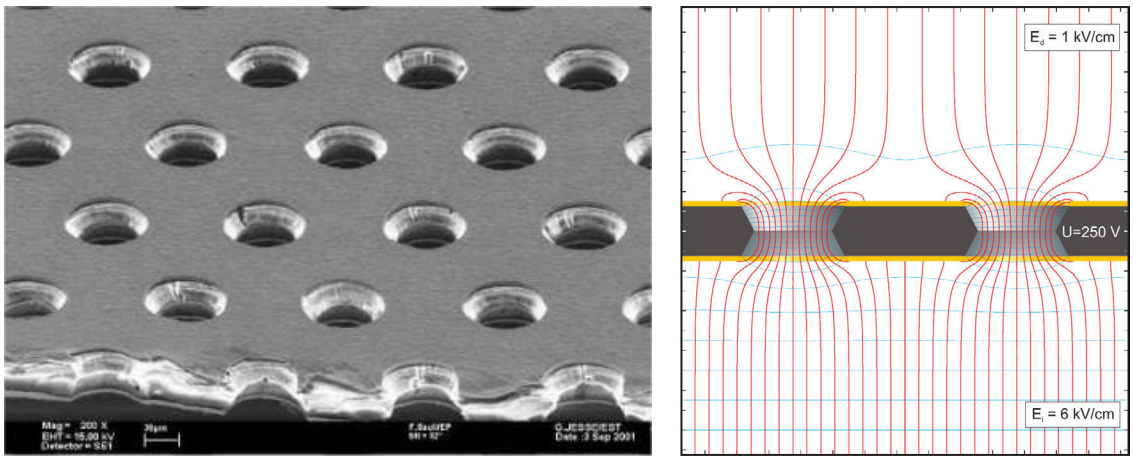

(a) Microscope image of a GEM [162]. **(b)** GEM field geometry [123].

Figure 3.4.: Design and working principle of GEMs. (a) A microscope image of a GEM produced in the workshop of the CERN Gas Detectors Development group. The holes have a diameter of 70 µm and are spaced at a pitch of 140 µm. (b) A sketch of the field line geometry around the holes of a GEM for a representative field configuration.

The base material most commonly used for GEMs is copper coated polyimide, with a thickness of $\mathcal{O}(50\,\mu\text{m})$. The holes are typically formed using photolithographic etching processes. This method scales well to large areas and it allows to control the shape of the holes [163], which has a big impact on the field geometry in the vicinity and thus on the overall behaviour of the GEM. For most applications a two-sided etching technique is used that creates double-conical holes, as shown in figure 3.4. The achievable hole pitch is of order 100 µm. Similar devices are produced using other insulator materials such as different polymers, ceramic and glass substrates, see e.g. [164, 165]. For some applications GEM-like devices made from standard PCB materials with a thickness of $\mathcal{O}(1\,\text{mm})$ are employed, see e.g. [166]. In these devices the holes are created by mechanical drilling, which does not allow to reach the same small hole sizes and high densities as etching techniques.

One issue with early MPGDs were electrical breakdowns and discharges that damage the amplification structure or even the readout electronics [161]. Electric breakdowns can never be avoided completely but GEMs are intrinsically robust against damage from such discharges. Therefore in most cases the GEM is only disabled briefly until the voltage is recovered. Only rarely a permanent conductive connection between the two electrodes of the GEM is formed in a discharge, leaving it unusable. Furthermore, discharges rarely propagate from the GEM to the readout electronics since both are spatially and electrically separated. To further reduce the probability of a discharge damaging a GEM, the area of the electrodes can be limited to reduce the stored charge and energy. For larger area GEMs this is achieved by segmenting one of the electrodes into isolated sectors.

In principle a typical thin GEM can achieve an effective gain of up to 10^4 before electric breakdown [167]. However, this is rarely reached in practice since already a single local defect can reduce the breakdown voltage of the whole device. To minimise the probability of discharges while still reaching the required gain, it is possible to stack several GEMs

in a cascade. By choosing suitable fields between the GEMs, the electrons extracted from one are transferred to the next and amplified again. Up to five GEMs have been stacked successfully [168]. In such a stack, individual GEMs are typically only operated at gains of $\mathcal{O}(10\text{–}100)$. This way, total effective gains of up to 10^4 to 10^5 can be reached.

The effective gain of a GEM depends not only on the amplification inside the holes but also on its transparency to electrons [167]. Therefore three factors contribute: First an electron has a finite probability C^- to be collected into one of the holes, instead of being absorbed by the facing electrode. Then the amplification with gain G_0 occurs. Finally each electron again has a finite probability X^- to be extracted from the hole, and not be absorbed by the walls or the rear electrode. For a cloud containing many electrons this results in an effective gain $G = C^- G_0 X^-$. The real gain G_0 depends to good approximation only on the field inside the hole and thus, for any given geometry, only on the voltage between the two GEM electrodes. However, the collection and extraction efficiencies additionally depend on the external fields on the corresponding side of the GEM, or rather the ratio between the respective external field and the field inside the hole. This has been studied in detail in ref. [169]. Generally the collection efficiency increases for lower ratios while the extraction efficiency increases for higher ratios.

A similar behaviour is observed for the transfer efficiencies for ions. However, since the positive ions created in the gas amplification process are drifting in the opposite direction, the fields relevant for collection and extraction are swapped compared to the electrons. This allows to make a GEM almost opaque to ions while keeping it transparent to electrons. In multi-GEM stacks this can be used to full advantage. The transfer fields and GEM voltages can be tuned so that a large fraction of the ions produced in the GEMs deeper in the stack are absorbed by the GEMs closer to the drift volume. This has been successfully applied to suppress the ion back flow (IBF) into the drift volume by factors of $\mathcal{O}(10^{-2})$ [170, 171].

4. The Readout Module

The design goal for this readout module is to provide the largest possible total sensitive area and to minimise the size of gaps. Further, the material budget in terms of average radiation length X_0 should be kept as low as possible. The outer geometry of the module is given by the end plate of the large TPC prototype (LP), described in section 6.2, which has module slots with a shape similar to those intended for the TPC of the ILD. The footprint of a module is therefore limited to the sector of an annulus with an inner radius of 1430 mm and an outer radius of 1600 mm, encompassing an angle of about 8.4°. In addition the performance requirements of the ILD TPC stated in section 2.3.5 need to be taken into account in the design of the readout electrode and the amplification system.

4.1. General Design

Figure 4.1 shows an assembled module and an overview of the arrangement of the major components. The main structural component of the module is the aluminium back frame. It provides the required mechanical rigidity and is used to mount the module in the end plate of the TPC using an additional mounting bracket. It also defines the size of the module. To leave a margin between modules, all dimensions are kept 1 mm smaller than the bounding box defined above. This leads to inner and outer radii of 1430.5 mm and 1599.5 mm, respectively, and a correspondingly smaller azimuthal coverage. On its back side, the frame has a shoulder with which it is seated on the end plate. On this shoulder a groove that holds an O-ring gasket

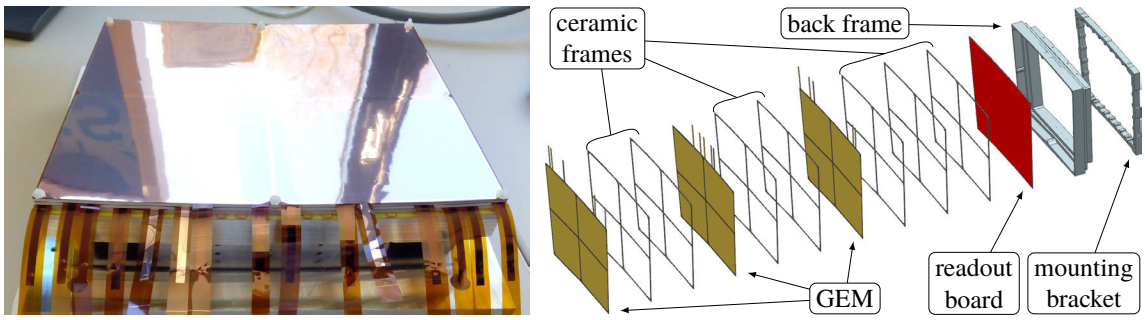

(a) A mostly assembled module. **(b)** Explosion view of the components.

Figure 4.1.: Overview of the GEM readout module. In (a) a photo is shown of an assembled module, before the GEM HV connections were trimmed and soldered. The explosion view in (b) shows from right to left the mounting bracket and aluminium back-frame in grey, the readout board in red, the GEMs in yellow and in between the GEMs the ceramic frames they are mounted on.

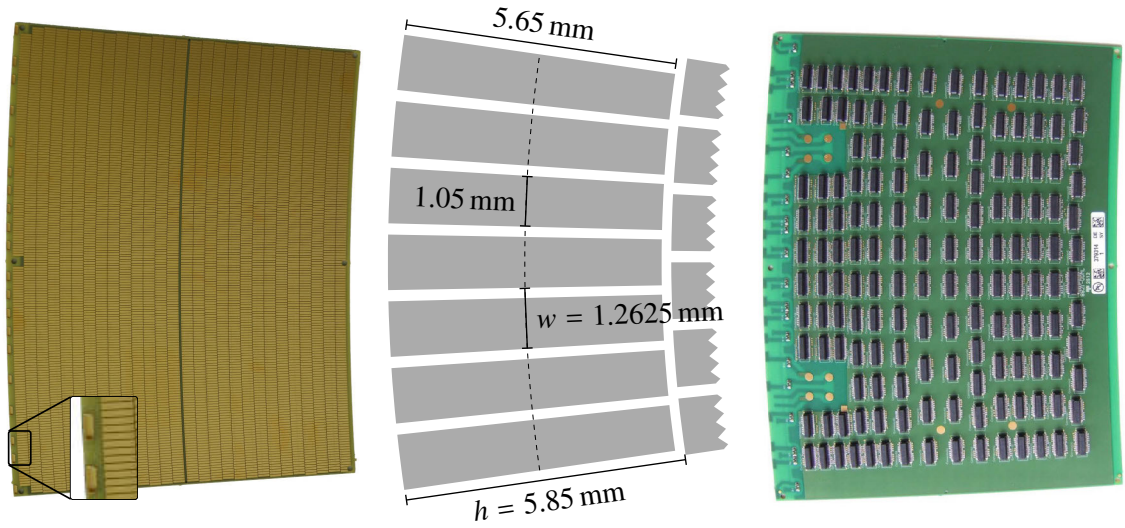

(a) Pad side. **(b)** Pad geometry. **(c)** Connection side.

Figure 4.2.: Overview of the readout board. (a) The pad side of the board, which faces the active volume. The 4828 pads are arranged in 28 staggered rows. The insert shows two of the 20 soldering slots for the GEM HV connections. (b) The layout of the pads, showing the row pitch h and the pad pitch w. (c) The connection side of the board, featuring 152 connectors for the signal lines. The free spaces at the left take up the HV connectors.

runs around the whole circumference of the module to make a gas tight seal between the two metal parts.

Directly glued onto the back frame is the readout board. It is a multi-layer PCB using glass-fibre reinforced plastic (GRP) as base material. Since the module is part of the gas containment, the board and its bond to the back frame need to be gas tight. The side of the board facing the active volume, shown in figure 4.2a, is segmented into 4828 readout electrodes, called pads in the following. These pads are arranged in 28 concentric rows. For future reference the rows are numbered from 0 to 27, starting at the inner radius of the module. The row and pad geometry is sketched in figure 4.2b. The rows have a pitch of 5.85 mm in the radial direction. Within each row the pads have a pitch of 1.2625 mm in the azimuthal direction, measured at their midpoint. As the pitch is the same in all rows, the number of pads in each row increases from 164 in row 0 to 182 in row 27. By carefully choosing the azimuthal offset of each row, the pads in adjacent rows are staggered over most of the width of the module, while keeping the layout symmetric along the centre line. From each pad a signal line is routed through the PCB to a channel in one of the 152 connectors on the other side of the board, shown in figure 4.2c. These connect to the readout electronics, described in section 6.3. Each connector houses 40 lines, eight of which are used for grounding, leaving 32 data lines per connector. Two high voltage (HV) connectors with four channels each can provide eight separate voltages. This allows to power each side of up to four GEMs independently. Having independent voltage supplies for each GEM electrode is important in the prototype phase, as it allows to test different operation conditions of the gas amplification stage. The board feeds through the HV lines for the GEM electrodes to solder connections

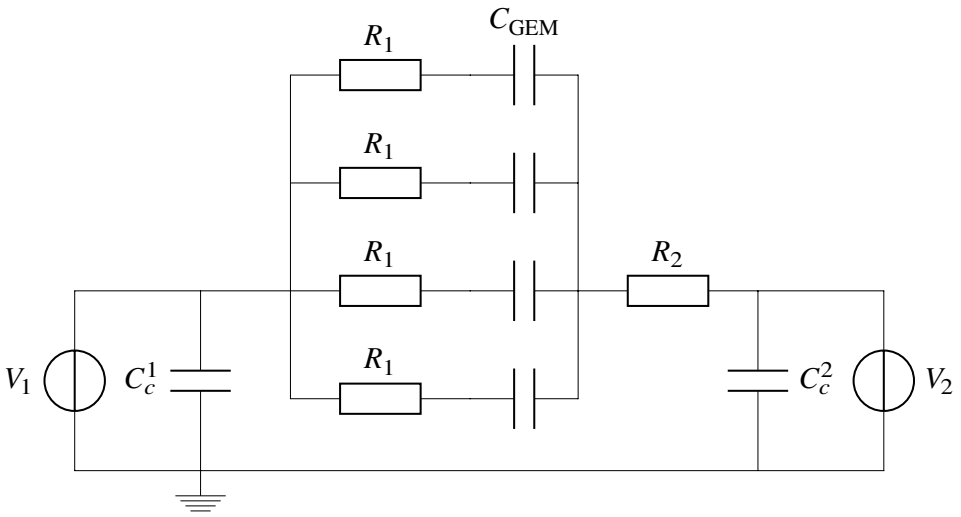

Figure 4.3.: Effective circuit diagram of the HV system of a single GEM. The four sectors are represented by the capacitors C_{GEM}. In reality the common electrode (facing R_2) is continuous. The protection resistors R_1 and R_2 are implemented as SMDs on the readout board. C_c^1 and C_c^2 represent the capacitance of the cable between the voltage supply and the module.

on the pad side at the outer radius of the board, shown in the insert in figure 4.2a. Figure 4.3 shows the effective circuit diagram of the HV supply for one GEM. On the board, half of the incoming HV lines are split into four channels each, as the electrode on one side of each GEM is subdivided into four sectors. As explained in section 3.5.1, the subdivision is done to reduce the energy stored in the individual sectors, for protection in case of a discharge of the GEM. Therefore SMD resistors on the PCB decouple the sectors from each other and from the comparatively large capacitance of the HV supply cable.

The amplification stage consists of three GEM foils, which are supported by thin ceramic frames. Due to the size of the modules, not much tension is needed to keep the GEMs from sagging under electric load or gravity. Therefore the total stretching force during mounting can be kept low, at $\mathcal{O}(10\,\mathrm{N})$ per side. As mentioned above, the electrode on one side of each GEM is subdivided into four sectors. To minimise the additional insensitive area introduced by the gaps between sectors, the GEMs and ceramic frames were designed such that the gaps coincide with the supports of the frame. To avoid distortions of the drift field close to the module, the GEMs are installed with the unsegmented side facing towards the drift volume of the TPC. As visible in figure 4.4, the HV lines from each sector end in connection straps on the larger radius edge. These straps are soldered directly into the respective slots on the readout board.

The support frames of the GEMs, visible in figure 4.4a, are laser cut from 1 mm thick aluminium-oxide (Al_2O_3) ceramic substrates [172]. This material was chosen since it combines a high dielectric strength of 19 kV/mm with good mechanical properties. With a Young's modulus of 331 GPa this material is much more rigid than the commonly used GRP FR-4 (20 GPa to 25 GPa [173]). This, together with the low tension of the GEM foils, allows the

(a) Previous design. **(b)** New design.

Figure 4.4.: Comparison of GEM designs. In both pictures the common electrode faces up and the connection straps are visible at the bottom of the pictures. Those of the split electrodes on the back side are visible as dark stripes through the foil. (a) The previous design with four connection straps per electrode. A ceramic frame was glued to this GEM. (b) One of the new designs with only one connection per electrode.

bars of the frame to have a width of only 1.4 mm. The frames have the same outer dimensions as the readout board except for a slightly smaller outer radius to leave space for the HV connections of the GEMs. With this design the modules have more than 90 % active area. The frames also define the transfer gaps between the GEMs and the induction gap after the last GEM of 2 mm and 3 mm, respectively. To reduce the field distortions caused by the gap between two modules, a field-shaping wire runs along the outer circumference of the topmost frame in the stack. To optimise the effect, the potential of this wire can be set independently from the GEM voltages.

4.2. Improvements over the last Module Generation

While the previous iteration of the modules performed well, some points for further optimisation have become apparent during the first beam tests and further investigations afterwards. Two of these points required dedicated studies. First, to avoid glue spills onto the active area of the GEM when gluing the ceramic frames, the optimal parameters for the application of the glue were reinvestigated, as described in section 4.2.1. Second, to provide a consistent high quality of the mounted GEM, a new tool for the gluing of the ceramic frames to the GEMs was developed and commissioned, as presented in section 4.2.2. An overview of the other points is given in the following.

Already early on it was recognised that the HV connection straps of the GEMs could provoke flashovers, since they are uninsulated and in close vicinity of each other. Electric discharges were also observed between the HV connection straps and the readout pads, which are separated by the ceramic frames. Adding to the risk was the fact that the same GEM design was used in all layers of the stack. Therefore, the design included the connec-

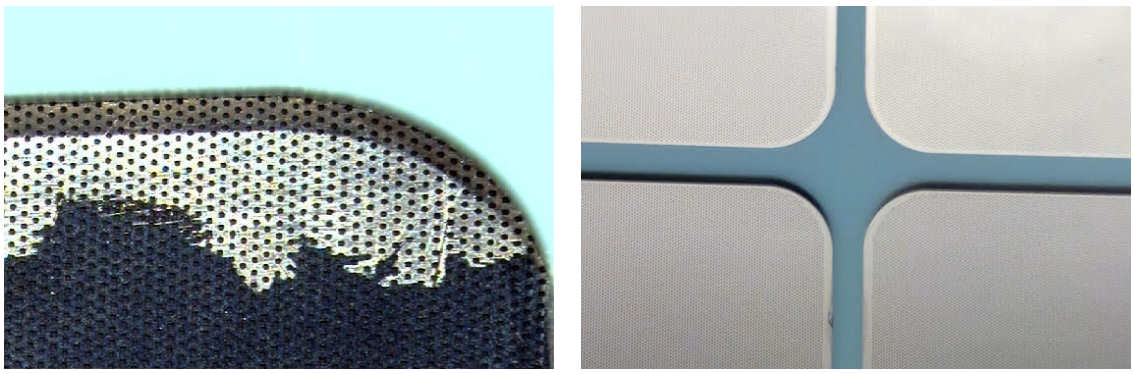

(a) Previous design. **(b)** Corrected design.

Figure 4.5.: (a) Overlap of active area and ceramic frame in a GEM as used for the previous modules. (b) On the new GEMs the added margin is visible as the slightly brighter band along the frame.

tion straps required for all possible positions of the GEM, i.e. 4 connections for each of the 5 electrodes, 20 in total, as visible in figure 4.4a. Cropping the unused straps in each layer leaves behind sharp edges, which create high potential gradients in their vicinity. Therefore great care had to be taken to insulate all remaining connections adequately within the limited space available. To relax this situation in the new modules build for this work, three individual GEM designs are used, each only featuring the five connection straps actually needed for the respective layer in the stack. An example is show in figure 4.4b.

During work with GEMs produced for the previous module generation, it was found that the ceramic frames and therefore also the glue bond partially overlapped with the active area of the GEMs, as shown in figure 4.5a. The source of the overlap was found to be an inconsistency in the design drawings. The experience with those modules lead to the suspicion, that glue on the active area of a GEM negatively affects the HV stability. Therefore, the design of the GEMs was adjusted to maintain a consistent margin between the ceramic frame and the active area of the GEM. The size of this margin was fixed at 0.15 mm, following the investigations on glue spills in section 4.2.1. Additionally, to obtain a fully consistent design for the new modules, the drawings of every part of the module were checked and corrected if necessary.

4.2.1. Investigation of Gluing Parameters

In this section first the gluing setup and procedure are described briefly. The goal of the following investigations of the gluing parameters is to ensure a strong, continuous bond between frame and GEM while avoiding glue spills onto the active area of the GEM. The latter is important, since the glue may cover or permeate the GEM holes. This not only introduces additional dead area in an uncontrolled manner but also may reduce the high voltage stability of the GEM, making it unusable in the worst case.

Two glues, both two-component epoxy resins, were tested for the GEM mounting. Both had been used already in previous gaseous detector projects. In the previous iteration of the

module the *Araldite® AY 103-1 / HY 991* adhesive [174] was used. However, tests done for the outer tracker of the LHCb experiment show detector ageing effects due to outgassing of this glue [175, 176]. Therefore, an alternative was searched for the new modules. The *STYCAST® 1266 A/B* encapsulant [177] was chosen as it was shown to produce no ageing effects [178]. Additionally, its much lower viscosity promised to simplify the glue application. The mixed Araldite and STYCAST compounds have a dynamic viscosity of (4-6) Pa s and 0.65 Pa s, respectively.

The glue is applied to the ceramic frames from a syringe with a Teflon (PTFE) tipped, hollow needle, using a *Techcon Systems TS9702* dispenser with a pressure range of 0.1 bar to 7 bar [179]. In most tests, needles with an inner diameter of 0.15 mm were used but also larger sizes were investigated. The syringe is moved along the frame by an xyz-stage consisting of an *LT8-LBMA* linear axis [180] mounted on a *GT9-NSMA* cross table [181], both by *LANG GmbH & Co. KG*, for the vertical and horizontal movement, respectively. All axes are steered via an *LSTEP express* controller [182] from the same company, which is programmed using a *LabVIEW* interface [183].

For the optimisation of the gluing procedure, the pressure p_{disp} of the dispenser and the movement speed v_{stage} of the xyz-stage were varied. The glue was applied to plates of the same ceramic material the frames are cut from. Multiple straight lines were deposited for each tested parameter combination. After curing, the resulting glue lines were inspected visually. Samples with discontinuous lines, drops or excessive amount of glue were excluded from further studies. Examples are shown in figure 4.6a. For samples with sufficiently uniform and narrow lines the width w_{glue} at randomly chosen points was measured under a microscope. The results from the latter measurements are summarised in table 4.1 and examples are shown in figures 4.6b and 4.6c. This measurement does not allow a direct comparison of the total amount of glue between the two types, as the thickness of the glue line can be different at the same width.

When using the Araldite glue the pressure and speed need to be adjusted simultaneously to keep the glue line continuous. For this reason the width of the line could not be reduced below a value of about 0.4 mm. Above speeds of 5 mm/s it becomes increasingly difficult to achieve a continuous line by compensating with higher pressure. With this glue the process is very sensitive to the size of the gap between the tip of the needle and the ceramic surface. An optimum was found at about 0.1 mm. Going much above that leads to drops forming, as the glue adheres to the tip of the needle, and thus an interrupted glue line. With a narrower gap the glue is smeared by the needle, resulting in a less uniform line. This can be translated in a requirement for the planarity of the surface, i.e. the ceramic frame, which needs to deviate less than about 10 µm from the movement plane of the xyz-stage, for a perfect glue line.

Due to the lower viscosity of the STYCAST glue, a large range of speeds can be covered without adjusting the pressure of the dispenser. The process also becomes less dependent on the width of the gap, which was increased from 0.1 mm to 0.25 mm in some of the tests without affecting the quality of the glue lines. The larger range of speeds covered with the same dispenser pressure, allows to interpolate the measured glue line widths. As the glue flow from the syringe is constant, the cross section of the glue line is expected to scale anti-proportional to the speed of the xyz-stage. Therefore a power-law dependency can be

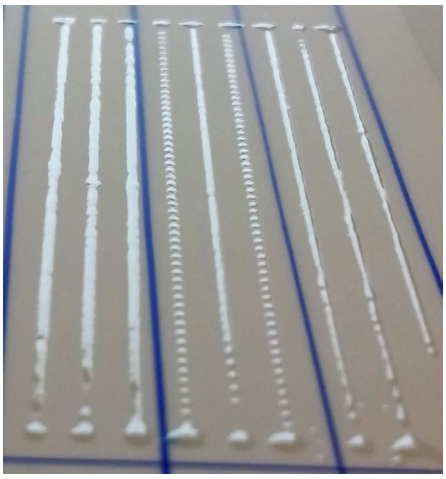

(a) STYCAST lines.

(b) Microscope view of a good Araldite line.

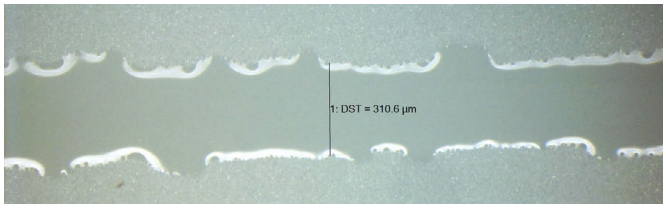

(c) Microscope view of a good STYCAST line.

Figure 4.6.: Examples of glue line quality. (a) STYCAST lines with different parameters. Each blue marking separates a parameter set. The left set shows continuous but quite wide lines. In the middle set the pressure was lowered reducing the flow and causing the line to break up into individual beads. For the rightmost set the speed was lowered to compensate. (b) An Araldite line and (c) a STYCAST line under the microscope.

Table 4.1.: Results from the measurement of the glue line width. Only samples are listed, that show a continuous line in a visual check. The errors given on the average line width correspond to one standard deviation of the measurements. The varied parameters are the pressure of the dispenser p_{disp}, the movement speed of the syringe on the xyz-stage v_{stage} and the gap between the needle tip and the surface h_{gap}.

adhesive	p_{disp} [bar]	v_{stage} [mm/s]	h_{gap} [mm]	line width [mm]
Araldite	0.4	1	0.10	0.419 ± 0.057
	0.7	3		0.392 ± 0.086
	1.0	5		0.391 ± 0.079
STYCAST	0.7	2	0.10	0.786 ± 0.109
		3		0.604 ± 0.093
		4		0.550 ± 0.084
		5		0.493 ± 0.126
		10	0.25	0.391 ± 0.064
		12		0.411 ± 0.100
		15		0.339 ± 0.075
		17		0.311 ± 0.040
		20		0.324 ± 0.064

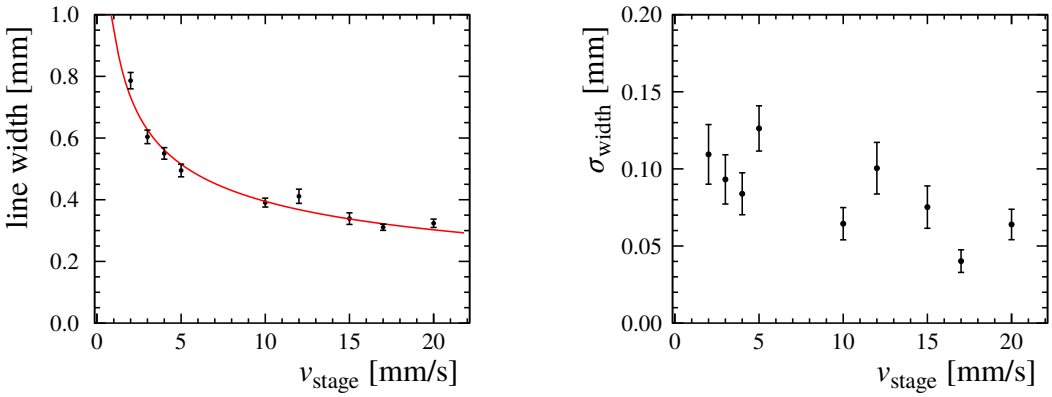

(a) Glue line width.

(b) Standard deviation.

Figure 4.7.: Graphical representation of the STYCAST data in table 4.1. (a) The width of the glue line shows the power-law behaviour explained in the text. The fit of $w_{\text{glue}} \propto (v_{\text{stage}})^k$ describes the data reasonably well ($\chi^2/n_{\text{df}} = 12.64/7$) and returns an exponent $k = -0.384 \pm 0.017$. (b) The standard deviation of the line width is also slightly reduced with increasing speed of the xyz-stage.

expected for the width of the line. This is confirmed for the STYCAST data in figure 4.7. As the data with both gap sizes can be interpolated by the same fit, it can be assumed that this change of the gap size does not affect the width of the line. This leads to relaxed requirements on the planarity of the surface compared to the Araldite glue.

Because of the larger flexibility in the parameters, it was decided to go ahead with the STYCAST adhesive. Using a pressure of 0.7 bar and speed settings of 4 mm/s, 10 mm/s, 15 mm/s, 17 mm/s and 20 mm/s, pieces of ceramic frame were glued onto transparent Kapton foil without copper coating, to study the flowing and smearing of the glue in the process. For this, the manual procedure described at the beginning of section 4.2.2 was used. At 4 mm/s the amount of glue is too large, causing it to spill out along all frame edges up to dis-

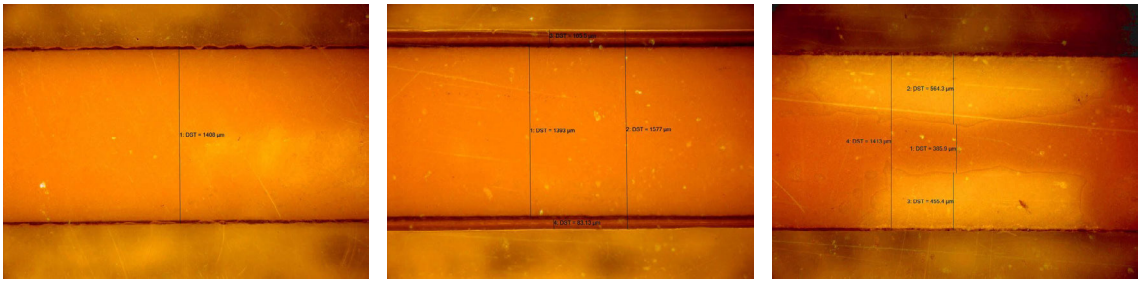

(a) Good distribution.

(b) Glue spill out.

(c) Missing glue.

Figure 4.8.: Examples of the STYCAST bond between ceramic frame and a clear Kapton foil, as seen through the foil. (a) Good glue distribution covering the frame fully but no glue spilling out. (b) Glue spilling out at the edges of the frame is visible as dark bands. (c) At the lighter spots the glue did not cover the frame fully.

tances of 0.2 mm. For the speeds of 10 mm/s and higher, a mostly good glue distribution was observed. Figure 4.8 shows some examples with different quality of the glue bond. It varied between the picture in (a), covering the full width of the frame but no glue spilling out, and in (b), with spills of up to 0.1 mm width at 20 mm/s and increasing for the lower speeds. At some spots the glue did not fully cover the frame, as seen in (c). The exact cause for this could not be determined but as the size and frequency of these spots are rather independent of the speed and therefore the amount of glue, this leaves non-uniform contact pressure as the most likely explanation. This issue was addressed by improving the mounting procedure as presented in section 4.2.2.

In a first attempt to apply these results, a working GEM was glued with the STYCAST epoxy, still using the manual procedure. Due to a handling error, a small amount of glue spilled onto the active area. While the affected area was comparable in size to spills on GEMs glued with the Araldite adhesive before the optimisations in this section, the HV stability of this GEM was reduced drastically, making it unusable. Because of the limited number of available GEMs no further potentially destructive tests were performed. Therefore, the exact cause of this difference in behaviour between the two adhesives was not determined. Due to the prior experience with the existing modules, where the Araldite adhesive did not cause problems to this extent, it was decided to keep using it for the new modules. While the detector ageing effects of this glue are not relevant for the prototypes, due to the shorter service life and the benign radiation environment at the test beam, the studies of alternative adhesives should be continued for future usability under the conditions at the ILC.

4.2.2. A new GEM Mounting Procedure

The main steps of the original mounting method for the GEMs were mostly manual. To achieve a higher and more consistent quality it was decided to develop dedicated tooling for the procedure. This section will present the new apparatus and briefly describe both the manual and the tool-assisted procedure. A comparison of the quality of both procedures in terms of the flatness of the framed GEMs is presented in sections 5.3 and 5.4.

In the manual procedure the GEM is laid out flat on a rolled aluminium holding plate and taped down while applying some tension. The ceramic frame is placed on a second plate. Both GEM and frame are positioned on their respective plate using two alignment pins each. Epoxy glue is applied to the frame using the dispenser system and xyz-stage, as described in section 4.2.1. The plate with the GEM is then lowered by hand onto the frame, making sure the alignment pins on each side match the remaining holes in the other. Weight is applied until the glue has cured and the framed GEM can be removed. For a double framed GEM the procedure is repeated on its other side with a second ceramic frame.

The mounting tool, shown in figure 4.9, consists of three sub-assemblies. The first is a rigid base plate including a lifting stage, intended to mate frame and GEM in a controlled manner. The stage is manually driven with a screw drive for precise control. The frame is held in place on top of the lifting stage by a vacuum jig that has a hole pattern following the geometry of the frame to apply suction. Correct positioning of the frame is ensured by alignment pins in the jig. The jig is detachable so it can also be used to hold the frame on the xyz-stage while applying the glue. This not only makes it easier to move the frame

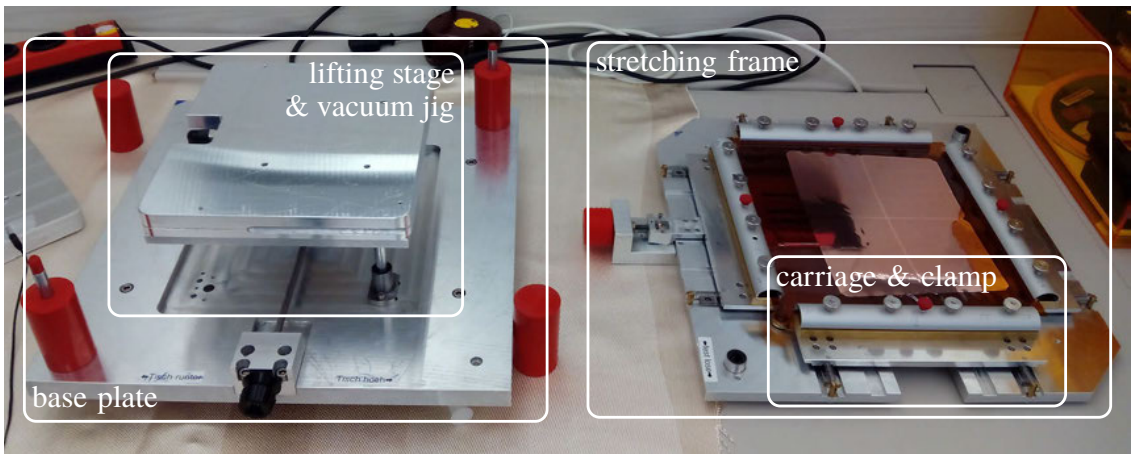

Figure 4.9.: The GEM stretching and mounting tool used for the production of the new modules. The base on the left includes the lifting table with a vacuum jig to hold the ceramic frame. On the right is the GEM tensioning frame, which is detachable to access the lifting table.

from the xyz-stage to the mounting tool, but also keeps the frame flat to ensure a uniform glue application. Alignment pins on the stage and corresponding holes in the bottom of the vacuum jig allow for precise repositioning between the steps. The last part is the GEM tensioning frame, which rests on support pillars on the base plate. Consistent positioning is assured by linear bearings riding on guide rods centred in two of the pillars in opposing corners. The GEM foil is clamped onto four carriages on the frame, each clamp held closed by four knurled nuts on threaded rods. The carriages are arranged in a rectangle and can slide in- and outwards on two rails each. Tension is applied by two coil springs per carriage, one mounted parallel to each rail, pulling the carriages outwards. The springs used have a spring constant of about 10 N/cm and the maximum travelling distance of the carriages is about 2 cm. The tension can be relieved by a wire-pulley system that pulls the carriages inwards.

The following steps of the mounting procedure using the tool are depicted in figure 4.10.

a) The tool is prepared by placing the vacuum jig and the tensioning frame on the base. The clamps of the tensioning frame are opened and the lifting stage is adjusted so that the surface of the vacuum jig is level with the lower jaws of the clamps, providing an even support for the GEM.
b) Then the GEM is placed in the stretching frame using the alignment pins of the vacuum jig to achieve alignment between GEM and ceramic frame in the end.
c,d) When the GEM is in place, the clamps on the tensioning frame are closed and the tension relieve is disengaged.
e) After that, the lifting stage is lowered to withdraw the alignment pins from the GEM. This is done to avoid damaging the GEM in the next step.
f) The tensioning frame is removed from the base and placed at the side.
g) Next the vacuum jig is removed from the lifting stage and moved to the xyz-stage. Then a ceramic frame is placed on top using the same alignment pins and suction is applied to keep it flat.

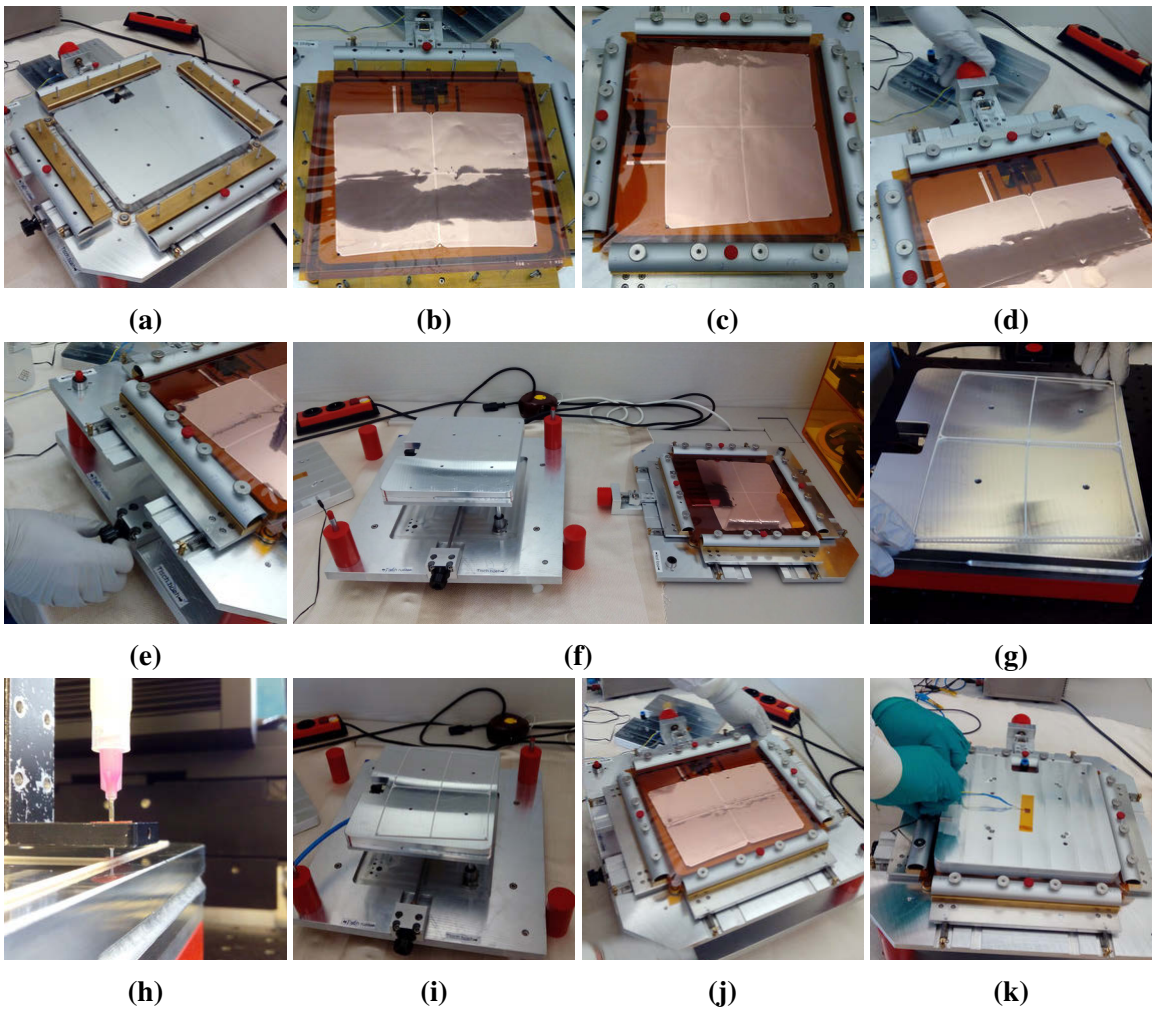

Figure 4.10.: The steps of the GEM mounting procedure described in the text.

h) The epoxy glue is applied in the same way as before using the dispenser system and xyz-stage, as described in section 4.2.1.
i) The vacuum jig with the frame is then moved back onto the lifting stage of the mounting tool in the same orientation as before, without removing the suction.
j) After remounting the tensioning frame on the base, the lifting stage is carefully raised again until the ceramic frame fully touches the GEM without distorting it.
k) A flat plate the size of the vacuum jig is put on top for additional contact pressure. As this is enough to keep the ceramic frame flat the vacuum can be released afterwards.

After the glue has cured, the weight is removed, the tension released and the GEM is removed from the tool. As in the manual procedure, a second ceramic frame can be added to the other side of the GEM by repeating the procedure.

After the tool was successfully used to build ten GEMs, of which six have a frame on both sides, further improvements were made based on the collected practical experience. One concern arose from the clamping mechanism, shown in figure 4.11a. Since the knurled

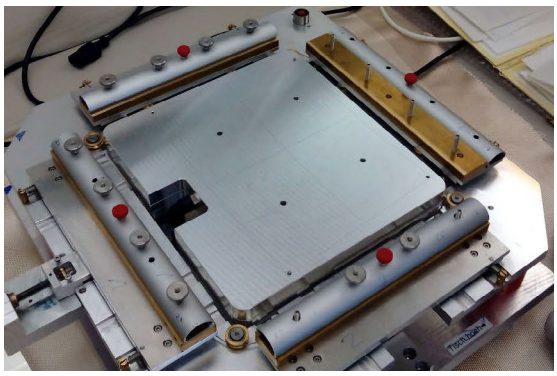

(a) Old mechanism.

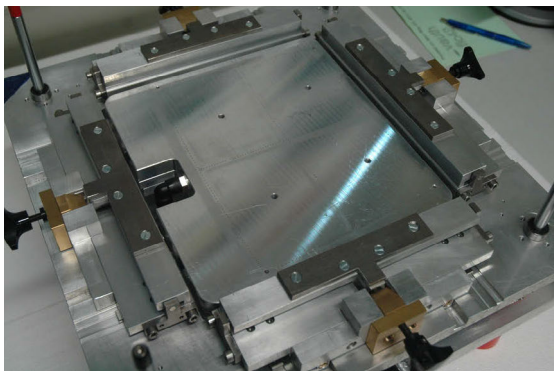

(b) New mechanism.

Figure 4.11.: Comparison of the original and improved clamping mechanism. (a) The original clamps had separate jaws held closed by knurled nuts. (b) The new mechanism uses hinged jaws locked by a screw actuated wedge.

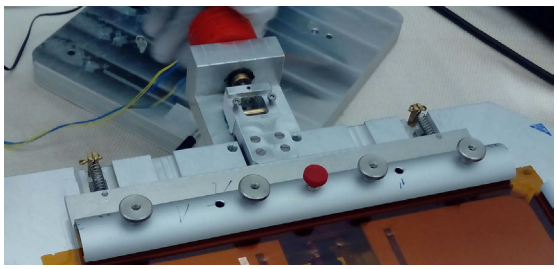

(a) Spring mechanism.

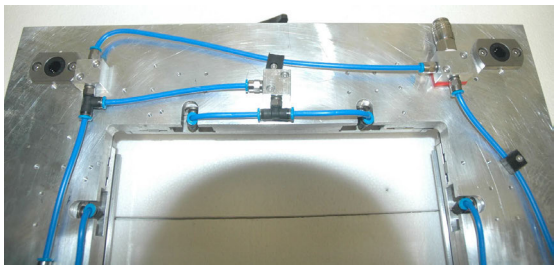

(b) Pneumatic mechanism.

Figure 4.12.: Comparison of the original spring tensioning mechanism and the new pneumatic system. (a) Each carriage was actuated by two springs parallel to the rails. (b) The pneumatic system uses two pistons per carriage.

nuts used to close the clamps had to be fully unscrewed and removed from the threaded rods to open the clamps, they could accidentally be dropped onto the GEM, damaging it in the procedure. Additionally, in some cases the GEM slipped partially out of one of the clamps. Therefore the clamps were reworked to avoid lose parts and increase the holding power. Now, the clamps are hinged, each held closed by a single screw pushing a wedge against a lever arm, as shown in figure 4.11b.

Another part to be redesigned was the tensioning mechanism. While the springs provided force in the correct order of magnitude, the actual force applied to the GEM foil depended on the initial elongation of the springs before disengaging the tension relive. Therefore the tension could not be accurately controlled. To address this issue a pneumatic system was implemented to replace the springs. Each carriage is now actuated by two pneumatic pistons and tension is applied by supplying compressed air. This allows to control the force using a pressure regulator. Figure 4.12 shows the details of the implementation of both systems.

Since the epoxy glue used to attach the ceramic frames to the GEMs needs several hours to fully cure, the production time for double framed GEMs could be roughly halved by gluing

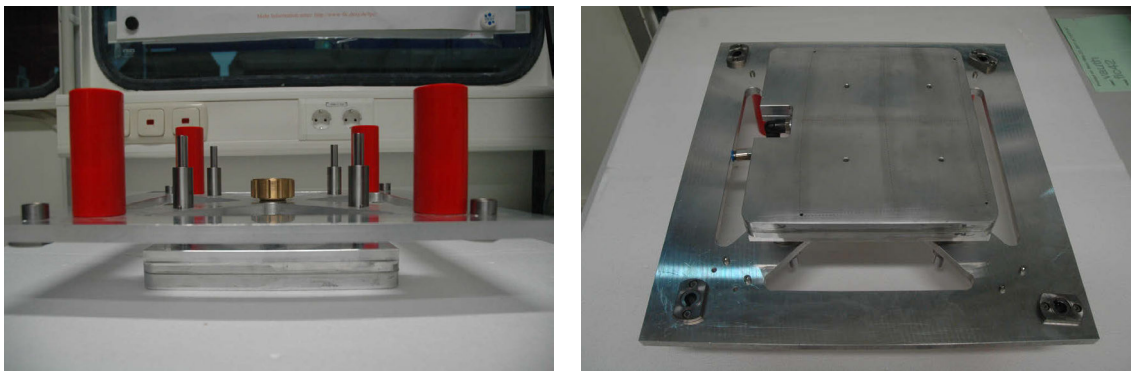

(a) Side view. **(b)** Bottom view.

Figure 4.13.: The assembly to attach the second frame to a GEM. (a) Seen from the side the four guide rods of the lifting stage are visible, as well as the brass knob for adjusting the height of the stage. (b) When turned around the stage and vacuum jig are easily accessible.

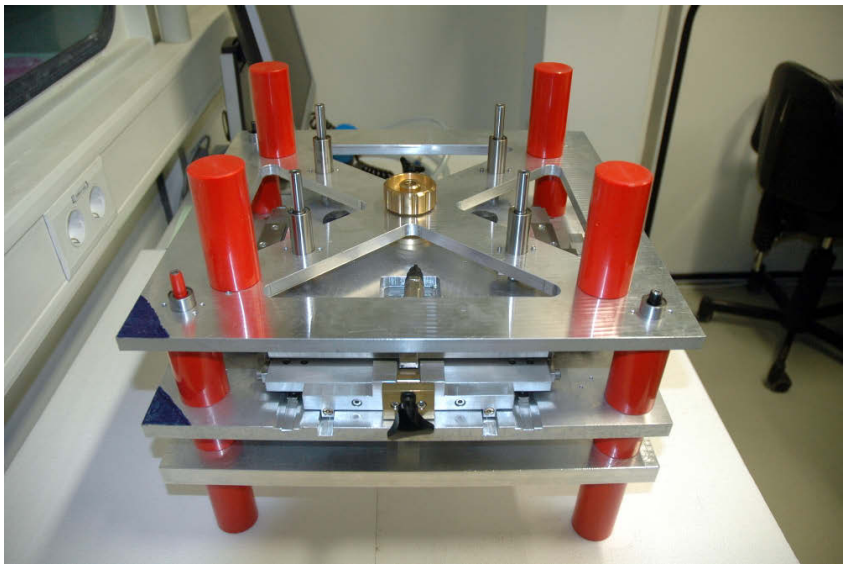

Figure 4.14.: The fully assembled GEM mounting tool.

both frames at the same time. For this purpose an additional assembly was build to lower a second ceramic frame onto the GEM from the top after the first one is in place for curing. The assembly, shown in figure 4.13, consists of a support frame that rests on additional pillars on top of the tensioning frame, using the same guide rods for relative positioning. The support frame holds a lifting stage, that is manually actuated via a screw drive. This way it can be lowered down onto the GEM in a precise and controlled manner. The ceramic frame is held against gravity by a second vacuum jig, identical to the one used before. To fasten the vacuum jig to the lifting stage, the whole assembly can be taken off and turned upside down. Since this assembly adds significant height and weight on top of the tool, the whole support structure was made more compact and rigid. The fully assembled tool is shown in figure 4.14.

5. GEM Flatness Studies

The ambitious performance requirements set for the tracking system regarding single point and momentum resolution as well as the dE/dx resolution put stringent demands on the quality of the readout modules for the TPC. Quality assurance procedures for components of a large scale GEM detector have already been established for the COMPASS experiment [184] and adapted by others, such as the ALICE TPC [171], to ensure a uniform response and stable operation. Many of the controlled parameters, such as the uniformity of the hole size over the GEM area, concern the individual GEM foils and thus are independent of the design and assembly procedure of the readout module. What is affected by these aspects, is the flatness of the mounted GEM foils, i.e. the magnitude of their deflections due to internal stresses or the geometry of their supports. Deflections of the GEM foils affect mainly two aspects of the detector performance. On one hand, the deflections locally change the distances between the individual GEMs in the stack. Since the potentials on the GEM surfaces are fixed, a local variation of the gap also changes the local field strength, see figure 5.1. As explained in section 3.5.1, this alters the electron transfer coefficients of the respective GEMs and thus the effective gain at that location. In turn this can affect the accuracy of the dE/dx measurement. On the other hand, the GEM electrode facing the drift volume is part of the field cage. Therefore, any deflections here create distortions of the drift field, which can have a negative impact on the spatial resolution.

A detailed study of these two effects is presented in ref. [185]. To assess the influence of GEM deflections on the effective gain, the height profiles of several GEMs with and area of 10 cm × 10 cm were measured, using a setup and method similar to those presented in the following sections. As in section 5.5, the measured profiles were combined into triple-GEM stacks and a parametrisation of the transfer coefficients and single GEM gain was used to calculate the effective gain at each point of the stack. The height difference between the highest and the lowest measured point ranged from about 400 µm to 900 µm for different GEMs. The resulting distribution of the effective gain had a relative root mean square (RMS) of 3 %. To judge the impact on the dE/dx measurement, the average of all gain maps was

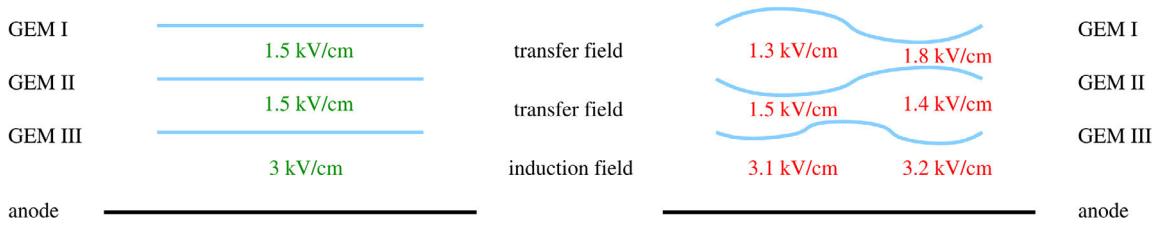

Figure 5.1.: Sketch of the effect of deflections of the GEM foils on the local field configuration in a GEM stack [185].

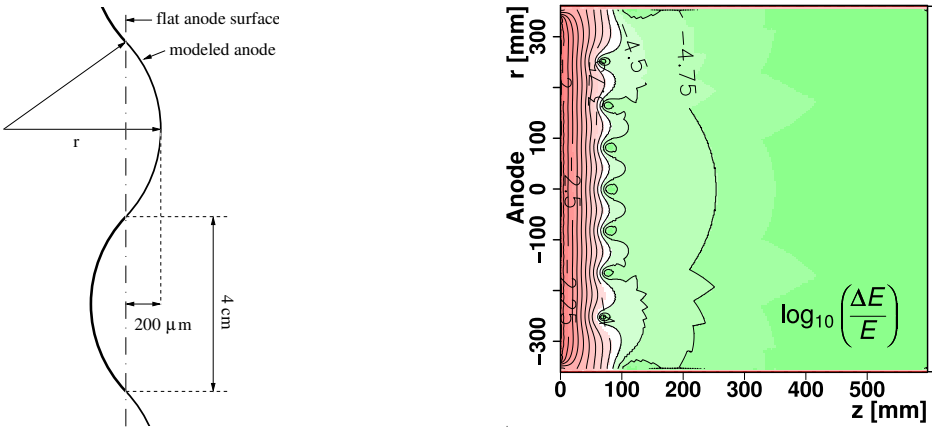

(a) Anode shape. **(b)** Field quality map.

Figure 5.2.: Simulation of a TPC field cage with deflected anode [185]. (a) Sketch of the anode shape used in the simulation. (b) The resulting field quality map. Green areas mark regions where the required field uniformity is reached, while in the red areas the limit of $\Delta E/E \leq 10^{-4}$ is exceeded.

taken and tracks were simulated passing over different areas of the map. Over the whole surface, the average gain of the tracks showed an RMS of 0.27 %. However, between different areas of the map the mean gain varied by up to 0.7 %. For reliable $\mathrm{d}E/\mathrm{d}x$ measurements, certain requirements on the stability and uniformity of the gain in drift chambers have been established from experience with the LEP experiments. While the variations of the gain along a track can be tolerated up to a magnitude of several percent, the mean value of the gain in different regions of the anode or directions from the IP should not vary by more than 10 % of the desired $\mathrm{d}E/\mathrm{d}x$ resolution and already variations of $\mathcal{O}(5\,\%)$ of the resolution are visible in the data [185]. For the goal of a relative resolution of 5 % for the ILD TPC, this means only gain variations up to 0.5 % are tolerable. The measured values above exceed this limit. While this can be corrected for by applying a calibration using a gain map, it is preferable to start out with small deviations. Therefore the goal is to control the size of the deflections already during the mounting of the GEMs and assembly of the modules.

To simulate the influence of GEM deflections on the drift field quality, in ref. [185] an electromagnetic model of the large TPC prototype – see section 6.2 – was adapted to include a simplified model of a deflected anode. It features a sinusoidal deflection pattern where the scale of the deflections was chosen to be 400 µm peak-to-trough with a transverse distance between two peaks of 8 cm, based on the previous measurements. Figure 5.2 shows a sketch of the anode geometry and a map of the resulting field deviations. To reach the required single point resolution better than $\sigma_{r\varphi} \leq 100\,\mu\mathrm{m}$, field deviations of $\Delta E/E \leq 10^{-4}$ can be tolerated [186]. Otherwise $E \times B$ effects become too large. In figure 5.2b it can be seen that this limit is exceeded up to ~8 cm away from the anode, as indicated by the red shaded area, and field distortions of up to $10^{-2.25}$ occur in direct vicinity of the anode. By simulating charged particle tracks in the distorted field and calculating the deviation of the reconstructed tracks from the true position, the impact on the spatial resolution was estimated. If a

magnetic field of 3 T to 4 T was applied in the simulation, the residuals were smaller than 25 µm [185]. Taking these residuals into account as a systematic uncertainty σ_{res}, the point resolution changes accordingly:

$$\sigma_{r\varphi} \rightarrow \sqrt{(\sigma_{r\varphi})^2 + (\sigma_{\text{res}})^2} = \sqrt{(100\,\mu\text{m})^2 + (25\,\mu\text{m})^2} = 103.1\,\mu\text{m} \ . \tag{5.1}$$

While this deterioration of 3 % is acceptable on its own, it is not the only effect that can have a negative impact on the drift field quality. Other influences of similar magnitude can arise from the accuracy of the field cage itself [187] and from ions flowing from the amplification region back into the drift volume [188]. Since all such effects add up, every one of them, including the flatness of the GEM foils, need to be tightly controlled to ensure the required measurement accuracy.

For this work, a method similar to the one used in ref. [185] was adapted to study the flatness of GEM foils as they are used in the modules described in chapter 4. Several height profiles of GEMs that were mounted on their ceramic frames using the newly developed tool presented in section 4.2.2 have been measured. To evaluate the advantage of the tool assisted procedure, these are compared to another set of GEMs mounted via the manual procedure described in the same section.

5.1. Measurement Setup

The measurement setup is shown in figure 5.3. It consists of a laser displacement sensor attached to a precision xyz-movement stage and a GEM mounting plate. Both the xyz-stage and the displacement sensor are controlled and read out via a common LabVIEW program [183].

The laser displacement sensor *LK-G10* by *Keyence* [190] works based on triangulation as sketched in figure 5.4. A laser diode projects a dot with 20 µm diameter onto the surface to be measured. The reflected light falls through a low aberration lens system onto an image sensor. When the distance to the measured surface changes, the position of the image of the laser dot on the image sensor changes. Therefore, the position of the reflecting surface can be deduced from the position of the image of the laser-dot on the sensor. The size of the optics and the image sensor limits the measurement range to ± 1 mm around the neutral position. Measurements can be taken either in single point mode or continuously at sampling frequencies up to 50 kHz. During continuous operation the data is stored in an internal buffer that can be read out after the measurement is stopped. Several statistical operations can be applied to the data online. Of interest for this work is the floating average with up to 16 384 samples, which can be used to increase accuracy on rough surfaces or in case of vibrations in the setup. The *LK-G10* specifications state a repeatability of 0.02 µm when averaging over 4096 measurements [190], suggesting a single point accuracy better than 2 µm. Effects from linearity of the measurement range and temperature dependence are below 1 µm.

The xyz-stage consists of an *LT8-LBMA* linear axis [180] mounted on a *GT9-NSMA* cross table [181], both by *LANG GmbH & Co. KG*, for the vertical and horizontal movement, respectively. Both are steered via an *LSTEP express* controller [182] from the same company.

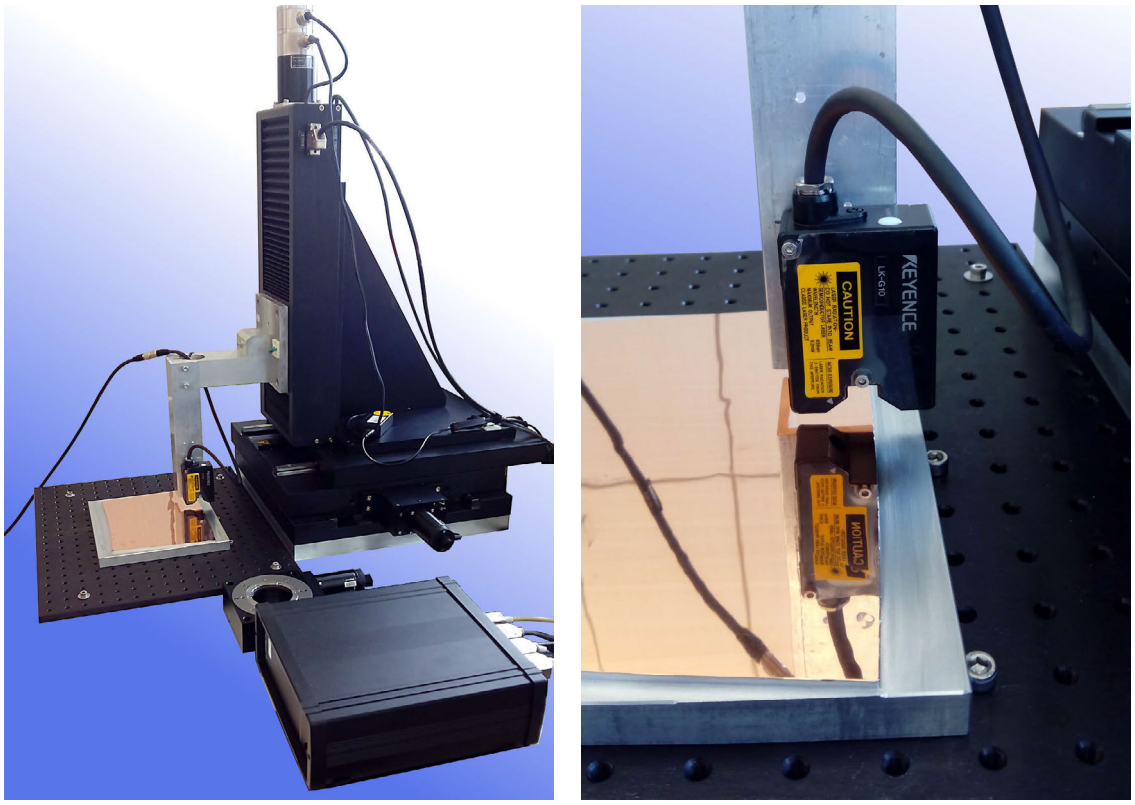

(a) Overview of the setup. **(b)** Displacement sensor.

Figure 5.3.: The GEM profile measurement setup during the measurement of a GEM dummy glued onto a cast-aluminium frame profile. (a) The xyz-stage with mounted displacement sensor in the back and the LSTEP controller in the front. (b) The displacement sensor mounted on the moving arm of the xyz-stage.

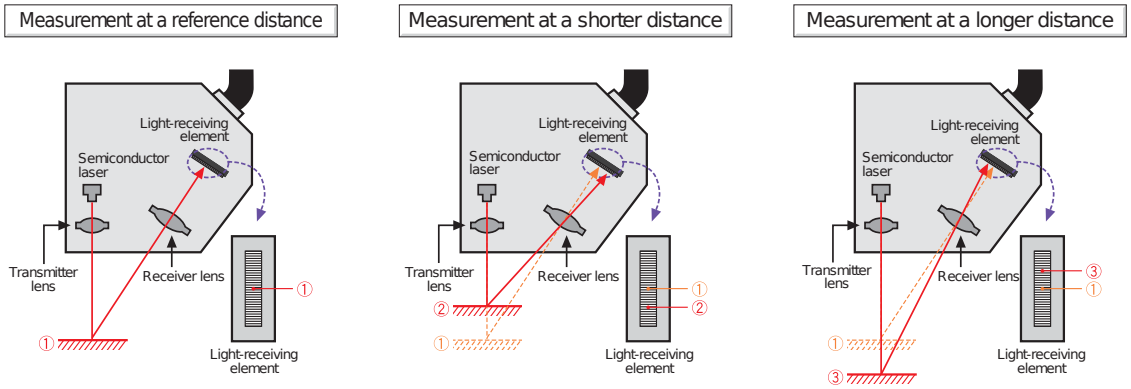

Figure 5.4.: Sketch of the working principle of the laser displacement sensor. © 2008 KEYENCE CORPORATION [189]

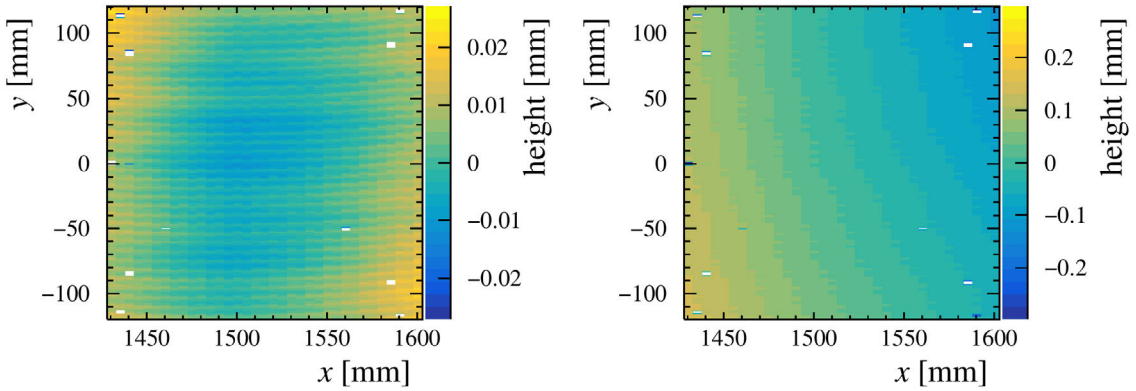

(a) After slope correction.

(b) Raw measurement.

Figure 5.5.: The height profile of the GEM mounting plate (a) after correcting for the relative inclination of the setup and (b) without the correction. Note the different scales of the height axes.

All axes provide a travel distance of 300 mm and a positioning accuracy of 3 µm using their internal high resolution measurement system. During the movement, vibrations of the laser device on the end of the mounting arm with an amplitude of $\mathcal{O}(10\,\mu\text{m})$ and wavelengths of $\mathcal{O}(100\,\mu\text{m})$ at the chosen movement speed were observed. This magnitude is not critical and is further mitigated by averaging the height measurement over sufficiently large movement distances. Since the vibrations are the single largest contribution to the uncertainty of the measurement, an accuracy of 10 µm is assumed for single points.

The GEM mounting plate provides a flat reference surface, on which the GEMs are placed during the measurement. To affix the GEM to the plate, it features a pattern of threaded holes matching the mounting holes in the GEMs and ceramic frames. The plate is milled from cast aluminium to limit distortions due to internal stresses. As can be seen in figure 5.5a, the milling process left a depression in the centre, about 30 µm deep compared to the corners. Since the measured deflections of the GEM are much larger and all mounting points for the GEM are on roughly equal height, this should have only little effect on the GEM profiles. All other measurement uncertainties introduced by the setup are negligible.

5.2. Measurement Procedure

For the measurements presented in this chapter the movement speed of the xyz-stage was set to 20 mm/s. The displacement sensor was operated in continuous mode with a sampling rate of 5 kHz, resulting in 250 measurement points per mm. To account for the vibrations of the setup, a floating average with 64 samples was used in the first measurements. However, this was found to be redundant due to the binning of the data in the analysis. Therefore no floating average was used in later measurements.

For the measurement of a GEM height profile the framed GEM is fixed on the mounting plate using nylon screws. The mounting plate can be placed in either horizontal or vertical

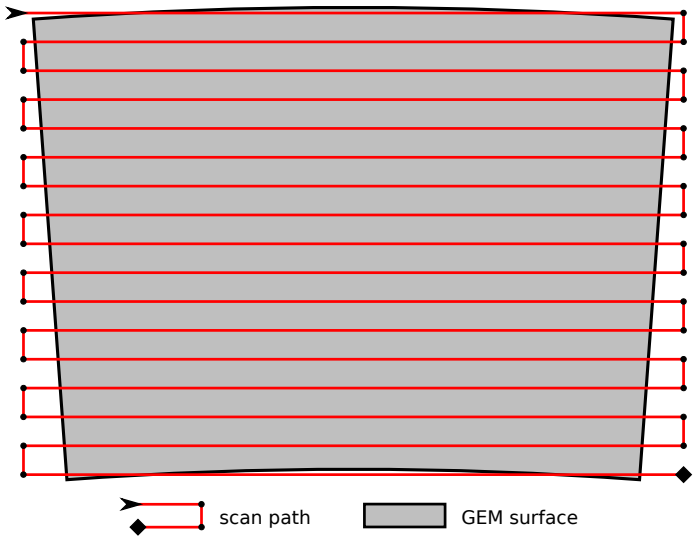

Figure 5.6.: Sketch of the meander pattern used to scan the GEM surface.

orientation in the operating volume of the xyz-stage. The vertical orientation was included because the GEMs would be mounted this way in the TPC. Compared to the horizontal orientation, potential sagging of the foil due to gravity could be reduced. However, measurements showed no significant difference of the height profiles between both orientations. Therefore only the horizontal orientation was used for the measurements in this chapter.

To ensure the whole surface of the GEM is in the measurement range of the displacement sensor, the xyz-stage is used to adjust the distance between the sensor and the surface so that it is in the centre of the measurement range. Then, starting from one corner of the GEM, the stage moves the displacement sensor across the surface, following a meander pattern as shown in figure 5.6. The step distance between the horizontal lines was first set to 1 mm. To reduce the time required for one measurement it was later increased to 5 mm, roughly matching the row pitch of the readout planes in the modules. Since the GEM surfaces are generally smooth on these scales, the deflections at adjacent locations are highly correlated and no significant effect is expected from this change. At the beginning of each line, the displacement measurement is started. The data is stored in the internal buffer and at the end of the line the buffer is written to hard disc and reset. Since the displacement sensor and the xyz-stage are independent devices in terms of data flow, the exact position of the stage is not synchronised with the displacement measurement. Therefore only the position of the xyz-stage at the start and end of each line is stored by the LabVIEW program.

In the analysis the two-dimensional position for each point of the displacement measurement is calculated from the start and end positions of the corresponding line based on the acceleration and speed of the xyz-stage. After calculating the positions, the data are input into a 2D histogram to create a map of the height deviations, in the following called a height profile. The binning perpendicular to the measured lines is given by the step size of the meander, i.e. 1 mm or 5 mm. Parallel to the lines, a bin width of 1 mm was chosen. Each bin value is given by the average of all data points included in the bin area. The height axis

is centred around zero by subtracting from each bin value the total average height. Since this process averages over 250 measurement points per bin, the statistical uncertainty of the height value in each bin, as calculated from the single point uncertainty given in the previous section, is smaller than 1 µm.

As can be seen in figure 5.5b on page 69, there is a relative inclination between the movement plane of the xyz-stage and the surface of the mounting plate. To correct for this inclination a profile measurement of the bare mounting plate is taken whenever the setup was changed. A two dimensional linear fit is performed on the resulting height profile. Then, for each bin in the corresponding GEM profiles the value of the fit at that position is subtracted from the measured height value. A comparison of both images in figure 5.5 shows the effect of this correction on the mounting plate profile itself. The fit is performed on the profile of the base plate and not the GEMs themselves to avoid introducing biases into the fit due to the deflections that this analysis intends to measure.

5.3. Testing the manual GEM Mounting Method

A set of five GEMs that were assembled using the manual mounting method described in chapter 4 were measured using the method introduced above. This sample contains three GEMs with a single ceramic frame and two double framed GEMs, i.e. one frame on each side of the foil, as listed in table 5.1. The corresponding height profiles are displayed in figure 5.7. The observed height deviations are comparable in size to the 10 cm × 10 cm GEMs investigated in ref. [185], which were mounted using a similar method. The stripes of large negative values in the upper area of *GEM_4* in figure 5.7e result from interaction of the laser dot of the displacement sensor with the holes of the GEM. An attempt was made to detect these patterns in the reconstruction and correct the corresponding values using adjacent measurement points. However, this was not successful and a more involved approach was not in the scope of this work. Therefore the quantitative analysis described below is designed to eliminate the impact of these patterns.

To get a measure for the magnitude of the height deviations in different areas of the GEMs, the RMS of the deviations between all five GEMs is calculated for each bin. The resulting map is shown in figure 5.7f. The RMS is preferable to the mean deviation since the deflections have no preferred direction. Therefore in the mean, positive and negative deviations cancel, resulting in an underestimation of the total deviations. The structures in figure 5.7f are dominated by the GEMs *LPD_10* and *LPD_17*, cf. figures 5.7a and 5.7b. However, some similar patterns are visible in most of the GEMs. Except for *GEM_1* in figure 5.7c, the largest deflections appear in the centre of the panels of the frames. The cause of this is most likely insufficient stretching force during the mounting of the GEM, resulting in preexisting deflections persisting through the process. An additional, different structure is visible in *LPD_10* and *GEM_4* in figures 5.7a and 5.7e in the form of diagonal and horizontal ridges that do not follow the location of the frame. These may indicate tension lines where the GEM foil bends due to internal stresses induced by non-uniform tension. This non-uniformity can be caused by the manual GEM stretching procedure or by stresses introduced into the ceramic frame during mounting. The above may also explain the dipole-like structure in figure 5.7d,

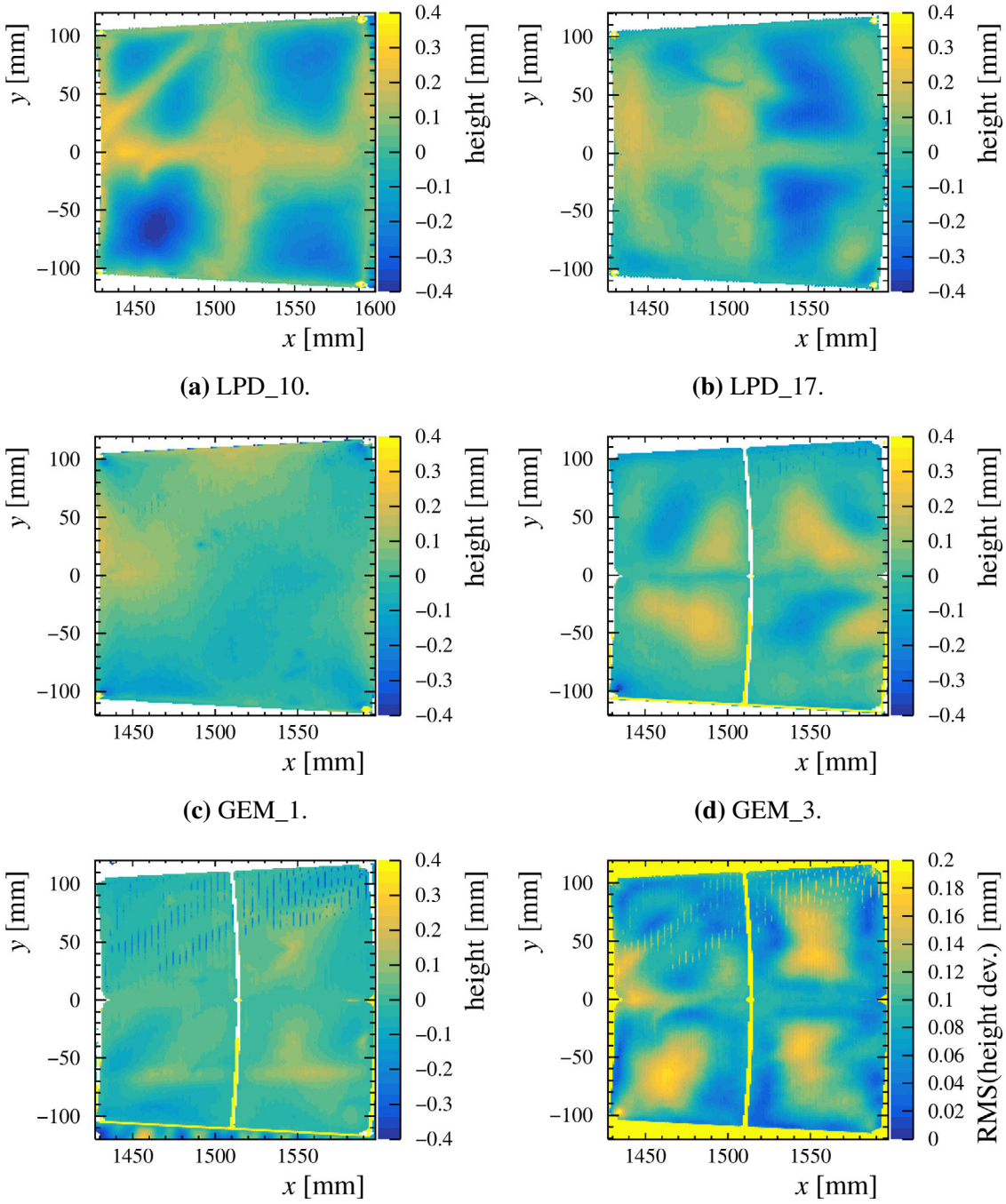

(a) LPD_10.

(b) LPD_17.

(c) GEM_1.

(d) GEM_3.

(e) GEM_4.

(f) Height deviation RMS.

Figure 5.7.: Deflections of the manually mounted GEMs. (a) to (e) Height profiles mounted GEMs. The average height deviations are listed in table 5.1. The stripes of large negative values in the upper area of (e) result from interaction of the laser dot of the displacement sensor with the holes of the GEM. (f) A map of the RMS of the height deviation between all five measured GEM.

Table 5.1.: Summary of the flatness measurement results of GEMs assembled using the manual procedure. Given are the RMS_{90} of the height as well as the smallest and largest value measured on each foil and the peak-to-peak difference. In addition to the individual measurements, the averages of the single and double framed GEM subsets and of all GEMs are shown. For the individual measurements purely statistical uncertainties are given. For the averages the standard error of the mean is displayed, see the text for details.

GEM ID	frame	RMS_{90} [µm]	min [µm]	max [µm]	Δ [µm]
LPD_10	single	140.14 ± 0.57	-397	298	695
LPD_17	single	116.70 ± 0.47	-329	222	551
GEM_1	single	64.04 ± 0.26	-158	185	343
GEM_3	double	86.14 ± 0.35	-182	239	421
GEM_4	double	43.61 ± 0.18	-170	170	340
average single		107.0 ± 22.5	-295 ± 71	235 ± 33	530 ± 102
average double		64.9 ± 21.3	-176 ± 6	205 ± 35	380 ± 41
average all		90.1 ± 17.4	-247 ± 49	223 ± 22	470 ± 68

where each of the frame panels is divided diagonally, with one half depressed and the other elevated. In *LPD_10* and *GEM_1* large deflections are visible at locations of the ceramic frame. Since the stretching forces of the foil are oriented within the plane of the GEM, they should not deflect the frames in this way. Therefore these deformations are likely induced by stresses in the material of the frames themselves.

The quality of the GEM mounting is evaluated using the distribution of the measured height values on each GEM. To avoid biases from measurement points on the ceramic frames on top of the GEM and from untrimmed foil outside of the frame, geometric cuts are applied to exclude measurements in these areas. The value chosen to compare the flatness of the GEMs is the RMS of the smallest interval of the height distribution containing 90 % of the entries (RMS_{90}). This is done to eliminate any influence from other outliers, in particular produced by the interaction of the laser dot with the GEM holes described above. The RMS_{90} is scaled such that for a Gaussian distribution the value is equal to the standard deviation. The results of these calculations are summarised in table 5.1. The consistency and repeatability of the mounting procedure can be judged by looking at the difference in the average height deviations between the GEMs. The table shows that they differ by almost 100 µm between the flattest GEM and the most uneven one, *GEM_4* and *LPD_10*, respectively. This means the variation of the average height deviations between individual GEMs is of the same order of magnitude as the deflections themselves. A different way to approach this, is to calculate the mean of the RMS_{90} of all five GEMs and the corresponding standard deviation. This average, given in the last line of table 5.1, is (90.1 ± 17.4) µm, where the uncertainty is the standard error of the mean. Accordingly the standard deviation of the sample is (39.0 ± 12.3) µm.

To estimate the influence of the stiffness of the frame on the achieved flatness, the average RMS_{90} is also calculated for the two subsamples of single and double framed GEMs, see

also figure A.2a on page 191. A difference of $(42.1 \pm 31.0)\,\mu m$ between the two averages is observed. This result is not significant, mainly because the large differences between the individual GEMs are dominated by insufficient or non-uniform tension of the GEM foils. Therefore based on this small sample an advantage of double framed GEMs can not be reliably concluded. It is to be noted that for the small sample sizes used here, the sample standard deviation tends to underestimate the standard deviation of the population [191], e.g. by ~6 % for $N = 5$ and ~25 % for $N = 2$, further reducing the significance of the result.

5.4. Test of the Tool Assisted Procedure

To assemble the three modules used for the test beam measurements in chapters 8 and 9, nine GEMs were glued to their frames using the stretching and mounting tool described in section 4.2.2. Due to availability of the setup, the flatness measurement was only performed for seven of these. Of these seven GEMs, two have a single frame and five are double framed, as listed in table 5.2. The height profiles are displayed in figure 5.8. For the GEM *LPD_M_5*, the measurement area was not correctly aligned with the GEM and the profile appears shifted along the y-axis compared to the others. As for the manually mounted GEMs in section 5.3, the RMS of the deflections between the GEMs is calculated for each bin. The resulting map is shown in figure 5.8h. It can be noted that the overall scale of the deflections is much reduced compared to the manually mounted GEMs. Additionally, the map in figure 5.8h is not dominated by the deflections of only a couple of GEM foils and it shows fewer structures in general. The largest deviations no longer occur in the centre of the panels of the frame, as is the case for the manually mounted GEMs. Instead they show up at the edges and along the struts of the frame, mostly at points further away from the fixing screws. Only *LPD_M_5*, shown in figure 5.8d, exhibits some structures similar to those observed in *GEM_3* in figure 5.7d. All this indicates that with the tool-assisted mounting procedure the deflections of

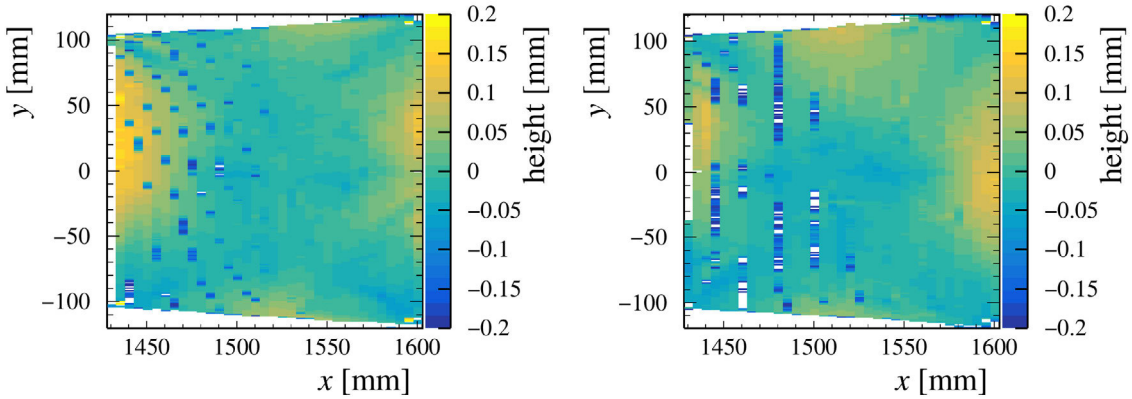

(a) LPD_D_3. **(b)** LPD_D_5.

Figure 5.8A: Deflections of the GEMs mounted using the tool assisted procedure. Continued on the facing page.

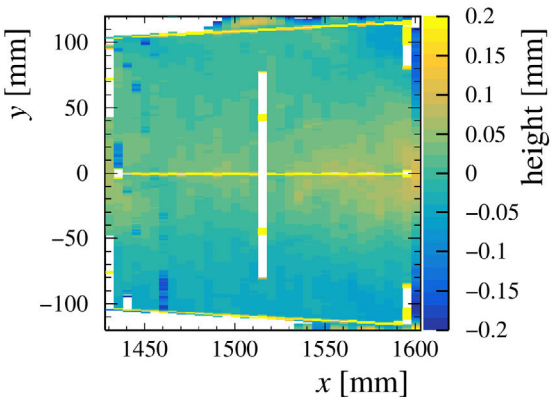

(c) LPD_M_1.

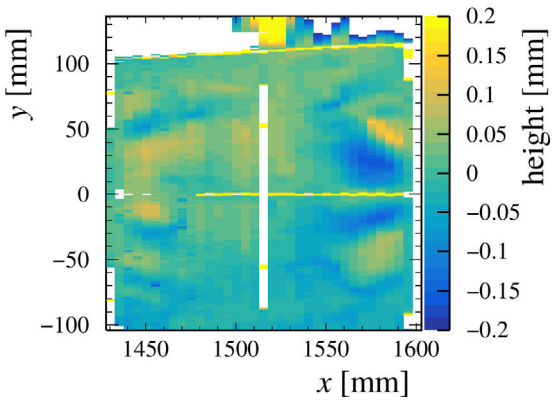

(d) LPD_M_5.

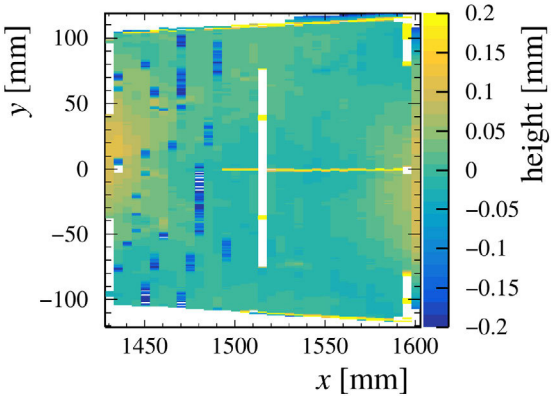

(e) LPD_B_1.

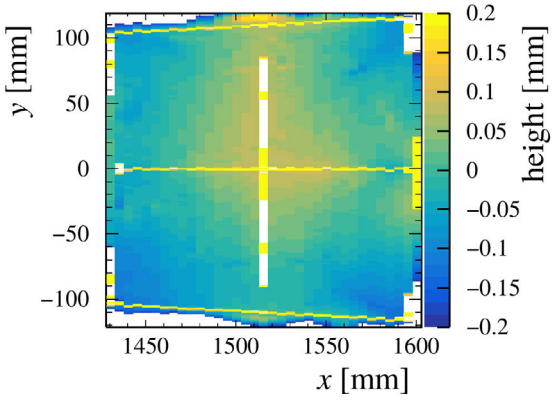

(f) LPD_B_4.

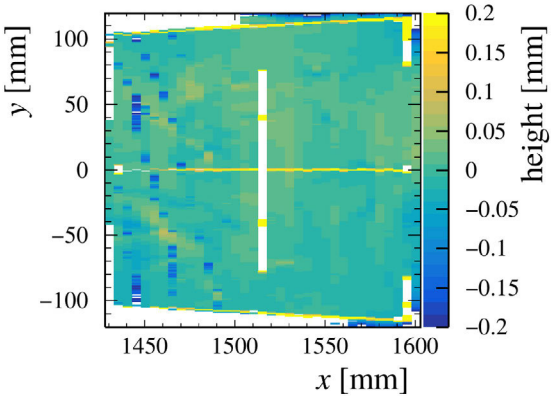

(g) LPD_B_5.

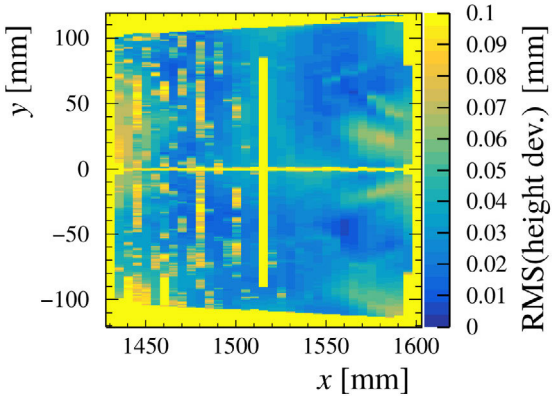

(h) Height deviation RMS.

Figure 5.8B: Deflections of the GEMs mounted using the tool assisted procedure. Continued from the preceding page. (a) to (g) Height profiles of the mounted GEMs. The average height deviations are listed in table 5.2. The spots and stripes of larger negative values on the left side of some of the profiles result from interaction of the laser dot of the displacement sensor with the hole pattern of the GEM. (h) A map of the RMS of the height deviation between all measured GEM. Note that the colour scales are reduced by a factor of 2 compared to figure 5.7.

Table 5.2.: Summary of the flatness measurement results of GEMs assembled using the mechanised procedure. Given are the RMS_{90} of the height as well as the smallest and largest value measured on each foil and the peak-to-peak difference. In addition to the individual measurements, the averages of the single and double framed GEM subsets and of all GEMs are shown. For the individual measurements purely statistical uncertainties are given. For the averages the standard error of the mean is displayed.

GEM ID	frame	RMS_{90} [µm]	min [µm]	max [µm]	Δ [µm]
LPD_D_3	single	31.53 ± 0.29	−80	183	263
LPD_D_5	single	36.32 ± 0.34	−60	125	185
LPD_M_1	double	30.57 ± 0.28	−70	88	158
LPD_M_5	double	39.97 ± 0.37	−164	142	306
LPD_B_1	double	21.46 ± 0.20	−42	114	156
LPD_B_4	double	49.40 ± 0.46	−133	91	225
LPD_B_5	double	16.81 ± 0.16	−70	79	149
average single		33.9 ± 2.4	-70 ± 10	154 ± 29	224 ± 39
average double		31.6 ± 5.9	-96 ± 23	103 ± 11	199 ± 30
average all		32.3 ± 4.2	-89 ± 17	117 ± 14	206 ± 23

the GEM foils due to non-uniform tension are mostly eliminated. Also deformations of the frames due to the tension of the foil do not seem to contribute significantly, as then similar patterns would be expected in all GEMs. In this case the deflections of the single-framed GEMs would also be expected to be significantly larger than the double-framed ones. Instead, the deflections seem to be dominated by the deformations of the ceramic frames under their own internal stresses.

To compare the flatness of the GEM foils and thus the quality of the mounting procedure quantitatively, also here the RMS_{90} of the distribution of the height values is calculated for each GEM, as described in section 5.3. As for the manually mounted GEMs, also the average RMS_{90} of the full sample as well as the single and double framed subsamples are calculated. The results are summarised in table 5.2. As was the case for the manually mounted GEMs, the difference of the average deflections between the flattest and the most uneven GEM, *LPD_B_5* and *LPD_B_4*, respectively, is of the same scale as the deflections themselves. However, in comparison with table 5.1 the average size of the deflections on the individual GEMs is much smaller. This can also be seen comparing the overall distributions of the height deviations for both samples in figure 5.9a. The mean RMS_{90} of the total sample is (32.3 ± 4.2) µm, where the uncertainty is again the standard error of the mean. The standard deviation of the average deflections across the whole sample is accordingly (11.0 ± 2.9) µm. Compared to the manually mounted GEMs the average size of the deflections is reduced by a factor of about 2.8. The variation between individual GEMs, indicated by the standard deviations of both samples, is reduced by a factor of about 3.5. Additionally, for the GEMs mounted using the tool assisted procedure there is no large difference in the average scale of the deviations between the single and double framed subsamples,

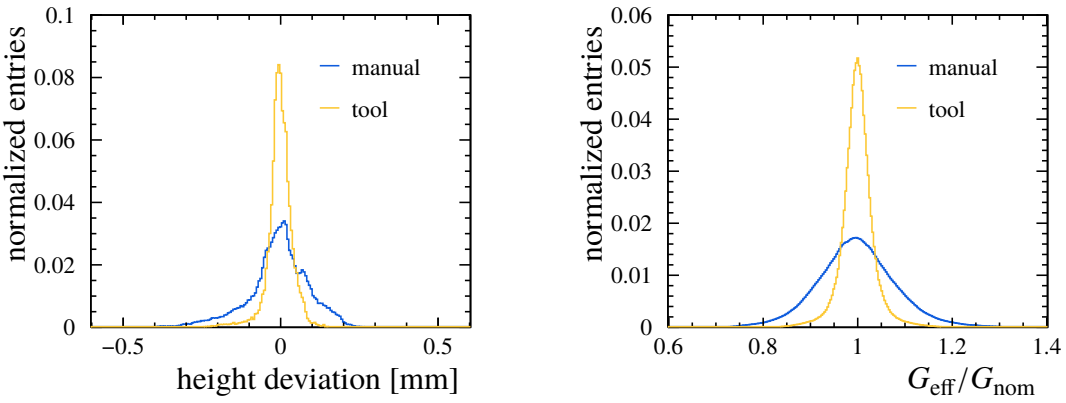

(a) GEM height distributions.

(b) Gain distributions.

Figure 5.9.: Distributions of (a) the GEM height deviations and (b) the resulting effective gain normalised to the nominal gain, using the parametrisation for T2K gas. Shown are the distributions for the two samples of GEMs, the manually mounted ones and the ones using the tool-assisted procedure, respectively.

see also figure A.2b on page 191. As in the previous section, also here the sample sizes are small and the given uncertainties may greatly underestimate the standard deviation of the population [191]. Therefore, a sizeable difference can not be fully excluded.

5.5. Effective Gain Calculation

To study the effect of the GEM deflections on the effective gas gain of the triple GEM stack in a module, the method used in ref. [185] – which itself is based on studies in ref. [192] – was adapted. It uses a parametrisation of the electron transfer coefficients and immediate gas gain of GEM foils, see section 3.5.1. Here mainly a parametrisation for T2K gas ($\mathrm{Ar} : \mathrm{CF_4} : \mathrm{HC(CH_3)_3}$ in a ratio of 95 : 3 : 2 [193]) without a magnetic field – based on measurements in ref. [169] – is used, since it is the gas intended for the ILD TPC and is also used for the test beam measurements in chapters 8 and 9. Unfortunately, parameters including a magnetic field were not available for this gas at the time of this work. Additional input parameters are the voltages across the GEM foils and the fields in the drift region as well as the transfer and induction gaps, as given in table 5.3. The voltages are set to 250 V for all three GEMs. The nominal fields are 240 V/cm for the drift field, 1500 V/cm for the transfer fields and 3000 V/cm for the induction field. Stacks of three GEMs are build from the height profiles measured in sections 5.3 and 5.4. Using the binning of the profiles as described in section 5.2, the local width of the transfer and induction gaps is modulated according to the height deviations in each bin. The nominal values are 2 mm and 3 mm, respectively. Using the known, fixed potentials on the GEM surfaces, this change in the size of each gap is translated into a change of the local field strength, as sketched in figure 5.1 on page 65. For each bin the transfer coefficients of each GEM are recalculated and the total effective gain is determined from the product of all three GEMs.

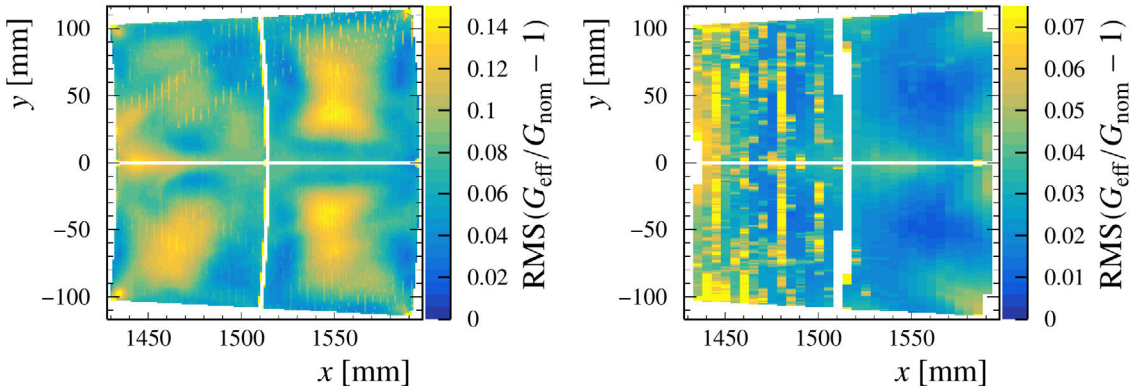

(a) Manually mounted GEM.

(b) Tool assisted mounting.

Figure 5.10.: Maps of the average deviation from the nominal gas gain as given by the RMS in each bin, for (a) the manually mounted GEM and (b) the GEM mounted using the new tool assisted procedure. The vertical stripes and spots of enhanced RMS in both maps result from the corresponding structures in the height measurements. Note that the scales in the two figures are different by a factor of two.

With the number of measured height profiles in the two samples, five and seven, respectively, the number of possible combinations is limited. Therefore, each profile is mirrored at its symmetry axis, i.e. the x-axis in figures 5.7 and 5.8, to double the number of profiles. By inverting the height deviations in each profile, original and mirrored, the statistics is doubled again. This leads to final sample sizes of 20 and 28 profiles and in total 6840 and 19 656 possible combinations of three different GEMs. However, care is taken to avoid double counting by rejecting combinations that are fully mirrored versions of already used stacks. This is achieved by never using a mirrored profile as the first GEM in the stack. Additionally, to avoid artificial accumulation or cancellation of deviations in certain areas, the same GEM is not used multiple times in one stack, neither is it used in combination with its inverted profile. These restrictions lead to the final numbers of valid combinations of 2880 and 8736 for the two GEM samples.

For each of these combinations an effective gain map is calculated as described above. To judge the spatial distribution of the largest gain deviations, for each bin the RMS of the effective gain deviation across all stack combinations is determined. The results for both samples are shown in figure 5.10. Unfortunately, the presence of the stripe patterns in several of the height profiles is translated to the gain maps. In particular for the tool mounted sample this makes it harder to see patterns in the left half of the map. However, it is still easily visible that the overall scale of the gain deviations is much smaller in this sample than in the manually mounted one. The locations of the largest gain deviations generally follow the largest height deviations, as is expected. In the manually mounted sample, this means there are areas of large deviations in the centre of the frame panels and regions of small deviations close to the frame. In the sample of GEMs using the mounting tool the picture is somewhat inverted, with large deviations close to some areas of the frame.

Table 5.3.: The fields and GEM voltages used for the different gasses in the effective gain calculation. Values for P5 gas are taken from ref. [185]. Values for TDR gas are taken from ref. [194].

gas	GEM HV [V]	fields [V/cm]		
		drift	transfer	induction
T2K	250	240	1500	3000
P5	325	90	1500	3000
TDR	310	240	2500	5000

Table 5.4.: The mean and the average deviations of the effective gain from the nominal gain as given by the RMS_{90} of the gain distribution of all combinations of three GEMs. Values are given for the two data sets of manually mounted and tool mounted GEMs, each for the three gasses T2K, TDR and P5 as well as with magnetic fields of 0 T and 4 T. For T2K gas no parametrisation for a magnetic field of 4 T was available.

gas	B [T]	mean		RMS_{90} [%]	
		manual	tool	manual	tool
T2K	0	0.9979	1.0005	8.36	3.15
P5	0	1.0006	0.9996	2.49	0.92
	4	0.9996	0.9997	2.46	0.91
TDR	0	1.0012	1.0002	1.89	0.69
	4	1.0006	1.0004	3.25	1.20

To judge the gain deviations quantitatively, for both samples the distribution of the effective gain in all bins, normalised to the nominal gain, is created. The result is shown in figure 5.9b. For comparison the distributions of the GEM deflections are displayed in figure 5.9a. As can be seen the reduction of the deflections of the tool mounted GEM directly translates to the deviations of the effective gain. To mitigate the biases on the quantitative comparison due to the stripe patterns in the height maps, again the RMS_{90} is used. For better comparison with earlier results and to judge the influence of the magnetic field, the calculation is repeated with parametrisations of P5 gas ($Ar : CH_4$ in a ratio of $95 : 5$), which was used for the simulations in ref. [185], and a mixture proposed in the TDR of the TESLA project [195] (TDR gas; $Ar : CH_4 : CO_2$ in a ratio of $93 : 5 : 2$), both without a magnetic field and a 4 T field. The GEM voltages and values of the drift, transfer and induction fields used for these gasses are summarised in table 5.3.

The results are presented in table 5.4. In all cases the mean is close to 1, i.e. on average the nominal gain is preserved. In T2K gas the manually mounted GEMs show a gain RMS_{90} of 8.36 % while the distribution of the tool mounted GEMs is less than half as wide with a width of 3.15 %. As the results show, the scale of the relative gain deviations depends strongly on the gas choice. Most notably the gain deviations in T2K gas are significantly

larger than in the other two gasses. However, the improvement by going from the manual mounting procedure to the tool assisted one is always similar, with an average reduction factor of 2.70 ± 0.01. Therefore, while in P5 gas the manually mounted GEMs already reach a better gain uniformity than the GEMs presented in ref. [185], in T2K gas a similar level is only reached with the tool assisted mounting procedure.

Additionally, it is of note that the gain deviations in TDR gas increase by ~70 % with the introduction of the 4 T magnetic field. However, in P5 gas they are unchanged. Therefore these simulations give no indication for the behaviour of the deviations in T2K gas. A corresponding parametrisation of the gain should be prepared to investigate further. If a similar increase as in TDR gas arises for T2K gas, the gain uniformity of the GEM stack would need to be further improved by other means. In this case additional quality control for the GEM foils may be necessary.

5.5.1. Influence on $\mathrm{d}E/\mathrm{d}x$ Measurements

As explained at the beginning of this chapter, for particle identification (PID) via the measurement of $\mathrm{d}E/\mathrm{d}x$, the important quantity is not the total fluctuation of the gain over the anode but the variation of the average gain of tracks in different sectors of the anode or in different directions from the IP. To estimate the impact of the calculated gain variations on $\mathrm{d}E/\mathrm{d}x$ measurements, the gain is simulated for tracks, using a similar method as ref. [185]. However, instead of an average gain map, here the individual maps are used, and rather than the parametrisation of P5 gas, the one of T2K gas is applied. For this procedure, gain maps similar to sectors of the ILD TPC anode are build, each using eight individual gain maps that are selected randomly from the corresponding sample. Similar to the rings of modules in the ILD TPC end plate, these are arranged in eight staggered rows, as is shown in figure 5.11. Each map is only used once in this process, leading to a total number of sectors of 360 for the manually mounted sample and 1092 for the tool mounted one. For each sector created this way, simple straight tracks are simulated. Starting from each of the 233 bins in the first column of the map, tracks to all bins of the last column are created, i.e. in total $233^2 = 54\,289$ tracks per sector. The bins are 1 mm wide in the y-direction of the maps, i.e. perpendicular to the track. In each column a mock hit is formed using the three bins closest to the track. To emulate the charge distribution found in reconstructed hits in the beam test data, see figure 7.2 on page 107 as well as sections 7.3.2 and 8.1.3, the two outer bins in

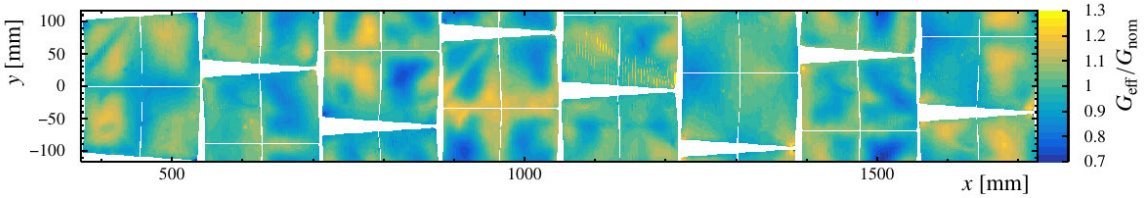

Figure 5.11.: An example of an eight-module gain map, as used for the investigation of the average gain on tracks. It consists of eight randomly selected individual gain maps, based on the height profiles of the manually mounted GEMs.

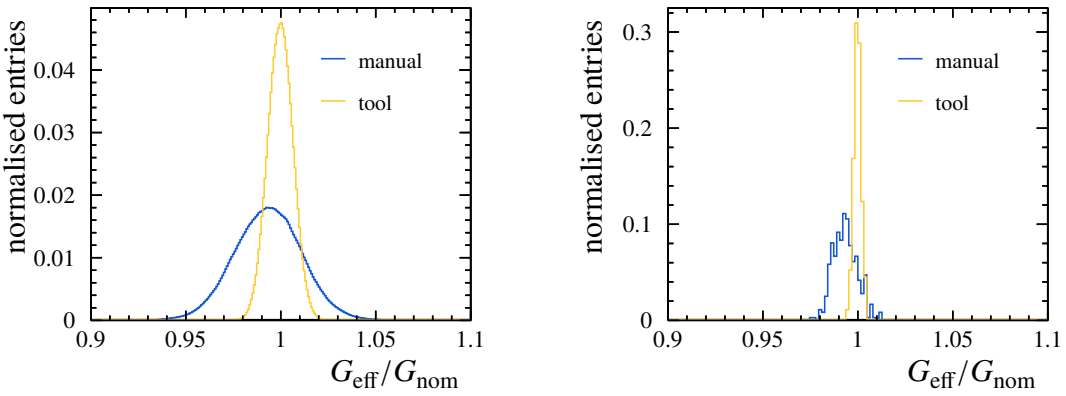

(a) Track gain distribution.

(b) Distribution of means.

Figure 5.12.: The average gain on tracks simulated with the gain maps using the two samples of GEMs, manually mounted and tool assisted mounting. (a) The distribution of the average gain for all tracks. (b) The distribution of the mean gain of the tracks in each of the sectors.

Table 5.5.: Summary of the results of the track gain calculation.

sample	standard deviation [%]	
	track gain	sector means
manual	1.75	0.625 ± 0.033
tool-assisted	0.66	0.1946 ± 0.0048

each column contribute only with half the weight of the central one in the calculation of the average gain of the hit. Since there are many gaps with invalid gain values in the sector gain maps, hits are discarded if their gain is further than $\pm 6\,\text{RMS}_{90}$ from the nominal gain, using the values in table 5.4. This also serves to mitigate the effect of the stripe patterns in some GEM profiles. From the remaining hits the average gain of the track is calculated.

In figure 5.12a the distributions of the average gain of all tracks in all sectors normalised to the nominal gain are shown. In addition, the mean gain of the tracks in each sector is calculated. The resulting distributions are shown in figure 5.12b. In both figures the distributions for the manually mounted GEMs are slightly offset from the nominal gain with a mean of 0.993, while for the tool mounted GEMs they are nicely centred around 1. It could not be determined what causes this offset but it also does not influence the conclusions to be drawn from this analysis. Since all four distributions are well described by Gaussian distributions, their width is extracted by corresponding fits within a range of $\pm 3\,\sigma$ around the central value. The distribution of the gain of all tracks using the manually mounted GEMs has a standard deviation of $\sigma = 1.75\,\%$, while the one for the tool mounted GEMs has $\sigma = 0.66\,\%$. For these two distributions the statistical uncertainties of the fit are negligible ($\delta_\sigma/\sigma \approx 10^{-4}$). The corresponding distributions of the mean gain in the different sectors have standard deviations of $\sigma = (0.625 \pm 0.033)\,\%$ and $\sigma = (0.1946 \pm 0.0048)\,\%$. These results are summarised in table 5.5.

This shows that the overall non-uniformity of the gain for tracks in different regions of the anode is dominated by the variation of the gain within each sector, rather than the shift of the mean value between the sectors. Regarding the requirements set in the beginning of this chapter, it can be seen that with the tool assisted mounting procedure the track gain variation between individual sectors is unproblematic, as it is smaller than even the stricter threshold of $0.05\,\sigma_{\mathrm{d}E/\mathrm{d}x} = 0.25\,\%$ for the visibility in the data. While the total variations for either sample of GEMs exceed the defined acceptable limit of $0.1\,\sigma_{\mathrm{d}E/\mathrm{d}x} = 0.5\,\%$ for the ILD TPC, the tool-assisted sample gets close to this value.

5.6. Conclusions of the Flatness and Gain Studies

Using the tool assisted mounting procedure, the average size of the deflections is reduced to an RMS_{90} of $(32.3 \pm 4.2)\,\mu\mathrm{m}$, which represents a factor of about 2.8 compared to the manual procedure. In addition to the overall smaller deflections, the tool assisted procedure produces much more consistent and repeatable results. Due to this improvement the flatness of the GEMs is no longer limited by non-uniform stretching forces during the mounting procedure. Instead the measurements indicate that the distortions of the ceramic frames under their own internal stresses now dominate the deflections. Therefore, further improvements of the GEM flatness could be achieved by reducing the distortions of the frames. While the measurements show no significant improvement from applying two frames to a GEM compared to single framed GEMs, the geometry of the frames does influence their rigidity. This is studied in the next section. For additional possibilities for improvement, different materials or production techniques that introduce less stress into the material could be investigated.

The gas gain calculations reveal that the impact of the GEM deflections on the gas gain is much larger for T2K gas than for other gasses studied so far. Additionally, they show that the introduction of a magnetic field can have a negative impact on the size of the gain fluctuations. Considering this, it is important that the measured reduction of the GEM deflections directly translates into an improvement of the variation of the gas gain over the surface of the anode. In the calculations, the variations for the GEMs mounted with the tool assisted procedure are reduced by a factor of 2.7 compared to the manually mounted GEMs, e.g. from an RMS_{90} of 8.36 % to 3.15 % using T2K gas. This also holds true for the fluctuations of the average gain of tracks in different areas of the anode, which have a standard deviation of 0.66 % for the tool mounted GEMs using T2K gas. This is close to the acceptable limit of $0.1\,\sigma_{\mathrm{d}E/\mathrm{d}x} = 0.5\,\%$ after calibration for the ILD TPC. Therefore this is an important step to help reduce the demands on the calibration or to improve the yield of acceptable GEMs after quality control and selection.

5.7. Testing different Frame Geometries

The current geometry of the ceramic frames with its central crossing struts forming 2×2 panels, shown in the bottom right of figure 5.13a, is mainly dictated by the need to subdivide one of the GEM electrodes into four sectors of roughly equal size without creating additional

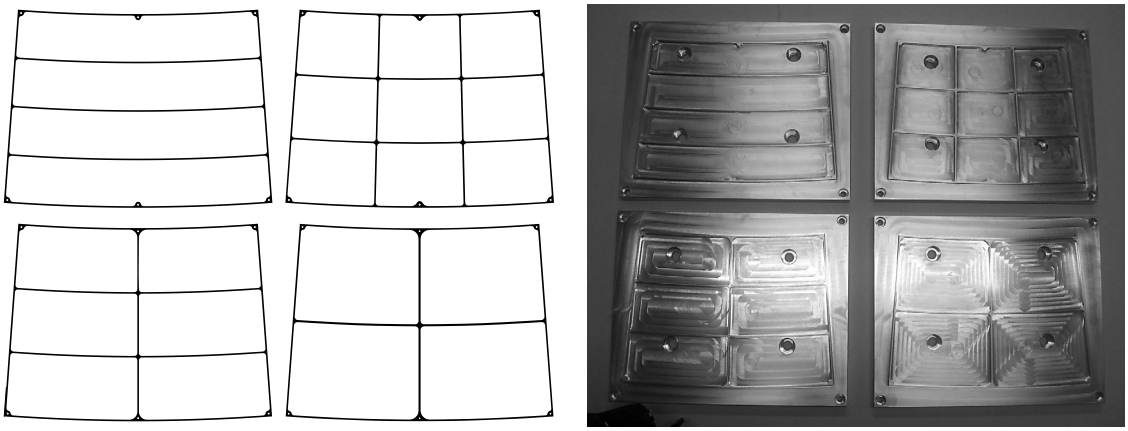

(a) The frame geometries. **(b)** The aluminium frame dummies.

Figure 5.13.: Overview of the four investigated frame geometry options. From top left to bottom right, in either figure, these are referred to as 1 × 4, 3 × 3, 2 × 3 and 2 × 2. The 2 × 2 geometry is used in the current modules. (a) Sketches of the geometries. (b) The implementation as aluminium dummies.

dead space. For this purpose the current geometry is the most simple design, using the lowest number of struts. However, the divisions of the GEM electrode and the frame panels are technically independent and other frame geometries could be employed. Considering the results of section 5.5, a geometry resulting in an improved flatness of the mounted GEM foils would be welcome. Therefore, on one hand, a new design could provide more support and rigidity. On the other hand, a design without radial struts would be beneficial since these dead areas are aligned with the interaction point and the resulting long gaps in radial tracks affect the reconstruction and pattern recognition performance. An azimuthal strut adds a similar amount of dead area and affects a larger number of tracks. However, it creates only a short gap in each track, which is much easier to handle by pattern recognition algorithms. In any case, any new geometry should introduce as little additional dead area as possible.

To test the influence of the geometry of the ceramic frames on the GEM deflections, the forms of the current and three additional geometry options, displayed in figure 5.13a, were milled out of cast aluminium plates, shown in figure 5.13b. The 1 × 4 geometry was chosen as it avoids radial struts. The 2 × 3 and 3 × 3 designs are potentially more rigid and the smaller size of the frame cells may also help to reduce warping of the GEM foil. The frame dummies were equipped with sheets of unprocessed GEM base material, using multiple versions of the mechanical mounting tool and procedure described in section 4.2.2. The height profiles were measured using the setup and procedure described in sections 5.1 and 5.2.

Due to the rigidity of the aluminium plate, these dummies eliminate all distortions present in the ceramic frames. Therefore mechanical simulations of their distortion under load were performed [196] using the finite-element analysis program Ansys `16.0` [197]. These can be used to estimate the relative distortion of the frames under internal stresses and the tension of the GEM foil. In addition to the default 1 mm thick frames, the mechanical advantage of 2 mm thick frames is investigated, to study the behaviour of double framed GEMs.

5.7.1. Height Profile Measurements with Dummy Frames

Unfortunately only a very limited number of GEM dummies were successfully created during this work. This is due to two reasons. First, in the earliest tests air got trapped in some of the cavities between the foil and the aluminium plate with the frame, resulting in a ballooning of the foil. For the later tests holes were drilled into the plates in each panel of all frames to allow for the equalisation of pressure. Secondly, there were issues with the later iteration of the mounting tool, which were only discovered as a result of these measurements. When operated in combination with a heat box, which is used to accelerate the curing of the epoxy glue, the stretching forces become non-uniform, resulting in distortions of the foil and invalidating the sample. Due to a limited availability of the GEM-foil base material, only two good tests each of the 1×4 and 2×2 geometry options and only one each of the 2×3 and 3×3 geometries are available. With these small sample sizes only preliminary conclusions can be drawn from the results.

All six measured height profiles are displayed in figure 5.14. The high spot in the lower right panel of the frame dummy in figure 5.14c is the result of a handling error, as are the small crescent shaped spots in the top left of figure 5.14e and the centre right of figure 5.14f. Since these have no impact beyond their immediate vicinity, only the corresponding panels are ignored in the rest of the analysis. Except for the damaged spots, these three dummies show the least distortions of the sample. The most and largest distortions are visible on the 1×4 dummies. For the 1^{st} one in figure 5.14a they seem to be randomly distributed. However, for the 2^{nd} one in figure 5.14b some structures that seem to be related to the shape of the frame panels are visible. First, it shows a zig-zag pattern of depressed and elevated areas in the second-to-left panel. It is clearly delimited by the frame but extends over the full panel. Secondly, there are diagonal ripples in the foil within the rightmost panel of the same figure. Since similar structures are observed in some of the real GEMs with 2×2 geometry, the influence of the frame is not clear. The 2^{nd} 2×2 dummy in figure 5.14d shows a large low area, taking up about half the bottom-right panel of the frame. This is similar to some of the real GEMs in figure 5.7 on page 72. Other structures appear to be more localised and are not so clearly delimited by the frame geometry. In comparison with the real ceramic frames in figure 5.8 on page 75, the dummies show no deflections in the vicinity to the frames, as is expected due to the rigidity of the aluminium plates.

The distributions of the height deviations of each measured profile are displayed in figure 5.15. They are mostly symmetric, except for those of the 2×2 dummies, which have tails corresponding to the visible high and low spots. For a quantitative comparison the RMS_{90} is calculated for each of the distributions. The results are given in table 5.6. For these few examples the 3×3 geometry delivers the flattest foil. When taking the average width for the two 1×4 dummies and the two 2×2 dummies, the next flattest option is the 2×3 geometry, followed by the 1×4 and finally the 2×2. However, the large difference between the two tests of the 2×2 geometry shows that the variations due to the mounting procedure can be much larger than the apparent impact of the frame geometry. As can be seen in comparison with table 5.2 on page 76, most of the dummies are much flatter than the average real GEM. This is expected, since the deflection of the real GEMs is dominated by the distortions of the ceramic frames. Only the 2^{nd} 2×2 dummy is on a similar level as the GEMs, which is

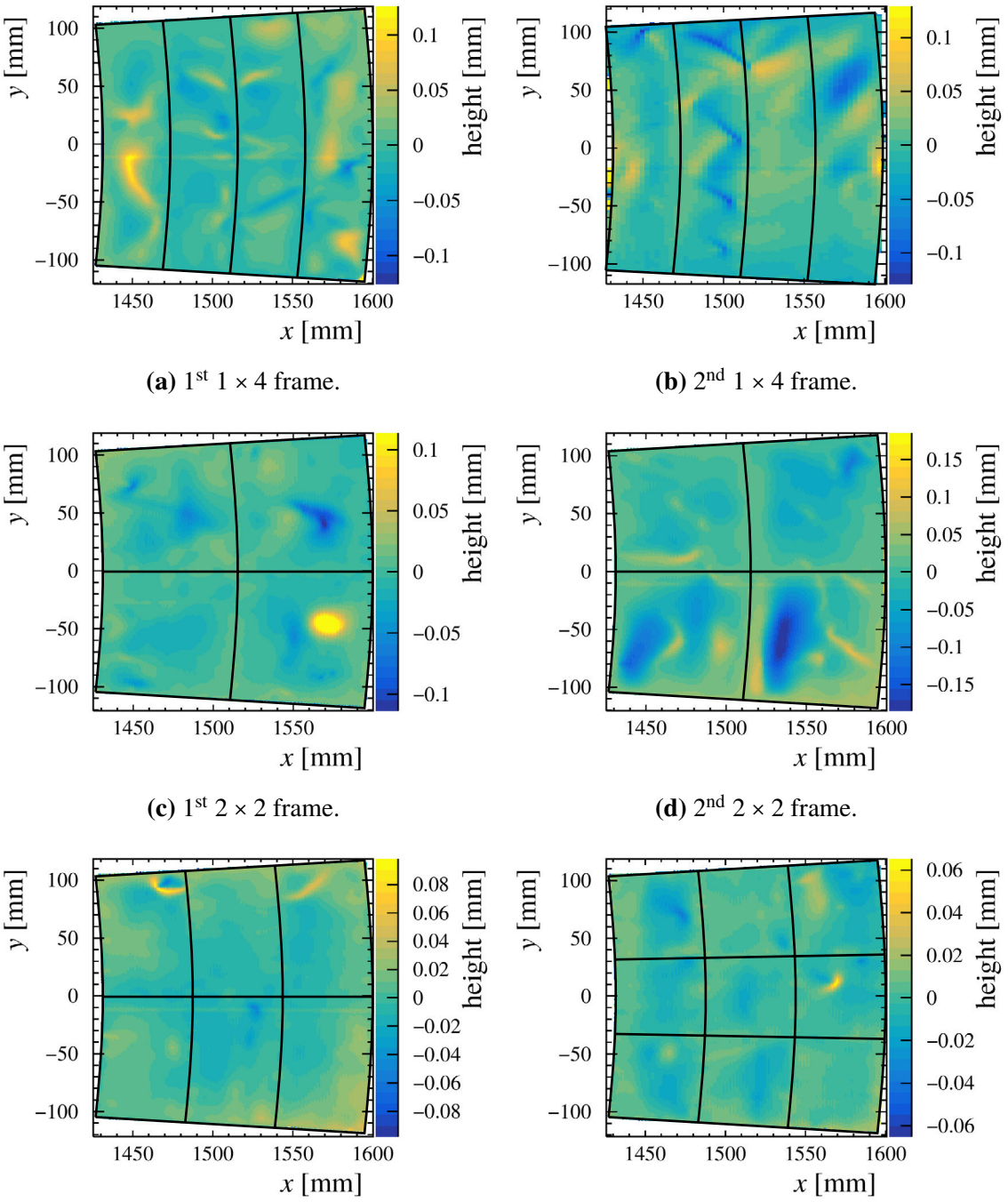

(a) 1st 1 × 4 frame.

(b) 2nd 1 × 4 frame.

(c) 1st 2 × 2 frame.

(d) 2nd 2 × 2 frame.

(e) 2 × 3 frame.

(f) 3 × 3 frame.

Figure 5.14.: Height profiles of the GEM foil on the four frame-dummy geometry options. Note the different height scales of the profiles. The high spot in (c) resulted from a handling error after production and does not influence the other sectors of the foil.

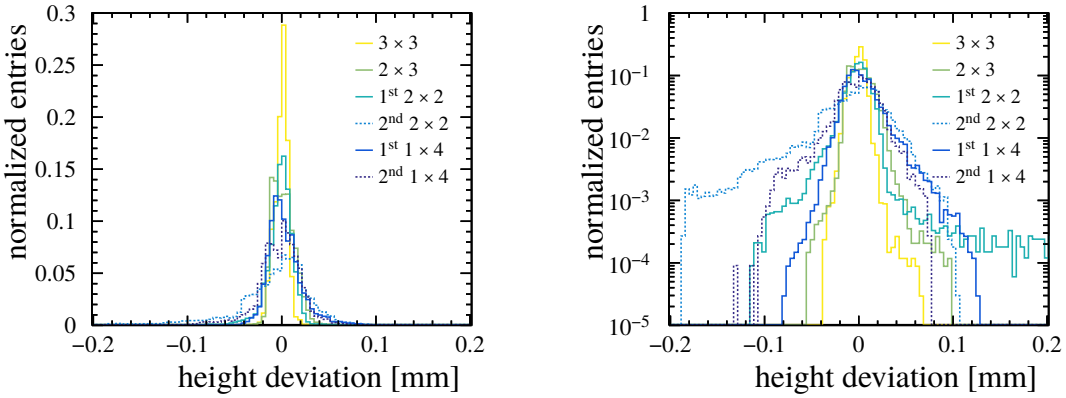

Figure 5.15.: Distributions of the height deviations of the dummy GEMs. The different geometries are described in the text. On the right is is the same plot as on the left except the *y*-axis is Logarithmic.

Table 5.6.: The RMS_{90} of the height deviations for the four investigated frame geometries. The uncertainties are purely statistical. The last column gives the reference to the height profile in figure 5.14.

geometry	RMS_{90} [µm]	figure
1 × 4	16.493 ± 0.067	(a)
	19.785 ± 0.140	(b)
2 × 2	11.924 ± 0.049	(c)
	32.052 ± 0.130	(d)
2 × 3	12.222 ± 0.049	(e)
3 × 3	7.639 ± 0.031	(f)

mostly due the one large depression. This leads to the conclusion that the mechanical rigidity of the frame is more important for the flatness of the mounted GEMs, than the details of the geometry. The fact that only few deflection patterns are observed that are clearly induced by the frame geometry, seems to confirm this.

5.7.2. Mechanical Simulations of the Frame Options

To study the mechanical rigidity of the different frame geometries, two scenarios with different acting forces are investigated in Ansys simulations. In all cases the value of the forces was chosen to be 10 N, based on the magnitude of the tension of the GEM foils in the mounting tool. In either scenario the ceramic frames are fixed at the six screw locations. In the first scenario a force is applied perpendicular to each of the four outer edges of the frame, acting inwards. This simulates the forces from the tensioning of the GEM foil acting on the frame. The second scenario applies a force uniformly distributed over the top surface of the frame. This has no direct equivalent in the real system but it can give an impression on how strongly

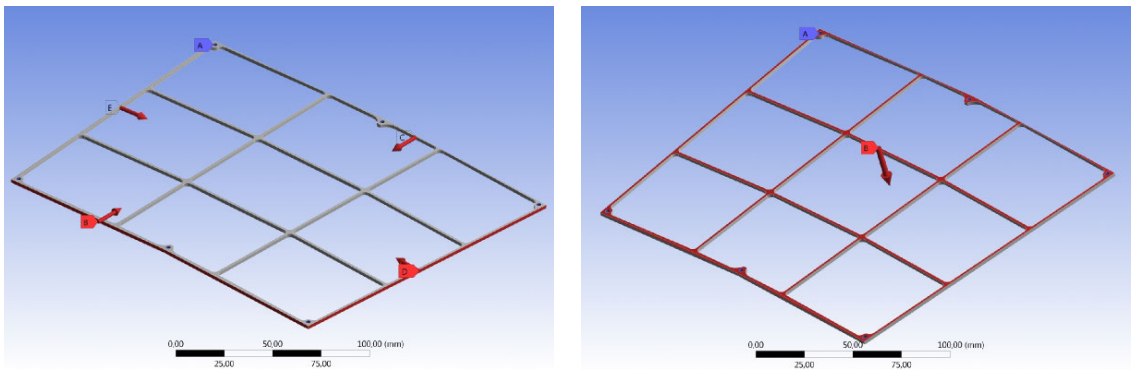

(a) Forces on the edges. **(b)** Force from the top.

Figure 5.16.: Visualisations of the forces acting in the two simulation scenarios applied to test the distortions of the ceramic frames [196]. The surfaces a force is acting on are shaded red and the respective directions are indicated by the red arrows. All forces have a magnitude of 10 N.

the frames may warp due to internal stresses. Visualisations of the forces in both scenarios are shown in figure 5.16. The results of the simulations for the four geometry options are summarised in table 5.7 in terms of the maximum deflection of the frame. Additionally, the maximum bending stress is given, which has to be compared to the flexural strength of the material of 400 MPa [172]. In all cases the induced stress is well below the strength of the material.

First Simulation Scenario

In the first scenario, the distortions of the 2 mm thick frames are generally only about half as large as for the 1 mm frames. In addition, the maximum deflections are similar between all geometries except the 3 × 3 option. This can be explained by noting where the largest deflections are occurring. Generally this is the longest unsupported strut section of the frame. As can be seen in figure 5.17, this usually are the azimuthal struts at the perimeter of the frame. In the 3 × 3 frame these are supported by a radial strut at about $^2/_3$ of the distance between the two fixed points. This reduces the maximum deflection from over 100 µm to 31 µm. In the 1 × 4 frame on the other hand, the much longer azimuthal struts in the centre bend even slightly further under the mostly axial load. Looking away from the maximum deflections, it can be seen that the deflections of the radial struts at the perimeter of the frame in the 2 × 2 geometry are significantly reduced in the other geometries, due to the additional azimuthal struts.

The above can be understood by approximating the struts of the frame as thin rectangular beams of constant cross section. For such a beam the area moment of inertia is $I = b\,h^3/12$, where b is the width of the beam perpendicular to the force and h is its thickness in the direction of the force [198]. Then the maximum deflection w due to a load $q = F/l$ uniformly distributed over the length l of the beam is given by

$$w \propto \frac{q\,l^4}{I} \propto \frac{F\,l^3}{b\,h^3} \quad . \tag{5.2}$$

Table 5.7.: Maximum deflection and tensile stress in the material of the frame in the simulation scenarios in figure 5.16 for the different frame geometries and thicknesses.

scenario	geometry	max. deflection [µm]		max. shear stress [MPa]	
		1 mm	2 mm	1 mm	2 mm
(a)	1 × 4	126	64	51.0	25.8
	2 × 2	110	55	50.3	23.6
	2 × 3	111	56	48.3	25.2
	3 × 3	31	16	24.7	12.2
(b)	1 × 4	3270	525	121.5	31.4
	2 × 2	711	92	65.6	16.9
	2 × 3	738	99	76.4	21.7
	3 × 3	949	152	54.4	14.3

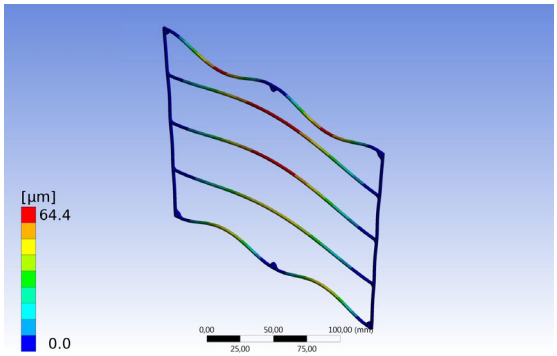

(a) Distortion of the 1 × 4 frame.

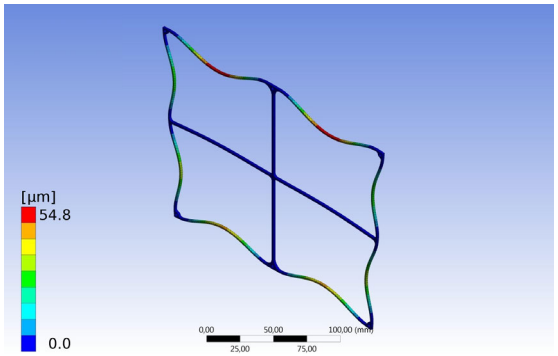

(b) Distortion of the 2 × 2 frame.

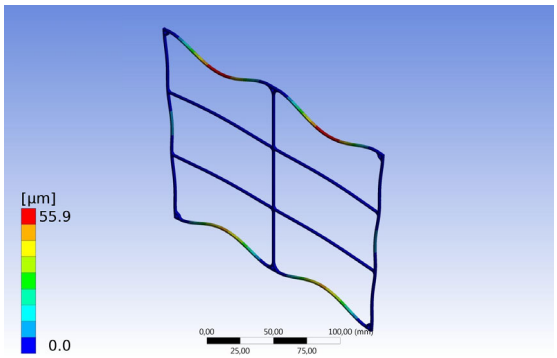

(c) Distortion of the 2 × 3 frame.

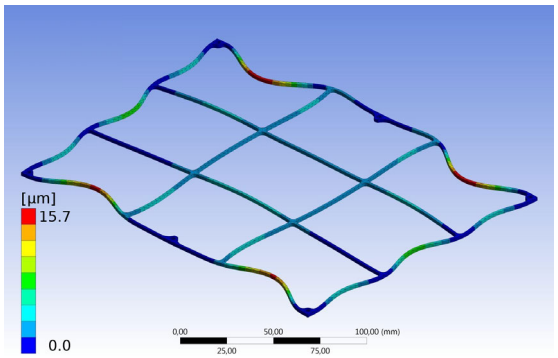

(d) Distortion of the 3 × 3 frame.

Figure 5.17.: The simulated distortions of the 2 mm thick (a) 1 × 4, (b) 2 × 2, (c) 2 × 3 and (d) 3 × 3 frames in the test scenario in figure 5.16a [196]. The displayed deflections are greatly exaggerated. Note the different absolute scales between the figures. Qualitatively, the distortions of the 1 mm frames are the same, see table 5.7 for detailed numbers.

This shows that the achieved reduction of the deflections for the 2 mm thick frames is as expected. On the other hand, for the comparison of the 3 × 3 frame with the other geometries, the observed reduction by a factor of ~0.28 is less than expected from the shorter length of the beam, $(2/3)^4 \approx 0.2$, since the radial struts also bend under the load. Finally, the deflection of the central azimuthal struts in the 1 × 4 frame is not described by equation (5.2), since here the load is mostly parallel to the axis of the struts.

Since the forces in this scenario are introduced by the tension of the GEM foil, the distortions of the frame partially relax some areas of the foil while other stay under full tension. This leads to non-uniform stresses in the GEM, which can cause it to bend. Since the central struts in the 1 × 4 frame are deflected to a similar degree as the azimuthal struts at the perimeter of the frame, the foil is submitted to much larger stress gradients than in the other geometries. This is similarly true for the outer radial struts in the 2 × 2 frame. However, it is not straight forward to translate the distortions of the frames into a scale for the deflections of the GEM foil.

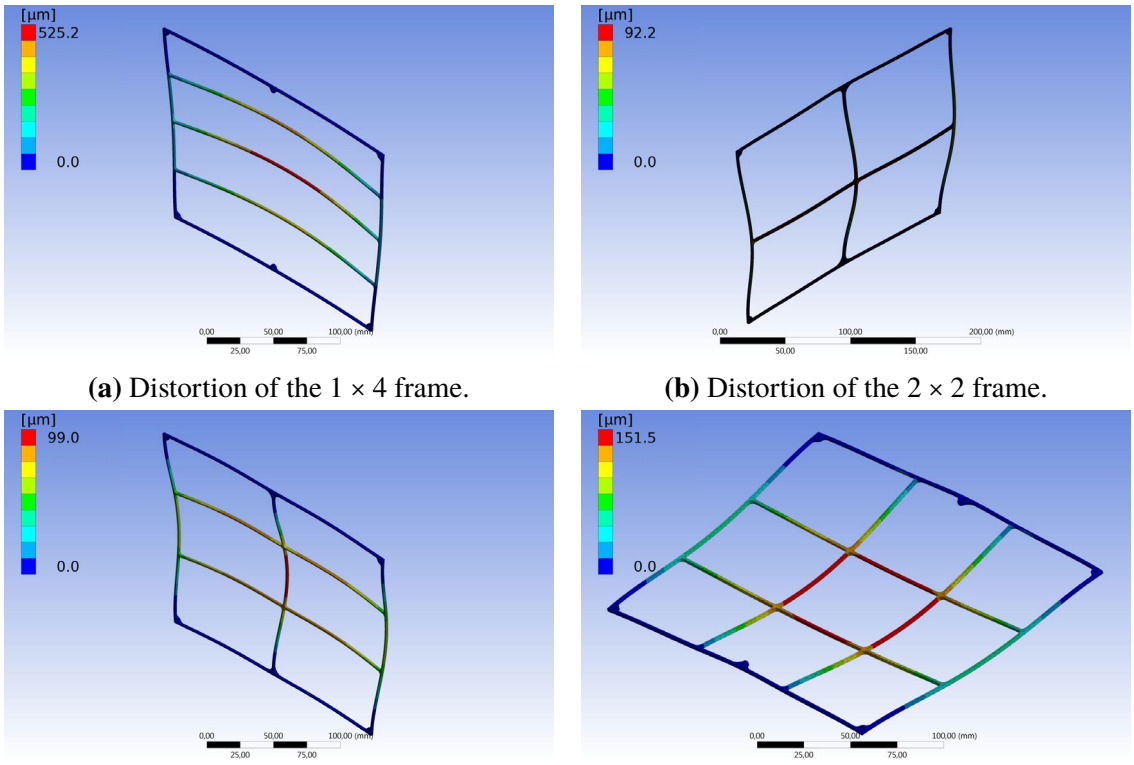

(a) Distortion of the 1 × 4 frame.

(b) Distortion of the 2 × 2 frame.

(c) Distortion of the 2 × 3 frame.

(d) Distortion of the 3 × 3 frame.

Figure 5.18.: The simulated distortions of the 2 mm thick (a) 1 × 4, (b) 2 × 2, (c) 2 × 3 and (d) 3 × 3 frames in the test scenario in figure 5.16b [196]. The displayed deflections are greatly exaggerated. Note the different absolute scales between the figures. Qualitatively, the distortions of the 1 mm frames are the same, see table 5.7 for detailed numbers.

Second Simulation Scenario

The second simulation scenario is intended to study the behaviour of the frames when introducing additional forces that are not in the plane of the GEM foil. Such forces bend the frame out of the plane, leading to further deflections of the foil. They can arise from internal stress in the material of the frame, e.g. from the production process or from the mounting of the frame in the module. However, the simulation assumes perfect, stress-free materials. Therefore, this scenario applies a force perpendicular to the plane of the frame. This allows to estimate the relative size of the deflections due to such forces in the different geometry options. Real internal stresses will not be as uniform as assumed here. Therefore, the deflections will be smaller than simulated but a qualitative comparison can still be done. The results of this test are also summarised in table 5.7. An overview of the location of the deflections is given in figure 5.18. The largest deflections appear in the centre of the frame, which is the point furthest away from the six fixed screw locations. As expected the long central struts of the 1×4 frame show the largest deflection of all geometries under this load. Interestingly, the 3×3 frame also shows larger deflections than the 2×2 and 2×3 frames. This is because the central, radial struts are offset from the two fixed points at the middle of the outer azimuthal struts, creating longer lever arms.

Since in this scenario the force is now acting from the top, the dimensions referred to by b and h in equation (5.2) are swapped. Therefore, the deflections here should be roughly inversely proportional to the third power of the frame thickness and going from the 1 mm to the 2 mm thick frames results in an expected reduction of the distortions by a factor of $1/8$. The 2×2 and 2×3 geometries show improvements close to the expected factor since their maximum deflection is defined mostly by the central radial strut connecting the fixed points. The 1×4 and 3×3 frames show a reduction by a factor of only about $1/6$, since the geometry of the frames leads to torsion of the struts under this load, so that equation (5.2) is not applicable in this case.

5.7.3. Conclusions of the Frame Geometry Studies

The height measurements of the foil on the aluminium frame dummies show an average RMS_{90} of $(16.5 \pm 3.5)\,\mu\mathrm{m}$, which is about half of the value measured for the real GEMs mounted with the tool assisted procedure. Additionally, only very few deflection patterns are observed that appear to be linked to the geometry of the respective frame. This confirms the conclusion in section 5.6 that there the distortions of the ceramic frames are the dominant contribution to the GEM deflections. Therefore, a higher mechanical rigidity of the frame could help to further improve the flatness.

The 1×4 geometry is the only example where measured deflection patterns of the foil indicate a direct impact of the geometry. Additionally, the mechanical simulations show that it is generally weaker than the others due to the long central struts, which are prone to bending under internal stresses. Their deformation behaviour under tension of the foil could exaggerate the deflections of the GEM foil in certain areas. Whether the advantage of the removed central, radial strut is worth this trade-off is difficult to judge since various performance parameters of the TPC are affected. This level of fine-tuning requires in depth

studies, which are not in the scope of this work.

The 3 × 3 geometry is the strongest against the forces arising from the tension of the foil. However, it may be weaker against internal stresses, because the two central radial struts are offset from the locations of the middle screws. Since the measurements in section 5.4 indicate that the internal stresses of the frame are the dominant source of GEM deflections, the 3 × 3 geometry does not provide a clear mechanical advantage over the other geometries. The additional radial strut also introduces another pointing gap in the active area. Therefore this geometry is disfavoured.

The 2 × 3 and 2 × 2 geometries behave very similar in both simulation scenarios, with the exception of a reduced deformation of the outer radial struts in the 2 × 3 geometry under tension of the GEM foil. The added azimuthal strut may affect the $\mathrm{d}E/\mathrm{d}x$ measurement, as is explained in chapter 9 for the current geometry. However an extra azimuthal strut is less disadvantageous for the track reconstruction than an additional radial strut. Therefore it may still be worthwhile to further investigate the 2 × 3 geometry.

The mechanical simulations indicate that thicker frames should be much more resistant to deformations due to internal stresses. While the small sample sizes and the resulting large uncertainties of the real GEM measurements do not allow conclusions in either direction, a change this large should be visible. However, the simulations do not take into account potential changes of the magnitude of the stresses with increased material thickness. Further investigations should be performed, in particular because for the final module design for the ILD TPC the option is considered to bond the whole GEM stack to the pad plane with epoxy glue. This is mainly done to eliminate the mounting screws protruding into the drift volume. In this case the stack is essentially a monolithic structure. Additionally the pad plane and back frame would provide a rigid base at any point of the ceramic frames instead of only the six screw locations. This could greatly reduce the distortions of the frames and allow to use a less rigid geometry, such as the 1 × 4 design.

5.8. Summary

To assess the quality of the manual and tool assisted GEM mounting procedures described in section 4.2.2, the height profiles of two corresponding samples of GEMs were measured. These measurements show that the tool assisted procedure results in deflections of the mounted GEM foils with an RMS_{90} of $(32.3 \pm 4.2)\,\mu\mathrm{m}$, which is a reduction by a factor of 2.8 compared to the manual mounting procedure. Additionally, a more consistent flatness and improved repeatability is observed. With the new method the flatness of the GEMs seems to be limited by the deformations of the ceramic frames due to their internal stresses, instead of stresses in the foils due to non-uniform stretching.

Parametrised calculations of the effective gas gain in triple-GEM stacks made up of the measured GEMs height profiles show a reduction of the gain fluctuations by a factor of 2.7, equivalent to the improvement of the flatness. The calculations also reveal that the impact of the GEM deflections on the gain stability depends on the gas mixture. With an RMS_{90} of 3.15 % for the tool mounted GEMs the fluctuations in T2K gas are much larger than the other two tested mixtures, P5 and TDR gas with 0.92 % and 0.69 %, respectively. Additionally,

the calculations with TDR gas indicate that the introduction of a magnetic field can have a large negative impact on the gain stability.

To assess the impact of the frame geometry on the deflections of the GEM foil, height measurements with aluminium dummies of four different frame geometries were performed. The options included the existing frame design with 2×2 cells, a 1×4 design without a central radial strut, as well as a 2×3 and a 3×3 design with additional struts. The measurements show only very few deflection patterns that appear to be linked to the geometry of the respective frame. Also in the height variations, no significant difference between the four geometries is found. Including all options, the height variations result in an average RMS_{90} of $(16.5 \pm 3.5)\,\mu\mathrm{m}$, which is only about half of the value measured for the real GEMs mounted with the tool assisted procedure. Since the aluminium dummies eliminate any distortions of the frame, this difference confirms the finding above, that the deflections of the real GEMs are dominated by the distortions of the frames.

To investigate the distortions of the four frame geometries under external loads and internal stresses, mechanical simulations were carried out. These disfavour the 1×4 frame design because of its lower rigidity compared to the other designs. The 3×3 design does not provide a clear advantage over the remaining two options, while adding more dead area. The 2×2 and 2×3 geometries behave very similar but the latter is slightly more rigid in some scenarios. Additional studies are required to investigate the effect of bonding several frames together, on the deflections due to their internal stresses.

6. Test Beam Setup

The readout modules build implementing the changes and using the new process as described in chapter 4 were tested with an electron beam at the DESY II Test Beam Facility. In this chapter the setup is described, starting with the beamline equipment in section 6.1, the TPC prototype in section 6.2 and the readout electronics in section 6.3. Then the gas choice is explained in section 6.4. Finally the settings and conditions used in the setup are given in section 6.5.

6.1. Area T24/1 at the DESY II Test Beam Facility

The DESY II Test Beam Facility [199] utilises the DESY II synchrotron to provide electron or positron beams in three independent beam lines. The synchrotron accelerates electrons (or positrons) to an energy of 6.3 GeV. Each test beam is produced by inserting a target consisting of a single 7 µm thin carbon fibre into the orbit of the DESY II beam. The resulting bremsstrahlung photons then tangentially exit the beam pipe of the DESY II accelerator through a 0.5 mm aluminium window. In a secondary converter target, consisting of a thin (1 mm to 10 mm) copper or aluminium plate selectable by the user, the photons undergo pair conversion. A spectrometer system consisting of a dipole magnet and a variable collimator allows the user to select electrons or positrons with momenta between 1 GeV and 6 GeV by

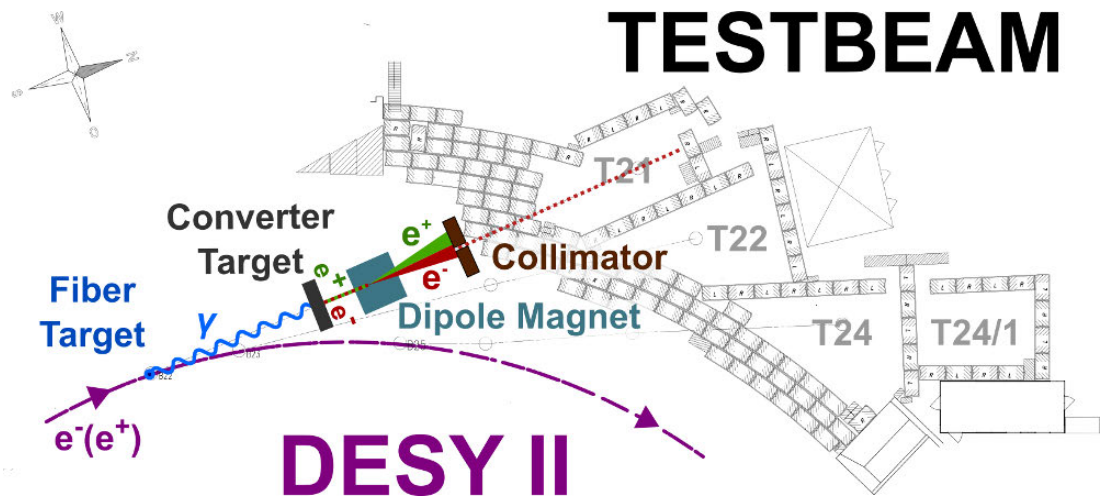

Figure 6.1.: Sketch of the beam production at the DESY test beam. Also shown in the background is the arrangement of the experimental areas of the three beam lines T21, T22, and T24 [199].

Figure 6.2.: The PCMag solenoid magnet mounted on its movable stage in the DESY test beam area T24/1. The electron beam is entering from the wall behind the magnet, perpendicular to the bore axis of the solenoid.

controlling the magnet current and polarity. In beam area T24/1 only electrons are available due to a second dipole magnet in the beam line, which has a fixed polarity. A sketch of the process of beam generation as well as the layout of the beam lines and areas is provided in figure 6.1. The beam rates are generally of $\mathcal{O}(\text{kHz})$, depending on the selected beam energy and opening of the variable collimator as well as the thickness and material of the converter target, but drop rapidly for energies approaching the nominal energy of the DESY II synchrotron. Where the beams enter the areas and at the transition from area T24 to T24/1 final lead collimators can be installed with apertures of 1 mm to 20 mm.

6.1.1. The PCMag Solenoid Magnet

Beam area T24/1 houses a superconducting solenoid magnet, the so-called persistent current magnet (PCMag) [200], shown in figure 6.2. It has a design field strength in the centre of the 85 cm diameter bore of up to 1.25 T at a current of 520 A. Since the magnet does not have a field return yoke, the total wall thickness including coil and vacuum insulation vessel amounts to only 20 % of a radiation length. Because the electron beam must pass through the magnet wall to reach the device under test inside, a low material budget is important to minimise energy loss of the beam particles due to multiple scattering and bremsstrahlung. A downside of the missing yoke and the accompanying design choices is a less homogeneous field in the end regions of the solenoid, limiting the usable length of the bore [201, 202]. Therefore, careful placement of the large TPC prototype, see section 6.2, in the centre of the coil is required to minimise effects from the field distortions.

The PCMag is mounted on a movable stage that is able to move the whole setup perpendicular to the beam direction, both vertically and horizontally. Additionally the stage can

be rotated around the vertical axis by up to $\pm 45°$ relative to the beam direction. The positioning accuracy of the linear axes was determined to be better than 0.3 mm, which is much smaller than the spread of the electron beam of ~10 mm with the final collimator used for the measurements with the LP and therefore negligible for most measurements.

6.1.2. The TPC Gas System and HV Supply

A gas monitoring system was developed for the TPC tests at DESY and is available in the test beam area [123, 203]. It provides basic monitoring of environmental conditions, i.e. pressure and temperature, and gas impurities, i.e. water and oxygen content, as well as control of the gas flow. The Distributed Object-Oriented Control System (DOOCS) [204, 205] is used to provide the interface between the monitoring devices and the user. A flow controller of type *MKS 1179A* [206] can be used to regulate the gas flow to the TPC between 1 l_{N_2}/h and 60 l_{N_2}/h. It also provides a measurement of the actual flow rate. Directly before the inlet and behind the outlet of the TPC, thermometers are placed in the gas lines to assess the temperature of the gas inside the chamber. Further downstream a chilled-mirror dew-point hygrometer of type *DP3-D-SH* from the company *MBW Calibration* [207] monitors the water content of the gas in the $\mathcal{O}(10\,\text{ppm})$ regime. Last in the line is the oxygen measurement, which is provided by a fuel cell device (*XLT-12-123* by *Analytical Instruments Inc.* [208]) with an accuracy of 2 % of the chosen range. During the measurements presented in this work the active range was generally 0 ppm to 100 ppm. The gas exhaust line is vented to the atmosphere through a gas bubbler to avoid additional contamination by air. As the field cage of the large TPC prototype was designed to operate close to atmospheric pressure, an overpressure protection valve is installed downstream of the chamber, which opens at 20 mbar pressure difference to the environment to limit the deformation of the field cage and prevent damage. A static gas line directly connects the TPC to a set of manometers that measure the absolute pressure inside the chamber and the difference to atmospheric pressure.

Two power supplies are used to deliver the HV to the field cage of the TPC and the GEMs in the amplification structure. A power supply model *HCN 80M-20000* by *FuG Elektronik GmbH* [209] produces the HV needed for the cathode of the field cage. It can generate negative voltages up to 20 kV, with ripple and long term stability over 8 h of 10^{-5} of this value. The slow control system reads out the actual voltage via a voltage divider. For the GEM amplification system and the field termination plane a modular power supply system by *CAEN* with a model *SY2527* main frame is available [210]. Two high voltage boards of type *A1732N* [211] with 12 channels each are used to accommodate the required number of high voltage lines. Each channel provides negative voltages up to 6 kV with an accuracy of ± 3 %. Voltage ripple is less than 30 mV peak-to-peak. The ramp-up and -down gradients can be set independently between 1 V/s and 500 V/s. An overcurrent condition can be set for each channel in steps of 0.1 µA, either as a current limit or a trip condition. The main frame can be programmed to propagate the trip signal to other channels. This feature is used to prevent extreme potential differences between the various electrodes of the field cage and the modules.

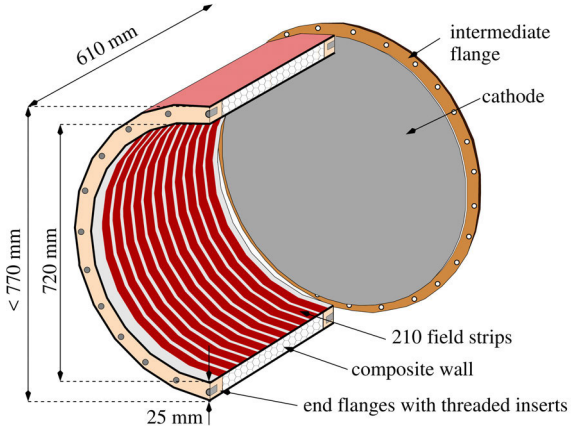

(a) Sketch of the LP field cage [187].

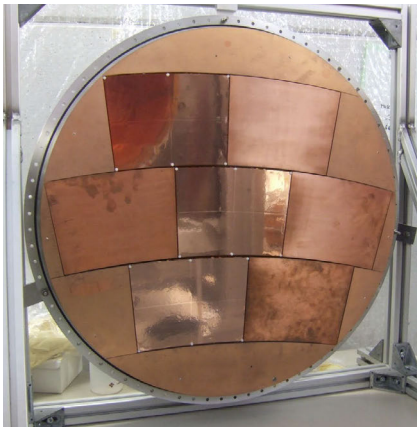

(b) The LPTPC anode end plate [212].

Figure 6.3.: The large TPC prototype. (a) Sketch showing the dimensions of the LP field cage. (b) Picture of the anode end plate with three mounted GEM modules and four dummy modules. The GEM modules can be distinguished by their more shiny surfaces.

6.2. The Large TPC Prototype

The large TPC prototype (LP) was build as a common infrastructure for tests of potential readout technologies for the ILD TPC [213, 187]. The cylindrical field cage, sketched in figure 6.3a, has an inner diameter of 72 cm and allows for a maximum drift length of ~57 cm. The wall of the field cage barrel consists of a composite structure made from a 23.5 mm thick aramid honeycomb material sandwiched between two 300 µm layers of GRP. Together with a 125 µm polyimide layer on the inside this structure provides the necessary rigidity and high voltage insulation. The innermost layer is the field-strip foil, which is needed to achieve a homogeneous electric field. It consists of a 75 µm thick polyimide foil that is metallised with 35 µm copper on both sides. On each side 210 field strips with a pitch of 2.8 mm are etched into the copper layer, alternating and overlapping between the two sides. On the outside of the field cage structure a thin copper-coated polyimide foil is applied to shield the chamber from electromagnetic noise. In total the field cage wall is 25 mm thick and constitutes only about 1.2 % of a radiation length. The field cage was designed to be operated only a few mbar above ambient pressure and should deform less than 100 µm at 10 mbar pressure difference. An overpressure of that magnitude is just enough to suppress contamination of the gas with air in case of small leaks. The field cage can sustain voltages up to 25 kV allowing for a drift field strength of at most 440 V/cm for an anode at ground potential. Higher anode potentials required by the various technologies used in the different readout module designs reduce the reachable drift field. However, in most common gas mixtures used in drift chambers the optimal drift field is far below this value. Therefore it is generally not a limiting factor for the module design.

On the cathode side an end plate made from ~10 mm thick GRP is used to close the gas volume. The cathode itself consists of a copper-plated aluminium disc that is mounted in three points on an intermediate flange, which attaches it to the field cage barrel. The

mounting can be adjusted to align the cathode to be parallel with the anode plane. The cathode is electrically connected to the field-strip at the same depth. The voltage is stepped down towards the anode potential at the other end of the field cage via two resistor chains on the field-strip foil.

The end plate on the anode side was milled from cast aluminium to achieve the required accuracy and rigidity [214]. An O-ring provides the seal between the end plate and the flange of the field cage barrel to which it is attached. The end plate houses up to seven readout modules arranged in three staggered rows, as show in figure 6.3b. Since all the module slots have the same shape, they are annular sections with common inner and outer radii, the three rows are not concentric and the gaps between them are not of constant width, potentially leading to enhanced distortions of the electric field in these regions. To maintain a flat anode plane of the drift volume the end plate is equipped with field termination plates in the areas not taken up by the module slots. The 7^{th} field strip is on the same depth as the field termination plates and can be powered to the same voltage. Unused slots can be equipped with dummy modules to provide field termination. The total instrumented path length using active modules in all three rows is about 50 cm.

6.3. Readout Electronics

The readout electronics is derived from the front-end electronics used in the TPC of the ALICE detector at the LHC [215, 160]. It was developed by Lund University with support by the EUDET programme [216] as part of the linear collider TPC (LCTPC) collaboration and is provided to its members. The charge collected on the readout pads is transferred to the front-end cards (FECs) of the readout electronics via flexible flat cables plugged onto the connectors on the backside of the pad board (see section 4.1). Each FEC houses eight programmable charge-sensitive preamplifier/shaper chips, called PCA16 [217]. The output of each of these is passed on to a separate ALICE TPC Readout (ALTRO) chip for digitisation [218].

The PCA16 is a 16 channel analogue charge-to-voltage amplifier with a built-in shaper. The term *programmable* refers to the possibility to change several of its parameters online. This is done by setting an 8 bit shift register via a field-programmable gate array (FPGA) located on the FEC. This allows to switch the polarity of the input and to put the PCA16 in pure preamplifier mode by turning off the shaping function. The gain of the amplifier can be set to 12 mV/fC, 15 mV/fC, 19 mV/fC or 27 mV/fC and the shaping time of the shaper to 30 ns, 60 ns, 90 ns or 120 ns. The decay time constant of the preamplifier can be tuned by setting an octal digital-to-analogue converter (DAC). For input signals shorter than the shaping time τ, the output of the shaper can be approximately described by a Γ_4-function of the form

$$\Gamma_k(t) = B + A \cdot \left[\frac{t - t_0}{\tau} \cdot \exp(1 - \frac{t - t_0}{\tau}) \right]^k \cdot \Theta(t - t_0) \quad . \tag{6.1}$$

Here B denotes the signal baseline (pedestal), A the amplitude of the shaped signal, t_0 the start time, $k = 4$ the order of the Γ-function and Θ the Heaviside step function.

The ALTRO chip is a 16 channel analogue-to-digital converter (ADC) with 10 bit resolution. It can run with sampling clock frequencies of 5 MHz, 10 MHz, 20 MHz or 40 MHz but at the highest frequency the effective number of bits is reduced to 9 or less [219]. While a number of modified chips was produced that allow for almost full resolution at 40 MHz, these do not provide enough channels for the measurements with the large TPC prototype [220]. Therefore, the system is run at a reduced sampling frequency of 20 MHz. At this frequency the event storage memory of 1024 samples corresponds to a drift time of 50 µs. For all settings presented in section 6.4 the expected drift time over the full length of the drift volume in the large TPC prototype does not exceed ~10 µs.

The ALTRO chip provides sample by sample pedestal subtraction and can do automatic zero suppression, reducing the requirements on the data acquisition (DAQ) system. The pedestals are determined regularly during operation in dedicated pedestal runs. For these runs the electronics is triggered by a pulse generator while the beam shutter is closed. For each channel ~80 000 samples are recorded. Typically, the recorded ADC values follow a Gaussian distribution for each channel. The mean value of the distribution is equivalent to the pedestal level, while the standard deviation is a good estimate of the electronics noise level. The pedestal values can then be stored in the ALTRO chips to be used for pedestal subtraction. Subsequently, zero suppression can only be applied if pedestal subtraction was performed.

With eight PCA16 and eight ALTRO chips each FEC provides 128 channels. Up to 32 FECs are connected to one Readout Control Unit (RCU) [221] via adapter boards, the so-called back planes. The RCU handles the distribution of the trigger signals to all connected FECs. It also collects the recorded data from the ALTRO event memory and transmits it via an optical link to a Detector-Readout Receiver Card (DRORC) installed in the DAQ computer.

6.4. TPC Gas Choice

The gas mixture used for the tests with the LP was first applied in the TPCs of the near detector ND280 of the Tokai to Kamioka long baseline neutrino experiment (T2K) [222, 193] and is therefore referred to as T2K gas in the following. It is an argon based gas mixture with additions of tetrafluoromethane (CF_4) and 2-methylpropane ($HC(CH_3)_3$) in a ratio of Ar : CF_4 : $HC(CH_3)_3$ of 95 : 3 : 2. The quencher gasses CF_4 and $HC(CH_3)_3$ are added to absorb ultra violet (UV) photons produced in the amplification process, as described in section 3.3. Generally noble gases are a good choice for detector gas mixtures as they do not tend to capture drifting electrons, forming negative ions and reducing the signal. The negative ions can also produce unwanted time delayed signals at the anode. They also do not react with the detector materials, which could lead to ageing of the amplification structure. Argon in particular is attractive for large volume detectors, due to its comparatively low cost. This specific mixture was chosen for its high maximum drift velocity and the good behaviour of the longitudinal and transverse diffusion coefficients. A high drift velocity is preferable in a TPC, as it leads to a faster readout time, reducing occupancy and dead time. The transverse diffusion in T2K gas is small at the drift field strength required for maximum drift velocity,

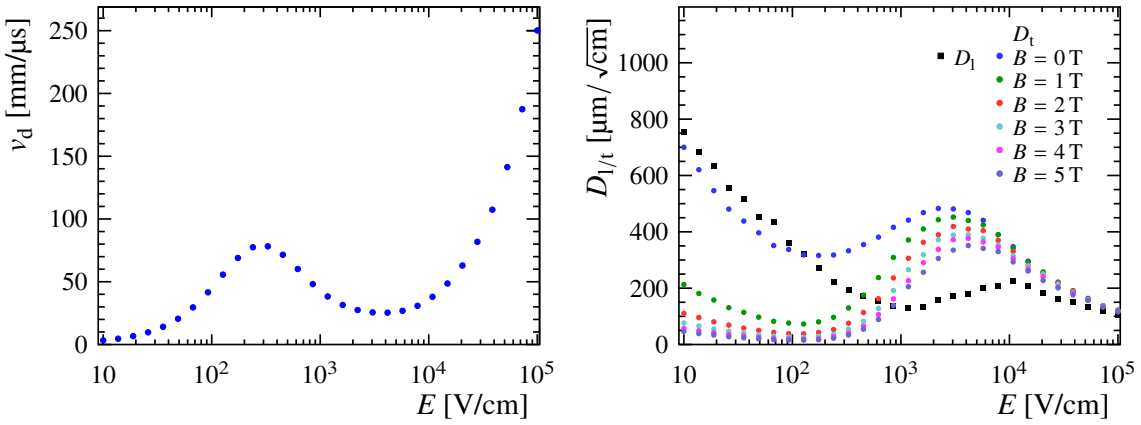

(a) Drift velocity.

(b) Diffusion coefficients.

Figure 6.4.: Simulated behaviour of the electron drift parameters of T2K gas at STP for varying electric field strength [169]. The parameters shown are (a) the drift velocity and (b) the longitudinal diffusion coefficient as well as the transverse diffusion for various magnetic field strengths.

allowing for good spatial resolution at long drift distances. It increases strongly at the higher field strengths applied in the transfer and induction gaps in the GEM stack, see table 6.1. This is important to defocus the electron cloud and achieve sufficient charge sharing between the readout pads. Figure 6.4 shows the behaviour of the drift velocity and the diffusion coefficients for varying electric field strength at standard temperature and pressure (STP) of 20 °C and 1013.25 mbar.

6.5. Working Point

The working point for the beam test measurements was chosen, taking into account the experience from the previous beam test campaign presented in refs. [212, 223] and dedicated measurements with smaller TPC prototypes, e.g. ref. [169]. It includes the settings of the electric field in the drift volume and the voltages and fields in the GEM stack of the readout modules as well as the gas conditions and the settings of the readout electronics.

6.5.1. Field Settings

Measurements were performed with different settings of the drift field and the voltages in the GEM stack. These settings are summarised in table 6.1. A sketch of the location of the different field and voltage parameters is shown in figure 6.5. The drift field was usually kept at 240 V/cm, close to the maximum of the drift velocity in T2K gas to minimise the effect of field inhomogeneities and environmental conditions on the drift time and therefore the position measurement in drift direction. A different point of interest is the minimum of the transverse diffusion at 130 V/cm, which results in an improved resolution in the transverse direction but a slightly worse resolution in drift direction [223]. Most data presented

Figure 6.5.: Location of the fields and voltages in the GEM stack of the readout module defined in the text and in table 6.1. The readout pads indicated by the yellow stripes at the bottom are on ground potential.

Table 6.1.: Electric field and GEM voltage settings used in the beam tests with the large TPC prototype and, where applicable, the respective diffusion coefficients and drift velocity at STP taken from Magboltz simulations. The simulation uncertainty on the drift velocity is omitted, as it is much smaller than 0.1 %.

	default					MIBF	
setting	E [V/cm]	U [V]	D_{t} [µm/$\sqrt{\text{cm}}$]	D_{l} [µm/$\sqrt{\text{cm}}$]	v_{d} [mm/µs]	E [V/cm]	U [V]
E_{drift}	240	–	98.1 ± 0.7	220.3 ± 1.4	77.50	240	–
	130	–	72.0 ± 0.5	315.2 ± 2.8	56.74	130	–
$U_{\text{GEM,drift}}$	–	255	–	–	–	–	230
$E_{\text{trans,1}}$	1500	–	405.2 ± 1.3	137.2 ± 0.4	32.75	2500	–
$U_{\text{GEM,middle}}$	–	250	–	–	–	–	260
$E_{\text{trans,2}}$	1500	–	405.2 ± 1.3	137.2 ± 0.4	32.75	290	–
$U_{\text{GEM,anode}}$	–	250	–	–	–	–	280
E_{ind}	3000	–	455.6 ± 1.5	170.5 ± 0.8	25.57	3000	–

in chapters 8 and 9 were acquired with a magnetic field of 1 T. In addition, data were taken without magnetic field, but these conditions differ drastically from those expected at the ILD with its 3.5 T magnetic field and therefore do not allow for a good extrapolation. With the default settings the voltages across the GEMs are first set to equal voltages of 250 V on all three GEMs in the stack to distribute the load and minimise the probability of discharges. The voltage on the GEM facing the drift volume is adjusted from there, such that the full dynamic range of the ADC is used while only in a small fraction of cases saturation is reached, resulting in a slightly higher voltage. The induction field is set to 3000 V/cm to maximise the transverse diffusion in the induction gap and thus the charge sharing between readout pads. The two transfer fields are set to 1500 V/cm to achieve a good electron transparency of the GEM stack. The field termination plates and any dummy modules are set to the same potential as the GEM electrode facing the drift volume. The potential of the field shaping wire is finally set to 50 V higher than this [169].

As explained in section 3.5.1, GEMs provide an intrinsic suppression of the back flow of ions created in the amplification process into the drift volume. While an ion-gating structure is foreseen for the readout modules at a future point, it is still advantageous to reduce the number of ions already in the GEM stack, so the opaqueness of the gate is not a critical parameter. Therefore additional measurements were performed using settings of the GEM stack voltages and fields designed to provide minimal ion back flow (MIBF). These settings are adapted from ref. [169]. The general idea is to reduce amplification and thus ion production in the GEM facing the drift volume by applying a lower voltage, since ions produced here can directly enter the drift volume. The reduced gain is compensated by a higher voltage in the last GEM in the stack, which is closest to the anode. Additionally the second transfer field is lowered to reduce the ion extraction efficiency for the anode GEM to close to zero, thus directly capturing most of the ions created there. Finally, the first transfer field is increased to reduce the ion collection efficiency of the drift GEM, so that more of the ions produced in the middle and anode GEM are caught here.

In the originally proposed MIBF settings the induction field is increased to 4500 V/cm to achieve a higher extraction efficiency of electrons for the anode GEM. However, since in ref. [169] it was also shown that the electron attachment coefficient of T2K gas rises rapidly for field strengths above 2000 V/cm, this is rather counter productive in terms of total effective amplification. Therefore the induction field was left at the default value of 3000 V/cm. Furthermore, the voltage of the anode GEM used here is lower by 10 V compared to the proposed settings to ensure the stability of the setup against discharges.

6.5.2. Gas Conditions

The field cage of the TPC at ILD is intended to operate close to environmental pressure. First and foremost this is due to the requirement of minimal material, which constrains the possible structural rigidity of the field cage and directly conflicts with the presence of a pressure vessel. Furthermore a higher pressure and therefore density of the gas also leads to more multiple scattering, which negatively affects the achievable momentum resolution. While a high pressure TPC offers improved resolution of the specific energy loss, the first two points were deemed to outweigh the possible gain in this regard. Therefore also the

large TPC prototype at the DESY II test beam is operated at environmental pressure. The flow resistance of the gas system behind the TPC leads to an intrinsic overpressure inside the chamber of ~10 mbar at the chosen flow rate of 40 l_{N_2}/h. At this flow rate the gas in the chamber is exchanged roughly once every four hours.

While leaks in the system are kept minimal and the slight overpressure further reduces diffusion of air into the chamber, some contamination of the gas can not be prevented. During the beam test measurements the water content was observed to vary between 45 ppm and 80 ppm. Unfortunately, the 2-methylpropane content of the gas starts to precipitate on the chilled mirror of the dew-point hygrometer, described in section 6.1, at similar temperatures as a water content within that range. Therefore the measured water content can only be taken as an upper limit. The oxygen content was measured to be constant at ~65 ppm. Oxygen is mostly introduced through leaks in the system and by contamination of the gas bottle, with the former being the dominant source in the prototype setup. Therefore it is a reasonable assumption that the measured oxygen content represents the contamination with air. Accordingly, in absence of a direct measurement, the nitrogen content is assumed to be ~240 ppm. Another important source of contamination can be outgassing of volatile compounds from detector components or substances in the gas system, e.g. glues, sealants, polymers, etc., which can not be estimated from the available measurements. Therefore care was taken to only use materials that are inert in this regard.

6.5.3. Electronics Settings

The settings of the readout electronics are based on the experience gained in ref. [223]. The signal polarity is negative, since for the GEM system the signal on the pads is induced by the electrons, as described in section 3.5. Pedestal subtraction and zero suppression are always applied to reduce the amount of data to transfer and store. The zero suppression threshold is set to 3 ADC counts, corresponding to a signal-to-noise ratio of ~4. The signal is required to stay above this threshold for at least two time samples. The gain of the preamplifier was kept at the lowest setting of 12 mV/fC, as the gas amplification system already provides an adequate signal charge, and a higher preamplifier gain would increase the noise level. The shaping time was set to 120 ns, as this setting was found to provide the best performance regarding transverse spatial resolution, due to increasing noise at shorter shaping times. While shorter values for the shaping time result in better timing resolution, the better transverse spatial resolution was deemed more important.

To cope with trigger delays the electronics continuously stores 15 samples in memory. When a trigger arrives, these samples are kept in addition to the data recorded after the trigger. The maximum event length is adjusted according to the expected maximum drift time, to minimise dead time of the readout. Of the available buffer length of 1024 samples, 200 and 300 samples are used for the drift field settings of 240 V/cm and 130 V/cm, respectively. With a sampling frequency of 20 MHz this corresponds to drift lengths of 775 mm and 851 mm at the respective drift speeds.

7. Software Framework and Data Reconstruction

This chapter describes the software used for the reconstruction and analysis of the beam test data in chapters 8 and 9. Section 7.1 introduces the common software framework of the linear collider development effort, iLCSoft. In particular the Marlin framework and the MarlinTPC package, described in section 7.1.3, were used for all steps of the analysis process. Furthermore, in section 7.2 Magboltz, a program to calculate transport parameters of electrons in gasses, is introduced. Finally, in section 7.3 an overview of the reconstruction steps for the beam test data is given.

7.1. iLCSoft

For the development efforts of the linear collider community a common software framework is being developed under the name iLCSoft [224, 225]. It comprises various software packages needed for the simulation, reconstruction and analysis of data, mainly for full scale models of the collider detectors, e.g. the ILD. Important tools used in this part of the work are the common data model LCIO [226] and the geometry description model GEAR [227]. The actual reconstruction and analysis methods are defined in the Marlin framework [228]. In this framework the LCTPC collaboration is developing the MarlinTPC package [229], a dedicated suite of tools for the analysis of data from TPC prototypes. It is also intended to provide input to the simulation and reconstruction of data for the full scale detectors. For this part of this work, version `v01-17-11` of iLCSoft is used, whereas the Monte Carlo (MC) data used in part II were simulated and reconstructed with version `v01-16-04` and the analysis is based on version `v02-00-02`.

7.1.1. LCIO

The Linear Collider I/O (LCIO) package provides a persistence framework and common data model for studies regarding the linear collider detectors. It comprises data objects for all reconstruction steps of the subdetectors, in particular the TPC, as well as MC objects needed for simulated data. The data is structured into events, which contain all objects related to a common occurrence, e.g. a detector trigger or a simulated particle collision.

Also defined within LCIO is the parametrisation of particle trajectories, described in detail in ref. [231]. In a detector with a homogeneous magnetic field a charged particle follows a circle in the plane perpendicular to the magnetic field (xy-plane in figure 7.1) while its momentum parallel to the field direction (z-axis) is constant, resulting in a helical path. In

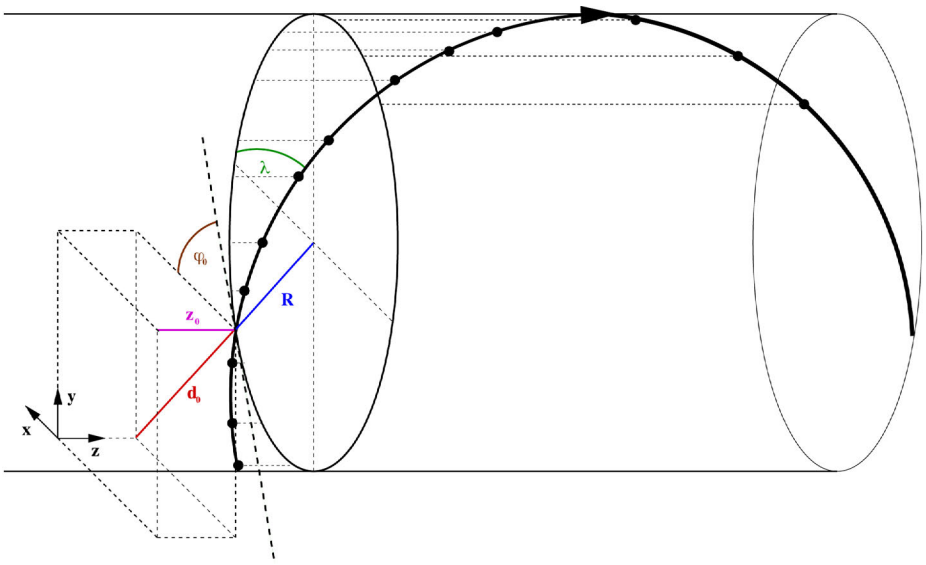

Figure 7.1.: Sketch of the five track parameters in LCIO [230].

the perigee parametrisation chosen for LCIO, a trajectory is defined at its point of closest approach (PCA) to a reference point. For collider detectors the global origin, typically placed at the interaction point of the beams, is chosen as the reference point. For beam tests other points may be more suitable. In addition to the reference point, a track is defined by five parameters:

d_0 the distance in the bending plane from the reference point to the PCA,

φ_0 the azimuthal angle of the track at the PCA,

Ω the curvature of the circle in the bending plane ($|\Omega| = 1/R$),

$\tan\lambda$ the slope of the track relative to the bending plane and

z_0 the position of the PCA relative to the reference point along the field direction.

The sign of these parameters depend on the direction of motion of the particle. This allows to distinguish between particles following the same trajectory in opposite directions. In particular, the sign of the curvature Ω encodes the sign of the charge of the particle. In the limit of $\Omega = 0$ the parametrisation describes a straight line, which is often accurate enough to describe particles with very high momentum or, in the case of beam tests, without the influence of a magnetic field. The various cases of the signs of the parameters are shown in detail in ref. [230].

7.1.2. Gear

The Geometry API for Reconstruction (GEAR) package is a framework used to provide information on the detector geometry during data reconstruction and analysis. As such it

does not contain information on the detector materials but only the geometry of the readout. The detector description has to be prepared in form of an XML file. Different base classes of geometries are available to describe detectors of various shapes, e.g. cylindrical layers as present in a TPC or planar Cartesian geometries as found in silicon sensors.

7.1.3. Marlin and MarlinTPC

The Marlin package provides a software framework for the reconstruction and analysis of data in the LCIO format. Each task, e.g. a reconstruction step, is defined in a self contained piece of software, a so-called processor. The list of processors to execute and the order of execution of these processors as well as the input objects, potential output objects and other steering parameters for each processor are defined in an XML steering file. The output of a processor can be used directly as input to processors later in the chain without the need to store it on hard drive. Marlin executes the processors event by event, but after all events have been processed a processor can perform additional tasks that require information from the complete data set.

The MarlinTPC package is being developed as a common software framework for the LCTPC collaboration. As a companion package to Marlin, most tools are integrated in Marlin processors. The package includes various processors used for the reconstruction and analysis of data from TPCs, as well as tools for the simulation and digitisation of TPCs with different readout technologies at several levels of detail. For the analyses in chapters 8 and 9 revision `r5491` [232] was used.

7.2. Magboltz

Magboltz is a simulation program for the transport of electrons under the influence of electric and magnetic fields in various gas mixtures [233]. It calculates the macroscopic transport parameters, such as electron drift velocity, diffusion coefficients and attachment rates for electrons and ions, see section 3.2. The user input for the calculations are the gas composition, the electric and magnetic field strength as well as the pressure and temperature of the gas. The gas composition is given by up to six gas components with their respective relative fractions in the mixture. The fields are assumed to be perfectly homogeneous but they can be set at an angle towards each other. Internally Magboltz uses a database of energy dependent collision cross sections between electrons and the various gasses as input to a MC simulation, which then yields the aforementioned macroscopic gas parameters. The precision of the output parameters depends on the number of collisions performed in the simulation. To reach a relative precision of $\mathcal{O}(1\,\%)$ on the diffusion coefficients in T2K gas, see section 6.4, the number of collisions was set to $200 \cdot 10^7$.

In chapter 8 Magboltz version `11.2` was used to identify possible gas or environmental parameters affecting the performance of the large TPC prototype.

7.3. Beam Test Data Reconstruction

In this section a brief overview over the reconstruction steps from the raw data to the final tracks is given. The reconstruction generally follows the steps used in ref. [223], where a more detailed description of all the involved methods and algorithms is provided.

7.3.1. Pulse Finding

The raw data from the readout electronics, see section 6.3, consists of the time stamped and digitised charge information for each readout channel, as displayed in figure 7.2a. In the figure, each bar in one of the charge profiles represents a single sample of the readout. In each of these charge profiles, signals have to be identified that rise significantly over the pedestal noise. These signals are called pulses. To discriminate the signal from noise, two thresholds are applied, as sketched in figure 7.2b. When the charge in a channel exceeds the first threshold, this defines the start of a potential pulse. The pulse ends when the charge drops below the second threshold. Additionally a minimum peak value and minimum length of the pulse can be defined. To avoid discarding part of the rising and falling edge of the pulse, additional samples before and after the thresholds are included in the pulse. The default settings of the pulse finder are given in table 7.1. These are used in the analyses in chapters 8 and 9, unless noted otherwise.

The electronics are designed such that the peak value of a shaped pulse corresponds to the collected charge. However, the integral over the full pulse length is proportional to the peak value and can also be used as a measure of the pulse charge. The integral has a distinct advantage in the case of pulses that saturate the ADC. For these signals the peak is cut of in the digitised pulse, resulting in the loss of the information of the pulse height. In this regime also the integral stops being proportional to the charge of the signal but it still increases with higher charge, due to the increase in the total pulse length. This can enable the reconstruction of the full charge information, since the pulse shape is well approximated by equation (6.1). While no methods to take full advantage of this possibility are applied, yet, the integral was used to at least benefit from the partial recovery of the charge information.

Table 7.1.: List of the settings used for the pulse finder. For details on the individual settings, see the text.

setting	value
pulse start threshold	$5 \cdot \mathrm{RMS}_{\mathrm{noise}}$
pulse end threshold	$3 \cdot \mathrm{RMS}_{\mathrm{noise}}$
minimal pulse length	5 time samples
minimal peak value	8 ADC counts
samples saved before start	3
samples saved after end	7

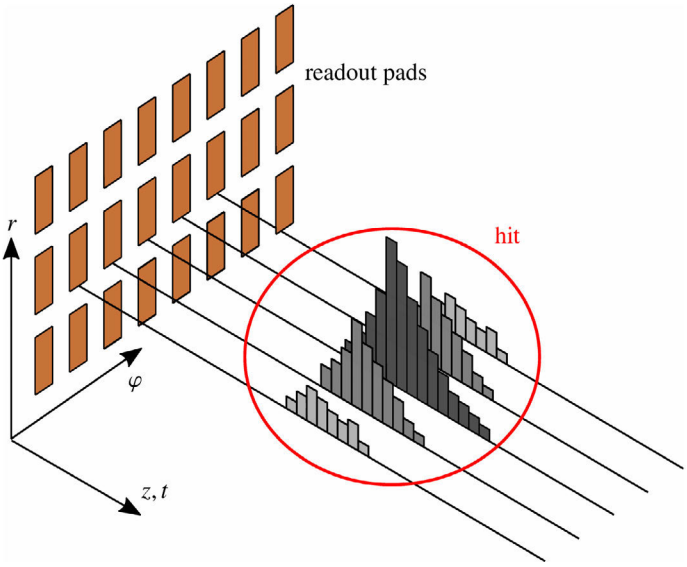

(a) Measurement principle.

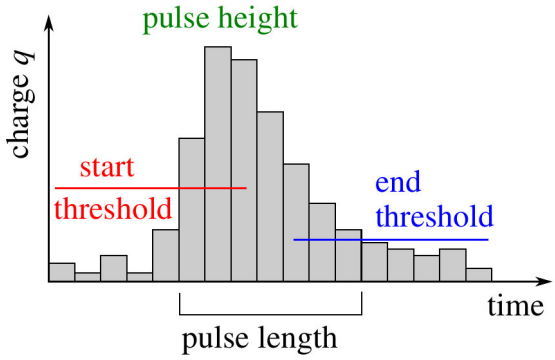

(b) Pulse identification.

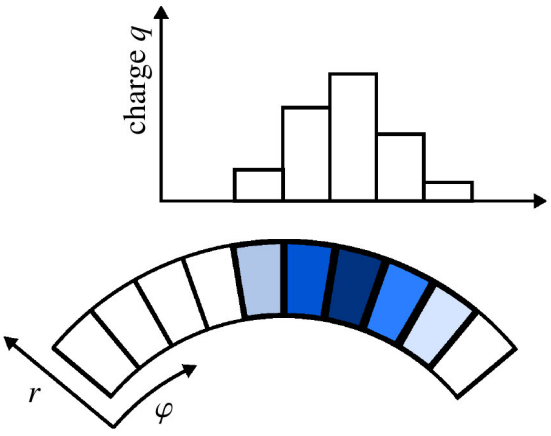

(c) Hit identification.

Figure 7.2.: Overview of the pulse and hit finding process [223]. (a) The digitised charge information is collected from each readout channel. (b) Pulses are identified as peaks in the charge development in each channel. The indicated parameters are explained in the text. (c) Clusters of adjacent pulses with matching arrival times are combined into hits, starting from a seed pulse with the highest charge. The sketch shows the charge distribution within a hit. A darker colour represents a higher charge.

7.3.2. Hit Finding

Hit finding is the process of combining pulses to form points with full three dimensional space information. By design it is expected that most particles pass through the detector such that in the transverse plane they travel perpendicular to the rows of pads, in the prototype as well as in the eventual ILD TPC. Therefore each row is defined as one measurement layer and adjacent pulses in one row are combined to hits, as sketched in figure 7.2c. Looking only at single pulses the information on the location in the transverse plane is limited by the pad pitch $w = 1.2625\,\text{mm}$ to

$$\sigma_{r\varphi} = w/\sqrt{12} = 364\,\mu\text{m} \ ,$$

which would not allow to fulfil the requirement of ILD of a resolution better than 100 µm over the full drift length. For this reason, the amplification stage in the GEM module is designed such that the cloud of electrons from the amplification process is spread over several pads. This allows to determine a more accurate position by calculating the charge weighted mean of a group of adjacent pads in one row. The task of the hit finding algorithm is to identify these groups while separating close-by particles or noise. The algorithm uses the pulse with the highest charge on each row as a seed. It then adds pulses on adjacent pads on both sides until it either reaches the edge of the readout module or no pulses were found on a number of neighbouring pads. Except for pads connected to dead channels of the readout it is not expected to find larger gaps in a hit. Therefore the maximum number of empty pads is set to two. The algorithm also requires the pulses to have similar arrival times within a user defined time frame. For the setup used here adjacent pulses were required to arrive with a difference of less than 500 ns.

When no more pulses can be added to the hit, the full positional information and its total charge are calculated. The position of the hit in the radial direction, perpendicular to the row, is defined by the radius at half the height of the row. Since the electrons from the primary ionisation process are expected to be equally distributed along the length of the track on average, the uncertainty on this position estimate is given by the height $h = 5.85\,\text{mm}$ of the row as $\sigma_r = h/\sqrt{12} = 3.46\,\text{mm}$. The position in the φ-direction is calculated from the charge weighted mean of the pad positions of all contributing pulses. In ref. [234] the systematic effects of this method on the determined position have been investigated. For hits with more than three pulses the weighted mean was found to be a perfect estimator of the hit position. The z-position can be determined from the arrival time of the pulses in the hit and the drift velocity of the electrons in the drift volume. The determination of the hit time and systematic effects on the pulse arrival time have been studied in detail in ref. [223]. It was found that the measured arrival times are systematically shifted with respect to the seed pulse, depending on their charge as well as their distance to the seed pad. Therefore only the seed pulse is taken into account for the calculation of the z-position. The total charge of the hit is calculated as the sum of the charge of all contributing pulses.

7.3.3. Tracking

Finally, the trajectory of the particle is reconstructed from the hits constructed in the previous step. This tracking procedure generally involves two steps, track finding and track fitting. Track finding is the process of identifying and collecting all hits that belong to one initial particle. While most track finding algorithms already produce an estimate of the track parameters, dedicated track fitting algorithms are employed afterwards to gain the best estimate of the properties of the true trajectory.

Various track finding and fitting methods that are implemented in Marlin have been compared in ref. [223] regarding their execution speed, hit finding efficiency and spatial resolution. The tested track finding methods were two implementations of a Hough transformation, described in refs. [230, 235], a triplet chain [236] and two versions of a Kalman filter [237], that were originally developed for the full ILD simulation [238]. No significant differences were found in the performance of the various algorithms, regarding the track finding efficiency and impact on final spatial resolution after fitting. However, the triplet chain and the implementation of the Hough transformation in ref. [235] were found to be an order of magnitude faster than both Kalman filters. Therefore, the Hough transformation was chosen as track finder.

The Kalman filters can also be applied as a track fitter, since they provide a precise recursive least-square fit. Another track fitting method implemented in Marlin is the general broken lines (GBL) method [239, 240]. In addition several very fast fitting methods are available. Straight tracks in the absence of a magnetic field can be fitted using a linear regression. For helical trajectories the Karimäki method [241] gives an approximate solution. These methods ignore energy loss and multiple scattering of the particle in detector materials, which is a reasonable approximation for a gas filled TPC with its low material density in the tracking volume. In ref. [223] the Kalman filters were found to be an order of magnitude slower than GBL, which in turn is an order of magnitude slower than the linear regression and the Karimäki method. The spatial resolution in the transverse plane was found to be nearly independent of the used fitting algorithms. Since the GBL method can be used for both straight and helical tracks, it was chosen as the default track fitting method. An exception is the determination of the point resolution, which requires a separate track fit for each hit on the track. To reduce the required processing time resulting from the large number of hits, the linear regression and Karimäki fit are used in this process.

8. Comparison of Beam Test Results

In this chapter the existing data from a beam test in March 2013 [223, 212] are compared to data gathered in December 2016 in a beam test performed as part of the work for this thesis. The latter measurements were taken with a new generation of readout modules, produced using the improved design and construction methods described in section 4.2. The goal of this chapter is to test the reproducibility of the results over long periods of time and understand the sources of potential differences. This allows understanding of detector effects, like stability of the electronics and differences in production between the modules as well as influences from environmental conditions like atmospheric pressure and temperature. First, a comparison of several observables in both data sets is provided in section 8.1. Then, observed discrepancies are investigated further in section 8.2. Finally, an extrapolation of the $r\varphi$-resolution measured in both data sets to the full size and magnetic field of the ILD TPC is performed in section 8.3.

The data used in the comparison were taken in a magnetic field of $B = 1\,\mathrm{T}$ at various drift distances over the full length of the large TPC prototype. For technical reasons, the magnetic field was inverted between both beam test campaigns, leading to an inverted track curvature. During each beam test, data were taken with drift fields of 240 V/cm, close to the maximum drift speed of the gas, and 130 V/cm, in the minimum of the transverse diffusion. Both the azimuthal and polar angle of the beam relative to the detector were kept at zero for the presented data.

The two beam test campaigns were performed under different environmental and gas conditions. A gas pressure and temperature around 1006 mbar and 17.4 °C were recorded for the 2013 beam test and around 1034 mbar and 17.1 °C for 2016. The measured gas contamination with water and oxygen was similar for both beam tests, with 60 ppm of each in 2013 and 50 ppm water and 64 ppm oxygen in 2016. As explained in section 6.5.2, it is expected that the oxygen content indicates a contamination with air. Therefore a nitrogen content of 224 ppm and 239 ppm is assumed for 2013 and 2016, respectively.

8.1. Comparison of the Observables

The focus of the comparison is on the high level observables, in particular the point resolution and related quantities. These have already been studied extensively in the 2013 data set in ref. [223] and therefore can be readily compared using established analysis methods. In the following, first several basic performance parameters are analysed, i.e. the drift speed and average hit charge, and good agreement is found. Small differences are observed in the investigation of the pad response function and the transverse point resolution.

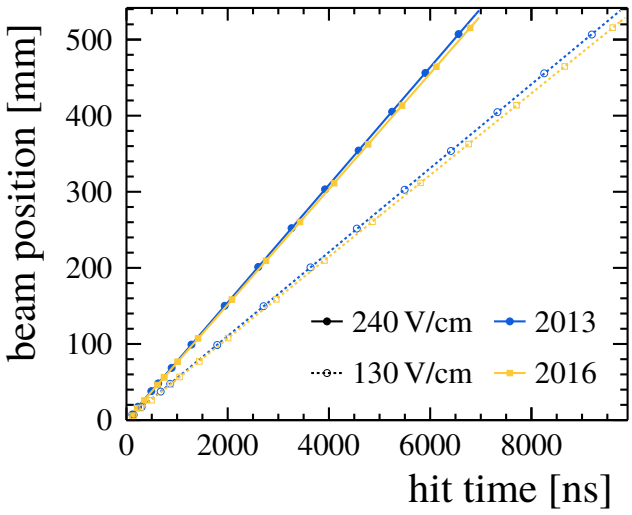

Figure 8.1.: Determination of the drift velocity from the mean arrival time of pulses for various distances of the beam to the readout plane. The solid and dashed lines represent the linear fits used to extract the drift velocity.

8.1.1. Drift Velocity

In a TPC the position of the impinging particle along the drift direction is determined from the arrival time of the measured signal. The drift velocity of the electrons in the gas is needed as an input for this calculation and therefore needs to be known precisely. While simulation tools like Magboltz can provide an estimate of the drift velocity with very small statistical uncertainty, the gas composition in the beam test setup, including any contaminants, is not known well enough to reduce the systematic uncertainties to a similar level. Therefore, the drift velocity must be determined by other means.

Some experiments employ dedicated monitoring TPCs to continuously measure the drift velocity. A good example of this are the gas monitor chambers for the TPCs of the near detectors of the T2K experiment [193]. In this example, two radioactive ^{90}Sr sources are placed at a well defined distance along the drift direction of the chamber, creating tracks perpendicular to the drift field. Measuring the time difference between the arrival of signals from both sources allows to calculate the drift velocity. A measurement of the drift velocity in this way, combined with measurements of the environmental conditions, allows to infer corrections for the main TPC.

Since no gas monitoring setup was available for either beam test, the drift velocity has to be determined from the data. The method adopted in ref. [223] uses as a reference the recorded position of the movable stage of the PCMag, in which the TPC is mounted as described in section 6.1.1. Performing measurements with the beam at various positions along the drift direction, for each the mean arrival time of the recorded pulses is determined. In figure 8.1 the resulting relation between beam position and arrival time is shown for both data sets. A linear fit is applied, where the slope corresponds to the drift velocity. The lowest point is not included in either fit, since at this position the beam partially passes below the

Table 8.1.: Results for both data sets of the drift velocity measurements with drift fields of 240 V/cm and 130 V/cm and the corresponding simulated values from Magboltz. The uncertainties of the simulated values are negligible compared to the measurement errors.

year	drift field [V/cm]	v_d [mm/µs] measurement	simulation
2013	240	77.28 ± 0.04	76.87
2016	240	75.97 ± 0.03	76.45
2013	130	55.14 ± 0.03	55.64
2016	130	53.66 ± 0.02	54.50

anode termination plane of the field cage, introducing a bias between the position of the stage and the centre of gravity of the visible part of the beam. The statistical uncertainty of this measurement is dominated by the uncertainty of the stage position of ~0.3 mm. The results of the measurements are shown in table 8.1, including corresponding values from Magboltz simulations using the amount of gas contamination as well as temperature and pressure as stated above. The observed discrepancies can be explained by systematic effects, e.g. due to unmeasured gas contaminants, differences in pressure and temperature, as well as the uncertainty of field inhomogeneities. Considering these effects, the values from both data sets are in good agreement with the simulation and also agree well with each other.

8.1.2. Hit Charge

In addition to tracking of charged particles a TPC also provides a measurement of the particle's $\mathrm{d}E/\mathrm{d}x$ along its trajectory, which is investigated in detail for the 2016 data set in chapter 9. This measurement is based on the number of electrons liberated in the primary ionisation process, which is related to the energy loss as described in section 3.1.1. The primary electrons drift through the gas to the GEM stack, where they are amplified and a signal is created in the readout pads. Therefore, attachment of primary electrons to the gas during drift must be avoided and a stable gas amplification is crucial for a precise measurement. Additionally, a calibration of the readout electronics and the gas amplification is generally necessary. Unfortunately, the setup does not provide dedicated calibration mechanisms. Improvised electronics and gain correction methods were tested for the 2016 setup, as described in section 9.3, but not applied for the purpose of this comparison.

In figure 8.2a the average charge of all hits in both data sets is plotted for various drift distances. In the 2016 data the average charge falls off with increasing drift distance, indicating attachment of the electrons during drift (see section 3.2.2). Fitting an exponentially decaying curve to the data, results in an attachment rate of $A = (0.0023 \pm 0.0002)\ \mathrm{cm}^{-1}$. To interpret the 2013 data, in particular the jump between 70 mm and 100 mm, it is important to note the order in which the data points were taken. First, the points from 100 mm to 500 mm were measured before recording the data from 70 mm to 10 mm. Therefore the jump hints at an effect that increases the measured charge over the course of the scan, most likely related to changing environmental conditions, e.g. atmospheric pressure. Regrettably no slow control

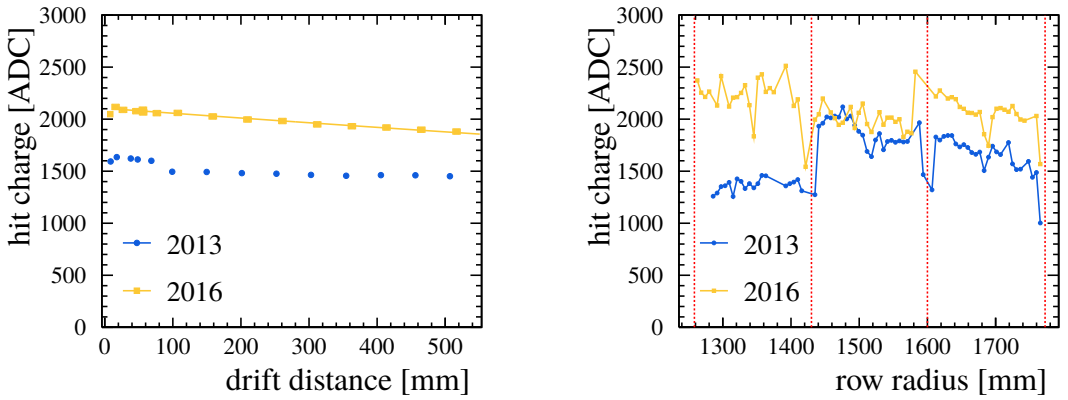

(a) Drift distance dependency.

(b) Average charge per row.

Figure 8.2.: The average hit charge in both data sets. (a) The average measured charge of all hits at various drift distances. The jump in the 2013 data is explained in the text. An exponentially decaying function is fitted to the 2016 data. (b) The average charge of hits on the individual rows of all three modules. The vertical dashed lines mark the extent of the modules.

data with the required time resolution exists any more, preventing a more detailed investigation of the effect. Since the points at 500 mm and 70 mm were taken in direct succession, a comparison still allows to estimate the attachment to be of a similar magnitude as in the 2016 data. While the jump is visible in some other low level observables, e.g. the average number of pulses per hit, it is not reflected in the relevant higher level observables, i.e. pad response function and spatial resolution.

Comparing the absolute value in both data sets shows the average charge to be higher by a factor of ~1.3 in the 2016 data. Since the same settings for the fields and the high voltage in the GEM stack were used for both beam tests, a difference this large is not expected. As shown in figure 8.2b, the discrepancy is mainly caused by a lower charge on the first module in 2013. During the 2016 beam test campaign a similar effect was observed. It was caused by a shift of ~5 V in one insert of the HV power supply for the GEMs (see section 6.1.2) over the first few hours of operation, which lead to a reduced amplification in the last module. Since each GEM and each module is powered separately, the voltage offset in the affected channels was corrected manually. The 2013 beam test used the same power supply. Therefore it is likely that the same effect is responsible for the reduced charge observed here. On the central module, which is the only one apparently unaffected in both beam tests, the measured charge is the same in both data sets. Therefore it can be concluded that the GEM amplification system provides a consistent performance between the two module generations. However the issue outlined above also shows the importance of a stable voltage supplied to the system.

8.1.3. Pad Response Function

The pad response function (PRF) describes the average distribution of the charge within a hit on the pad plane. It is determined from data by plotting the charge of each pulse in a hit

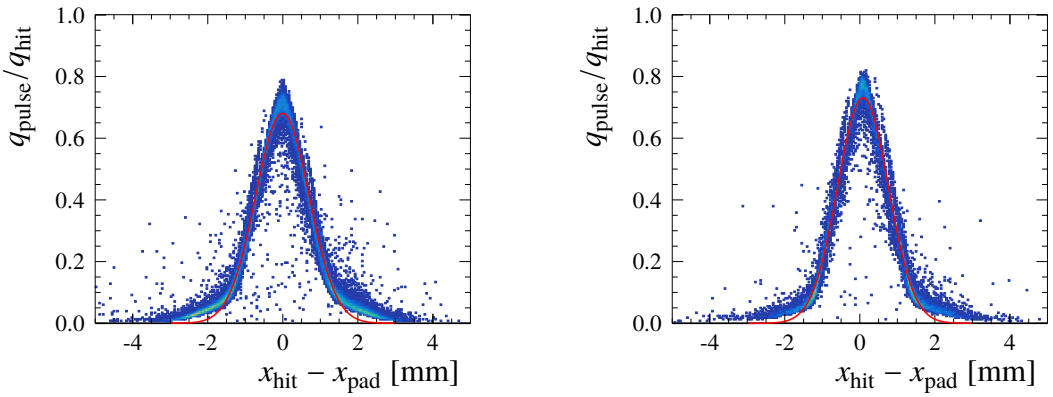

(a) PRF in 2013.

(b) PRF in 2016.

Figure 8.3.: Examples of the pad response function for the (a) 2013 and (b) 2016 data sets. The PRF describes the charge distribution of hits on the pad plane. The data in both figures were recorded at ~20 mm drift distance in a drift field of 240 V/cm with $B = 1$ T. The lines represent a fit as described in the text.

against the position of the pad the pulse was detected on within the row. To be able to average over several hits, the charge of each pulse is normalised to the total charge of the hit and the position is taken relative to the reconstructed centre of the hit. In figure 8.3 examples of the distribution are shown for data from each data set, taken with a magnetic field of 1 T at short drift length, resulting in low diffusion. The width of the PRF follows the width of the charge distribution, which is expected to be Gaussian due to diffusion. Therefore, the hypothesis for the shape of the distribution is a convolution of a Gaussian with a uniform distribution, that takes into account the uniform probability distribution of the initial position of the electron relative to the pad centre. A fit of this distribution within a range of ± 3 standard deviations around the mean is used to extract the width of the charge distribution. The width of the uniform distribution is defined by the pad pitch and therefore not a free parameter in the fit.

As can be seen in the figure, the fit matches the central part of the distribution well but fails to describe the tails. As explained in ref. [223], these tails are artefacts resulting from the behaviour of the readout electronics. While an electron traverses the induction gap, it already induces a signal into each pad. If an electron is not collected on a specific pad, the positive and negative part of the signal cancel each other, resulting in a vanishing integral of the signal on this pad. If pedestal subtraction is applied in the readout electronics, it records samples below the baseline as zero, since it is only sensitive to signals of the selected polarity. This results in a biased estimate of the total charge of the pulse. Since they only collect a small fraction of the electrons, pads at the edges of the charge cloud have a higher probability to see a signal part below baseline, resulting in an artificially increased charge in the recorded data. Still, the result of the chosen fit describes the central part of the PRF well, which can be taken as a confirmation of the assumed Gaussian shape of the charge distribution.

Determining the width of the PRF at several drift lengths allows to extract the transverse

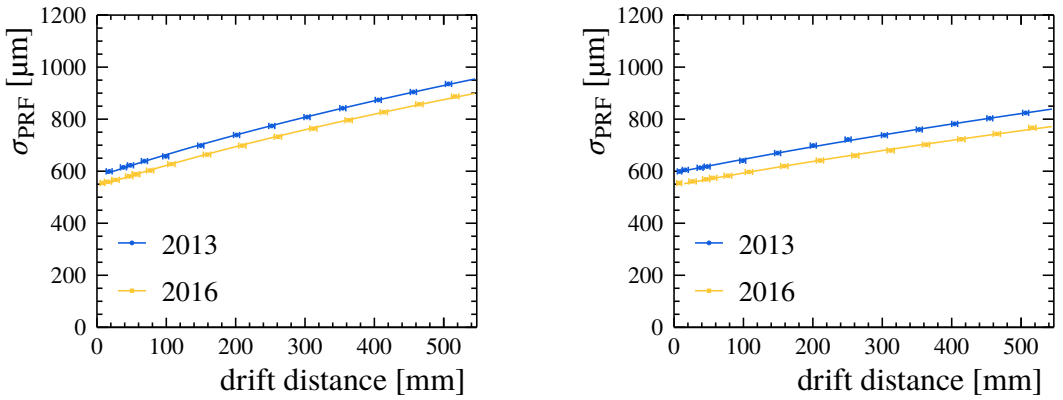

(a) $E_{drift} = 240\,V/cm$. **(b)** $E_{drift} = 130\,V/cm$.

Figure 8.4.: The measured average width of the PRF at various drift distances in both data sets. The solid lines represent fits of equation (8.1). The fit results are given in table 8.2.

Table 8.2.: Results for both data sets of a fit of equation (8.1) to the width of the PRF, and the corresponding simulated values of D_t from Magboltz.

year	drift field [V/cm]	$\sigma_{PRF,0}$ [µm] measurement	σ_{diff} [µm] simulation	D_t [µm/$\sqrt{cm}$] measurement	simulation
2013	240	578.2 ± 1.9	354.4 ± 0.6	102.87 ± 0.38	97.49 ± 0.70
2016	240	540.8 ± 1.9	348.7 ± 0.9	97.28 ± 0.40	95.48 ± 0.63
2013	130	593.6 ± 1.2	354.4 ± 0.6	80.29 ± 0.30	74.17 ± 0.48
2016	130	544.6 ± 1.3	348.7 ± 0.9	74.11 ± 0.33	74.08 ± 0.71

diffusion coefficient D_t. The width of the PRF is expected to follow the function

$$\sigma_{PRF} = \sqrt{(\sigma_{PRF,0})^2 + (D_t)^2 \cdot z}\ , \tag{8.1}$$

where $\sigma_{PRF,0}$ is the width of the PRF at zero drift distance due to the diffusion of the electron cloud inside the GEM stack and signal induction:

$$\sigma_{PRF,0} = \sqrt{(\sigma_{ind})^2 + (\sigma_{diff})^2} = \sqrt{(\sigma_{ind})^2 + (D_t^{trans})^2 \cdot 2\Delta_{trans} + (D_t^{ind})^2 \cdot \Delta_{ind}}\ , \tag{8.2}$$

with the transfer and induction gaps of the module $\Delta_{trans} = 2\,mm$ and $\Delta_{ind} = 3\,mm$, respectively, and the corresponding diffusion coefficients D_t^{trans} and D_t^{ind}. The first term σ_{ind}, which is currently not well understood, accounts for the difference between the measured $\sigma_{PRF,0}$ and the simulated diffusion in the GEM stack σ_{diff}.

In figure 8.4 the width of the PRF in data from both beam tests is shown for various drift distances at drift fields of 240 V/cm and 130 V/cm, including fits of equation (8.1). The results of the fits are given in table 8.2 including the corresponding values from a Magboltz simulation. The diffusion coefficients measured in the 2016 data agree reasonably well with

the simulated values, while the 2013 measurements are significantly larger than expected from the simulation. Additionally, the intrinsic width $\sigma_{\mathrm{PRF},0}$ is significantly larger in the 2013 data than in the 2016 data, while a very similar diffusion in the GEM stack is expected from the simulation. In ref. [223] the discrepancy of the diffusion coefficient between measurement and simulation is attributed to the inhomogeneities and resulting transverse components of the electric and magnetic fields in the setup, which are not considered in the simulation. Under this assumption the results presented here would be qualitatively consistent with the increased field homogeneity expected due to the improved flatness of the GEMs in the new modules described in chapter 5. The reduced $\sigma_{\mathrm{PRF},0}$ would then indicate an improved homogeneity of the transfer and induction fields in the new modules.

Comparing the two distributions of the pad response in figure 8.3, they show the same shape with a similar fraction of charge in the tails but the tails appear more populated in the 2013 data. Since the differences found here are likely related to the discrepancies observed in the following sections, possible common causes are explored in section 8.2.

8.1.4. Pulse Shapes

As described in section 6.3, the pulse shape as seen by the ADC is given by the shaper function (6.1). Since each pulse in a hit is only affected by a part of the electron cloud, the longitudinal profile and thus the signal length varies between the pulses within each hit. For this reason two groups of pulses with common features were investigated separately. The first group contains the leading pulses of each hit, which contribute the most charge. The other group consists of the pulses with the least charge in each hit, which are expected to be located at the edges of the hits. The digitised pulses are normalised to an integral of one and from each group an average pulse shape is calculated. Pulses with irregular shapes, e.g. due to saturation of the ADC, are excluded. Finally, the shaper function (6.1) is fitted to the

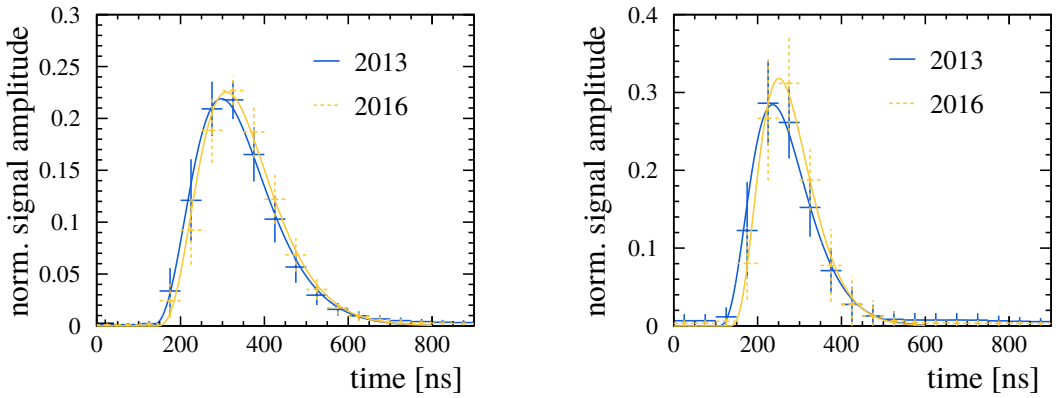

(a) Leading pulses.

(b) Lowest pulses.

Figure 8.5.: The average normalised pulse shapes from data with $E_{\mathrm{drift}} = 240\,\mathrm{V/cm}$ at a drift distance of ~20 mm for (a) the leading pulses with the highest charge and (b) the pulses with the least charge in each hit. The lines in both figures represent fits of the shaper function (6.1).

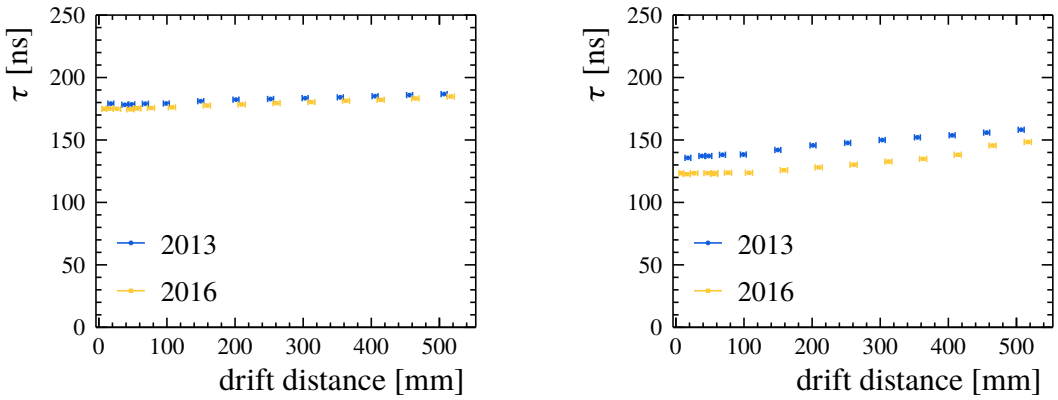

(a) Leading pulses.

(b) Lowest pulses.

Figure 8.6.: The rise time τ from a fit of equation (6.1) to the average pulse shape from data with $E_{\text{drift}} = 240\,\text{V/cm}$ for (a) the leading pulses with the highest charge and (b) the pulses with the least charge in each hit.

average pulse shapes to extract the rise time τ. Examples of the average pulse shapes in both data sets are shown in figure 8.5.

In figure 8.6 the rise times of the average leading pulse (a) and lowest pulse (b) are shown for 240 V/cm data from both beam tests. In figure A.3 on page 192 the same is shown for a drift field of 130 V/cm. The leading pulses in all data sets show a similar average rise time of 170 ns to 190 ns at short drift distance, with only little change over the drift length in the 240 V/cm data. In the 130 V/cm data a stronger dependence on the drift distance is visible, consistent with the expected higher longitudinal diffusion (see table 8.4). Here also a difference of ~10 ns in the rise time can be observed between the two beam test periods, with the 2016 data showing the shorter pulses. For the lowest charge pulses the picture is different. The average rise time is shorter with values from 120 ns to 140 ns at short drift distances. In both drift fields the rise time shows a stronger dependence on the drift distance than the corresponding leading pulses. Here also, the rise time is consistently lower in the 2016 data than in the 2013 data, by ~10 ns to 20 ns for the 240 V/cm drift field and ~20 ns to 40 ns for the 130 V/cm drift field. More notably, the 2016 data behaves very similar in both cases, while the 2013 data shows the expected stronger drift dependence expected from the larger longitudinal diffusion in the 130 V/cm drift field. Additionally, the 2016 data shows a flat behaviour at drift distances below 100 mm for both drift fields.

This difference in behaviour can be seen as a hint that the small pulses in the 2016 data are artificially biased, e.g. by thresholds. This is investigated further in section 8.2.4. The rise time is related to the length of the signal, i.e. the longitudinal extent of the electron cloud due to diffusion, cf. the transverse case in equations (8.1) and (8.2). However, there is no direct analytical conversion between the two parameters. Still, interpreting the observations in terms of the shape of the charge cloud indicates a smaller longitudinal diffusion within the GEM stack in the 2016 setup. This is consistent with the reduction in the transverse diffusion observed in the PRF in section 8.1.3.

8.1.5. Spatial Resolution

The theoretical behaviour of the spatial resolution in a TPC was investigated in detail in refs. [242, 243], for a pad based readout with rectangular geometry and the use of a charge weighted mean to calculate the position in the readout plane. The final result is the following formula, which considers most important processes and detector effects in a TPC:

$$\sigma_x = \sqrt{A(z,\alpha) + \frac{1}{N_{\text{eff}}} B(z) + \frac{1}{\hat{N}_{\text{eff}}} C(\alpha)} \quad , \tag{8.3}$$

with

$$A(z,\alpha) \coloneqq \int_{-1/2}^{1/2} \mathrm{d}\left(\frac{\tilde{x}}{w}\right) \left(\sum_a (aw) \left\langle \left\langle F_a \right\rangle_{\Delta x}^{y} \right\rangle_y - \tilde{x} \right)^2 \quad , \tag{8.4}$$

$$B(z) \coloneqq \int_{-1/2}^{1/2} \mathrm{d}\left(\frac{\tilde{x}}{w}\right) \left\langle \left(\sum_a (aw) F_a - \sum_a (aw) \left\langle F_a \right\rangle_{\Delta x} \right)^2 \right\rangle_{\Delta x} \quad , \tag{8.5}$$

$$C(\alpha) \coloneqq \frac{h^2 \tan^2 \alpha}{12} \quad , \tag{8.6}$$

$$N_{\text{eff}} \coloneqq \left(\left\langle \sum_{i=1}^{N} k_i \left\langle \left(\frac{G_i}{\sum_{i=1}^{N} k_i G_i} \right)^2 \right\rangle_{G}^{\sum_{i=1}^{N} k_i} \right\rangle_{N,k} \right)^{-1} \tag{8.7}$$

and

$$\hat{N}_{\text{eff}} \coloneqq \left(\int_{-1/2}^{1/2} \mathrm{d}\left(\frac{\tilde{x}}{w}\right) \left\langle \sum_{i=1}^{N} \left\langle \left(\sum_a (aw) \left\langle F_a \right\rangle_{\Delta x}^{y} - \sum_a (aw) \left\langle \left\langle F_a \right\rangle_{\Delta x}^{y} \right\rangle_y^{k_i} \right)^2 \right\rangle_y^{k} \right. \tag{8.8}$$

$$\left. \times \left\langle \left(\frac{\sum_{j=1}^{k_i} G_{ij}}{\sum_{i=1}^{N} \sum_{j=1}^{k_i} G_{ij}} \right)^2 \right\rangle_{G}^{k, \sum_{i=1}^{N} k_i} \right\rangle_{N,k} \Bigg)^{-1} \quad ,$$

where the pointed brackets represent integration or summation over the variables given by the subscripts, and the superscripts show dependent variables afterwards. The symbols used are

- a the pad identifier,
- w the pad width (pitch in x direction),
- h the pad height (pitch in y direction),
- $\tilde{x}$ the track position in x at half the height of the pad row,
- α the relative angle between pad and track direction in the pad plane,

N the number of primary clusters,

k_i the number of primary electrons from the primary cluster i,

G_{ij} the gas gain for electron j from cluster i and

F_a the response function of pad a.

The A term (8.4) takes into account the systematic error of the charge weighted mean method that is introduced due to the finite size of the pads. This method is only a perfect estimator for hits with four or more pulses [234]. If the charge sharing between pads is to small, i.e. for hits with less than four pulses, the calculated position is biased, due to a non-linear response depending on the actual position of the centre of the electron cloud relative to the pad centre. This is called the hodoscope effect or S-shape systematics. The result is a worse resolution in the transverse plane in cases where a significant fraction of hits consist of three or less pulses. In the prototype setup for the working points presented here this effect should only be visible for drift distances below ~100 mm, as otherwise diffusion ensures a sufficient width of the charge distribution.

The B term (8.5) describes the effect due to diffusion of the electrons in the drift volume and the distribution of the charge on the readout pads. It is attenuated by the effective number of primary electrons N_{eff} (8.7) contributing to the signal on one row.

The C term (8.6) represents the systematic uncertainty on the track position within a row, which is introduced for inclined tracks due to the finite height of the row. It is scaled by the effective number of primary cluster $\hat{N}_{\text{eff}}$ (8.8).

For most working points in the large TPC prototype, i.e. for drift distances above 100 mm, diffusion ensures sufficient charge sharing ($\sigma_D \gtrsim w$) but is small enough to prevent large correlations between the individual rows ($\sigma_D \ll h$). Under these conditions equation (8.3) can be simplified to

$$\sigma_{r\varphi} = \sqrt{\left(\sigma_{r\varphi,0}\right)^2 + \frac{\left(D_{\text{t}}\right)^2}{N_{\text{eff}}} z + \frac{h^2}{12\hat{N}_{\text{eff}}} \tan^2 \alpha} \ , \tag{8.9}$$

where the coordinates x and y from the rectangular pad layout have been identified as $r\varphi$ and r in the concentric row layout, respectively, and $\sigma_{r\varphi,0}$ denotes the intrinsic resolution of the readout and D_{t} the transverse diffusion coefficient. Further, the measurements presented here were performed under small inclinations of the beam to the detector leading to small angles α. Under this condition the behaviour of the transverse and longitudinal resolution are similar, as they mainly differ in their angular dependencies. Additionally, the original formula ignores attachment of the drifting primary electrons to components or contaminants of the gas, e.g. oxygen, which is expected to be negligible in the ILD TPC but may play a role in the prototype setup. Adjusting the formula for these considerations yields

$$\sigma_{r\varphi/z} = \sqrt{\left(\sigma_{r\varphi/z,0}\right)^2 + \frac{\left(D_{\text{t/l}}\right)^2}{N_{\text{eff}} \cdot e^{-Az}} \cdot z} \ , \tag{8.10}$$

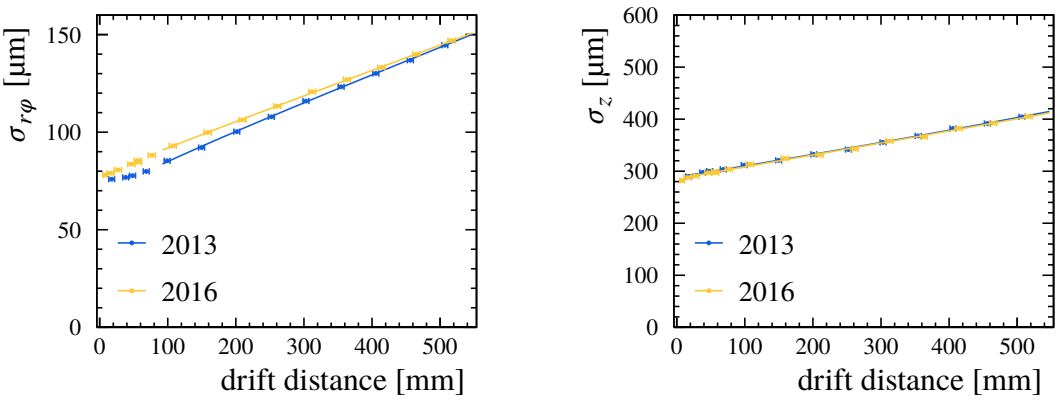

(a) $r\varphi$-resolution. **(b)** z-resolution.

Figure 8.7.: The point resolution in both data sets for a 240 V/cm drift field at various drift distances in (a) the transverse plane and (b) the drift direction. The solid lines represent fits of equation (8.10). The fit results are given in tables 8.3 and 8.4.

with A denoting the exponential attachment rate and D_l the longitudinal diffusion coefficient, equivalent to the transverse case. The parameters $D_\mathrm{t/l}$, N_eff and A are strongly correlated, with $D_\mathrm{t/l}$ and N_eff being completely ambiguous. This correlation can be partially resolved by providing either $D_\mathrm{t/l}$ or N_eff from other sources. As explained in ref. [223], estimating N_eff from a simulation introduces large uncertainties. Therefore it is preferable to provide the diffusion coefficients, which can be simulated rather precisely using Magboltz. The transverse diffusion coefficient D_t can alternatively be determined from the measurement of the width of the PRF, as explained in section 8.1.3.

In figure 8.7 the measured point resolution in (a) the transverse direction and (b) the drift coordinate is shown for both data sets at a drift field of 240 V/cm. In figure A.4 on page 192 the same is shown for a drift field of 130 V/cm. To resolve the correlation between D_t and N_eff in equation (8.10) a combined fit of equation (8.1) to the width of the PRF in figure 8.4 and equation (8.10) to the $r\varphi$-resolution is performed. The fit to the $r\varphi$-resolution is only performed in the valid range of equation (8.10) for drift distances above 100 mm. The resolution of the drift coordinate σ_z is fitted independently with $D_\mathrm{l}/\sqrt{N_\mathrm{eff}}$ as one free parameter. N_eff is then calculated using D_l as determined from a Magboltz simulation. The results of the fits are summarised in tables 8.3 and 8.4. Since in the combined fit $\sigma_{\mathrm{PRF},0}$ and D_t are fully constraint by the width of the PRF, the values of these parameters do not change from table 8.2 on page 116.

First, it should be noted that the quality of the fits to the 130 V/cm data, in particular the z-resolution, is much worse than for the 240 V/cm data. In terms of χ^2 per degree of freedom this means $\chi^2/n_\mathrm{df} \approx 2$ and 3 for the $r\varphi$-resolution in the 2013 and 2016 data, respectively, and $\chi^2/n_\mathrm{df} \approx 10$ for the z-resolution in both data sets. The reason is visible in figure A.4b on page 192, which shows large fluctuations between individual measurements. This indicates the presence of systematic effects, which are not considered in the uncertainties of the fits. At least partially these may be caused by anomalously high noise observed in the measurements

Table 8.3.: Results for both data sets of a combined fit of equations (8.1) and (8.10) to the width of the PRF and the $r\varphi$-resolution, respectively. The combined fit allows to resolve the correlation between D_t and N_{eff}. The values of D_t are unchanged from table 8.2.

year	drift field [V/cm]	$\sigma_{r\varphi,0}$ [µm]	D_t [µm/$\sqrt{\text{cm}}$]	N_{eff}	A [1/cm]
2013	240	68.1 ± 1.6	102.87 ± 0.38	43.4 ± 2.8	0.0054 ± 0.0011
2016	240	77.7 ± 1.6	97.28 ± 0.40	41.6 ± 3.2	0.0054 ± 0.0013
2013	130	72.3 ± 0.8	80.29 ± 0.30	48.2 ± 2.7	0.0089 ± 0.0010
2016	130	82.5 ± 0.8	74.11 ± 0.33	46.8 ± 3.3	0.0084 ± 0.0012

Table 8.4.: Results for both data sets of an independent fit of equation (8.10) to the z-resolution. The values of D_l are simulated with Magboltz to determine N_{eff}.

year	drift field [V/cm]	$\sigma_{z,0}$ [µm]	D_l^{sim} [µm/$\sqrt{\text{cm}}$]	N_{eff}	A [1/cm]
2013	240	288.4 ± 0.6	221.6 ± 1.6	39.9 ± 1.4	0.0050 ± 0.0006
2016	240	285.4 ± 0.7	227.1 ± 1.4	39.4 ± 1.4	0.0038 ± 0.0007
2013	130	268.0 ± 1.3	319.8 ± 3.3	46.5 ± 1.8	0.0093 ± 0.0007
2016	130	256.8 ± 2.6	319.5 ± 3.9	32.7 ± 1.6	0.0007 ± 0.0008

between 150 mm and 250 mm drift distance in both data sets. Additionally, due to the greater longitudinal diffusion in the 130 V/cm drift field, the length of the charge cloud, given by the $\pm 3\,\sigma$ interval of the distribution, exceeds the shaping time of the preamplifier of 120 ns already for drift distances of 150 mm. This may affect the pulse shape in unforeseen ways and bias the z-resolution in particular. Therefore, the affected data is considered mostly qualitatively.

Good agreement between the data sets is found in the z-resolution. The intrinsic resolution at zero drift distance is consistent between all data sets. The effective number of primary electrons N_{eff} agrees well between the two 240 V/cm data sets. The systematic effects in the 130 V/cm data sets mentioned above lead to a significantly higher value of N_{eff} in the 2013 data and a lower one in the 2016 data. The corresponding values of the attachment rate A diverge in the same manner, compatible with the correlation of the two parameters in the fits. For the two 240 V/cm data sets the values determined for N_{eff} and A from the z-resolution are compatible with the values extracted from the $r\varphi$-resolution. This serves as an important cross check between the measurements. The attachment rates determined in these measurements are also of a similar magnitude as the direct estimate from the charge measurements. Since the resolution measurement is independent of fluctuations of the gas gain, a discrepancy to the direct charge measurement can be expected. A significant discrepancy between the 2013 and 2016 data sets is found in the $r\varphi$-resolution at lower drift distances, present for both drift fields. Where the 2013 data shows the resolution flattening at drift distances below ~60 mm, turning into a slight rise towards zero drift distance, consistent with

the expected hodoscope effect, the 2016 data shows a strictly monotonic behaviour and a slightly worse intrinsic resolution $\sigma_{r\varphi,0}$. Due to the lower transverse diffusion measured in the 2016 data this difference is reduced over the drift length of the LP.

In section 8.1.3, the assumption is made that the new modules used in the 2016 beam test create more homogeneous electric fields leading to lower transverse diffusion and a narrower PRF. Under this assumption one would generally expect an improved resolution in the 2016 data, which conflicts with the observations in this section. This contradiction can be resolved by taking into account the observations in section 8.1.4. The the conjecture is that the longitudinal diffusion is also reduced leading to shorter charge clouds in the 2016 data. The shorter average pulse length may lead to a lower pulse finding efficiency for the smallest pulses, deteriorating the transverse resolution.

8.2. Investigation of Discrepancies

In section 8.1 small discrepancies between the 2013 and 2016 data sets were observed in the width of the PRF σ_{PRF}, the transverse diffusion coefficient D_{t} and the transverse spatial resolution $\sigma_{r\varphi}$, as well as the average pulse rise time τ of the smallest pulses in each hit. An assumption on the cause for these discrepancies made in the respective sections, is the improved homogeneity of the electric fields, i.e. drift, transfer and induction field, due to the reduced deflections of the GEMs in the new modules used in the 2016 beam test. Since the field homogeneity is only inferred from the GEM deflections and can not be tested directly, also other potential causes are investigated. Starting in section 8.2.1, systemic effects caused by differences in environmental and gas conditions and the electric and magnetic field strength are explored. Following in section 8.2.2, the influence of different track angles is discussed. The potential of an effect due to the electronics noise levels is briefly shown in section 8.2.3. Finally, the pulse threshold settings are studied in section 8.2.4, according to the observations in section 8.1.4.

8.2.1. Gas and Field Conditions

The most obvious candidates for creating the observed differences are variations of the environmental and gas conditions as well as the electric and magnetic field settings, as they have a direct impact on the performance parameters in all parts of the TPC. As detailed in section 6.1.2, these conditions are generally well observed, with the exception of the exact gas composition. For the gas composition, only oxygen and water contaminations are monitored directly. Other contaminations as well as variations of the gas mixture can not be tested in-situ. This led to some concern regarding the 2-methylpropane content of the gas supplied to the TPC during the 2013 beam test. In the gas bottle, the 2-methylpropane content starts to condense at temperatures below 4 °C, staying unmixed even after rewarming the bottle. Since this fact was not known at first, some gas bottles for the 2013 beam test were temporarily stored outside in cold weather, making a lowered 2-methylpropane content a possible cause for the observed discrepancies.

Table 8.5.: Overview of the settings for the various conditions used in the Magboltz simulations. One parameter is varied at a time within the given range, keeping all others at their respective default values. Separate simulations are performed for each of the electric field settings.

parameter	unit	default value	simulated range
electric field	V/cm	240	200 to 320
		130	100 to 175
		1500	1200 to 1800
		3000	2400 to 3600
magnetic field	T	1.0	0.8 to 1.2
pressure	mbar	1013	950 to 1100
temperature	°C	20	10 to 30
oxygen (O_2)	ppm	0	0 to 500
air (79 % N_2 : 21 % O_2)	ppm	0	0 to 1500
water (H_2O)	ppm	0	0 to 500
2-methylpropane ($HC(CH_3)_3$)	%	2.0	0.0 to 2.5

Regrettably the slow control data for the 2013 beam test period was only stored in a reduced format with daily averages. While the environmental conditions are not expected to change strongly over that period, the averages may still be biased. For the field conditions, which are set manually and may change multiple times during a day, the averages do not provide any good information and also the manually curated run logbook and database may not reflect erroneous settings. Luckily the impact of all the variables above can be simulated in Magboltz. Comparing both the simulated electron drift speed and diffusion coefficients to the measured values provides a good cross check. To assess the impact on the intrinsic width of the PRF, simulations are not only performed for the nominal drift field strength of 240 V/cm and 130 V/cm but also for the transfer and induction fields within the GEM stack of 1500 V/cm and 3000 V/cm, respectively. The simulated ranges of the various parameters and their default values are summarised in table 8.5. When varying one setting, all others are kept at their respective default value. The ranges are chosen larger than any expected variation, to be able to determine the general behaviour of the observables around the nominal values. The nominal field settings are identical to the default values given in the table. The nominal gas and environmental conditions for each beam test period are given at the beginning of this chapter and in section 6.5.2.

Gas Composition

The impact of the measured gas contaminants, oxygen, air and water, is shown in figure A.5 on page 193 and figures 8.8 and 8.9, respectively. Oxygen does not produce any significant change in any of the investigated gas parameters, even at concentrations of ~10 times the measured value. For air and water there is some visible influence on some of the relevant parameters. For air in particular, the diffusion coefficients at 1500 V/cm and 3000 V/cm are

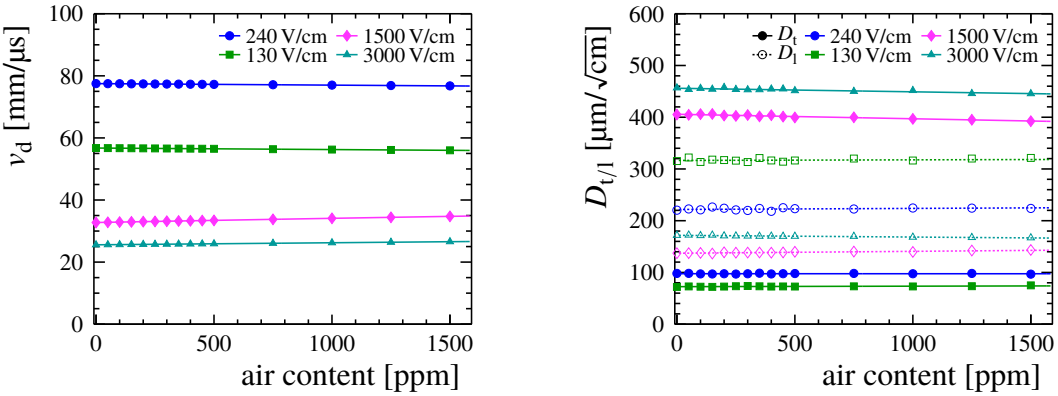

(a) Drift speed. **(b)** Diffusion coefficients.

Figure 8.8.: The influence of contamination of the gas with air on (a) the drift speed and (b) the diffusion coefficients. During both beam tests ~300 ppm air are expected from the oxygen measurement. The lines represent polynomial fits of up to third order to guide the eyes and assess the rate of change.

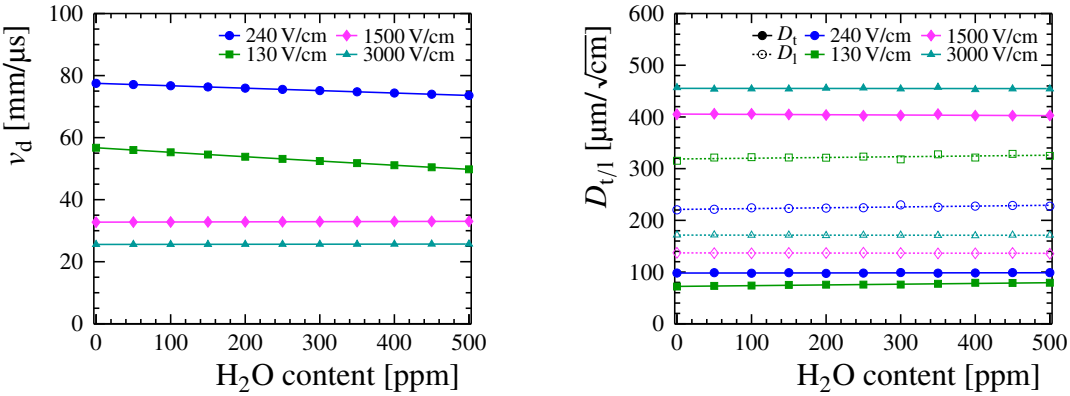

(a) Drift speed. **(b)** Diffusion coefficients.

Figure 8.9.: The influence of contamination of the gas with water vapour on (a) the drift speed and (b) the diffusion coefficients. During the beam tests 50 ppm to 60 ppm H_2O were recorded. The lines represent polynomial fits of up to third order to guide the eyes and assess the rate of change.

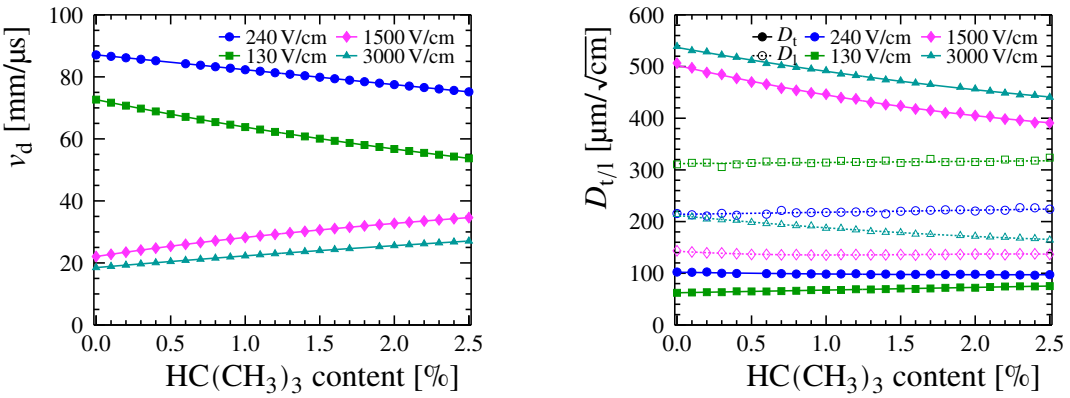

(a) Drift speed.

(b) Diffusion coefficients.

Figure 8.10.: The influence of the 2-methylpropane content of the gas on (a) the drift speed and (b) the diffusion coefficients. The lines represent polynomial fits of up to third order to guide the eyes and assess the rate of change.

affected. For water the drift speed and longitudinal diffusion at 240 V/cm and 130 V/cm change slightly. However, these parameters only change by less than ~1 % for a variation of the contamination of 100 % of the respective measured value. Since under stable operating conditions variations this large are not expected, the measured gas contamination can be excluded as a cause of the observed discrepancies.

Varying the 2-methylpropane content produces more drastic changes in the gas parameters, as shown in figure 8.10. In particular, the transverse diffusion in the transfer and induction fields increases by ~0.75 % per 0.1 points lower 2-methylpropane content and is reduced by ~0.5 % in the 130 V/cm drift field. Additionally, the drift speed at 240 V/cm and 130 V/cm is increased by ~0.5 % to 1 % per 0.1 points lower 2-methylpropane content. The transverse diffusion in the 240 V/cm drift field increases by a few percent towards zero 2-methylpropane but does not change at all for small variations. Since the measurement in section 8.1.1 shows a rather consistent drift speed between the two beam test periods, the 2-methylpropane content can not have dropped below 1.8 % during the 2013 beam test. Otherwise the deviation of the drift speed would be much larger than the observed difference between the data sets. Therefore, an unmixing of the 2-methylpropane from the gas on a significant scale due to low temperatures can be excluded. This limits the modulation of the diffusion in the GEM stack to 1.5 % or less and does not allow for any significant change of the transverse diffusion in the drift field.

Pressure & Temperature

The pressure inside the TPC is mainly defined by the exterior pressure, since the gas system is vented to the atmosphere. During both beam test periods the atmospheric pressure in the area changed by 10 mbar or less over any given day [244]. At the nominal flow rate of 40 l_{N_2}/h the flow resistance of the gas system introduces a slight overpressure of ~6 mbar inside the TPC. The gas temperature is affected by the temperature of the gas bottle, the tem-

perature of the environment and the flow rate. Since the bottles are generally stored in the test beam hall for several hours before use, the temperature should have equalised with the rather stable temperature in the hall. Therefore the available daily average pressure and temperature during the 2013 beam test period should be sufficiently accurate as a starting point. The simulated impact on the gas parameters is shown in figures A.6 and A.7 on page 193 and on page 194. Any expected modulation caused by a reasonable deviation of pressure and temperature from the recorded values is negligible.

Field Conditions

As the magnetic and electric fields are set manually, the most probable cause of field values diverging from the nominal settings is an error in the operator's input. Since large deviations are likely to be discovered, when the settings are changed again, the variation can be expected to be relatively small. The potentials in the GEM stack are controlled individually for each module, making a consistent error across all three modules unlikely. A divergence of one module would be readily visible in the data, as observed in section 8.1.2. That variation, consistent with a shift of ~5 V in some of the GEM HV channels as discussed there, has a negligible impact on the drift field strength and also the diffusion in the GEM stack. As shown in figure 8.11, to reproduce the discrepancy in the transverse diffusion coefficient the drift field would need to be changed by 10 V/cm to 15 V/cm (~4 % to 6 %), equivalent to a modulation of the cathode voltage of 570 V to 850 V at a nominal voltage of ~15.9 kV. As this would not influence the intrinsic width of the PRF, an additional variation of some of the GEM potentials would be necessary. Therefore, erroneous voltage settings can be safely excluded as a cause of the observed discrepancies, due to the required magnitude of the modulation and number of affected HV channels.

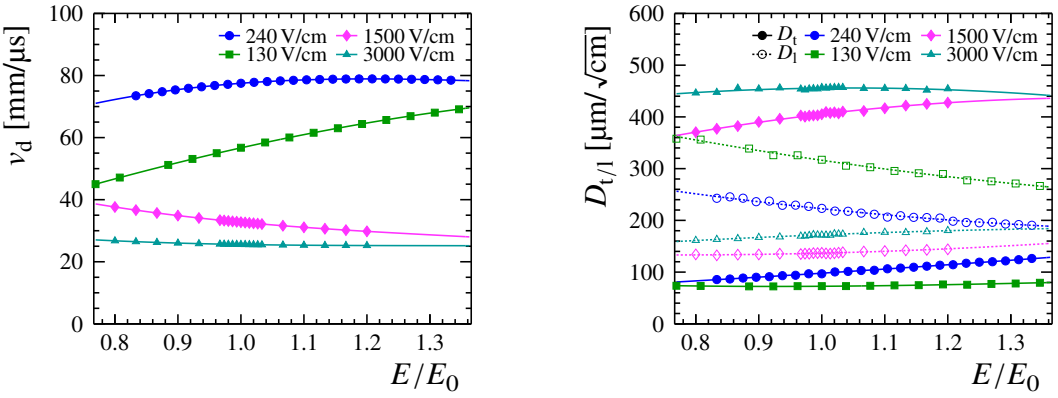

(a) Drift speed.

(b) Diffusion coefficients.

Figure 8.11.: The influence of the electric field strength inside the TPC on (a) the drift speed and (b) the diffusion coefficients. The field strength is normalised to the respective nominal field given in the legend. The lines represent polynomial fits of up to third order to guide the eyes and assess the rate of change.

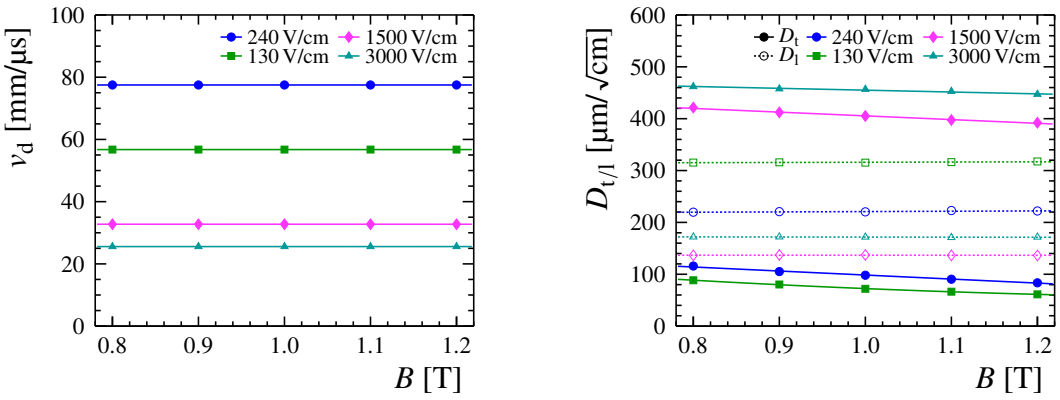

(a) Drift speed.

(b) Diffusion coefficients.

Figure 8.12.: The influence of the magnetic field strength inside the TPC on (a) the drift speed and (b) the diffusion coefficients. The lines represent polynomial fits of up to third order to guide the eyes and assess the rate of change.

On the other hand, the magnetic field influences the transverse diffusion in both the drift volume and the GEM stack, while leaving the drift velocity unaffected, as shown in figure 8.12. The required modulation to recreate the observed diffusion during drift is ~0.05 T, equivalent to a change of the coil current of 22 A from a nominal 441 A for a 1 T field [200]. However, the variation required to achieve the observed difference of the diffusion in the GEM stack is far outside the simulated range. Since both discrepancies cannot be resolved using the same magnetic field setting and because the necessary changes are so large, the magnetic field can also be excluded as a cause for the discrepancies.

8.2.2. Track Angle

The azimuthal angle of the TPC relative to the beam is controlled by manually rotating the TPC around the axis of the field cage. Since during both beam tests no measurement device for this angle was available, the accuracy of the position is of $\mathcal{O}(1°)$. Additionally, the magnetic field was inverted between the two beam test periods, resulting in an inverted curvature of the beam and different angles relative to the individual pad rows. This angle directly affects the transverse point resolution measured at zero drift distance according to equation (8.9) on page 120, but also the transverse diffusion is effectively broadened for larger angles, as shown in figure 8.13a. Since N_{eff} and $\hat{N}_{\text{eff}}$ are expected to be proportional to the length of the track segment above each row, they also increase with larger inclination as

$$D_t(\alpha) \approx \frac{D_t(0)}{\cos\alpha} \quad , \quad N_{\text{eff}}(\alpha) \approx \frac{N_{\text{eff}}(0)}{\cos\alpha} \quad , \quad \hat{N}_{\text{eff}}(\alpha) \approx \frac{\hat{N}_{\text{eff}}(0)}{\cos\alpha} \quad . \tag{8.11}$$

Also the width of the PRF is affected by the inclination of the track. Equivalent to the convolution of the Gaussian charge distribution due to diffusion and the uniform probability distribution of the track position over the pad width, the uniform distribution over the width

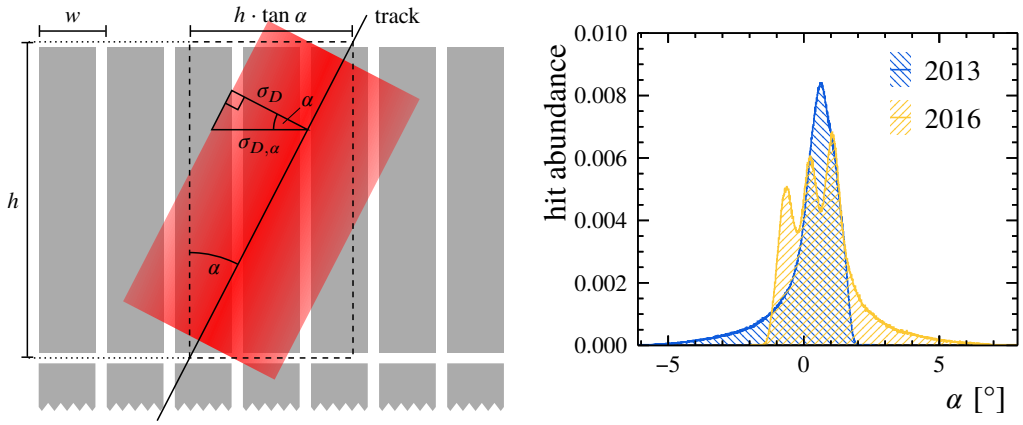

(a) Pad angle effect.

(b) Pad angle distributions.

Figure 8.13.: (a) The effects of inclined tracks on the resolution and width of the PRF. (b) Distribution of the track inclination relative to hits on each pad row for both beam test periods. The three peaks visible in the 2016 data result from the offset between the three rows of modules.

$W = h \cdot \tan\alpha$ traversed by the track on the pad row needs to be included, such that

$$\sigma_{\text{PRF}} = \left(\sigma_{D_t} * \Pi(w)\right) * \Pi(W) \quad , \tag{8.12}$$

where $\Pi(d)$ is the uniform distribution between $-d/2$ and $d/2$.

Until now the track inclination was ignored in all these cases, as the respective angles are expected to be small. In figure 8.13b the distribution of the track inclination α relative to the individual rows is shown and confirms this expectation. The inverted direction of the magnetic field between the two data sets is visible by the opposite direction of the tails of the distributions, which result from energy loss of the electrons due to interaction with the magnet wall in front of the TPC. As expected, the angles are small with $|\alpha| \leq 2°$ for electrons with negligible energy loss. While there is a small offset between the two distributions, they mostly overlap. With $\cos\alpha > 0.99$ and $|\tan\alpha| < 0.1$ the involved angles are too small to have any significant effect on the transverse point resolution or the width of the PRF.

8.2.3. Electronics Noise

In the comparison of the PRFs in figure 8.3 in section 8.1.3 the different abundance of entries in the tails of the distributions was noted, with less populated tails in the 2016 data. While the thresholds for the pulse finding process, as described in section 7.3.1, are small, they affect the small pulses at the edge of each hit most. Since the thresholds are scaled with the noise level in each channel, differences in the overall noise level can have a significant impact on the tails of the PRF. In figure 8.14 the distribution of the noise in all used electronics channels, measured as the RMS of the pedestal in each channel, is shown for both beam tests. In both cases the noise roughly follows a Landau distribution with similar width and a MPV of ~0.72 ADC. While the distribution of the 2016 beam test shows a few more channels in the tail towards higher noise, the difference is too small to have an impact of the observed magnitude on the efficiency of the pulse finding process.

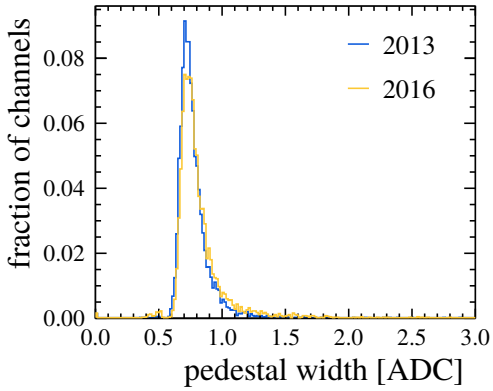

Figure 8.14.: Pedestal noise distributions for the 2013 and 2016 data sets.

8.2.4. Pulse Thresholds

The difference in the pulse shapes observed in section 8.1.4 between the two beam tests may also be responsible for the difference in the tails of the PRF in figure 8.3. Since the pulse shapes differ in the rise time, the most obvious adjustment is to reduce the required minimum pulse length. The observed difference in the rise time of up to ~40 ns results in a difference of ~50 ns in total pulse length for the smallest possible pulses passing the default thresholds. To put it differently, due to the shorter rise time the smallest pulses require up to ~50 % more charge to exceed the minimum pulse length. Since the chosen sampling rate of the ADC is 20 MHz the sampling period is exactly 50 ns. Therefore, reducing the required minimum pulse length from 5 to 4 samples should be sufficient.

First, as a cross check, the minimum pulse length is reduced for both the 2013 and 2016 data set. The effect on the rise time of the average smallest pulses is shown in figure 8.15 for both drift fields. In comparison to figure 8.6b on page 118 and figure A.3b on page 192 the average rise time in the 2016 data is reduced by ~50 ns, indicating that a large number of additional shorter pulses now pass the thresholds. On the other hand, the 2013 data shows a reduction by only 10 ns or less, meaning only few additional pulses are included. The rise time of the leading pulses is unaffected in all cases. A further reduction of the minimum pulse length to 3 samples has no additional effect on the observed average rise times. This confirms the need for a relaxed pulse length requirement in the 2016 data only, to ensure an equivalent treatment of the data.

Therefore the comparison is now done between the 2013 data using the default settings and the 2016 data using the reduced minimum pulse length. In figure 8.16 the resulting transverse resolution is shown for both drift fields. The width of the PRF and the z-resolution are shown in figures A.8 and A.9 on page 194 and on page 195, respectively. The fit results are given in tables 8.6 and 8.7. As in section 8.1.5, the results at 130 V/cm must be considered with care, since in both data sets there are large fluctuations between the individual measurements of the z-resolution that could not be fully investigated in the scope of this work. With the adjusted thresholds the behaviour of the $r\varphi$-resolution is almost identical between the 2013 and 2016 data sets, while the width of the PRF and the z-resolution are almost un-

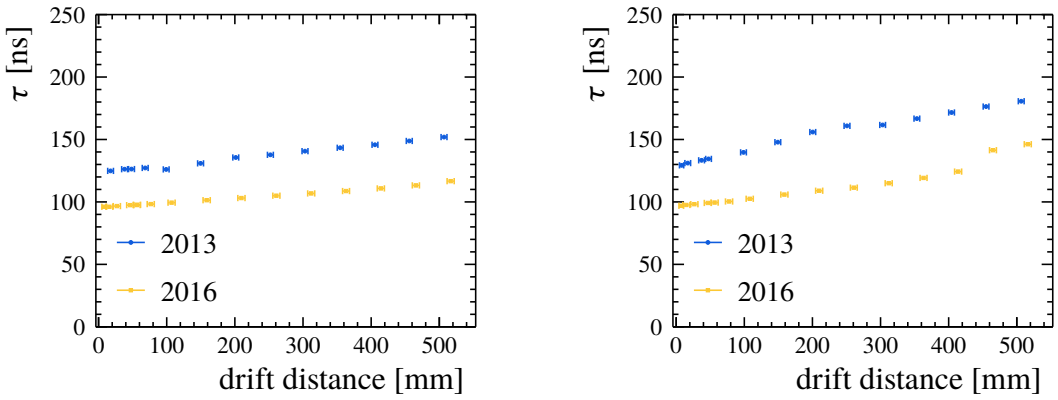

(a) $E_{\text{drift}} = 240\,\text{V/cm}$. **(b)** $E_{\text{drift}} = 130\,\text{V/cm}$.

Figure 8.15.: The rise time τ from a fit of equation (6.1) to the average pulse shape from data with the minimum pulse length reduced from 5 to 4 samples.

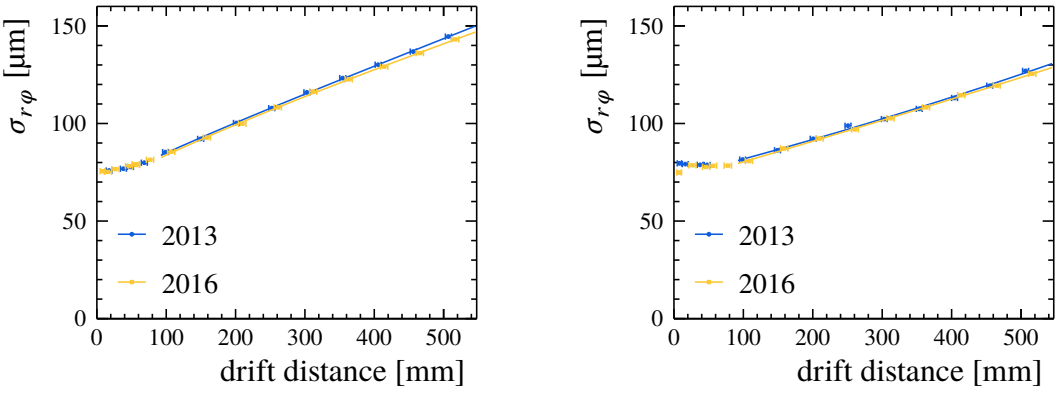

(a) $E_{\text{drift}} = 240\,\text{V/cm}$. **(b)** $E_{\text{drift}} = 130\,\text{V/cm}$.

Figure 8.16.: The transverse point resolution at various drift distances. The minimum pulse length was reduced for the 2016 data The solid lines represent fits of equation (8.10) on page 120. The fit results are given in table 8.6.

Table 8.6.: Results for both data sets of a combined fit of equations (8.1) and (8.10) to the width of the PRF and the $r\varphi$-resolution, respectively. The minimum pulse length was reduced for the 2016 data. The 2013 results are unchanged from tables 8.2 and 8.3.

year	drift field [V/cm]	$\sigma_{r\varphi,0}$ [µm]	D_{t} [µm/$\sqrt{\text{cm}}$]	N_{eff}	A [1/cm]
2013	240	68.1 ± 1.6	102.87 ± 0.38	43.4 ± 2.8	0.0054 ± 0.0011
2016	240	66.2 ± 2.1	99.06 ± 0.40	38.7 ± 3.0	0.0040 ± 0.0013
2013	130	72.3 ± 0.8	80.29 ± 0.30	48.2 ± 2.7	0.0089 ± 0.0010
2016	130	69.7 ± 1.2	75.58 ± 0.34	38.3 ± 2.9	0.0067 ± 0.0013

Table 8.7.: Results for both data sets of an independent fit of equation (8.10) to the z-resolution. The values of D_l are simulated with Magboltz to determine N_eff. The minimum pulse length was reduced for the 2016 data. The 2013 results are unchanged from table 8.4.

year	drift field [V/cm]	$\sigma_{z,0}$ [µm]	$D_\mathrm{l}^\mathrm{sim}$ [µm/$\sqrt{\mathrm{cm}}$]	N_eff	A [1/cm]
2013	240	288.4 ± 0.6	221.6 ± 1.6	39.9 ± 1.4	0.0050 ± 0.0006
2016	240	286.0 ± 0.7	227.1 ± 1.4	38.6 ± 1.3	0.0033 ± 0.0006
2013	130	268.0 ± 1.3	319.8 ± 3.3	46.5 ± 1.8	0.0093 ± 0.0007
2016	130	251.3 ± 2.9	319.5 ± 3.9	30.0 ± 1.5	-0.0009 ± 0.0008

affected. This is expected since the thresholds mostly affect the small pulses at the edges of the hits, which are not used for the calculation of the z-coordinate and are likely to lie outside of the fit range for the PRF width. All data sets now show a consistent intrinsic resolution $\sigma_{r\varphi,0}$, including the hodoscope effect for drift distances below ~80 mm. The numbers of effective primary electrons N_eff are changed but still compatible between the measurements at 240 V/cm. Moreover, the values of N_eff for the 2016 data are now compatible for all fits except the z-resolution at 130 V/cm, which as the worst fit quality and should be treated with care. Now the main difference between the two data sets in the transverse resolution is due to the discrepancy of the transverse diffusion, which is still significantly lower in the 2016 data.

8.3. Extrapolation to ILD Parameters

The measurements of the point resolution can be used to estimate the resolution in the ILD TPC with a magnetic field of 3.5 T and a drift length of 2350 mm. The TDR for the ILC [105] states the requirements for the TPC. The transverse point resolution is supposed to be below 100 µm at the full drift length and to reach ~60 µm at zero drift distance. The corresponding goals for the longitudinal resolution are 1.4 mm and 0.4 mm for the full drift length and zero drift distance, respectively.

For the extrapolation of the transverse point resolution, the reduced transverse diffusion due to the higher magnetic field needs to be taken into account in equation (8.9) on page 120. Therefore, Magboltz is used to simulate the diffusion coefficients D_t for T2K gas in the 3.5 T magnetic field. For the drift fields of 240 V/cm and 130 V/cm the resulting values are (31.83 ± 0.36) µm/$\sqrt{\mathrm{cm}}$ and (21.81 ± 0.20) µm/$\sqrt{\mathrm{cm}}$, respectively. The other parameters, i.e. $\sigma_{r\varphi,0}$, N_eff and A, including their correlations are taken from the fits to data using the final settings in table 8.6. From experience with existing experiments with large gaseous detectors, e.g. the ALICE and T2K TPCs [171, 193], gas contaminations causing electron attachment, i.e. oxygen, can be expected to be well under control in the final detector, with values of less than 5 ppm being a realistic assumption. Therefore, an additional extrapolation is performed with the electron loss removed, by setting the attachment coefficient A to zero. In contrast to ref. [223], here also the uncertainty on the attachment coefficient is assumed

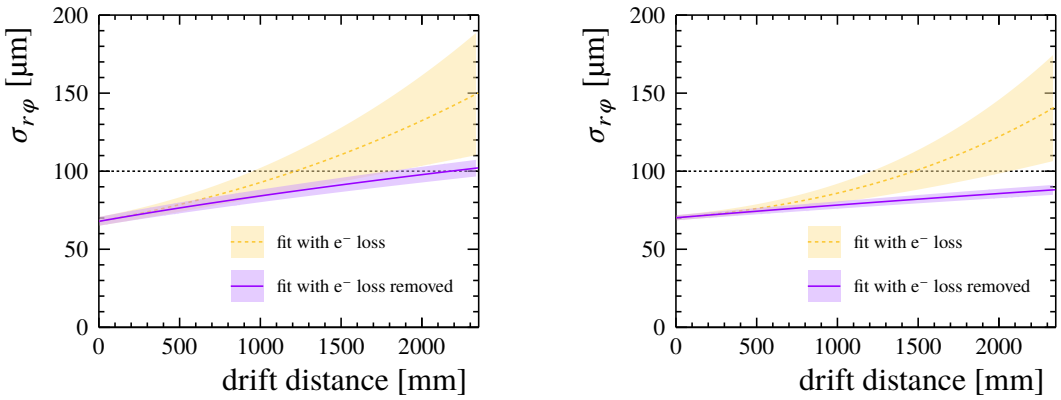

(a) $E_{\text{drift}} = 240\,\text{V/cm}$. **(b)** $E_{\text{drift}} = 130\,\text{V/cm}$.

Figure 8.17.: Extrapolation of the transverse point resolution to the ILD TPC. The coloured bands represent the 95 % confidence interval. The horizontal dotted lines at 100 µm mark the goal for the ILD TPC at the full drift length of 2350 mm.

to be zero, leading to an overall smaller uncertainty on the extrapolation. In the following the results for the 2016 data set are shown, as here the measured diffusion coefficient D_t agrees better with the corresponding simulation than for the 2013 data. Since apart from this the parameters are very similar in both data sets, also the extrapolations are in good agreement. In figure 8.17 the predictions of the $r\varphi$-resolution for the ILD TPC are shown for the drift fields of 240 V/cm and 130 V/cm. The coloured bands represent the 95 % confidence intervals calculated from the uncertainties of the parameters. It is clearly visible that the goal of a transverse resolution better than 100 µm over the full drift length of 2350 mm cannot be reached with the rate of electron attachment present in the prototype setup. On the other hand, if the attachment is well suppressed the requirement can be fulfilled with either drift field. The lower diffusion coefficient in the 130 V/cm drift field results in an improved transverse resolution at long drift distances, making the goal easier to achieve.

For the longitudinal resolution the projection is straight forward, since the longitudinal diffusion is not influenced by the magnetic field strength. Therefore, the fitted parameters in table 8.7 can be used directly. In figure 8.18 the projections of the z-resolution for the ILD TPC are shown for the drift fields of 240 V/cm and 130 V/cm. Due to the fluctuations between the measurements in the 130 V/cm data the fitted parameters N_{eff} and A differ significantly from the other data sets. To be noted in particluar is that the fitted value of A is negative for this drift field. Since this is unphysical, the extrapolation from this measurement is of doubtful accuracy and only shown for completeness. With the drift field of 240 V/cm the requirements for the z-resolution of the ILD TPC are easily fulfilled.

Generally, using the new data set the applicability of the presented readout system for the ILD TPC is confirmed and the results are in concordance with the results from ref. [223] for the extrapolation of both the $r\varphi$-resolution and z-resolution.

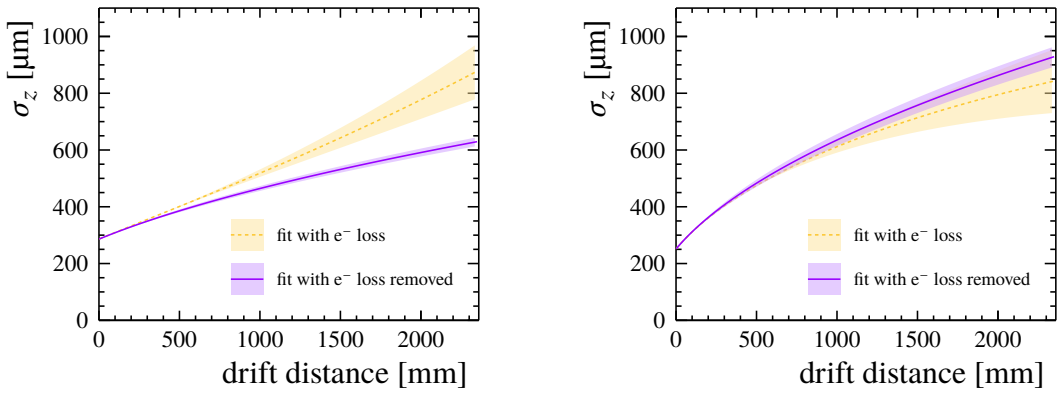

(a) $E_{\text{drift}} = 240\,\text{V/cm}$. **(b)** $E_{\text{drift}} = 130\,\text{V/cm}$.

Figure 8.18.: Extrapolation of the longitudinal point resolution to the ILD TPC. The coloured bands represent the 95 % confidence interval. For the drift field of 130 V/cm the fitted electron attachment coefficient is negative, see table 8.7, resulting in the seemingly better performance of the *fit with* e^- *loss*. This behaviour is unphysical and the plot is only shown for completeness.

8.4. Summary

The existing data from a beam test in 2013 was compared in several observables with the results from a beam test with a new generation of readout modules in 2016. Good agreement between both data sets as well as corresponding simulations was found in the drift velocity and the measured charge, i.e. the gas amplification. Small differences were found in the width of the PRF, the average length of the charge pulses and the transverse resolution. Various influences on these observables were investigated and subsequently excluded as possible causes, including the gas quality, environmental conditions and field settings as well as the angle of the beam relative to the detector and the noise of the electronics. Since no underlying cause could be determined conclusively, the pulse thresholds were adjusted according to the observed difference in the signal length. This resulted in a very good agreement of the transverse resolution but did not resolve the difference in the PRF nor does it provide an explanation for the observed discrepancies. As the narrower PRF and shorter signal length in the 2016 data suggest a lower transverse and longitudinal diffusion, respectively, it was hypothesised that this may be caused by more homogeneous electric fields due to the less distorted GEMs used in the new setup. This hypothesis could not be verified with the available data and a dedicated measurement or simulation study was not in the scope of this thesis. Finally, the results of the resolution measurement were extrapolated to the size and conditions of the ILD TPC. Here it was found that the defined goals can be achieved if a high gas quality is ensured, confirming the findings in ref. [223].

9. Analysis of the Specific Energy Loss

In this chapter the capabilities of the GEM readout system regarding the measurement of the specific energy loss $\mathrm{d}E/\mathrm{d}x$ of particles are explored. The data set used for this was recorded during the beam test in 2016. The data was taken at various drift distances with a drift field of 240 V/cm in a magnetic field of 1 T. Most of the analysis is performed on data where the electron beam traverses the TPC under small angles relative to the readout.

First, the general method to determine the $\mathrm{d}E/\mathrm{d}x$ resolution of the data sample is described in section 9.1. This is followed by the determination of the best $\mathrm{d}E/\mathrm{d}x$ estimator in section 9.2. In section 9.3 two methods are presented that emulate the calibration of the charge measurement as it would be performed in the final detector. Finally, in section 9.4 a method is presented that allows to extrapolate the results to the size of the ILD TPC based on the measured data alone.

9.1. Determining the $\mathrm{d}E/\mathrm{d}x$ Resolution

As detailed in section 3.1, the energy loss of particles in the momentum ranges that are of concern here proceeds mainly through ionisation of the surrounding medium. Therefore the liberated charge is expected to be proportional to the lost energy. This allows to determine the resolution of the specific energy loss directly from the measured charge. The average energy loss of a particle is estimated from the individual charge measurements of the hits associated to its track in the TPC. To avoid a biased result, the hits are required to fulfil certain quality criteria, which are discussed in section 9.1.1. Afterwards, on average 56.5 hits per track are viable for the $\mathrm{d}E/\mathrm{d}x$ calculation. The charge of each hit is determined as described in section 7.3. To calculate the specific energy loss the charge Q of each hit is normalised to the sample length Δx of the track segment over the corresponding row:

$$\frac{\Delta E}{\Delta x} \propto \frac{Q}{\Delta x} \tag{9.1}$$

$$\text{with} \quad \Delta x = \Delta s / \cos\lambda \quad , \tag{9.2}$$

where the length Δs is the path length between the two intersection points of the reconstructed track with the inner and outer edges of the respective row in the projection onto the readout plane. To simplify the calculation, instead of the full arc length, the straight distance between these two points is used, as is sketched in figure 9.1. While this ignores the curvature of the track, the error is expected to be negligible due to the small height of the rows compared to the track curvature. This length is then adjusted for the dip angle λ of the track relative to the readout plane.

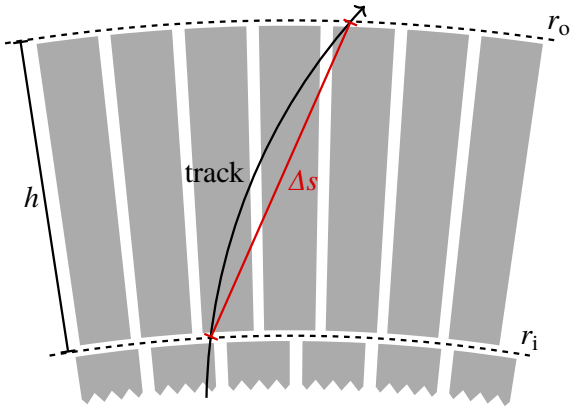

Figure 9.1.: The definition of the track segment length Δs. It is given by the straight distance between the intersection points of the projection of the track onto the readout plane with the inner and outer radius of the row, r_i and r_o, respectively. The curvature of the track is greatly exaggerated.

As explained in section 3.1, the statistical fluctuations of the primary ionisation density are expected to follow a Landau distribution, which does not have a well defined mean value due to a strong tail towards large values of $\Delta E/\Delta x$. A proven method to gain a robust estimate for the energy loss of a track from such a distribution is to discard a fixed fraction of the highest charge hits and calculate the mean of the truncated distribution [245]. The optimal fraction of samples to use in the calculation of the mean was determined to be ~75 %, as is shown in section 9.2. Using this method the average energy loss $\mathrm{d}E/\mathrm{d}x = \langle \Delta E/\Delta x \rangle_{75}$ is calculated for each track, resulting in the distribution in figure 9.2a. A Gaussian fit in a range of $\pm 3\,\sigma$ around the mean of the distribution is performed. As can be seen in comparison with the fit, the distribution is not perfectly Gaussian but slightly skewed due to a small enhancement of the upper edge. Therefore, the resolution is determined not from the fit but from the RMS of the central 90 % (RMS_{90}) of the distribution. The RMS_{90} value is scaled such that for a perfect Gaussian distribution it is equal to the standard deviation. Since no absolute calibration of the charge measurement is available, the relative resolution as given by $\mathrm{RMS}_{90}/\mathrm{mean}$ is used in all following analyses.

As is shown in figure 9.2b, no significant dependence of the $\mathrm{d}E/\mathrm{d}x$ resolution on the drift distance, e.g. as could be expected from electron attachment, can be observed. This allows to use the average of the individual measurements as a more accurate estimate of the resolution. This average value is calculated to be $\sigma_{\mathrm{d}E/\mathrm{d}x} = (8.95 \pm 0.02)$ %, where the uncertainty is the standard error of the weighted mean of the individual measurements. The standard deviation of these measurements of 0.14 % can be interpreted as an additional systematic uncertainty.

9.1.1. Hit Selection

To avoid biases on the $\mathrm{d}E/\mathrm{d}x$ measurement, hits that are expected to have a biased measurement of the charge are excluded from the calculation. The best example are hits that contain a dead readout channel, causing part of the arriving electron cloud to be lost. The same goes

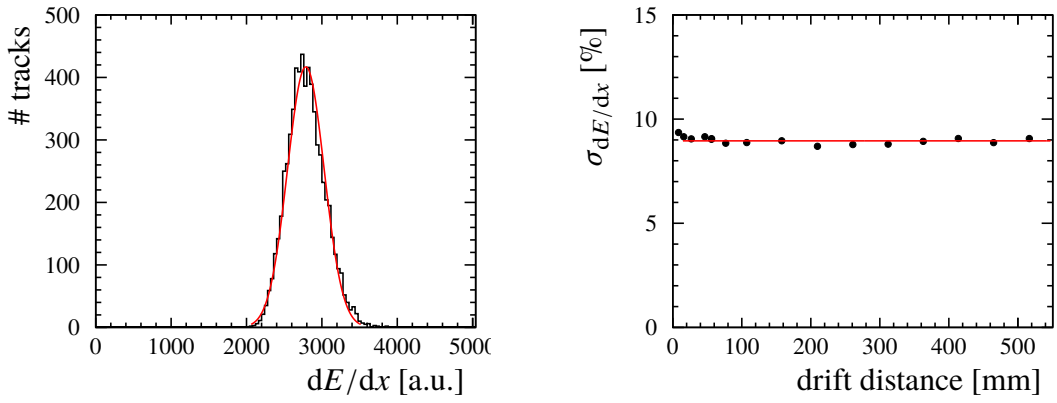

(a) dE/dx distribution. **(b)** Drift distance dependence.

Figure 9.2.: dE/dx measurement with the large TPC prototype. (a) The distribution of the dE/dx values from all tracks in one measurement, which is used to determine the dE/dx resolution. (b) The dependence of the dE/dx resolution on the drift distance. The horizontal line marks the weighted average of the measurements.

for hits directly next to a dead channel, since here it is unknown how much charge ended up on the dead pad. Due to faulty connections of some of the readout cables in the prototype setup, 15 pad rows had too many dead channels in the path of the beam to produce a significant amount of valid hits. Since such an issue would not be present in the final system, these rows are excluded from the analysis before any of the following cuts, reducing the maximum possible number of viable hits from 84 to 69. This number is used for the calculation of the presented cut efficiencies. Outside of the excluded rows, in total 2 % of hits are affected by dead channels.

Events with more than one reconstructed track are excluded from this analysis. However, the data may still contain remnants of unresolved tracks and in the worst case unresolved overlapping hits. These double hits contain charge from two tracks and thus must either be separated or excluded. Therefore both the pulse and the hit finding algorithm try to identify double hits. The pulse reconstruction algorithm searches for double peak structures in the pulse shapes, which indicate two hits in close vicinity in the drift direction. While the pulse finder can attempt to separate these pulses, the resulting estimate of the charge is questionable since the shaper may react in unforeseen ways to the irregular signal shape. The hit finding algorithm checks for double hits in the drift direction as well as the transverse plane. In the drift direction, hits are tagged as potential double hits if any pad contains more than one pulse within the allowed window of arrival time. In the transverse plane, double hit candidates are identified by looking for a local minimum in the charge distribution between adjacent pads. In total, about 5 % of hits are considered multi hit candidates by either of the algorithms.

Due to the field distortions at the module edge a fraction of the drifting electrons are deflected onto the frame of the GEM or into the gap between modules. From simulation studies presented in ref. [169] a charge loss of up to ~20 % on row 0 and ~40 % on row 27

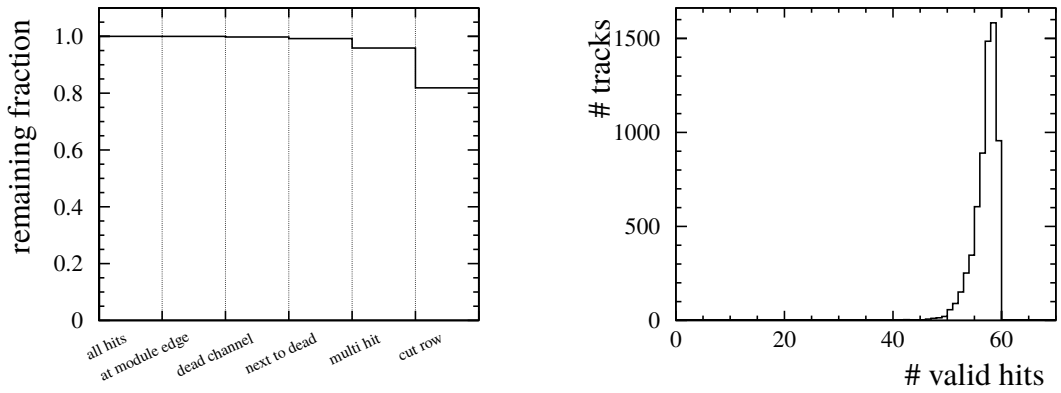

(a) Cumulative cut efficiency.

(b) Number of valid hits.

Figure 9.3.: The effect of the hit quality cuts. (a) The efficiency of the cuts if applied successively. (b) The distribution of the resulting number of valid hits on a track after all cuts.

could be expected. For the row numbering scheme see section 4.1. In figure 9.8b on page 144 the average measured charge corrected for the local inclination of the track on each row is shown. It is visible, that the actual losses are smaller than predicted with only ~20 % on row 27 and no visible loss on row 0. The difference might result from the higher potential used on the field shaping wire during the beam test compared to the simulation. Also visible is an apparent reduction of the charge on rows 13 and 14, the two rows next to the central azimuthal strut of the GEM frame. The causes for this are different for the two rows. On the one hand, the bar partially overlaps with row 14, reducing the effective row height, which is not reflected in the geometry description. On the other hand, for technical reasons the pitch of row 13 in the geometry description is slightly larger than the actual physical height of this row. In both cases the result is an overestimated length of the track segment. As is shown in section 9.3, these effects, actual charge loss at the module edges and erroneous row height, can be recovered through calibration of the charge on each row. However, since the channel calibration method in section 9.3.1 is strongly affected by the vicinity of the ceramic frames, hits on the four rows next to the frame are excluded from all $\mathrm{d}E/\mathrm{d}x$ calculations to make the results comparable between the correction methods. This is also the reason no attempt was made to adjust the geometry description to account for rows 13 and 14. In principle the same issue arises for hits at the ends and in the centre of each row, next to the radial struts of the GEM frames. However, the beam was positioned such that there are almost no hits at these locations.

Figure 9.3a shows the cumulative efficiency of the successive application of each cut for a representative run. The final efficiency of all cuts combined is about 0.82. As can be seen in the distribution in figure 9.3b, after the cuts on average 56.5 hits per track are viable for the $\mathrm{d}E/\mathrm{d}x$ calculation, with a standard deviation of 2.3 hits. If the four rows at the edges and next to the central azimuthal bar of each module can be recovered as described above, the total efficiency is increased to ~0.95.

9.2. Comparison of different Estimators

As described in section 9.1, due to the shape of the distribution of $\Delta E/\Delta x$, shown in figure 9.4a, its mean is strongly influenced by the tail towards large values and may not even be well defined, as in the case of a Landau distribution. Therefore, the resolution depends on the method used to estimate the average $\mathrm{d}E/\mathrm{d}x$ value of a track from the individual samples. A widely used approach to gain a robust value is to calculate the mean of a truncated distribution, ignoring fixed fractions of the hits with the highest and lowest charge [245, 246]. The optimal fractions of samples to reject in the calculation of the mean need to be determined experimentally. A different approach, which was adopted for the drift chamber of the H1 experiment at HERA [247], is to apply a transformation to the measured values of $\Delta E/\Delta x$ that results in a more well behaved distribution. The transformation that was found to produce the best results is

$$f(\Delta E/\Delta x) = \frac{1}{\sqrt{\Delta E/\Delta x}} \quad . \tag{9.3}$$

As can be seen in figure 9.4b, the resulting distribution is much narrower than the original one, since the tail is compressed into a shoulder on the rising edge. The effect of this shoulder may be further reduced by applying a truncation before the transformation. The inverse transformation is applied to the average calculated for each track to determine the resolution.

With the increase in available computing power it has become feasible to perform a maximum-likelihood fit of the expected distribution to the measured samples of $\Delta E/\Delta x$. This of course requires knowledge of the shape of the expected distribution [124]. As can be seen in figure 9.4a, the measured distribution diverges from the Landau shape expected from the fluctuations of the primary ionisation [138]. The Landau distribution is still a sensible description of the measured distribution but it overestimates the tail. A similarly good match to the core of the distribution is found in the log-normal distribution but this strongly underestimates the tail seen in the measurement. As shown in figure 9.4b, the distribution

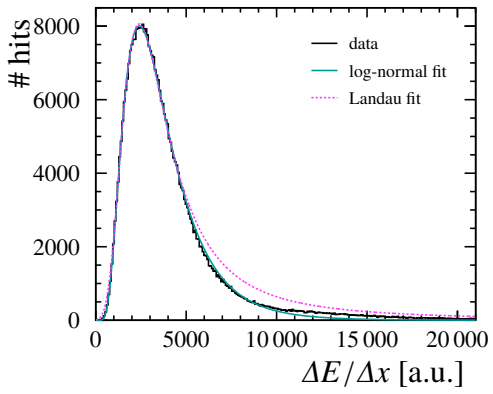

(a) Sample value distribution.

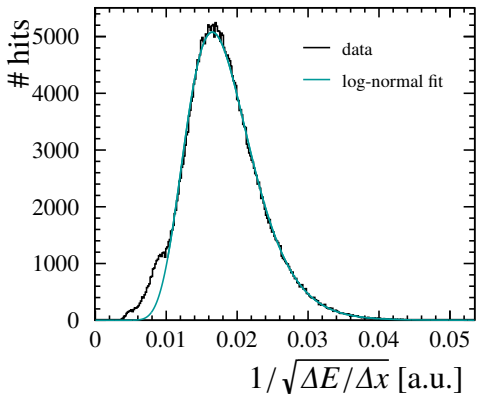

(b) Transformed distribution.

Figure 9.4.: The distribution of the measured $\Delta E/\Delta x$ sample values. (a) The distribution directly as measured. (b) The distribution under the transformation (9.3).

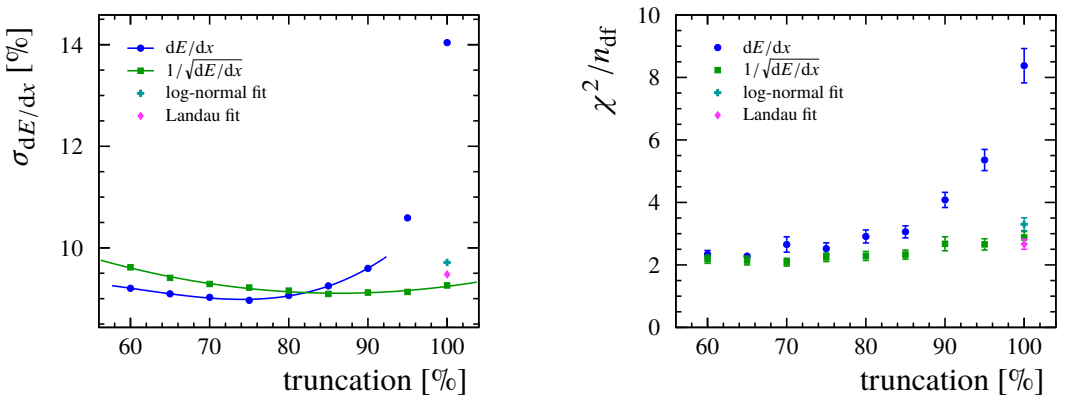

(a) $\mathrm{d}E/\mathrm{d}x$ resolution.

(b) Gaussian fit χ^2/n_{df}.

Figure 9.5.: Comparison of the different $\mathrm{d}E/\mathrm{d}x$ calculation methods. (a) The achievable resolution with each method. The solid lines represent polynomial fits of third order, used to determine the location and value of the minimum. (b) The χ^2/n_{df} of a Gaussian fit to the $\mathrm{d}E/\mathrm{d}x$ distribution.

transformed under equation (9.3) is equally well described by a log-normal distribution. While neither the Landau nor the log-normal distribution describe the data perfectly, they are close enough to test the general concept.

The different approaches introduced above are applied to the beam test data to determine the method that achieves the best $\mathrm{d}E/\mathrm{d}x$ resolution. For the first two methods, the traditional truncated mean and the truncated mean under the transformation (9.3), this includes optimising the fractions of samples to reject at the edges of the distribution. Truncation at the low charge edge is found to only deteriorate the resolution. Therefore, truncation is only performed at the high charge edge. The results for various fractions of samples remaining in the distribution are shown in figure 9.5, split in (a) the resulting resolution and (b) the χ^2 value per degree of freedom of a Gaussian fit to the $\mathrm{d}E/\mathrm{d}x$ distribution. The latter can be seen as a measure of potential biases on the $\mathrm{d}E/\mathrm{d}x$ measurement that are not accounted for by the determined resolution.

The truncated mean shows a shallow minimum of the $\mathrm{d}E/\mathrm{d}x$ resolution at a fraction of ~75 % of samples used for the calculation. As can be seen in figure 9.5a, this also marks the best resolution gained by any of the methods. Therefore, this method is used for all other results presented in this chapter. For the transformed data the best achievable resolution is slightly worse at an optimal truncation fraction of ~90 %. For both methods the Gaussian fit reaches $\chi^2/n_{\mathrm{df}} \approx 2$ at these fractions and does not improve for stronger truncation. As visible in figure 9.2a on page 137, this deviation from the optimal value of $\chi^2/n_{\mathrm{df}} = 1$ is caused by a slight asymmetry of the distribution, due to an enhancement of the falling edge.

The best result with the maximum-likelihood method is achieved using the Landau distribution but the resolution is again slightly worse than either of the truncation methods. The presented log-normal fit is performed on the transformed distribution, since the result using the untransformed distribution is much worse. This is likely due to the bad description of

the tail of the distribution, which can bias the fit significantly. In the transformed distribution the samples making up the tail are confined to a narrow interval, reducing the possible impact on the positional parameter of the fit, but it does not quite reach the resolution of the Landau fit. In general, the maximum-likelihood method requires about 10 times more computing time than the other options.

9.3. Charge and Gain Calibration

Identification of particles by their specific energy loss requires that systematic errors on the measurement of the energy loss be kept below ~1 % [248, 246]. Therefore, local variations of the charge measurement that lead to a dependence on the track direction must be known and corrected for with this precision. This requires a calibration of the gas amplification and the electronics gain for each readout channel.

Various methods can be applied to measure the local gas gain. Outside of the detector, i.e. after assembly of a module, X-ray sources with a known energy spectrum, e.g. iron-55 (^{55}Fe) or X-ray tubes, can be used to scan the readout area of each module. This allows to determine an absolute calibration factor for each position due to the known energy equivalent of the produced charge clusters. This method was used to test the gain homogeneity of the GEM readout chambers of the ALICE TPC upgrade [171]. The downside of this method is that it cannot easily account for changes of the gas amplification over the lifetime of a readout module. This can be overcome by an in-situ measurement of the gas gain in the assembled detector, which can be repeated at any point during the lifetime of the TPC. Here the challenge is to introduce clusters of known charge into the active volume of the TPC. A method that was developed for the ALEPH [249, 250] and DELPHI [251] experiments and has been applied successfully by the NA49 [252] and ALICE [160] experiments is to inject a small concentration of a radioactive isomer of Krypton-83 (^{83m2}Kr) into the counting gas. Unfortunately, none of these methods is applicable for the prototype setup used in the beam test. To start, the Krypton-83 method requires a complex system for the generation and injection of the ^{83m2}Kr, since the short half-life of the isomer prevents effective storage of the gas. It is further complicated by the precautions necessary for the use of a radioactive gas in the existing gas system, since it would prohibit the exhaust to stay open to the environment but require an equally complex system for recovery and filtering of the gas mixture. An ex-situ scan with an ^{55}Fe source, while in principle possible, was prevented by time constraints, since in absence of an automated setup the scan would have to be performed manually.

The calibration of the electronics gain is best achieved by an internal calibration circuit that induces pulses of predetermined amplitude into each channel, allowing to measure the response curve. Unfortunately, no such system is implemented in the present readout electronics.

Therefore, alternative methods for both calibrations were investigated. To calibrate the electronics of the ALICE TPC the cathode wire planes of the readout chambers could be pulsed, injecting a charge into the readout pads via the capacitive coupling [160]. In a similar way it is possible to pulse the GEM electrode facing the pad plane in the readout modules. This process is described in section 9.3.1. To calibrate the gas amplification, the data from

the beam test were used. Since in each measurement run the beam passes only over a narrow section of each pad row, a relative correction can be determined from the average charge measured on all rows, as explained in section 9.3.2. In section 9.3.3 the effect of these corrections on the $\mathrm{d}E/\mathrm{d}x$ measurement and in particular the resolution is discussed.

9.3.1. Electronics Gain Calibration

The current implementation of the ALTRO electronics used for our setup does not provide a channel calibration functionality but a similar effect is achieved by pulsing the common electrode of the GEM closest to the readout anode, which then induces a rather uniform signal into all readout channels. Unfortunately, this process was not foreseen in the design of the modules. Therefore the common electrodes of all GEMs are facing away from the pad plane but tests showed that enough signal is transmitted even when pulsing the electrode facing away from the pad plane. Additionally, the protection resistors in the HV lines of the GEMs prevent an effective pulsing through these lines and no bypass is implemented in the modules. On two of the three modules the hindering resistor could be bridged manually in the running setup by connecting the pulse generator via a probe to a soldering pad behind the resistor, thus enabling the measurement. On the third module the access to the pad was blocked by the data cables connecting the module to the readout electronics. A sketch of the electric scheme of the pulsing setup is shown in figure 9.6.

By inducing square pulses of various peak voltages a calibration curve from ADC counts to pulsing voltage can be measured for each channel. Due to the unknown capacitance C_{pad} no absolute calibration to charge is possible. The response curves are linear but include an offset that is not expected after pedestal subtraction. In channels up to three pads away (~3 mm) from the ceramic frames of the GEMs, much higher calibration factors are observed than in other channels. This is due to the high permittivity of the alumina ceramics compared to the gas, which increases the capacitive coupling between the GEM electrode

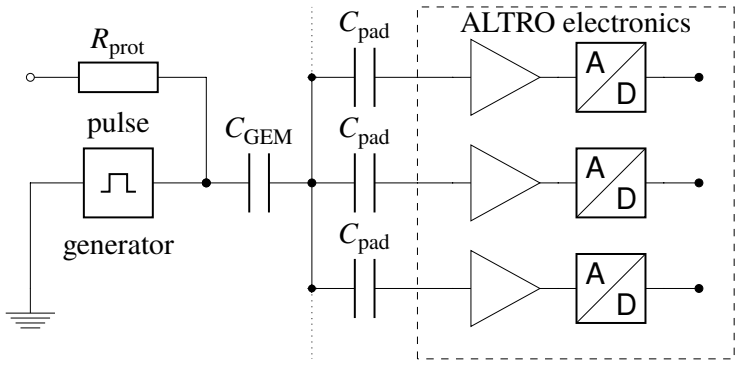

Figure 9.6.: Sketch of the electric scheme of the pulsing setup for the calibration of the electronics channels. C_{GEM} denotes the capacitance of the GEM and C_{pad} is the capacitance between the GEM electrode facing the pad plane and a single pad. R_{prot} is the bridged protection resistor, which is R_2 in figure 4.3 on page 53.

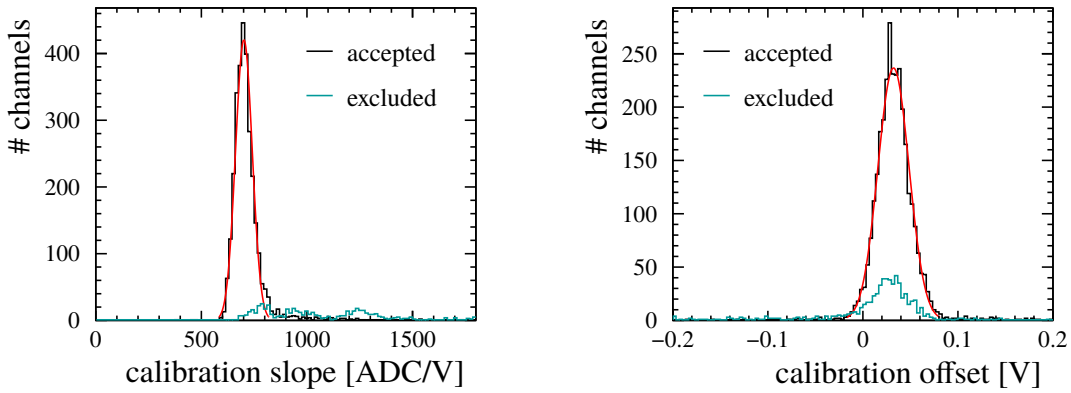

(a) Calibration slopes.

(b) Calibration offsets.

Figure 9.7.: Distributions of the channel calibration parameters as determined from the pulsing measurements. The red curves represent Gaussian fits to the data within a range of ± 3 standard deviations around the mean.

and the pads and leads to a higher charge being induced at the same voltage. Since the actual electron signals are not affected by the presence of the ceramics in this way, the calibration gives wrong results for these channels. Therefore all analyses in this chapter that make use of this calibration method exclude hits with pulses on pads adjacent to the ceramic frames, in particular all hits on rows 0, 13, 14 and 27 of each module. The distributions of slopes and offsets in the accepted and the excluded channels are shown in figure 9.7. The calibration factors in the accepted channels are distributed around a mean of $\langle s \rangle = (701.41 \pm 0.85)$ ADC/V and the average offset is $\langle \Delta q \rangle = (32.17 \pm 0.31)$ mV, both determined from Gaussian fits to the distributions. In addition a time calibration could be performed on this data but first studies showed that the variation between channels is small ($\mathcal{O}(\mathrm{ns})$) and not relevant for this analysis.

Using these calibration parameters the measured charge on a pad is corrected according to

$$q_i^{\mathrm{corr}} = \frac{q_i^{\mathrm{meas}}}{s_i} - \Delta q_i \ , \tag{9.4}$$

with the calibration factor s_i and offset Δq_i of the respective readout channel i. To be able to compare the calibrated measurements to the uncorrected data the resulting values are again multiplied by the average calibration factor $\langle s \rangle$:

$$q_i^{\mathrm{corr}} \to q_i^{\mathrm{corr}} \cdot \langle s \rangle \ . \tag{9.5}$$

Since the average offset is greater than zero, the mean of the $\mathrm{d}E/\mathrm{d}x$ distribution is shifted to lower values compared to the uncalibrated data. As the absolute width of the distribution is unaffected by the offset, this results in a worse relative $\mathrm{d}E/\mathrm{d}x$ resolution. Therefore for the comparison of the calibration methods in section 9.3.3 the data that is not calibrated in this way is shifted by the average offset $\langle \Delta q \rangle \cdot \langle s \rangle = (22.55 \pm 0.22)$ ADC to allow for a fair comparison. As is shown in figure 9.8a, this results in a consistent $\mathrm{d}E/\mathrm{d}x$ mean value between the calibrated and uncalibrated data.

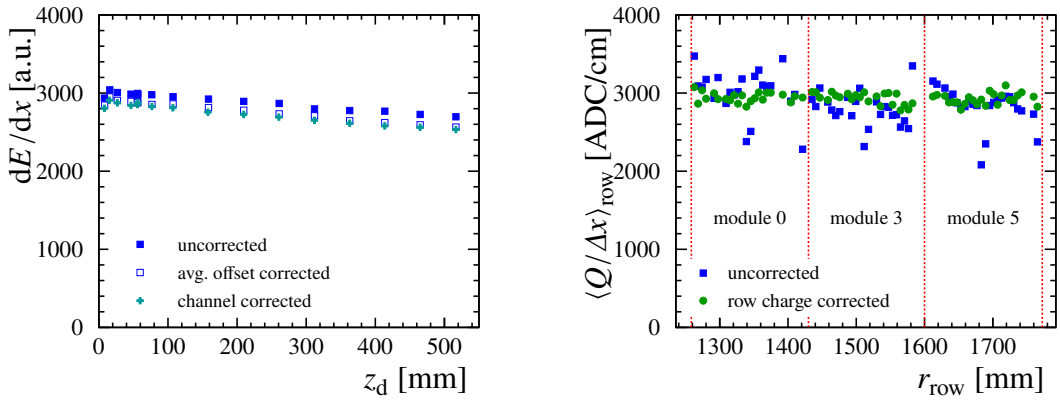

(a) Channel calibration offset.

(b) Row charge correction.

Figure 9.8.: (a) Comparison of the mean dE/dx value in the channel calibrated data to the uncorrected data with and without the average charge offset applied. (b) Comparison of the average charge of hits on each row between the uncorrected data and the data with the row charge correction applied. The vertical dashed lines mark the location of the module edges.

9.3.2. Average Row Charge Correction

To emulate the effect of a local gas gain calibration, a correction method was applied that uses the measured data to determine a correction factor for each row of the readout. Since the angular spread of the electron beam is quite small all tracks intersect each row in only a narrow region. This allows to reduce the normally required two dimensional correction map, i.e. one calibration factor per readout pad, to a one dimensional problem with one correction factor per readout row. To reduce biases, the correction factors are calculated only from a subset of 1000 events in each run and then applied to the remaining events. For straight tracks with a constant inclination relative to every row these correction factors could be calculated from the average measured charge of hits on each row $\langle Q \rangle_{\text{row}}$. Since the tracks bend in the magnetic field and the inclination changes from row to row, the measured charge needs to be corrected for angular effects. Therefore, the measured charge on each row is normalised to the length of the track segment over the respective row according to equation (9.1). The average of this quantity on each row $\langle Q/\Delta x \rangle_{\text{row}}$ is again normalised to the mean of all rows so that the correction is given by

$$Q_{\text{row}}^{\text{corr}} = Q_{\text{row}}^{\text{meas}} \cdot \frac{\frac{1}{N_{\text{rows}}} \sum_{i=0}^{N_{\text{rows}}} \langle Q/\Delta x \rangle_{\text{i}}}{\langle Q/\Delta x \rangle_{\text{row}}} \tag{9.6}$$

and the average correction factor over all rows is one.

In figure 9.8b the effect of this correction on the average charge on each row is shown. By eye, the fluctuations between the rows are greatly reduced. Quantitatively, the relative standard deviation of all rows before the correction is 9.5 % and afterwards it is 2.4 %. Ignoring the rows at the module edges and next to the central bar of the GEM frames, which in section 9.1.1 were found to measure a reduced charge, the corresponding values are 6.5 %

and 2.3 %. As visible in the figure, in particular these rows are brought back closer to the average. This shows that after a calibration of the local gain, samples in locations where some charge is expected to be lost, e.g. due to field distortions, can be recovered for the measurement of $\mathrm{d}E/\mathrm{d}x$. Also visible in the figure is a difference in the average charge measured on the individual modules, likely caused by slight differences in the HV supplied to the GEMs. The difference between the module with the highest average (*module 0*) and the lowest average (*module 3*) is reduced from 10.0 % without to 0.8 % with the correction. This shows the importance and the effectiveness of such a calibration to reduce regional biases like this.

9.3.3. Effect on the $\mathrm{d}E/\mathrm{d}x$ Measurement

To gauge the effect of the charge calibration on the $\mathrm{d}E/\mathrm{d}x$ measurement the same data were processed in total four times. Once with each of the two calibrations applied, once with neither, and once with both. As explained at the end of section 9.3.1, in the cases were the channel calibration is not used, still the average charge offset is corrected for a fair comparison. Figure 9.9a shows the $\mathrm{d}E/\mathrm{d}x$ resolution determined in several measurements at various drift distances for these four cases. There is no large difference visible between any of the calibration states, which is expected since the $\mathrm{d}E/\mathrm{d}x$ resolution is dominated by the fluctuations of the primary ionisation. The average improvement from the uncalibrated to the fully corrected data is (0.089 ± 0.078) % absolute, which is almost compatible with zero and anyway smaller than the systematic uncertainty of 0.14 % absolute due to the fluctuations of the resolution between the individual measurements.

On one hand, this shows the equal importance of a charge calibration against environmental effects, i.e. changes of temperature and pressure, which have a strong influence on

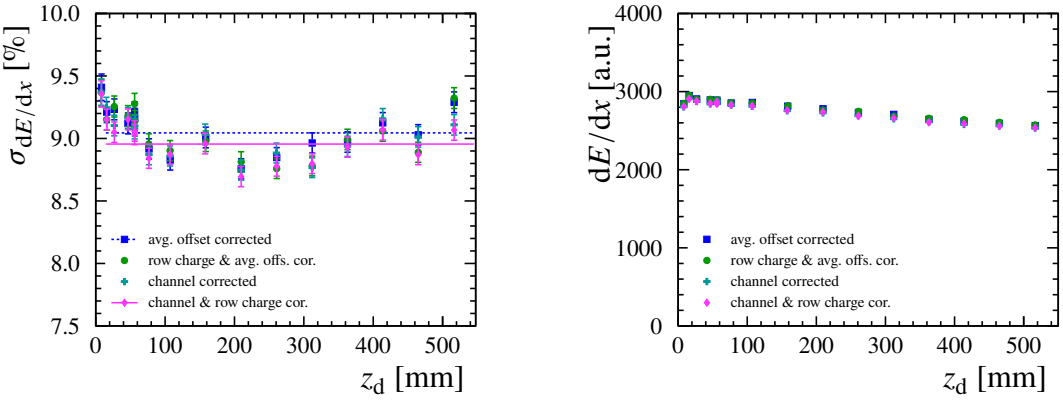

(a) $\mathrm{d}E/\mathrm{d}x$ resolution.

(b) $\mathrm{d}E/\mathrm{d}x$ mean.

Figure 9.9.: Comparison of the $\mathrm{d}E/\mathrm{d}x$ measurement with different levels of charge calibration. (a) The $\mathrm{d}E/\mathrm{d}x$ resolution. The horizontal dashed and solid lines mark the average resolution of the uncalibrated data and the fully corrected data, respectively. (b) The corresponding average energy loss.

the gas gain. As can be seen in figure 9.9b, the average measured energy loss changes significantly over the course of several measurement runs, since in the current setup no system for such a calibration is implemented. One possibility to continuously determine a correction for these effects are dedicated monitoring chambers that measure the gas gain under the same conditions as the main chamber. An example for the successful implementation of such a system are the TPCs in the near detector of the T2K experiment [193].

On the other hand, the rather small active area and number of channels in the large TPC prototype limit the probability of large local variations in the charge measurement. In a larger setup such as the ILD TPC these calibrations become important to avoid local or directional biases of the $\mathrm{d}E/\mathrm{d}x$ measurement and achieve the required precision as established in chapter 5.

9.4. Extrapolation to ILD Parameters

To extrapolate the $\mathrm{d}E/\mathrm{d}x$ resolution to the size of the ILD TPC with up to 220 hits one needs to determine the improvement with increasing number of samples N on a track. Experience with past experiments has shown that this dependence does not follow the naively expected $1/\sqrt{N}$ behaviour. Instead, power laws $\sigma_{\mathrm{d}E/\mathrm{d}x} = \sigma_0 \cdot N^{-k}$ with exponents $k < 0.5$ are found to describe the data best [253–255], e.g. $k = 0.43$ at the OPAL Jet Chamber [246].

To determine the exact dependence from the beam test data itself, a method is applied that combines recorded $\mathrm{d}E/\mathrm{d}x$ samples of real tracks to emulate the energy loss of pseudo tracks with an arbitrary number of samples. For each pseudo track, $\mathrm{d}E/\mathrm{d}x$ samples are randomly selected from the existing real tracks until the chosen number is reached. Due to the implementation of the analysis software the data is processed event by event. Therefore it is infeasible for this process to choose samples randomly from all tracks in one measurement. Instead they are taken from the track in one event at a time until each sample from this track is used exactly once. If the pseudo track is supposed to contain more samples than are available from the real track in the event, it is continued with samples from the next event. This is possible since the beam energy spectrum is reasonably narrow and at the beam energy the energy loss of electrons depends only weakly on their momentum. This process is repeated for various numbers of $\mathrm{d}E/\mathrm{d}x$ samples on the pseudo tracks until all samples associated to a real track in the measurement are used exactly once. In total 25 ensembles of pseudo tracks with 4 to 220 samples are created this way.

For each ensemble of pseudo tracks the $\mathrm{d}E/\mathrm{d}x$ resolution is determined as described in section 9.1. Similar to there, for each point the average resolution of all individual measurements at different drift distances is calculated. In figure 9.10 the resulting resolution for the various track lengths up to 220 samples is shown. A power-law fit finds an exponent of $k = 0.480 \pm 0.003$ and $\sigma_0 = (58.7 \pm 0.9)\,\%$ for the fluctuation of single samples, which is dominated by the fluctuations of the primary ionisation. Using these parameters the resolution is determined to be $\sigma_{\mathrm{d}E/\mathrm{d}x}(220) = (4.41 \pm 0.02)\,\%$ and $\sigma_{\mathrm{d}E/\mathrm{d}x}(165) = (5.06 \pm 0.02)\,\%$ for the large and small option of the ILD TPC, respectively. In both cases the standard deviation of the individual measurements, indicating an additional systematic uncertainty, is ~0.10 %.

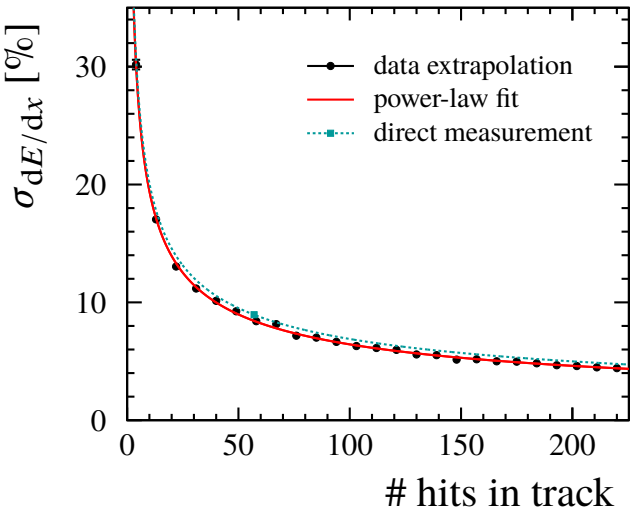

Figure 9.10.: The dE/dx resolution achieved with pseudo-tracks of different length, created as described in the text. The solid line describes a power-law fit. As a comparison the value directly measured with the large TPC prototype is included. The dashed curve represents a power law adjusted to fit this measurement as described in the text.

Calculating the resolution for the average track length in the LP setup from the fit parameters results in $\sigma_{dE/dx}(56.5) = (8.43 \pm 0.03)\,\%$, deviating significantly from the value of $\sigma_{dE/dx}(\mathrm{LP}) = (8.95 \pm 0.02)\,\%$ determined in section 9.1, even when considering an additional systematic uncertainty of 0.16 % absolute due to the spread of the number of hits in the LP data. This may hint at a bias caused by the pseudo-track method. A potential source of this bias are correlations between samples on one pad row in consecutive events, that are included in the same pseudo track. Under this assumption, pseudo tracks with a small number of samples should be least affected by this bias. Therefore the fitted value of σ_0 is assumed to be correct. Then, the bias on the extrapolation can be estimated by adjusting the exponent k so that the power law matches the measurement with the large TPC prototype. This results in $k = 0.465 \pm 0.004$ and a resolution of $\sigma'_{dE/dx}(220) = (4.77 \pm 0.03)\,\%$ and $\sigma'_{dE/dx}(165) = (5.46 \pm 0.03)\,\%$ for the large and small ILD TPC, respectively. The adjusted power law is displayed in figure 9.10 as the dashed curve.

In either of the cases above, perfect efficiency of the TPC is assumed but as detailed in section 9.1.1 the number of available samples on real tracks is reduced by hit quality cuts. As is shown in section 9.3.2, hits at the edges and next to the ceramic frames of the modules can be recovered after calibration. Therefore the cut that removes hits on these rows can be ignored here. From figure 9.3a on page 138 it can be seen that this leaves an inefficiency of ~5 % from the remaining cuts, mostly due to multi-hit candidates. Taking this into account and ignoring the potential bias, the dE/dx resolution for the large and small option of the ILD TPC is increased to $\sigma_{dE/dx}(0.95 \times 220) = (4.52 \pm 0.02)\,\%$ and $\sigma_{dE/dx}(0.95 \times 165) = (5.19 \pm 0.02)\,\%$, respectively.

This shows that the expectation of a dE/dx resolution of 5 % stated in ref. [105] can be

fulfilled with the GEM modules in the default large option of the ILD. Also with the small option of the ILD that value is exceeded only slightly.

9.5. Summary

A procedure was established to determine the resolution of the specific energy loss measurement for the large TPC prototype setup. To this effect the optimal $\mathrm{d}E/\mathrm{d}x$ estimator was determined to be a truncated mean calculated on a fraction of 75 % of the smallest charge samples. Estimators based on a maximum-likelihood fit of the charge spectrum were found to give slightly worse resolution at a much higher computing cost. However, with further investigation these methods may still be improved. Furthermore, two methods for a calibration of the charge measurement in the prototype setup were successfully implemented, which are a prerequisite for avoiding directional biases caused by local deviations of the gas gain or response of the electronics. Finally, the data was extrapolated to estimate the $\mathrm{d}E/\mathrm{d}x$ resolution achievable with the ILD TPC, showing that the expected value of 5 % can be reached.

10. Summary of Part I

In this part of this work the design and production procedure for the GEM readout modules were reviewed and revised. In particular the method for gluing and mounting the GEMs on the ceramic frames was improved. To this end the parameters for application of the glue were optimised. Furthermore a new tool was commissioned that was designed to make the mounting process more accurate and reproducible. To assess the quality of the tool assisted GEM mounting procedure, the deflections of several mounted GEMs were measured. These measurements show that the new tool assisted procedure reduces the average size of the deflections by a factor of 2.8 compared to the previously used method. Additionally, a more consistent flatness and improved repeatability is observed. Parametrised calculations of the effective gas gain in triple-GEM stacks show a corresponding reduction of the gain fluctuations across the area of the GEMs. The calculations also revealed that the impact of the GEM deflections on the gain stability depends on the gas mixture. With an RMS_{90} of 3.15 % the fluctuations in T2K gas are much larger than the other two tested mixtures, P5 and TDR gas with 0.92 % and 0.69 %, respectively. Additionally, the calculations indicate that the introduction of a strong magnetic field can have a large negative impact on the gain uniformity.

To assess the impact of the frame geometry on the deflections of the GEM foil, deflection measurements with dummies of four different frame geometries were performed. Additionally, mechanical simulations were carried out to investigate the distortions of the different frame geometries under external loads and internal stresses. The options included the existing frame design with 2×2 cells, a 1×4 design without a central radial strut, as well as a 2×3 and a 3×3 design with additional struts. The measurements reveal only little difference between the four geometries. The simulations show that the current design is already close to optimal in terms of mechanical rigidity.

Using the new production method a set of three modules was build and tested at the DESY II Test Beam Facility. The resulting data was then compared to existing data from a previous beam test, using several observables related to the spatial resolution. Good agreement between both data sets was found for the drift velocity and the measured charge, i.e. the gas amplification. Small differences were found in the width of the PRF, the average length of the charge pulses as well as the transverse point resolution. Various influences on these observables were investigated and subsequently excluded as possible causes, including the gas quality, environmental conditions and field settings as well as the angle of the beam relative to the detector and the noise of the electronics. Since no underlying cause could be determined conclusively, the pulse thresholds were adjusted according to the observed difference in the signal length. This resulted in a very good agreement of the transverse resolution. However, it did not resolve the difference in the PRF nor does it provide an explanation for the observed discrepancies. The narrower PRF and shorter signal length in

the new data suggest a lower transverse and longitudinal diffusion of the drifting electrons, respectively. Therefore it can be hypothesised that the cause may be the more homogeneous electric fields due to the less distorted GEMs used in the new setup. This hypothesis could not be verified with the available data. In future, a dedicated study could provide valuable insight in the performance impact of the flatness of GEMs. The results of the resolution measurement were extrapolated to the size and conditions of the ILD TPC. It was found that the defined goals can be achieved if a high gas quality is ensured, confirming the results in ref. [223].

Finally a procedure was established to determine the resolution of the specific energy loss measurement at ILD using the large TPC prototype setup. In the absence of an in-situ charge calibration method for the prototype setup, two procedures for a relative calibration were successfully implemented. While one method uses the beam test data to determine the calibration, the other relies on signals induced by pulsing the lowest GEM in each module stack. The optimal $\mathrm{d}E/\mathrm{d}x$ estimator was determined to be a truncated mean calculated on a fraction of 75 % of the smallest charge samples, reaching a relative resolution of $8.95 \pm 0.02 \pm 0.14$ % with the LP. Estimators based on a maximum-likelihood fit of the charge spectrum were found to give slightly worse resolution at a much higher computing cost. However, the analytical functions used to fit the charge spectrum do not describe it perfectly. Thus, with further investigations these methods may be improved. Lastly a method was developed to extrapolate the data from the prototype to the ILD TPC. The results show that the $\mathrm{d}E/\mathrm{d}x$ resolution goal of 5 % can be well achieved with the large ILD model but would be exceeded slightly with the small ILD model.

Part II.

Measurement of Light Quark Branching Fractions of the Z at the ILC

11. Introduction

The method used in this work was originally proposed in ref. [256] to determine the branching fractions of the Z into individual light quark flavours using the experiments at the Large Electron-Positron Collider (LEP). Using a data set of $4.3 \cdot 10^6$ hadronic Z decays collected at the OPAL experiment, the branching fraction into d or s quarks $R_{\mathrm{d,s}}$ was determined to a total relative precision $\delta_{R_{\mathrm{d,s}}}/R_{\mathrm{d,s}} \approx 6\,\%$ [257], with about equal contributions from statistical and systematic uncertainties. With the intended data set of the ILC at 250 GeV containing about $120 \cdot 10^6$ $\mathrm{e^+e^-} \to q\bar{q}$ events a drastic improvement in the statistical precision could be expected. In addition, advances in detector technologies and design for the ILD may help to make better use of the data set by increasing efficiencies and reducing systematic uncertainties. The analysis presented here is intended to explore the possible improvement and discuss the necessary reduction of systematic uncertainties.

11.1. Motivation

Within the Standard Model of particle physics, introduced in chapter 1, the interactions of the fermions via the strong and electroweak forces are supposed to be universal for all three generations except for effects resulting from the differences in mass. For leptons the universality has been confirmed to high precision for both charged and neutral electroweak currents [18]. The flavour universality of the strong interaction has been tested to a precision of a few percent for b quarks, c quarks and inclusive light quark samples and to $\mathcal{O}(10\,\%)$ for the individual light flavours [258–260]. The electroweak couplings have been precisely measured for the heavy b and c quarks [18]. The measurement in ref. [257] quoted above represents the precision achieved for the individual couplings of the light quarks to the Z. Therefore, it is desirable to reach a higher precision also here to further test the flavour universality of the gauge couplings.

The approach presented in ref. [256] tries to minimise the dependence on the specifics of any models of the hadronisation process in the identification of the individual quark flavours. Since the hadronisation process is non-perturbative, one has to make assumptions on how to parametrise the production of hadrons. As the parameters of those models do not follow from basic principles of QCD, they are subject to significant uncertainties. To reduce these uncertainties, a variation of this method was explored in ref. [261]. While this approach is not followed here, the methods are similar enough that the results of this work may allow to estimate the possible reduction of uncertainties with the higher statistical power expected at ILC compared to LEP.

11.2. Method Overview

The basic observables intended to be measured in this analysis are the cross sections σ of the process $e^+e^- \to q\bar{q}$ for the individual light quark flavours q. In this work the analysis is performed at tree level, where this is equivalent to measuring the couplings of the quarks to the neutral electroweak gauge bosons γ and Z. The total cross section of the process depends on the centre-of-mass energy $\sqrt{s}$ and at tree level includes single photon and Z exchange, σ_γ and σ_Z, as well as the γ-Z interference term $\sigma_{\gamma Z}$ [18]:

$$\sigma_q^0(s) = \sigma_Z(s) + \sigma_\gamma(s) + \sigma_{\gamma Z}(s) \tag{11.1}$$

$$\sigma_Z(s) = \frac{12\pi}{{M_Z}^2} \frac{\Gamma(e^+e^-)\Gamma(q\bar{q})}{{\Gamma_Z}^2} \frac{s{\Gamma_Z}^2}{\left(s - {M_Z}^2\right)^2 + s^2{\Gamma_Z}^2/{M_Z}^2} \tag{11.2}$$

$$\sigma_\gamma(s) = \frac{4\pi\left(\alpha(s)\right)^2}{s} {Q_q}^2 \tag{11.3}$$

$$\sigma_{\gamma Z}(s) = -2\sqrt{2}\alpha(s)\, Q_q G_F \mathcal{G}_V^e \mathcal{G}_V^q \frac{\left(s - {M_Z}^2\right){M_Z}^2}{\left(s - {M_Z}^2\right)^2 + s^2{\Gamma_Z}^2/{M_Z}^2} \ . \tag{11.4}$$

At LEP corrections for initial-state radiation (ISR) were included by convoluting equation (11.1) over a *Radiator Function* [18] $H(s, s')$:

$$\sigma_q(s) = \int H(s, s')\, \sigma_q^0(s)\, \mathrm{d}s' \ , \tag{11.5}$$

where now $\sqrt{s}$ is the total collision energy and $\sqrt{s'}$ is the effective centre-of-mass energy after ISR. This analysis uses data with $\sqrt{s} = 250\,\mathrm{GeV}$ where effects due to ISR are much larger than at LEP, in particular due to the radiative return to the Z-pole, see section 12.2. To use these radiative return events, ISR must be fully reconstructed, as is discussed in section 13.1. However, a similar correction may be necessary to account for the spectrum of $\sqrt{s'}$.

For collisions with an effective centre-of-mass energy $\sqrt{s'}$ equal to the mass of the Z, the interference term $\sigma_{\gamma Z}$ vanishes and σ_γ is negligible compared to σ_Z. Therefore, the partial decay widths $\Gamma_{q\bar{q}}$ of the Z can be measured directly from the total cross section:

$$\Gamma_{q\bar{q}} \coloneqq \Gamma(q\bar{q}) \propto \sigma_Z(M_Z) \approx \sigma_q^0(M_Z) \ . \tag{11.6}$$

For events away from the Z-pole, the beam polarisation at the ILC can be used to disentangle the three contributions σ_Z, σ_γ and $\sigma_{\gamma Z}$. Then $\Gamma_{q\bar{q}}$ can be determined from σ_Z as above. Corrections due to QED and QCD effects in the final state can be included in the definition of the $\Gamma_{q\bar{q}}$ [18]. However, for the measurement in ref. [257] the corrections were found to be negligible.

As the analysis only looks at the hadronic events, the hadronic branching fraction

$$R_q \coloneqq \frac{\sigma(Z \to q\bar{q})}{\sum_q \sigma(Z \to q\bar{q})} = \frac{\Gamma_{q\bar{q}}}{\Gamma_{\mathrm{had}}} = \frac{N_q}{N_{\mathrm{had}}} \tag{11.7}$$

will be used instead, where Γ_{had} is the total hadronic width of the Z, N_q is the number of Z decays into the quark flavour q and N_{had} is the total number of hadronic Z decays in the data. The main issue is then to efficiently identify events with the various quark flavours in the detector. When identifying b and c quarks, secondary vertices as lifetime tags for B and D hadrons and high p_{t} leptons from semileptonic decays of these hadrons allow for purities of more than 95 %, while keeping reasonable efficiencies [262]. Furthermore, the efficiency can be extracted from data with high precision by taking advantage of double tagged events, where a tag is present in both jets [263]. Using only single tags, the tagging efficiency ϵ has to be estimated from MC simulations, introducing systematic uncertainties that directly affect the precision of the measurement. In case of R_{b}

$$N_{\text{b}}^{\text{tag}} = \epsilon_{\text{b}} \cdot 2N_{\text{had}}R_{\text{b}} + N_{\text{bkg}} \quad , \tag{11.8}$$

where N_{bkg} denotes contributions from misidentified charm and light quark jets. Instead, the tagging efficiency can be inferred directly from the data by measuring the ratio of double-tagged events to single tags. Ignoring backgrounds, the expected numbers of single and double tags are

$$\begin{aligned} N_{\text{b}}^{\text{tag}} &= \epsilon_{\text{b}} \cdot 2N_{\text{had}}R_{\text{b}} \\ N_{\text{bb}}^{\text{tag}} &= (\epsilon_{\text{b}})^2 \cdot N_{\text{had}}R_{\text{b}} \end{aligned} \quad \Rightarrow \quad \epsilon_{\text{b}} = 2 \cdot \frac{N_{\text{bb}}^{\text{tag}}}{N_{\text{b}}^{\text{tag}}} \quad , \tag{11.9}$$

reducing the uncertainty on the efficiency to $\delta_{\epsilon_{\text{b}}}/\epsilon_{\text{b}} \sim \left(N_{\text{bb}}^{\text{tag}}\right)^{-1/2}$, as long as the backgrounds from c and light quarks are negligible.

To select a sample of light quarks with small backgrounds from c and b quarks, one needs a different tag. For this, one can use stable or long-lived particles with high scaled momentum

$$x_p = 2p_h/\sqrt{s'} > x_{\text{cut}} \quad , \tag{11.10}$$

where p_h is the momentum of the particle. This method efficiently rejects heavy quark jets, since even though B and D mesons are often produced as leading particles, their high decay multiplicity reduces the probability to obtain stable particles with high energy [264]. Other than for b and c quark tags, this tag selects an unknown mixture of all three light flavours. Therefore one has to disentangle the contributions of the individual flavours to determine their branching fractions This can be achieved by identifying different leading particle species, e.g. by their specific energy loss in the TPC of the ILD, see chapter 9 in part I of this work. In ref. [47] it has been shown that the leading particle in each jet is more likely to carry the primary (anti-)quark from the initial interaction, e.g. the leading particles in jets from s quarks are expected to preferentially be kaons, while u and d quarks preferentially produce leading pions. Unfortunately, also tags like these are in no way pure. For one, there is the ambiguity, which of the valence quarks of the leading hadron carries the flavour information of the primary quark. In addition, even up to very high scaled momenta there is a significant fraction of leading particles that carry no flavour information from the primary quark, either resulting from decays of unstable resonances or directly from the hadronisation process [256]. The solution is to identify a set of hadron species with various flavour contents. Following [257], for this analysis the chosen tagging hadrons are $\pi^{\pm}$, $\text{K}^{\pm}$, $\text{p}(\bar{\text{p}})$, K_{S}^0 and $\Lambda(\bar{\Lambda})$, with the respective flavour contents of (ud), (us), (uud), (ds) and (uds).

These hadrons were chosen since they can be separated by their $\mathrm{d}E/\mathrm{d}x$ ($\pi^{\pm}$, $\mathrm{K}^{\pm}$, $\mathrm{p}(\bar{\mathrm{p}})$) or identified by the invariant mass of their decay products ($\mathrm{K}^0_{\mathrm{S}}$, $\Lambda(\bar{\Lambda})$) with reasonable purities and efficiencies, as is described in section 13.3. The different sensitivities of these hadrons to the various quarks allow to disentangle the contributions of the individual quark flavours, using only basic assumptions on symmetries of the hadronisation process following from SU(2) isospin symmetry and flavour independence of QCD. Analogous to the case of heavy quarks, the tagging efficiencies can be obtained from double-tagged events.

The basic observables are the number of tags N_h by a particle of species h and the number of double-tagged events N_{hk}, with a tagging particle h in one jet and k in the other. The relation of the N_h and N_{hk} to the branching fractions R_q are given by the probabilities η^h_q for a jet with primary quark q to be tagged by a particle h:

$$\frac{N_h}{N_{\mathrm{had}}} = 2 \cdot \sum_q \eta^h_q R_q \quad , \tag{11.11}$$

$$\frac{N_{hk}}{N_{\mathrm{had}}} = (2 - \delta_{hk}) \cdot \sum_q \rho_{hk} \cdot \eta^h_q \eta^k_q R_q \quad , \tag{11.12}$$

where δ_{hk} is the Kronecker delta and the sums run over the quark flavours $q = \mathrm{d}, \mathrm{u}, \mathrm{s}, \mathrm{c}, \mathrm{b}$. The ρ_{hk} take into account potential correlations between the tagging probabilities in opposite event hemispheres. These can arise from gluon radiation and exchange between the primary quarks during fragmentation as well as from geometrical and kinematic constraints imposed by the detector or the reconstruction and analysis. For the chosen set of five tagging hadrons, equations (11.11) and (11.12) represent a system of 20 coupled, non-linear equations. This includes 5 equations for the single tags N_h, 5 for double tags with identical tagging particles in both hemispheres N_{hh} and 10 equations for the double tags with different tagging particles N_{hk}, $h \neq k$, since the two tags are in no particular order. As is explained in section 14.3, the branching fractions into heavy quarks, R_{b} and R_{c}, can be determined independently, as can the contributions of the heavy quarks to the individual tagged samples. This leaves three unknown R_q and fifteen unknown η^h_q. Since the unknowns appear in terms of the products $\eta^h_q R_q$ and $\eta^h_q \eta^k_q R_q$, which are correlated, the 20 measurements are not sufficient to solve the equation system. Therefore additional constraints are needed.

These constraints can be introduced by relations between the η^h_q, which can be derived from isospin symmetry under the assumption of flavour independence of QCD [256]. Alternatively or in addition, relations between the R_q can be assumed. Again adhering to ref. [257], the following hadronisation relations were assumed:

$$\eta^{\pi^{\pm}}_{\mathrm{d}} = \eta^{\pi^{\pm}}_{\mathrm{u}} \quad , \tag{11.13}$$

$$\eta^{\mathrm{K}^0(\bar{\mathrm{K}}^0)}_{\mathrm{d}} = \eta^{\mathrm{K}^{\pm}}_{\mathrm{u}} \quad , \tag{11.14}$$

$$\eta^{\mathrm{K}^0(\bar{\mathrm{K}}^0)}_{\mathrm{u}} = \eta^{\mathrm{K}^{\pm}}_{\mathrm{d}} \quad , \tag{11.15}$$

$$\eta^{\mathrm{K}^0(\bar{\mathrm{K}}^0)}_{\mathrm{s}} = \eta^{\mathrm{K}^{\pm}}_{\mathrm{s}} \quad , \tag{11.16}$$

$$\eta^{\Lambda(\bar{\Lambda})}_{\mathrm{u}} = \eta^{\Lambda(\bar{\Lambda})}_{\mathrm{d}} \quad . \tag{11.17}$$

Here $\mathrm{K}^0(\bar{\mathrm{K}}^0)$ implies the sum of K^0_S and K^0_L, assuming equal contributions. An additional constraint is taken from the overall normalisation $\sum_q R_q = 1$, which translates to

$$R_\mathrm{light} = R_\mathrm{d} + R_\mathrm{u} + R_\mathrm{s} = 1 - R_\mathrm{c} - R_\mathrm{b} \quad , \tag{11.18}$$

allowing to use independent measurements of R_c and R_b to constrain the sum of the light flavour branching fractions R_light. Alternatively, one can use the partial light flavour branching fractions

$$R'_q = \frac{R_q}{R_\mathrm{light}} \quad , \tag{11.19}$$

to minimise the influence of measurements of the heavy flavour fractions. With these constraints the solution of the equation system is still not unambiguous. Therefore, the additional assumption of $R_\mathrm{d} = R_\mathrm{s}$ is made, motivated by the weak isospin structure of the standard model. This also leaves R_u fully constraint by equation (11.18).

11.2.1. Hadronisation Symmetries and Relations

The hadronisation symmetry relations (11.13) to (11.17) are motivated by the assumption that the probability η_q^h for a primary quark q to form a meson (baryon) h is proportional to the probability $\gamma_{q'}$ ($\gamma_{q'q''}$) to create the respective additional quark(s) from the hadronisation sea. Since these quarks are created by gluon splitting into $q\bar{q}$ pairs, the probabilities for quarks and antiquarks are equal. Furthermore, the probabilities to produce several quarks are independent and can be factorised, i.e. $\gamma_{q'q''} = \gamma_{q'}\gamma_{q''}$. For a meson with flavour content (qq') and a minimum scaled momentum $x_p > x_\mathrm{cut}$ [256]

$$\eta_q^{h=(qq')}(x_\mathrm{cut}) = \gamma_{q'} \int_{x_\mathrm{cut}}^1 \mathrm{D}_q^h(x_p)\mathrm{d}x_p = \gamma_{q'}\mathcal{D}_q^h(x_\mathrm{cut}) \quad , \tag{11.20}$$

where $\mathrm{D}_q^h(x_p)$ describes the shape of the fragmentation function of the quark q. Flavour independence of QCD implies, that the $\gamma_{q'}$ are independent of the flavour of the primary quark q [265]. This directly leads to the relations (11.14) and (11.15). The other three relations additionally assume that $\gamma_\mathrm{d} = \gamma_\mathrm{u}$, which follows from SU(2) isospin symmetry and is supported by measurements of hadron production rates at LEP [266].

All these assumptions only hold for direct production of the hadrons from the primary quark. Additional sources of high momentum hadrons are indirect production via decays of unstable resonances containing the primary quark and non-primary hadronisation including only sea quarks. While the latter process is independent of the primary flavour, using the same argument of QCD flavour independence as above, the former process still maintains some relation to the primary quark. For instance a $\mathrm{K}^*(892)^0$ produced from a primary d quark and decaying via $\mathrm{K}^*(892)^0 \to \mathrm{K}^+\pi^-$ may either produce a leading π^-, which would be indistinguishable from direct production, or a leading K^+. This makes it possible that $\eta_\mathrm{d}^{\mathrm{K}^\pm} > 0$, which is not permitted in direct production. Both indirect and non-primary production may break the hadronisation relations as they introduce mixing of the various η_q^h. Additionally, they reduce the purities of the individual hadron tags, leading to a reduced discrimination power. As shown in ref. [256], models of the hadronisation process imply that

the contributions of these unwanted processes can be reduced by choosing tagging particles with high scaled momenta x_p.

12. Simulation and Data Samples

This chapter introduces the Monte Carlo data samples used for the presented analysis. To this end, first the simulation setup used for the generation of the samples is outlined in section 12.1. Afterwards an overview of the signal process and potential backgrounds is given in section 12.2. Finally in section 12.3 the actual data samples are described including a discussion of the event weighting.

12.1. Simulation Setup

The production of the central MC data samples for studies of the ILD concept can generally be divided into three steps. First the hard scattering process between electron and positron is calculated and the resulting particles in the final state are generated. Then, using a model of the detector as it is described in the DBD [105], the passage of the particles through the detector is simulated, i.e. the interactions with the detector material and potential decays of particles. In this step also the response of the detector is determined. Lastly the event is reconstructed using various pattern recognition algorithms. The following paragraphs give a brief overview of the software tools used. A more detailed description of the all steps can be found in ref. [105].

To generate the MC event samples the event generator WHIZARD in its version `1.95` [267, 268] was used. It implements a detailed description of effects related to the beam parameters at the ILC, such as beam energy spread, polarisation and beamstrahlung as well as initial-state radiation. WHIZARD employs the Optimized Matrix Element Generator O'Mega [269] to calculate partonic tree-level matrix elements. The program then integrates the matrix elements over phase space and evaluates distributions of observables to determine the total cross section and eventually generate the hard scattering events. The hadronisation and fragmentation of final states including quarks or gluons is internally delegated to PYTHIA `6.422` [270, 271]. The default settings of PYTHIA were shown to not describe the observations at LEP accurately – in particular the amounts of produced stable and long-lived hadrons were overestimated [272]. Therefore the settings were tuned by the LCC generator group based on data from the OPAL experiment at LEP-II.

The background due to $\gamma\gamma$ interactions described in section 2.1.6 was not generated for each event individually. Instead a number of $\gamma\gamma$ events corresponding to the expected amount of background was randomly selected from a pregenerated sample and overlaid with the hard e^+e^- scattering.

The following steps of simulating the interactions of all the resulting particles with the detector and the detector response were performed using MOKKA [273, 274], a GEANT4 [275, 276] based full simulation tool, which is provided as part of the ILC software framework

iLCSoft [224]. More components of iLCSoft are described in section 7.1. For the central data production `v01-16-04` of iLCSoft was used. While GEANT4 is a full simulation framework on its own, it can be called also directly from within MOKKA thanks to its modular structure. Here the main use of GEANT4 is the functionality to simulate the interaction of particles with matter, using its extensive library of physics models, and to determine the detector response. The program can handle detailed detector geometries including various materials and user-defined sensitive volumes. The geometry description is provided by MOKKA via a database. MOKKA also handles the data output in the LCIO format [277].

The digitised data are then reconstructed using the Marlin framework [228], see also section 7.1.3. Two main steps of reconstruction are performed, tracking, i.e. track finding and fitting, and calorimeter clustering. The tracking starts by applying a series of pattern recognition algorithms dedicated to the various subdetectors of the tracking system, i.e. TPC, silicon barrel detectors (VTX, SIT) and forward detectors (FTD). The track segments in the subdetectors are then combined and a global fit of all tracks is performed [278, 279]. Afterwards an algorithm dedicated to finding the charged decays of long-lived neutral particles is applied. This process is described in more detail in section 13.3.1. Calorimeter clustering is performed as part of the Pandora particle-flow algorithm (PFA) [114, 115], which combines the information from the tracking system with the hits in the highly granular calorimeters and aims to reconstruct each individual particle in an event. In an iterative procedure various algorithms are employed to cluster the calorimeter hits and associate clusters and tracks. Reclustering steps are performed in case cluster energy and track momentum are too dissimilar. The algorithm also implements a first step of particle identification that is briefly described in section 13.3. The output of the PFA are particle-flow objects (PFOs) that represent each reconstructed particle in the detector. Any further reconstruction and analysis is performed using the PFOs. Additional reconstruction steps that are specific to the presented analysis are discussed in chapter 13.

12.2. Signal Process and Backgrounds

The signal process for this analysis is $e^+e^- \to q\bar{q}$. The tree-level diagram is shown in figure 12.1a. At the full centre-of-mass energy of $\sqrt{s} = 250\,\text{GeV}$ the Z in the propagator is created off-shell. Here the contributions from photon and Z to the total cross section are about equal. However, the availability of data sets with different polarisation states of the electron and positron beams, see chapter 2, allows to disentangle the two fractions, due to the different chiral behaviour of the weak and electromagnetic couplings, see chapter 1. While this allows to extract the pure branching fractions of the Z at the full collision energy, this work concentrates on a subset of the data where the Z is created on-shell and the photon contribution is negligible. In many events one or both of the colliding e^+ and e^- in the initial state radiate photons, as shown in figure 12.1b, so-called initial-state radiation (ISR), reducing the effective centre-of-mass energy $\sqrt{s'}$. The energy spectrum of the ISR photons generally follows a power law with an exponent of about -0.9 [280, 281] but the process is greatly enhanced at an effective centre-of-mass energy equivalent to the mass of the Z, $\sqrt{s'} = M_Z$. This is called the radiative return to the Z and caused by the increased cross

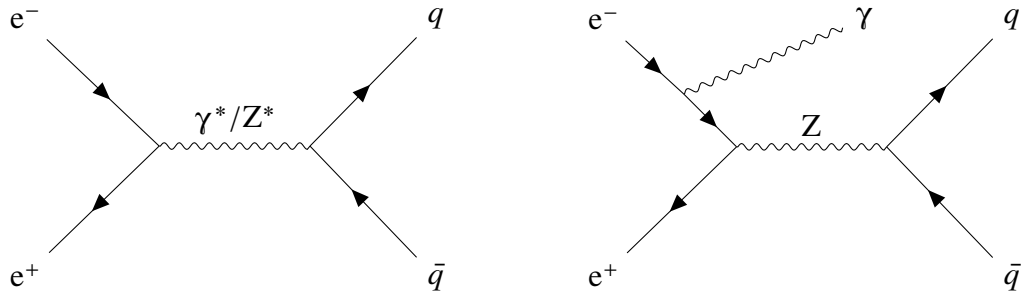

(a) $e^+e^- \to q\bar{q}$. **(b)** $e^+e^- \to q\bar{q}\gamma$.

Figure 12.1.: The Feynman diagrams of the signal process (a) at tree level with an off-shell propagator and (b) with an additional ISR photon. In this case $\sqrt{s'}$ is often reduced such that the propagator becomes an on-shell Z.

section due to the on-shell propagator. The process to reconstruct the momentum of the ISR photons and the resulting effective centre-of-mass energy is described in section 13.1.

A background to the signal process are hadronically decaying τ lepton pairs produced in the hard scattering, $e^+e^- \to \tau^+\tau^-$. If these events are not removed prior to the analysis they will be erroneously included in the total number of hadronic Z decays. Due to the low decay multiplicity of the $\tau^\pm$ the resulting hadrons will also rarely be rejected by the scaled momentum cut and therefore mostly be included in the tagged samples. Luckily the low multiplicity of these events also makes them easily distinguishable from real hadronic Z decays. In refs. [257, 261] a simple threshold cut of at least eight charged particles in an event was applied, reducing the background to negligible levels. Since the particle-flow approach reliably reconstructs also individual neutral particles, the cut could be adjusted accordingly for the ILD. A first estimate based on the distribution of the particle multiplicity of signal events in the MC suggests that a cut like this would reject about 2 % of the signal. Due to the small expected effect, at this first stage of the analysis no background samples were included and no corresponding cut was applied.

Another potential source of background are e^+e^- pairs and hadrons created in photon-photon interactions from beamstrahlung, as explained in section 2.1.6. While these particles generally have low transverse momenta, their total momentum may be large enough to be falsely identified as the leading particle in a jet. However, the forward direction of these particles allows to exclude most of them by simple fiducial cuts on the polar angle of the jets and the leading particle. Such cuts are applied anyway, as is described in section 14.1, to ensure that the events are well contained in the detector and to ensure optimal particle identification in the TPC. In the final sample of leading particles the contribution from these backgrounds is found to be negligible.

12.3. Data Samples

This analysis uses a sample of $2.86 \cdot 10^6$ $e^+e^- \to q\bar{q}$ events that were generated with a centre-of-mass energy of $\sqrt{s} = 250\,\text{GeV}$, including the effects of ISR and beam energy

Table 12.1.: The sharing of the total integrated luminosity L_{int} between the four polarisation settings and the corresponding cross sections $\sigma_{\mathcal{P}_{e^-,e^+}}$ for the process $e^+e^- \to q\bar{q}$ according to equation (12.1). The last two lines give the cross sections for fully polarised electrons and positrons, σ_{LR} and σ_{RL}, as calculated by the MC generator [283].

$\mathcal{P}_{e^-,e^+}$	L_{int} [fb^{-1}]	w_{LR}	w_{RL}	$\sigma_{\mathcal{P}_{e^-,e^+}}$ [fb]
$(-0.8, +0.3)$	900	0.585	0.035	78 047 $\pm$ 88
$(+0.8, -0.3)$	900	0.035	0.585	46 215 $\pm$ 60
$(-0.8, -0.3)$	100	0.315	0.065	45 315 $\pm$ 48
$(+0.8, +0.3)$	100	0.065	0.315	30 846 $\pm$ 34
$(-1, +1)$	—	1	0	129 149 $\pm$ 150
$(+1, -1)$	—	0	1	71 273 $\pm$ 102

spread (BES) as well as the background due to $\gamma\gamma$ interactions. The events were simulated and reconstructed using a fully detailed model of the ILD, using the process described in section 12.1. Of these, $1.54 \cdot 10^6$ events were generated using left-handed primary electrons and right-handed primary positrons, equivalent to a beam polarisation of $\mathcal{P}_{e^-,e^+} = (-1, +1)$. The remaining $1.32 \cdot 10^6$ events have the opposite polarisation of $\mathcal{P}_{e^-,e^+} = (+1, -1)$. Due to the vector boson, γ/Z, in the propagator, only the opposite-sign helicity interactions with $J = 1$ contribute to the signal process. As the beams at the ILC will not be fully polarised, the events need to be reweighted to reflect the actual polarisation. For an arbitrary beam polarisation, the cross section of a process mediated by s-channel vector boson exchange can be calculated according to ref. [282]

$$\begin{aligned}\sigma_{\mathcal{P}_{e^-,e^+}} &= \left(\frac{1-\mathcal{P}_{e^-}}{2}\right)\left(\frac{1+\mathcal{P}_{e^+}}{2}\right)\cdot\sigma_{\text{LR}} + \left(\frac{1+\mathcal{P}_{e^-}}{2}\right)\left(\frac{1-\mathcal{P}_{e^+}}{2}\right)\cdot\sigma_{\text{RL}} \\ &= w_{\text{LR}}\cdot\sigma_{\text{LR}} + w_{\text{RL}}\cdot\sigma_{\text{RL}}\ ,\end{aligned} \tag{12.1}$$

with the cross sections σ_{LR} and σ_{RL} for $\mathcal{P}_{e^-,e^+} = (-1, +1)$ and $(+1, -1)$, respectively. The nominal polarisations at the ILC are $\pm 80\,\%$ for electrons and $\pm 30\,\%$ for positrons [90, 84]. The corresponding cross sections of the signal process for the four possible polarisation combinations $\mathcal{P}_{e^-,e^+} = (-0.8, +0.3)$, $(+0.8, -0.3)$, $(-0.8, -0.3)$ and $(+0.8, +0.3)$ are given in table 12.1.

The running scenario introduced in chapter 2 foresees a total integrated luminosity of $L_{\text{int}} = 2000\,\text{fb}^{-1}$ at $\sqrt{s} = 250\,\text{GeV}$, shared between the four polarisation combinations as given in the table. To reflect this size of the expected real data set, the simulated data are scaled accordingly. The luminosity weights $w_{\text{LR},L}$ for simulated events with $\mathcal{P}_{e^-,e^+} = (-1, +1)$ needed for the individual polarisation combinations can be calculated as $w_{\text{LR},L} = w_{\text{LR}} \cdot \sigma_{\text{LR}} \cdot L_{\text{int}}(\mathcal{P})/N_{\text{LR,sim}}$, where $N_{\text{LR,sim}}$ is the number of simulated events, and analogous for $\mathcal{P}_{e^-,e^+} = (+1, -1)$. For the full data set, this results in total weights of 50.059 for events with $\mathcal{P}_{e^-,e^+} = (-1, +1)$ and 32.141 for $(+1, -1)$.

13. Additional Data Reconstruction

As detailed in chapter 12, the simulated data are subjected to a default reconstruction procedure during the data production. This process finishes at the level of individual particle candidates, with the Pandora PFA [114] combining information from all subdetector systems to gain the best estimate of the direction and momentum of each particle. Starting from there, additional reconstruction steps are necessary for the presented analysis. These steps are presented in this chapter, mostly following the order in which they are applied to the data. First, the treatment of photon radiation from the colliding particles is discussed in section 13.1. Then, the reconstruction of the jets formed by the primary quarks is explained in section 13.2. The last reconstruction step before the actual analysis concerns the identification of particle species. Two methods are applied for different groups of particles. The first method, which reconstructs long-lived neutral particles from their decay products, is actually part of the default reconstruction but due to its importance for this analysis, it is described in detail in section 13.3.1. The second method, presented in section 13.3.2, uses the specific energy loss measurement in the TPC to separate stable charged particles.

13.1. Treatment of Initial State Radiation

The following reconstruction and analysis steps rely on the knowledge of the effective centre-of-mass system and energy after beamstrahlung and initial-state radiation (ISR). Therefore, the momentum carried by the photons needs to be reconstructed. In some events one of the ISR photons is emitted within the acceptance of the detector. These photons can be identified if they are geometrically isolated from the hadronic activity. For such events the full kinematics can be reconstructed using only the well measured angular information of the two jets and the photon [284, 285] without relying on the measured energies, which have comparatively large uncertainties. Unfortunately ISR and beamstrahlung are preferably emitted under small angles relative to the momentum direction of the incoming beams. As is shown in figure 13.1a for ISR, this means that in a large fraction of events both photons are generated in the forward direction outside of the acceptance of the tracking system and can not be identified and reconstructed directly. Under these conditions the angular information is not enough to reconstruct the event kinematics unambiguously [286].

To resolve the ambiguity and recover this otherwise lost information, other analyses have successfully applied kinematic-fit methods [287, 288]. These deduce the best solution for the missing momentum using the precise knowledge of the centre-of-mass energy at an e^+e^- collider and the measured four-momenta of the jets. Additionally, constraints following from the conservation of energy and momentum or the event topology, e.g. invariant masses of intermediate resonances, are used. The performance of such an algorithm for the processes

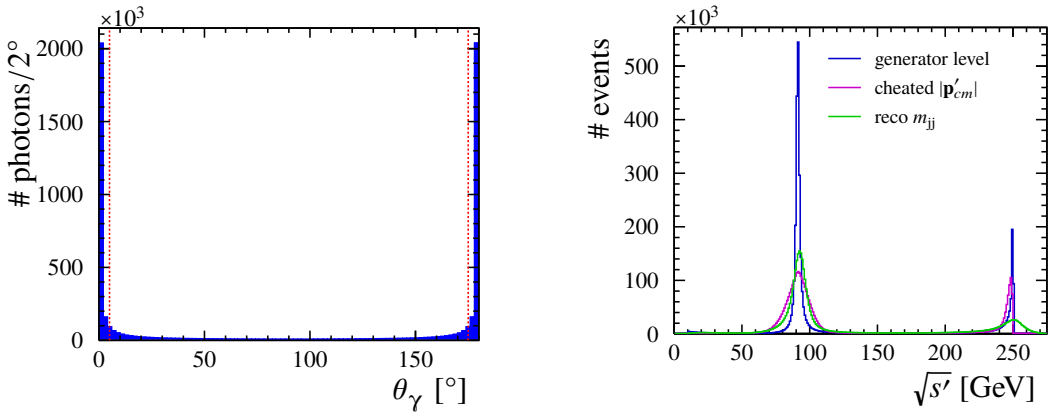

(a) ISR photon polar angle.

(b) Centre-of-mass energy.

Figure 13.1.: (a) The distribution of the polar angle θ_γ of the MC ISR photons peaks in the forward directions. The vertical dashed lines mark the edges of the tracker acceptance. (b) The effective centre-of-mass energy after ISR and beamstrahlung determined from MC truth (*generator level*), from the four-momentum of the centre of mass determined using the MC photons (*cheated* $|\mathbf{p}'_{\mathrm{cm}}|$) and from the reconstructed invariant di-jet mass m_{jj}.

$e^+e^- \to W^+W^-/ZZ \to$ hadrons at $\sqrt{s} = 500\,\mathrm{GeV}$ was investigated in ref. [287]. Using a set of constraints that would also be reasonable for the two-jet topology of $e^+e^- \to q\bar{q}$ a fraction of 87 % of good fits was achieved there. The photon momentum could be reconstructed with an RMS of 3.1 GeV, while the resolution of the invariant di-jet mass was improved by a factor of ~1.5 compared to a measurement without kinematic fit. Since the study cited above, the process was optimised further by using a better estimate of the uncertainties of the jet related input parameters [289].

As it was not in the scope of this work to adapt such an algorithm to the presented analysis, instead the four-momenta of the ISR photons are determined from MC information. Since beamstrahlung (BS) is not created as individual photons by the event generator but included as a reduced energy of the colliding electrons, its effect can not be separated from the beam energy spread (BES) of $\Delta E/E \lesssim 0.2\,\%$ [90], even in the Monte Carlo. Therefore only the combined effect of beamstrahlung and beam energy spread can be inferred from the total four-momentum of all MC particles in the final state. The combined four-momentum of the two possible ISR photons as well as BS and BES

$$\mathbf{p}_\gamma = \mathbf{p}_{\mathrm{ISR},1} + \mathbf{p}_{\mathrm{ISR},2} + \mathbf{p}_{\mathrm{BS+BES}} \quad , \tag{13.1}$$

serves as a starting point for the reconstruction of the effective centre-of-mass system. This momentum is smeared according to the determined resolution of the photon momentum in the kinematic fit in ref. [287]. By subtracting the smeared four-momentum of the photons $\mathbf{p}'_\gamma$ from the combined four-momentum of the colliding electrons $\mathbf{p}_{e^+e^-}$, the four-momentum of the effective centre-of-mass system

$$\mathbf{p}'_{\mathrm{cm}} = \mathbf{p}_{e^+e^-} - \mathbf{p}'_\gamma \tag{13.2}$$

is then determined. Here $\mathbf{p}_{e^+e^-} = (250;\, 1.75,\, 0,\, 0)\,\text{GeV}$ is assumed. The transverse momentum component results from the beam crossing angle of 14 mrad. Finally, a Lorentz boost from the lab system into the rest system of the effective centre of mass is calculated from $\mathbf{p}'_{\text{cm}}$ and applied to all PFOs. Likewise, all MC particles are boosted into the true effective centre-of-mass system.

The effective centre-of-mass energy $\sqrt{s'}$ after the photon emission on generator level and calculated from $\mathbf{p}'_{\text{cm}}$ is shown in figure 13.1b. The peak of the radiative return to the Z resonance – explained in section 12.2 – and the primary energy peak at $\sqrt{s'} = 250\,\text{GeV}$ are well visible in MC as well as in the mass associated with $\mathbf{p}'_{\text{cm}}$. Also shown is the invariant mass of the di-jet system m_{jj}, based on the jets defined in section 13.2. At the Z-return peak the true effective centre-of-mass energy is better estimated by the latter. This may indicate that the photon momentum resolution of the kinematic fit assumed above is an overestimate for these events. Therefore the di-jet mass is used in the following, which has the additional advantage of avoiding further use of MC information. As noted earlier, by applying an actual kinematic fit the di-jet-mass resolution can potentially be improved significantly. This would lead to a higher efficiency of the following cuts since fewer events migrate out of the intervals.

For the determination of the branching ratios of the Z boson in chapter 14, an event sample around the Z -return peak with $81.2\,\text{GeV} < m_{\text{jj}} < 101.2\,\text{GeV}$ is used. An average offset of about 1.3 GeV between the di-jet mass and the MC is observed in this sample and taken into account. Unweighted, the sample contains $1.79 \cdot 10^6$ events, corresponding to an efficiency of $(82.48 \pm 0.03)\,\%$ at a purity of $(98.36 \pm 0.01)\,\%$ compared to the same interval in MC. The efficiency here is defined as the number of correctly selected events on detector level divided by the number of selected events on generator level. The given errors result purely from the MC statistics. In a more detailed analysis systematic effects, e.g. due to differences between the real and simulated energy distributions, must also be considered. Potentially of interest is another sample around the full collision energy, i.e. restricted to events with soft or no ISR and $240\,\text{GeV} < m_{\text{jj}} < 260\,\text{GeV}$. With an efficiency of $(68.96 \pm 0.06)\,\%$ at $(91.27 \pm 0.05)\,\%$ purity this interval contains $0.40 \cdot 10^6$ events. The lower efficiency is caused by the larger di-jet-mass resolution of 5.9 GeV at 250 GeV compared to 3.5 GeV in the Z-return sample.

For the few events where an ISR photon is emitted within the acceptance of the detector, MC information is used to identify all related reconstructed particles. These are then excluded from the further reconstruction. This includes not only directly reconstructed photons but also any daughter particles, i.e. mostly electron-positron pairs created by pair production. Due to a known issue with the simulation of the LumiCAL [290] that was only fixed in later versions of iLCSoft [291], some ISR photons in the simulation are not correctly linked to the corresponding PFOs. This causes them to be included in the remaining analysis and also the calculation of the invariant-mass above. The corresponding events migrate to higher $\sqrt{s'}$, as is shown in figure B.1 on page 197. This effect degrades the purity of the sample at the full collision energy by $\mathcal{O}(1\,\%)$ while the efficiency of the Z-return sample is reduced by $\sim 1\,\%$. Since the effect is so small, no attempt is made to recover these events.

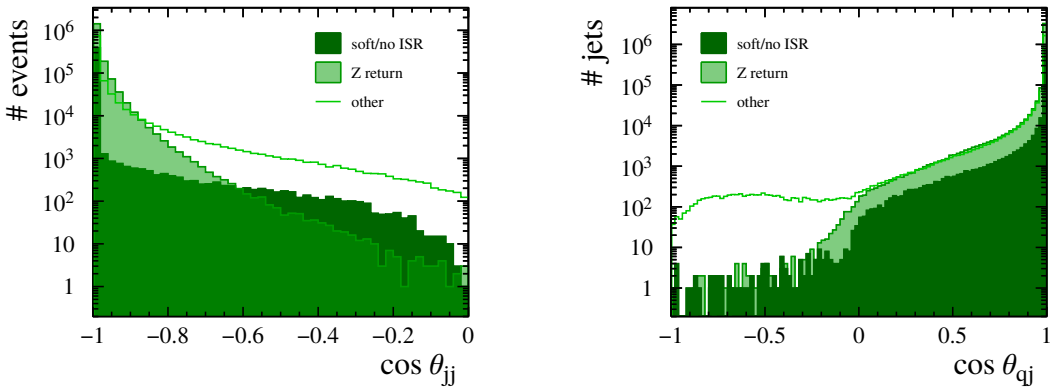

(a) Angle between reconstructed jets.

(b) Angle between quark and jet.

Figure 13.2.: Angular distributions of the reconstructed hemispheres in the lab frame for the two event samples defined in section 13.1. The *other* category includes events with a di-jet mass not contained in either of the two energy ranges. (a) The cosine of the opening angle between the two reconstructed hemispheres as defined in the text. (b) The cosine of the opening angle between the reconstructed hemispheres and the corresponding primary quarks in MC, as calculated in the reconstructed effective centre-of-mass system.

13.2. Jet Reconstruction

After the ISR is identified and the event is boosted into the new centre-of-mass system, the two jets are expected to be oriented back to back. Furthermore, the expected background from $\gamma\gamma \to$ hadrons is negligible for the beam parameters used in the simulation, cf. section 2.1.6 and table 2.1. This allows to forego more involved jet-finding algorithms in favour of the simpler approach of event hemispheres. For this the thrust axis of the event must be known [292]. The thrust axis is defined in the centre-of-mass system of the event as that line going through the centre of mass, for which the sum of the momentum vectors of all particles projected onto that axis is maximised. In the reconstruction it is calculated using the Tasso algorithm implemented in the *ThrustReconstruction* processor in iLCSoft. Each reconstructed particle is assigned to one hemisphere based on the projection of its momentum onto the thrust axis. One hemisphere contains all particles for which the projection has a positive sign and the other one contains all with a negative projection. As figure 13.2a shows, the opening angle between the reconstructed hemispheres θ_{jj}, defined by the directions of the total momentum of the respective constituent particles in the boosted reference frame, tends strongly towards 180° ($\cos\theta_{jj} \to -1$) in the two samples. This confirms the correctness of the Lorentz boost and the validity of the hemisphere approach. By construction no event exceeds $\cos\theta_{jj} = 0$.

On the generator level, MC jets are formed by applying a similar process to the MC particles as is done for the PFOs. While the MC information allows to trace back the decay chain of MC particles to the first colour neutral hadrons, these cannot be unambiguously linked to one of the primary quarks, due to gluon exchange and fragmentation in the hadronisation process. Instead, the primary hadrons are assigned to the quark for which the the projection

of their momentum onto the direction of the quark is positive. Since this is done in the MC centre-of-mass frame of the event, the quarks are perfectly back to back and the process is unambiguous. All subsequent decay products of the primary hadrons down to stable particles are then assigned to the same quark as their parent particle. To later be able to compare the generator and detector level results, the MC jets constructed this way are associated to the reconstructed hemispheres, again based on the projection of the corresponding primary quark momenta onto the reconstructed thrust axis. As figure 13.2b shows, the reconstructed hemispheres tend to be collinear to the primary quarks. In a small fraction of events the opening angle between a hemisphere and the corresponding primary quark is found to be larger than 90° ($\cos\theta_{\mathrm{qj}} < 0$). As can be seen in the figure, this mostly affects events that are not contained in the centre-of-mass energy range of either of the two event samples. This is mostly due to hadronic resonances at low effective centre-of-mass energy, which remove the correlation between the direction of the resulting decay products and the primary quarks. The few events remaining in the two selected energy samples should not affect the analysis.

13.3. Particle Identification

As noted in section 12.1, the Pandora PFA applied during the default reconstruction performs a first step of particle identification (PID). It uses the topology of the calorimeter response to distinguish photons, electrons, muons, charged hadrons and neutral hadrons. Photons (electrons) are distinguished from neutral (charged) hadrons by the shape of the showers in the calorimeters and the different fraction of energy deposited in the ECAL and HCAL. Photons and neutral hadrons are separated from their charged counterparts, electrons and charged hadrons, respectively, by the absence of a track associated to the calorimeter clusters. Muons are reconstructed by connecting a track in the muon system to a matching track-like deposit in the calorimeters. The charged decays of long-lived neutral particles (V^0) are reconstructed already on the track level, as the process does not require calorimeter information. The Pandora PFA matches them to the corresponding calorimeter clusters and replaces the four-momenta of the daughter particles with that of the parent. The V^0 finding algorithm and its performance are described in section 13.3.1.

The performance of the Pandora PFA and the PID algorithms in the following sections is only evaluated for the particles relevant to the analysis in chapter 14, i.e. the leading particles in each jet with a true scaled momentum $x_p > 0.5$. In addition to the momentum requirement, acceptance cuts as described in section 14.1 are applied. These cuts include the requirement of $|\cos\theta_{\mathrm{LP}}| < 0.8$ for the polar angle of the leading particle (LP) and $|\cos\theta_{\mathrm{j}}| < 0.95$ for the polar angle of the jet containing the corresponding LP.

After these cuts the charged hadron sample identified by the PFA contains about 99 % $\pi^{\pm}$, $\mathrm{K}^{\pm}$ and $\mathrm{p}(\bar{\mathrm{p}})$ on generator level. The remaining fraction comprises mostly heavier hadrons, mainly $\Xi^{\pm}$ and charged Σ baryons, as well as a smaller number of electrons and muons. The efficiency to correctly identify a leading $\pi^{\pm}$, $\mathrm{K}^{\pm}$ or $\mathrm{p}(\bar{\mathrm{p}})$ as a charged hadron is about 99 %. Normally, information on the specific energy loss in the TPC would be used to further distinguish between the charged hadrons, in particular $\pi^{\pm}$, $\mathrm{K}^{\pm}$ and $\mathrm{p}(\bar{\mathrm{p}})$. The expected $\mathrm{d}E/\mathrm{d}x$ PID performance of the ILD is described in detail in the IDR [87]. However, in version

v01-16-04 of iLCSoft, which was used for the simulation of the data samples, information on the energy loss was not stored and thus no real $\mathrm{d}E/\mathrm{d}x$ information is available. Therefore a toy Monte Carlo, which uses parametrised Bethe-Bloch curves of version v02-00-02 of iLCSoft, was implemented. This process and the achieved performance are described in section 13.3.2.

13.3.1. Long Lived Neutral Hadrons

This section describes the algorithm for the identification and reconstruction of the decays of long-lived neutral particles (V^0), i.e. K^0_S and $\Lambda(\bar{\Lambda})$. The same procedure is also used to find pair conversions of photons, since they show a similar topology. Due to the proper lifetimes of the K^0_S and $\Lambda(\bar{\Lambda})$, $\tau_{\mathrm{K}^0_\mathrm{S}} = (0.8954 \pm 0.0004) \cdot 10^{-10}\,\mathrm{s}$ ($c\tau \approx 27\,\mathrm{mm}$) and $\tau_\Lambda = (2.632 \pm 0.020) \cdot 10^{-10}\,\mathrm{s}$ ($c\tau \approx 79\,\mathrm{mm}$) respectively [18], their decay vertices are often significantly offset from the primary vertex. Similarly, since pair conversion of photons can only happen within the material of the detector, the corresponding vertices are only expected from the radius of the beam pipe ($r = 15\,\mathrm{mm}$) outwards.

The K^0_S preferentially decays via $\mathrm{K}^0_\mathrm{S} \to \pi^+\pi^-$ with about 69 % probability. In almost 31 % of cases it decays into two neutral pions instead. Similarly, the Λ decays via $\Lambda \to \mathrm{p}\pi^-$ for about 64 % of decays and for almost 36 % it produces a neutron and a π^0. For either particle, other decay modes have combined probabilities of $\mathcal{O}(0.1\,\%)$ [18]. As the reconstruction of the decay vertex requires the precise information from the tracking system, the neutral decays introduce a hard limit on the possible fraction of reconstructable decays. This does of course not apply to photon pair conversions, which can only produce charged particle pairs, almost exclusively $\mathrm{e}^+\mathrm{e}^-$.

The algorithm to reconstruct the charged decays is implemented in the *V0Finder* processor in iLCSoft [225]. All cut values below correspond to the default settings for the central production of the data set described in chapter 12. The algorithm goes through every combination of two tracks with opposite charge in the event. The combination is discarded if the distance of closest approach between two fitted track helices is larger than 1.5 mm or the PCA of the higher momentum track to the other one has a distance to the beam axis smaller than 5 mm. The latter cut excludes the region around the IP where secondary vertices from heavy quark decays are expected. This is done to give priority to vertexing and heavy flavour tagging algorithms, which are applied later in the reconstruction chain. Furthermore the high track density in this region greatly increases the probability to find unrelated tracks fulfilling the requirements below, thus leading to larger combinatorial background. For the remaining track combinations, different mass hypotheses corresponding to the charged decay channels stated above are used for the two tracks to calculate the combined invariant mass. For the photon pair conversion the electron mass is ignored, as it is negligible compared to the relevant momenta. Only the hypothesis that gives the smallest difference $\Delta m_{V^0} = |m_0 - m_{V^0}|$ between the calculated invariant mass m_0 and the nominal mass m_{V^0} of the respective V^0 is considered further. The masses assumed in the processor are $m_{\mathrm{K}^0} = 497.648\,\mathrm{MeV}$ and $m_\Lambda = 1115.683\,\mathrm{MeV}$ for the K^0_S and $\Lambda(\bar{\Lambda})$ respectively, while the photon is of course massless. The smallest mass difference must then fulfil $\Delta m_\gamma < 10\,\mathrm{MeV}$ for a photon hypothesis

Table 13.1.: The fractions of true particles contained in each reconstructed PID sample after the V^0 identification process. The sum of the entries in each line is normalised to 1. The diagonal elements represent the purity of the samples. The last line in each table lists the efficiencies to correctly assign the PID. The shown uncertainties are statistical only. Uncertainties given as zero are smaller than $5 \cdot 10^{-4}$.

(a) Z-return sample.

Assigned PID	True PID K_S^0	$\Lambda(\bar{\Lambda})$	other
K_S^0	0.991(1)	0.008(1)	0.001(0)
$\Lambda(\bar{\Lambda})$	0.078(5)	0.904(5)	0.018(2)
efficiency	0.798(5)	0.796(7)	—

(b) Sample at $\sqrt{s'} = 250\,\text{GeV}$.

Assigned PID	True PID K_S^0	$\Lambda(\bar{\Lambda})$	other
K_S^0	0.990(6)	0.010(6)	0.000(3)
$\Lambda(\bar{\Lambda})$	0.191(28)	0.765(26)	0.044(14)
efficiency	0.581(19)	0.667(29)	—

or $\Delta m_{K^0/\Lambda} < 20\,\text{MeV}$ for K_S^0 and $\Lambda(\bar{\Lambda})$. Additionally, to further reduce the combinatorial background, the PCA of the two tracks is required to have a distance to the beam axis of larger than 10 mm, 30 mm or 50 mm for the photon, K_S^0 or $\Lambda(\bar{\Lambda})$ hypotheses respectively.

Due to the selection of the most energetic particles in each event, the average momentum of the selected V^0 is about 30 GeV in the Z-return sample and 75 GeV in the sample at $\sqrt{s'} = 250\,\text{GeV}$, cf. figure 13.3b. At these momenta, relativistic time dilation allows large fractions of the V^0 to traverse the tracking system before decaying. Even for decays within the tracking volume there is a soft cut-off at a radius of ~1.5 m. This is mainly due to the following two effects. Firstly, the decay products have low transverse momenta relative to the high momentum of these V^0. Therefore in the lab frame their trajectories start out collinear and thus their tracks in the TPC overlap. The remaining distance in the TPC is often too short for the tracks to sufficiently separate in the magnetic field and only one track is reconstructed. Secondly, if the trajectories of the decay products separate far enough, they may no longer produce enough hits in the TPC to be accepted by the tracking algorithm. The MC predicts that due to these effects $(30.5 \pm 0.4)\,\%$ of K_S^0 and $(40.1 \pm 0.5)\,\%$ of $\Lambda(\bar{\Lambda})$ in the Z-return sample are not distinguished from other neutral hadrons by the reconstruction software. In the sample at $\sqrt{s'} = 250\,\text{GeV}$ these fractions increase to $(63.7 \pm 0.9)\,\%$ of K_S^0 and $(68.6 \pm 1.3)\,\%$ of $\Lambda(\bar{\Lambda})$.

The results of the reconstruction algorithm in terms of purity and efficiency of the K_S^0 and $\Lambda(\bar{\Lambda})$ samples are given in table 13.1. The population used to calculate these values

includes only those V^0 that could potentially be reconstructed, i.e. that undergo a charged decay within the tracking volume. High purities are achieved, $(99.1 \pm 0.1)\,\%$ for K^0_S and $(90.4 \pm 0.5)\,\%$ for $\Lambda(\bar{\Lambda})$ at the Z -return peak , where the uncertainties result from the MC statistics. At $\sqrt{s'} = 250\,\mathrm{GeV}$ the respective purities are $(99.0 \pm 0.6)\,\%$ and $(76.5 \pm 2.6)\,\%$. In all cases only a negligible amount of combinatorial background is found. The dominant source of background is confusion between the three particle species reconstructed with this algorithm. Therefore the *other* category contains mostly photons that underwent pair conversion and were reconstructed using the wrong mass hypothesis. The lower purities of the reconstructed $\Lambda(\bar{\Lambda})$ samples compared to K^0_S are due to the kinematics of the decays, which prevent an efficient rejection of K^0_S background in the $\Lambda(\bar{\Lambda})$ sample [257]. The efficiencies in the Z-return sample are about 80 % for either V^0 species. In the sample around $\sqrt{s'} = 250\,\mathrm{GeV}$ the efficiencies are lower with values of $(58.1 \pm 1.9)\,\%$ for K^0_S and $(66.7 \pm 2.9)\,\%$ for Λ. For the tagging efficiencies which are calculated in chapter 14, in addition to the PID efficiencies, the fraction of neutral decays and the fraction of V^0 reaching the calorimeter must be taken into account.

13.3.2. Stable Charged Hadrons

Charged particles that traverse the tracking system can be distinguished by the difference in their specific energy loss $\mathrm{d}E/\mathrm{d}x$ in the TPC. However as stated above, the data samples used for the analysis do not include $\mathrm{d}E/\mathrm{d}x$ information from the simulation. Therefore a toy MC method was implemented to emulate the particle identification process by $\mathrm{d}E/\mathrm{d}x$, according to the established performance of the ILD [87]. It is based on parametrised Bethe-Bloch curves, see also equation (3.7) on page 35, for electrons, muons, pions, kaons and protons, shown in figure 13.3a, that were generated using version `v02-00-02` of iLCSoft [293]. A relative $\mathrm{d}E/\mathrm{d}x$ resolution of 4.7 % is assumed for this analysis, based on the results presented in chapter 9 of this work and of beam tests with other readout technologies summarised in ref. [87]. This value applies for tracks traversing the full depth of the TPC perpendicular to the z-axis of the detector reference frame. The resolution is expected to improve for polar angles $\theta \neq 90°$ similar to $\sigma_{\mathrm{d}E/\mathrm{d}x} \propto L^{-0.34} \propto (\sin\theta)^{0.34}$ due to the increased track length L in the TPC [124]. On the other hand, for tracks that do not cover the full depth of the TPC, e.g. particles that are exiting through one of the end plates, or otherwise contain a different number of hits N, the $\mathrm{d}E/\mathrm{d}x$ resolution is expected to change similar to $\sigma_{\mathrm{d}E/\mathrm{d}x} \propto N^{-0.47}$, as shown in section 9.4. Both of these effects are taken into account in the toy PID process.

At the start of the procedure, the true particle species and the momentum in the rest frame of the detector are gathered from the MC simulation. Using this information, for each particle the expected average energy loss in the TPC is calculated from the parametrisation. Here, electrons and muons use the corresponding parameters in table B.1 on page 198. Any hyperons are treated as protons, since no dedicated parametrisations are available. However also in reality an efficient separation of these heavier hadrons from protons is generally not possible due to the relatively small mass differences. Since no assumptions are made for the hadronisation symmetries of the proton, and the total number of hyperons is small, this is not expected to significantly affect the final results. A random value is drawn from a

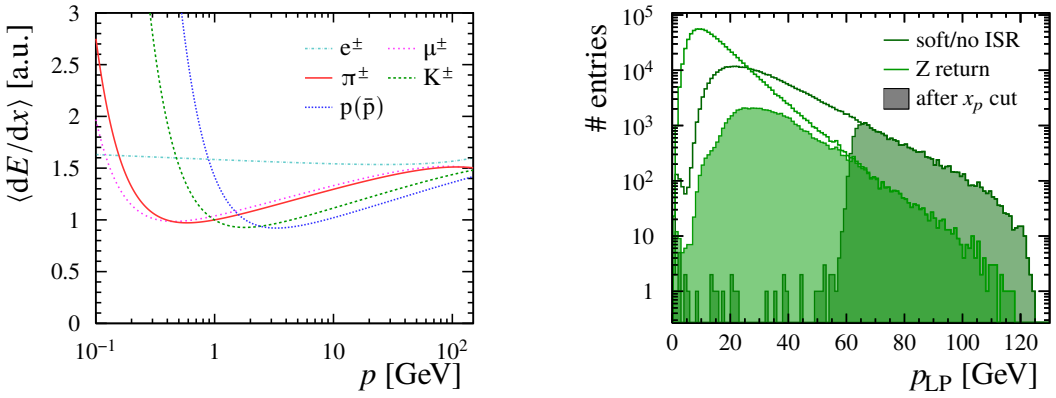

(a) Parametrised energy loss.

(b) Leading particle momentum.

Figure 13.3.: (a) The parametrised energy-loss curves used in the toy MC $\mathrm{d}E/\mathrm{d}x$ process. The parametrisation formula and the parameters for the individual particle species are given in equation (B.1) and table B.1 on page 198. (b) The true momenta in the lab frame, of the leading particles identified as charged hadrons by the PFA on detector level.

Gaussian distribution around the MC expectation value, with a standard deviation equal to the expected $\mathrm{d}E/\mathrm{d}x$ resolution based on the true direction of the particle and the number of its hits in the TPC. The resulting value represents the *measured* energy loss $\mathrm{d}E/\mathrm{d}x$.

This value is then compared to the expected energy loss for pions, kaons and protons, calculated from the parametrisations using the measured momentum of the particle. For each of the three hypotheses an acceptance interval is defined around the corresponding expectation value $\langle \mathrm{d}E/\mathrm{d}x \rangle_h$, taking into account the expected absolute resolution $\sigma_{\mathrm{d}E/\mathrm{d}x,h}$:

- for pion candidates: $\mathrm{d}E/\mathrm{d}x - \langle \mathrm{d}E/\mathrm{d}x \rangle_{\pi^\pm} > -r \cdot \sigma_{\mathrm{d}E/\mathrm{d}x,\pi^\pm}$;
- for kaon candidates: $r \cdot \sigma_{\mathrm{d}E/\mathrm{d}x,\mathrm{K}^\pm} > \mathrm{d}E/\mathrm{d}x - \langle \mathrm{d}E/\mathrm{d}x \rangle_{\mathrm{K}^\pm} > -r \cdot \sigma_{\mathrm{d}E/\mathrm{d}x,\mathrm{K}^\pm}$;
- for proton candidates: $r \cdot \sigma_{\mathrm{d}E/\mathrm{d}x,\mathrm{p}} > \mathrm{d}E/\mathrm{d}x - \langle \mathrm{d}E/\mathrm{d}x \rangle_{\mathrm{p}}$.

If a particle is a candidate for more than one species, the result is ambiguous and neither hypothesis is accepted. An interval of $r = 1$ was found to give a good compromise between efficiency and purity of the three samples. These intervals are visualised in figure 13.4. For larger intervals the efficiency of the kaon sample, in particular in the energy band around $\sqrt{s'} = 250\,\mathrm{GeV}$, is severely diminished due to the overlap with the intervals of the two other samples. For smaller intervals the purity of the proton samples is greatly reduced as more kaons are falsely accepted as protons. These intervals could be further improved by optimising the range for each particle species independently. However, such an optimisation relies on the precise knowledge of the relative abundance of the three particle species in the respective sample. The abundances can only be determined from the MC and thus could introduce biases related to the specifics of the hadronisation model. Therefore, this approach was not further pursued for this work.

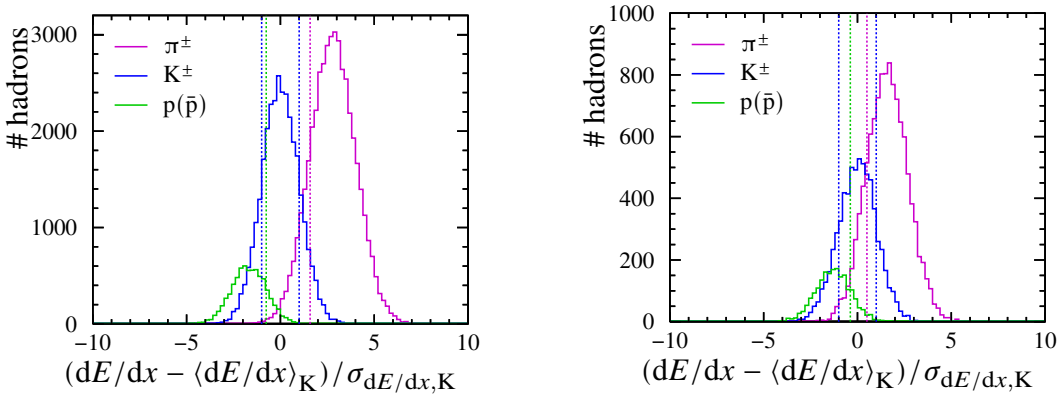

(a) Z-return sample.

(b) Sample at $\sqrt{s'} = 250\,\text{GeV}$.

Figure 13.4.: Distributions of the *measured* $\mathrm{d}E/\mathrm{d}x$ values for pions, kaons and protons, relative to the expected value for kaons and normalised to the $\mathrm{d}E/\mathrm{d}x$ resolution, in (a) the Z-return sample and (b) the sample around $\sqrt{s'} = 250\,\text{GeV}$. The vertical dashed lines represent the acceptance intervals defined in the text.

Table 13.2.: The fractions of true PIDs contained in each reconstructed sample after the full PID process of the Pandora PFA and the toy MC $\mathrm{d}E/\mathrm{d}x$. The sum of the entries in each line is normalised to 1. The diagonal elements represent the purity of the samples. The last line lists the efficiencies to correctly assign the PID. The shown uncertainties are statistical only. Uncertainties given as zero are smaller than $5 \cdot 10^{-4}$.

(a) Z-return sample.

Assigned PID	True PID $\pi^\pm$	$\mathrm{K}^\pm$	$\mathrm{p}(\bar{\mathrm{p}})$	other
$\pi^\pm$	0.951(1)	0.047(1)	0.000(0)	0.002(0)
$\mathrm{K}^\pm$	0.125(2)	0.823(3)	0.047(1)	0.005(0)
$\mathrm{p}(\bar{\mathrm{p}})$	0.003(1)	0.458(5)	0.498(5)	0.041(2)
efficiency	0.821(2)	0.593(3)	0.754(5)	—

(b) Sample at $\sqrt{s'} = 250\,\text{GeV}$.

Assigned PID	True PID $\pi^\pm$	$\mathrm{K}^\pm$	$\mathrm{p}(\bar{\mathrm{p}})$	other
$\pi^\pm$	0.878(3)	0.118(3)	0.002(0)	0.002(0)
$\mathrm{K}^\pm$	0.372(8)	0.551(8)	0.063(4)	0.015(2)
$\mathrm{p}(\bar{\mathrm{p}})$	0.039(4)	0.414(10)	0.458(10)	0.089(6)
efficiency	0.692(4)	0.315(6)	0.614(11)	—

The results of the toy MC process are summarised in table 13.2 in terms of the true particle contents of the three reconstructed hadron samples. The values in the table represent the combined performance of the Pandora PFA and the dE/dx PID. In the energy region around the Z-return peak the pion sample reaches an excellent purity of 95 % at an efficiency of over 80 %. The largest background with a fraction of almost 5 % is confusion of kaons. Since the pion interval is unconstrained towards higher dE/dx values, the charged leptons that are identified as hadrons by the PFA are almost exclusively reconstructed as pions by the dE/dx PID. However, their total fraction, given by the *other* column, is negligible. Also the kaon sample has a very good purity of about 82 %. The largest background are mis-reconstructed pions with a contribution of over 12 %. This fraction is larger than for the reverse migration because of the much greater abundance of pions in the overall hadron sample. The reconstructed kaon sample also includes a fraction of about 5 % of true protons and less than 1 % of heavier hadrons in the *other* category. Since the kaon acceptance interval is constrained on both sides, the efficiency of the sample of about 60 % is significantly lower than that of the other two samples. The purity of the proton sample suffers from the small separation of the kaon and proton dE/dx as well as the much smaller abundance of protons. Therefore it reaches only about 50 %, while kaons make up over 45 % of the reconstructed sample. The remaining fraction is comprised of heavier hadrons, which are almost exclusively reconstructed as protons. This low purity is accepted because for this smaller sample a high efficiency is deemed more important. This way an efficiency of over 75 % is achieved.

In the energy band around $\sqrt{s'} = 250\,\text{GeV}$ the picture is similar for the pion and proton samples. The respective purities are slightly lower with about 88 % for pions and ~46 % for protons. The loss of efficiency is larger with values of ~69 % and 61 % respectively. On the other hand, the performance for the kaon sample is drastically reduced. The purity drops to only ~55 % and the efficiency is halved with just over 30 %. The lower purities are mostly due to larger mixing between the three samples but also the fraction of heavier hadrons in the proton sample is increased.

To understand this reduced performance, it is important to consider the relevant momentum distributions of the leading particles produced in the two centre-of-mass energy ranges. These are shown in figure 13.3b. Due to the boosted event geometry after ISR in the sample at the Z-return peak, the full momentum range up to 120 GeV is covered, even after the cut on the scaled momentum. After the cut the sample has an average momentum of about 30 GeV. In the sample around $\sqrt{s'} = 250\,\text{GeV}$ a sharp cut-off is observed at a quarter of the centre-of-mass energy, as is expected after the $x_p > 0.5$ cut. The average momentum in this sample is over 75 GeV. Since the average energy loss of a particle depends its momentum, so does the separation power $S_{ab} = \Delta\mu_{ab}/\sigma_{\text{d}E/\text{d}x}$ for particle species a and b, where $\Delta\mu_{ab}$ represents the difference between the dE/dx expectation values and $\sigma_{\text{d}E/\text{d}x}$ is the resolution of the energy loss measurement. As is shown in figure 13.5, the separation power is highest at low to intermediate momenta. With the dE/dx resolution of 4.7 % assumed for this analysis $S > 2$ from ~2 GeV to 40 GeV for $\pi^{\pm}$-$\text{K}^{\pm}$ separation. For $\text{K}^{\pm}$-$\text{p}(\bar{\text{p}})$ separation it never exceeds $S = 2$ but is highest in a similar momentum range. Therefore the leading particles in the higher energy sample have momenta far above the optimal range. This is reflected in the large overlap between the distributions in figure 13.4b.

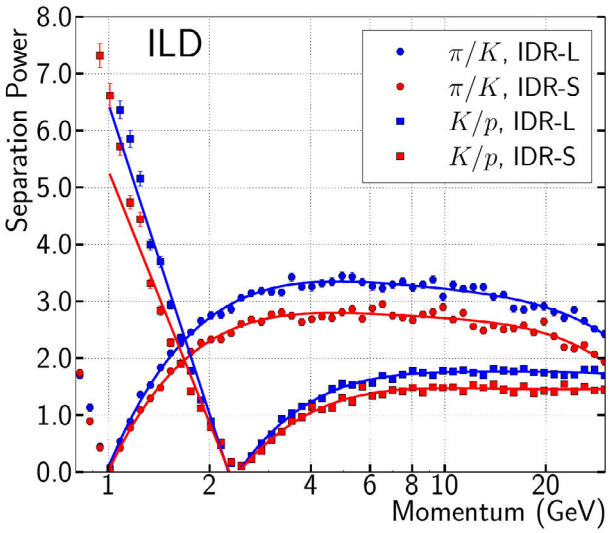

Figure 13.5.: Separation-power curves for discrimination of pions and kaons and of kaons and protons simulated with the large (IDR-L) and small (IDR-S) ILD models [87].

14. Finding the Branching Fractions

After the preparatory reconstruction described in the previous chapter, this chapter presents the steps and results of the actual measurement of the branching fractions. As inputs the procedure uses the reconstructed particles and jets in the effective centre-of-mass system after ISR emission as well as the corresponding generator level objects in the MC simulation. In the following, first the selection criteria for the events and the leading particles are described in section 14.1. Then in section 14.2 the treatment of tagging efficiencies is discussed. Section 14.3 explains how contributions of heavy c and b quark jets are taken into account. Section 14.4 discusses the fit to extract the branching ratios. Finally a brief discussion of potential systematic uncertainties follows in section 14.5.

14.1. Event Selection

The analysis uses the sample of $1.79 \cdot 10^6$ simulated events in the centre-of-mass energy band of $\pm 10\,\text{GeV}$ around the Z return peak defined in section 13.1. Weighted to the full integrated luminosity of the ILC at 250 GeV, as described in section 12.3, $73.9 \cdot 10^6$ events are expected, with an average event weight of 41.36.

To select events which are well contained in the detector, the polar angle of each of the two jets in the event, defined by the direction of their total momentum in the lab frame, must fulfil $|\cos\theta_\text{j}| < 0.95$. The distribution of the polar angle of both the more central and the more forward jet in each event is shown in figure 14.1a. The allowed range for the jet angle can be extended this far forward without risking to loose a significant number of leading particles down the beam pipes since their momentum tends to be collinear with the jet direction, as visible in figure 14.1b. After the cut on the jet angle, $1.16 \cdot 10^6$ unweighted ($47.8 \cdot 10^6$ weighted) events are retained, for an efficiency of $(64.72 \pm 0.04)\,\%$.

To enrich the fraction of hadrons from direct production and to suppress contributions from heavy flavours, as explained in section 11.2, only events are considered for tagging that have at least one PFO with a minimum scaled momentum of $x_p > 0.5$. In order to ensure good particle identification by $\mathrm{d}E/\mathrm{d}x$ in the TPC, the leading particles are required to have polar angles with $|\cos\theta_\text{LP}| < 0.8$ in the rest frame of the detector. For larger values of $|\cos\theta_\text{LP}|$ the particles are starting to pass through the end plate of the TPC and the $\mathrm{d}E/\mathrm{d}x$ separation of pions, kaons and protons rapidly degrades as the number of measurement points in the TPC decreases. Of the events passing the jet angle cut, 106 742 ($4.4 \cdot 10^6$ weighted) events have a potential tagging particle that passes the requirements above, in at least one jet. For comparison, the OPAL analysis in ref. [257] retains 198 309 events out of $4.3 \cdot 10^6$ hadronic Z-decays after all cuts.

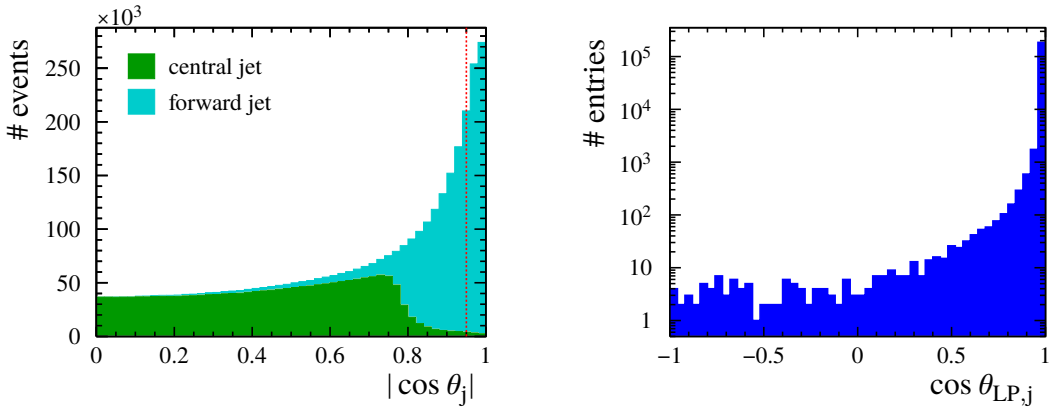

(a) Jet polar angle.

(b) Angle between LP and jet.

Figure 14.1.: Angular distributions of jets and their leading particles in the lab frame. (a) Stacked distributions of the polar angle of the more central and the more forward jet in each event. The vertical dashed line marks the cut value of $|\cos\theta_j| < 0.95$. (b) The angle between the leading particle and the jet direction for jets passing the polar angle cut and leading particles with a scaled momentum $x_p > 0.5$. Negative values arise from false jet assignments due to misreconstructed ISR boosts.

14.2. Treatment of Tagging Efficiencies and Purities

A precise knowledge of the composition of the tagged samples is crucial to this analysis. The different tagging efficiencies for the various particle species need to be taken into account to correctly apply the hadronisation symmetries introduced in section 11.2. The efficiency losses due to the finite geometric acceptance, i.e. the cuts on the polar angle of the jets and LPs, and the event energy selection are common to all particle species. Therefore they do not change the relative composition of the samples and can be absorbed into the values of the η_q^h. This eliminates the uncertainty of the cut efficiency as a systematic error on the branching fractions R_q.

Beyond that, the PID process introduces mixing between the different tagging particle species as well as efficiency losses, as discussed in section 13.3. Additional efficiency losses are introduced in the selection of the LP on detector level. This is mainly due to the error in the reconstruction of the event kinematics, i.e. the boost into the centre-of-mass system after ISR and the effective centre-of-mass energy, which causes particles with momenta close to the x_p threshold to migrate across. This way about 5 % of valid LPs on generator level are reconstructed with insufficient momentum, while about 8 % of LPs accepted in the reconstruction do not pass the threshold on generator level. To a much lesser extent ($\mathcal{O}(10^{-3})$) LPs are assigned to the wrong hemisphere or are selected from the products of a hard interaction of a particle with the detector material. The beam induced backgrounds described in section 12.2 are fully suppressed by the x_p requirement and the polar angle cut.

In total this leads to the true composition of the reconstructed tagged samples and the tagging efficiencies given in table 14.1. The efficiencies are defined as the number of correct tags on detector level divided by number of tags on generator level. The mixing between the

Table 14.1.: The true composition of the reconstructed tagged samples. The sum of the entries in each line is normalised to 1. The diagonal elements represent the purity of the samples. The last line lists the efficiencies to correctly tag a hemisphere. The shown uncertainties are statistical only. Uncertainties given as zero are smaller than $5 \cdot 10^{-4}$. Due to the effects explained in the text the values differ significantly from the pure PID performance in section 13.3.

Assigned tag	True tag $\pi^\pm$	$K^\pm$	$p(\bar{p})$	K^0_S	$\Lambda(\bar{\Lambda})$	other
$\pi^\pm$	0.845(2)	0.053(1)	0.000(0)	0.002(0)	0.000(0)	0.099(2)
$K^\pm$	0.134(3)	0.735(3)	0.045(2)	0.000(0)	0.001(0)	0.085(2)
$p(\bar{p})$	0.008(1)	0.414(5)	0.441(6)	0.000(0)	0.011(1)	0.125(4)
K^0_S	0.000(0)	0.000(0)	0.000(0)	0.904(4)	0.009(1)	0.086(4)
$\Lambda(\bar{\Lambda})$	0.000(0)	0.000(0)	0.000(0)	0.083(6)	0.809(9)	0.108(6)
efficiency	0.763(2)	0.546(3)	0.678(6)	0.334(4)	0.261(5)	—

samples is dominated by confusion in either of the two PID algorithms for V^0 and charged hadrons described in section 13.3. Therefore the composition of the tagged samples is similar to tables 13.1a and 13.2a. However, compared to the pure PID performance, the purity of each sample is reduced by a factor of ~0.9 due to LPs migrating above the x_p threshold in the reconstruction, as explained above. This is reflected by the increased fraction in the category *other*, which contains primarily these events. Only for protons and Λ a significant fraction of other particle species, not used for tagging, is included due to the backgrounds explained in sections 13.3.1 and 13.3.2. Also the efficiencies for the charged hadron samples generally follow those of the PID performance. For the V^0 samples the fractions of neutral decays and of V^0 penetrating the tracker reduce the achievable tagging efficiencies, as described in section 13.3.1. For all samples the efficiency is further reduced by ~5 % absolute due to LPs falling below the x_p threshold in the reconstruction.

The relations between the reconstructed tagging particle species k and the true particle species on generator level h can be described by a flow matrix $\mathscr{E}^h_k$, such that [257]

$$N^{\text{det}}_k = \sum_h \mathscr{E}^h_k N_h \ , \tag{14.1}$$

with the corresponding numbers of reconstructed tags N^{det}_k and true tags N_h. Using equation (11.11) on page 156 this implies

$$\eta^{k,\text{det}}_q = \sum_h \mathscr{E}^h_k \eta^h_q \ . \tag{14.2}$$

These relations are used in section 14.4 to convert from the tags observed on detector level to the underlying true tags, to fit the branching fractions R_q.

14.3. Treatment of Heavy Quark Contributions

To accurately determine the light quark branching fractions of the Z, it is important to know the contributions from c and b quarks to the tagged samples described in the previous section. These are given by the fractions f_{c}^{h} and f_{b}^{h}, where $\sum_q f_q^h = 1$. In addition, the branching fractions R_{c} and R_{b} of the Z into heavy quarks must be known.

Precise measurements of the branching ratios R_{c} and R_{b} are available from previous experiments, as detailed in section 11.1. An issue with the use of these values arises from the cut on the effective centre-of-mass energy introduced in section 13.1. Due to the presence of neutrinos in many heavy flavour jets, originating from semileptonic decays of charmed and bottom hadrons, the reconstructed invariant di-jet mass of such events is biased towards lower values. While efforts are ongoing to correct for this effect [289], the information cannot be fully recovered. Therefore a fraction of heavy flavour events is reconstructed below the lower m_{jj} threshold, while being valid on generator level. This means the cut on the di-jet mass is less efficient for heavy flavour events than for light flavour events. The MC simulation shows that in the sample around the Z peak the efficiencies for $\mathrm{e^+e^-} \to \mathrm{c\bar{c}}$ and $\mathrm{b\bar{b}}$ events are reduced relative to light quark events by factors of about 0.94 and 0.81 respectively.

When using externally measured branching fractions in the fit in section 14.4, these varying efficiencies would need to be taken into account. The use of the reduced branching fractions R'_q, as defined in equation (11.19), eliminates the $R_{\mathrm{c/b}}$ as parameters in the fit and thus avoids the related systematic uncertainties. The $R_{\mathrm{c/b}}$ are then needed to calculate the full hadronic branching fractions R_q from the R'_q. Also with this method the $f_{\mathrm{c/b}}^{h}$ are required, to subtract the heavy flavour contributions from the individual tagged samples. Additionally, the contribution of the heavy quarks to the total number of hadronic events N_{had} must be known to calculate the total number of light quark events $N_{\mathrm{light}} = N_{\mathrm{had}} - N_{\mathrm{c\bar{c}}} - N_{\mathrm{b\bar{b}}} = N_{\mathrm{had}} \cdot (1 - f_{\mathrm{c}} - f_{\mathrm{b}})$. In the OPAL analysis the f_{b}^{h} were determined from data by searching for a secondary vertex or a high p_{t} lepton in the hemisphere opposite to each tagging hadron [257]. Due to lack of an efficient tag for c-jets the f_{c}^{h} were taken from the MC. This introduces significant systematic uncertainties related to the specific properties of the hadronisation model. With the improved detector performance of the ILD and the much larger data set at the ILC, it will be possible to determine all the $f_{\mathrm{c/b}}^{h}$ from data, thus greatly reducing the uncertainties. However, the small size of the MC data set available for this analysis results in similar constraints as faced by the OPAL analysis. The $f_{\mathrm{c/b}}$ were identical to the $R_{\mathrm{c/b}}$ for the OPAL analysis. Due to the varying cut efficiencies for the different quark flavours discussed above, this is not the case for this work and the $f_{\mathrm{c/b}}$ must be determined independently.

Because implementing such a measurement is not in the scope of this work, the contributions of heavy quarks to the total number of hadronic events as well as to the individual hadron tagged samples are determined from the MC. The unweighted numbers of tags from heavy quark events $N_{\mathrm{c}}^{h_{\mathrm{det}}}$ and $N_{\mathrm{b}}^{h_{\mathrm{det}}}$ and the relative contributions $f_{\mathrm{c}}^{h_{\mathrm{det}}}$ and $f_{\mathrm{b}}^{h_{\mathrm{det}}}$ are shown in table 14.2. The contributions from charm quarks to the individual samples range from about 6 % for the $\pi^{\pm}$ sample to almost 10 % for the two kaon samples. The fraction of bottom quark events lies around 2 % in most samples except the pion sample where they make

Table 14.2.: The contributions of heavy quarks to the hadron tagged samples on detector level as determined from the MC. The errors are purely statistical and calculated from the unweighted event numbers.

hadron tag	$N_{\mathrm{c}}^{h_{\mathrm{det}}}$	$f_{\mathrm{c}}^{h_{\mathrm{det}}}$ [%]	$N_{\mathrm{b}}^{h_{\mathrm{det}}}$	$f_{\mathrm{b}}^{h_{\mathrm{det}}}$ [%]
$\pi^{\pm}$	1801	5.9 ± 0.1	1343	4.3 ± 0.1
$\mathrm{K}^{\pm}$	1656	9.6 ± 0.2	390	2.2 ± 0.1
$\mathrm{p}(\bar{\mathrm{p}})$	636	7.7 ± 0.3	185	2.3 ± 0.2
$\mathrm{K}_{\mathrm{S}}^{0}$	402	9.2 ± 0.4	84	1.9 ± 0.2
$\Lambda(\bar{\Lambda})$	131	6.3 ± 0.5	43	2.1 ± 0.3

up ~4 %. The contributions from charm and bottom quarks to the total number of hadronic events in the selected energy band are $f_{\mathrm{c}} = (17.06 \pm 0.03)$ % and $f_{\mathrm{b}} = (18.76 \pm 0.03)$ % respectively, with the errors resulting purely from the unweighted MC statistics.

14.4. Fitting the Branching Fractions

The final step in determining the branching fractions of the Z into the light quarks d, u and s is to solve the equation system defined by equations (11.11) and (11.12) for the five measured numbers of tagged hemispheres and the fifteen combinations of double tagged events. Using the five hadronisation symmetries in equations (11.13) to (11.17) leaves as unknown parameters the partial light flavour branching fraction $R'_{\mathrm{d,s}}$, the η_q^h and the correlation factors ρ_{hk}. The partial branching fraction into u quarks R'_{u} is fully constraint by equations (11.18) and (11.19). As visible in figure 14.2, the MC shows the ρ_{hk} to be independent of the hadron species and the flavour of the primary quark within uncertainties, confirming similar findings in ref. [256]. Therefore one global correlation factor ρ is used, leaving twelve unknowns.

The equation system is solved by minimising the χ^2 function

$$\begin{aligned}\chi^2 = &\sum_h \left(\frac{\tilde{N}_h^{\mathrm{det}} - 2N_{\mathrm{light}} \cdot \sum_q \tilde{\eta}_q^{h,\mathrm{det}} R'_q}{\sqrt{\tilde{N}_h^{\mathrm{det}}}} \right)^2 \\ &+ \sum_{h,k} \left(\frac{N_{hk}^{\mathrm{det}} - (2 - \delta_{hk}) \cdot N_{\mathrm{light}} \cdot \rho \cdot \sum_q \eta_q^{h,\mathrm{det}} \eta_q^{k,\mathrm{det}} R'_q}{\sqrt{N_{hk}^{\mathrm{det}}}} \right)^2 ,\end{aligned} \tag{14.3}$$

where the sums run over $q = \mathrm{d}, \mathrm{u}, \mathrm{s}$ and $h, k = \pi^{\pm}, \mathrm{K}^{\pm}, \mathrm{p}(\bar{\mathrm{p}}), \mathrm{K}_{\mathrm{S}}^{0}, \Lambda(\bar{\Lambda})$. In the second term the sum is applied such that double counting of the double tagged events with two different tagging hadrons $h \neq k$ is avoided. The corrections

$$\tilde{N}_h^{\mathrm{det}} = N_h^{\mathrm{det}} - \sum_k (1 + \delta_{hk}) N_{hk}^{\mathrm{det}} \tag{14.4}$$

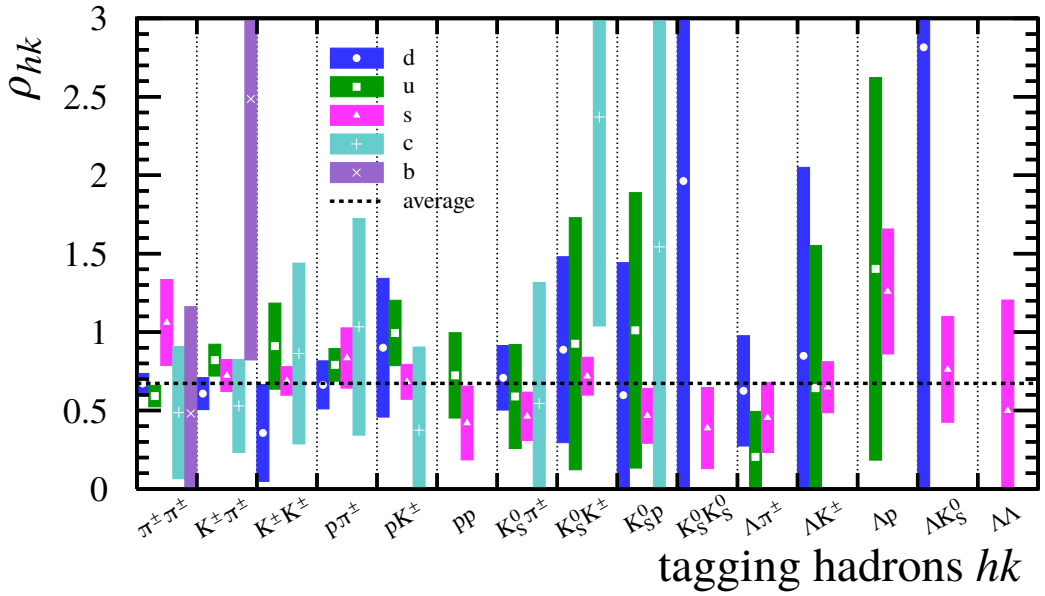

Figure 14.2.: The hemisphere correlation factors ρ_{hk} for all combinations of double tags and the five primary quark flavours. The coloured bars represent the uncertainty due to the MC statistics. For missing entries no corresponding double tag was present in the data sample. The average represented by the horizontal dashed line is determined as the weighted mean of all entries.

and

$$\tilde{\eta}_q^{h,\mathrm{det}} = \eta_q^{h,\mathrm{det}} - \rho \cdot \sum_k \eta_q^{h,\mathrm{det}} \eta_q^{k,\mathrm{det}} \tag{14.5}$$

are necessary to account for double counting between the samples of single-tagged hemispheres and double-tagged events [261]. The χ^2 function (14.3) is minimised using the measured numbers of tags given in table 14.3 as inputs. The total number of light quark $e^+e^- \to q\bar{q}$ events is $N_{\mathrm{light}} = 742\,387$ ($30.7 \cdot 10^6$ weighted). In each minimisation step the hadronisation symmetries are applied to the η_q^h, which are free fit parameters. Afterwards the detector level $\eta_q^{h,\mathrm{det}}$ are calculated from the η_q^h according to equation (14.2). This order avoids the need to correct the individual symmetries for the mixing of the samples. Some of the symmetry relations are broken by $\mathcal{O}(1\,\%)$ due to isospin-violating decays. Corrections for these effects are taken from the MC.

The full results of the fit for all parameters are given in table 14.4 for both the weighted and unweighted data. The unweighted fit has a χ^2 of 11.9 for seven degrees of freedom ($p = 0.11$). A comparison of the fit result with the MC input values is shown in figure 14.3. Within the errors the result agrees very well with the MC inputs.

The hemisphere correlation factor ρ is found to be significantly smaller than one. This is mostly due to the polar angle constraint applied to the leading particles. Due to the boosted event geometry the two jets can have vastly different polar angles in the lab frame. Therefore often one LP is rejected by the polar angle cut while the other is still counted. This way no

Table 14.3.: The numbers of tagged event hemispheres and double tagged events on detector level after subtraction of heavy quark contributions for (a) the unweighted data and (b) the weighted data with an average event weight of 41.36. The numbers are rounded to the nearest integer.

(a) Unweighted data.

hadron type	single tags	double-tagged events $\pi^\pm$	$K^\pm$	$p(\bar{p})$	K^0_S	$\Lambda(\bar{\Lambda})$
$\pi^\pm$	27 752	203	158	101	28	10
$K^\pm$	15 299		74	67	45	19
$p(\bar{p})$	7429			12	12	14
K^0_S	3873				4	7
$\Lambda(\bar{\Lambda})$	1911					1

(b) Weighted data.

hadron type	single tags	double-tagged events $\pi^\pm$	$K^\pm$	$p(\bar{p})$	K^0_S	$\Lambda(\bar{\Lambda})$
$\pi^\pm$	1 148 510	8434	6370	4253	1160	426
$K^\pm$	632 973		3004	2749	1931	773
$p(\bar{p})$	307 653			460	492	659
K^0_S	160 730				176	311
$\Lambda(\bar{\Lambda})$	79 053					49

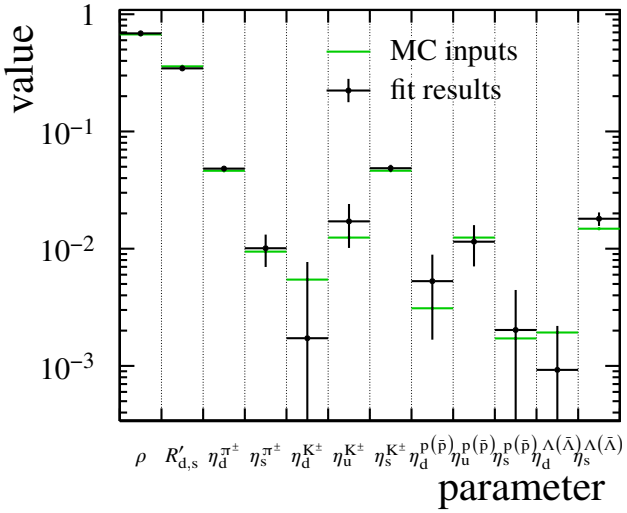

Figure 14.3.: Comparison of the fit result from the unweighted data with the MC input.

Table 14.4.: The fitted values of the free parameters in the equation system including statistical uncertainties. The uncertainties are highly correlated. Results from fits to both the weighted and the unweighted data are shown. For comparison the values from the MC input are given.

parameter	fitted value		MC input
	weighted	unweighted	
ρ	0.690 ± 0.004	0.687 ± 0.026	0.673
$R'_{\mathrm{d,s}}$	0.352 ± 0.004	0.345 ± 0.015	0.359
$\eta_{\mathrm{d}}^{\pi^{\pm}}$	0.0482 ± 0.0003	0.0482 ± 0.0017	0.0462
$\eta_{\mathrm{s}}^{\pi^{\pm}}$	0.0107 ± 0.0005	0.0101 ± 0.0031	0.0094
$\eta_{\mathrm{d}}^{\mathrm{K}^{\pm}}$	0.0027 ± 0.0010	0.0017 ± 0.0060	0.0054
$\eta_{\mathrm{u}}^{\mathrm{K}^{\pm}}$	0.0147 ± 0.0013	0.0171 ± 0.0070	0.0124
$\eta_{\mathrm{s}}^{\mathrm{K}^{\pm}}$	0.0494 ± 0.0005	0.0486 ± 0.0034	0.0462
$\eta_{\mathrm{d}}^{\mathrm{p}(\bar{\mathrm{p}})}$	0.0061 ± 0.0006	0.0053 ± 0.0036	0.0031
$\eta_{\mathrm{u}}^{\mathrm{p}(\bar{\mathrm{p}})}$	0.0111 ± 0.0008	0.0115 ± 0.0044	0.0124
$\eta_{\mathrm{s}}^{\mathrm{p}(\bar{\mathrm{p}})}$	0.0019 ± 0.0004	0.0020 ± 0.0024	0.0017
$\eta_{\mathrm{d}}^{\Lambda(\bar{\Lambda})}$	0.0009 ± 0.0002	0.0009 ± 0.0013	0.0019
$\eta_{\mathrm{s}}^{\Lambda(\bar{\Lambda})}$	0.0177 ± 0.0004	0.0180 ± 0.0024	0.0148

double tag is found but only a single tag, shifting their relative abundance. On generator level without any geometrical constraints the MC predicts a correlation factor of $\rho = 1.11$, which is caused by gluon exchange between the primary quarks.

The fit using the weighted data as input gives results very similar to the unweighted fit. The results are not expected to be exactly the same since the event weight for the less populated (double-tagged) samples can deviate significantly from the average, as can be seen in table 14.3. This modulates the relative influence of these samples in the weighted fit when compared to the unweighted fit. The value of χ^2 at the found minimum is 515.9. Taking into account the average event weight of 41.36 this is equivalent to $\chi^2/n_{\mathrm{df}} = 12.5/7$ ($p = 0.09$). From the weighted data the partial light flavour branching fraction for the down-type quarks is determined to be

$$R'_{\mathrm{d,s}} = 0.3519 \pm 0.0042$$

with a purely statistical error. The value of $R'_{\mathrm{u}} = 0.2961 \pm 0.0083$ is fully anticorrelated to the value of $R'_{\mathrm{d,s}}$, as described above.

Since the MC used for this analysis does not perfectly reflect the underlying physics, the central values of the parameters found by the fit presented here may differ significantly from the values found in the corresponding OPAL analysis in ref. [257]. Therefore, the potential improvement in statistical precision in this measurement is investigated using the relative uncertainties. In figure 14.4 a comparison is shown between the relative statistical uncertainties achieved here and the OPAL results. With the unweighted data the uncertainties are about the same as in the OPAL analysis while the data set used here is a factor of 2.4 smaller.

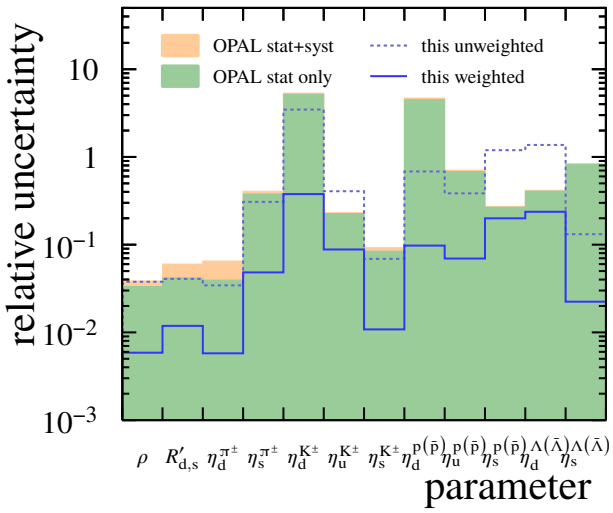

Figure 14.4.: Comparison of the relative statistical uncertainties achieved in the fits with the results from the analysis on the OPAL data presented in ref. [257]. For the OPAL measurement also the combined statistical and systematic uncertainties are shown.

This reflects the superior performance of the ILD, in particular regarding the V^0 PID, and the larger geometric acceptance.

Using the weighted data the uncertainties are on average reduced by about an order of magnitude compared to the OPAL result but with large fluctuations between individual parameters. For the partial light quark branching fractions $R'_{d,s}$, which are of particular interest, the relative uncertainty is improved by a factor of about 3.5 from 4.2 % to 1.2 %. Judging from the event numbers after all cuts in both analyses, as given in section 14.1, an improvement by a factor of 4.7 to a relative uncertainty of 0.9 % would be expected. Extrapolating from the unweighted result using the average event weight, gives an uncertainty of $4.3\,\%/\sqrt{41.36} \approx 0.7\,\%$. While the former is still reasonably close to the actual result, the latter is significantly better than what was achieved. A larger simulated data set that requires much lower event weights could help to resolve this discrepancy in a future analysis.

14.5. Discussion of Systematic Uncertainties

In the OPAL analysis [257] the systematic uncertainties on the branching fractions $R_{d,s}$ added up to a similar value as the statistical uncertainty. Therefore, to take advantage of the improved statistical precision expected at the ILC, the systematics need to be reduced by at least the same amount. A complete investigation of all potential systematic effects was not in the scope of this work, partially because the small statistics of the MC data sample, reflected in the high event weights, limit the accuracy to which the systematic uncertainties can be determined. Instead this section gives a first qualitative estimate of the expectation for the largest contributions to the total systematic uncertainty identified in the OPAL analysis.

Table 14.5.: The largest sources of systematic uncertainties in the measurement of the branching fractions $R_{\mathrm{d,s}}$ identified the OPAL analysis in ref. [257]. As opposed to the partial fractions $R'_{\mathrm{d,s}}$, the full branching fractions do depend significantly on the knowledge of the heavy quark fractions R_{c} and R_{b}, which is reflected in the contribution to the systematic uncertainty. The total systematic error given in the second to last line includes additional, smaller sources of error not shown here.

source of error	$\delta_{R_{\mathrm{d,s}}}$	$\delta_{R_{\mathrm{d,s}}}/R_{\mathrm{d,s}}$
$\mathrm{K}^0_{\mathrm{S}}$ purity and efficiency $\pm 4.1\,\%$	∓ 0.0077	∓ 0.034
$R_{\mathrm{c}} = 0.158 \pm 0.010$	∓ 0.0037	∓ 0.016
$f_{\mathrm{c}}^{\mathrm{K}^\pm} = 0.101 \pm 0.011$	± 0.0031	± 0.014
$f_{\mathrm{c}}^{\mathrm{K}^0} = 0.114 \pm 0.012$	± 0.0026	± 0.011
$\eta_{\mathrm{d}}^{\mathrm{K}^0}/\eta_{\mathrm{u}}^{\mathrm{K}^\pm}$, $\eta_{\mathrm{u}}^{\mathrm{K}^0}/\eta_{\mathrm{d}}^{\mathrm{K}^\pm} = 1.00 \pm 0.02$	∓ 0.0024	∓ 0.010
$\mathrm{d}E/\mathrm{d}x$ resolution $\pm 5\,\%$	∓ 0.0023	∓ 0.010
$f_{\mathrm{b}}^{\mathrm{K}^0} = 0.036 \pm 0.010$	± 0.0021	± 0.009
$f_{\mathrm{b}}^{\mathrm{K}^\pm} = 0.039 \pm 0.004$	± 0.0010	± 0.004
Total Systematic Error	0.0104	0.045
Total Statistical Error	0.0096	0.042

The effects and the corresponding uncertainties are listed in table 14.5. Most of the largest uncertainties are related to the charged and neutral kaons. This is due to the fact that the separation of up- and down-quark events depends strongly on the difference between the production of $\mathrm{K}^\pm$ and $\mathrm{K}^0_{\mathrm{S}}$. While kaons primarily tag strange-quark events, besides that charged and neutral kaons preferentially tag u and d events respectively, due to the flavours of their valence quarks.

The largest single contribution to the systematic error in the OPAL analysis was introduced by the uncertainty of the $\mathrm{K}^0_{\mathrm{S}}$ purity and efficiency. These values were estimated from the MC and the uncertainties are mostly due to correction factors needed to adjust for differing mass resolutions between data and the MC simulation as well as the simulation of other cut distributions [257]. Therefore it is difficult to judge the magnitude of this uncertainty for the presented analysis since no comparison with data is available for the ILD. However, the greatly increased statistics in data available at the ILC will help to optimise the detector simulations, reducing the reliance on correction factors. Furthermore, with the ILD the detection and identification efficiency for $\mathrm{K}^0_{\mathrm{S}}$ of $(79.8 \pm 0.5)\,\%$ established in section 13.3.1 is about 3 times higher than achieved at OPAL [294]. Therefore even when assuming the absolute magnitude of the errors is unchanged, their relative impact is reduced by this factor of 3, already achieving most of the needed improvement. Thus it can be expected that this error will be reduced well below the required magnitude.

The next highest contribution to the systematic error came from the branching fraction of the Z into charm quarks R_{c}. For the OPAL analysis a value of $R_{\mathrm{c}} = 0.158 \pm 0.010$ was used. By now the global average decay width of the Z into charm quarks reported by the Particle Data Group (PDG) is equivalent to $R_{\mathrm{c}} = 0.1721 \pm 0.0030$ [18]. This already achieves the

required reduction of the uncertainty. With further improvements in c-tagging performance future measurements will only shrink the error, e.g. [295].

A similar share of the systematic uncertainty was introduced by the contribution of charm-quark events to the $K^{\pm}$ and K^0_S samples, $f_c^{K^{\pm}}$ and $f_c^{K^0}$, as well as the b-quark contribution to the K^0_S sample $f_b^{K^0}$. In ref. [257] the values of the f_c^h were determined from the MC simulation, due to the low efficiency of the available c-tags. The c-tagging performance expected for the ILD with an efficiency of ~35 % at 95 % purity [87] surpasses the b-tagging performance reported in the OPAL analysis, ~16 % efficiency at the same purity. At the same time the b-tagging efficiency at the ILD will be improved to about 70 % at 95 % purity. Since this allows to determine the f_c^h from data, the large statistics available at the ILC can be used to reduce the uncertainties well below the required value. Therefore the systematic uncertainties introduced by the fractions of heavy-quark events should not pose an issue for this analysis.

The breaking of the kaon related hadronisation symmetries is estimated purely from MC, since measurements of the related η_q^h, e.g. [261], are affected by large uncertainties. As such the scale of the breaking will stay the best measure of this uncertainty. Therefore it is unlikely that this source of systematic error will shrink. Fortunately already the current magnitude allows to reach the required total systematic uncertainty if most of the other, larger uncertainties are sufficiently reduced.

In the OPAL analysis the uncertainty of the $\mathrm{d}E/\mathrm{d}x$ resolution was determined from data using pion and proton tracks from the charged decays of K^0_S and $\Lambda(\bar{\Lambda})$, respectively. Therefore the given error of the $\mathrm{d}E/\mathrm{d}x$ resolution of ± 5 % includes a statistical component from the number of tracks but also a systematic contribution from detector and calibration effects, which unfortunately were not given separately. This means higher statistics may help to reduce the $\mathrm{d}E/\mathrm{d}x$ related errors but the ultimately achievable precision depends strongly on the performance of the detector, e.g. the homogeneity and stability of the $\mathrm{d}E/\mathrm{d}x$ measurement, and the scale of the required calibrations. As for the symmetry relations above, the uncertainty due to the $\mathrm{d}E/\mathrm{d}x$ resolution is already small enough to allow the required total systematic uncertainty to be reached.

14.5.1. New Systematic Effects

Due to the centre-of-mass energy at the ILC being far above the Z-pole and the reliance of this analysis on events with a radiative return to the Z, new effects are introduced that may contribute to the systematic uncertainty. The major effect that comes to mind here is the selection of events on the Z return peak, as described in section 13.1, since the uncertainties of the selection efficiency and purity can only be determined from the MC. Additionally, as described in section 14.3, the selection efficiencies for the heavy flavours are different from the efficiency for the light flavours. If the efficiency was the same for all flavours it could simply be absorbed into the η_q^h, as it is done for the cuts on the polar angles of the jets and the leading particles. Fortunately, in determining the partial branching fractions R'_q, the heavy flavour contributions are measured independently and subtracted. This leaves only the efficiency common to all three light flavours that can again be absorbed into the η_q^h. This

shifts the issue to determining the heavy flavour contributions to the tagged samples and the total di-jet data sample, for which the systematic uncertainties have already been discussed above.

As seen above a precise knowledge of the $K^{\pm}$ and K^0_S tagging efficiencies is crucial for this analysis. Therefore the fraction of K^0_S that are not reconstructed since they decay too far out in the tracker or reach the calorimeter must be accurately known as well. In section 13.3.1 the fraction was determined from the MC, which may introduce biases if the momentum spectrum or the polar angle distribution are not well modelled. Fortunately isospin symmetry allows these to be accurately estimated from the corresponding distributions of charged kaons in data, thus benefiting from the greatly improved momentum resolution of the ILD compared to OPAL and the large statistics available at the ILC to reduce the uncertainties.

Other potential sources of error include, likely amongst others, the performance of kinematic fits to recover the information from unreconstructed ISR photons and beamstrahlung, and the much less well known effective centre-of-mass energy compared to the LEP measurements. The impact and magnitude of these effects are difficult to judge without a dedicated study.

14.6. Conclusions and Outlook

The presented analysis is only a first step that helps to gauge the possible improvement of the statistical measurement uncertainties of the Z branching fractions into light quarks with the data set of the ILC at $\sqrt{s} = 250\,\text{GeV}$. A significant reduction of the statistical error is found, indicating that it is possible to reduce the uncertainty to the level of 1 %. However, it depends on the development of the systematic uncertainties whether the increased statistical power can be benefited from fully. A qualitative look at the largest systematic effects found in the original analysis indicates that the required reduction can be achieved with the ILD at the ILC but a more detailed analysis is required to quantify all effects and judge the final, total uncertainty. In particular effects that are newly introduced due to the centre-of-mass energy away from the Z-pole and the use of events with a radiative return to the Z need to be investigated. Furthermore, the performance of the PID by $\mathrm{d}E/\mathrm{d}x$ should be validated using real $\mathrm{d}E/\mathrm{d}x$ information in a new simulated data set, instead of the toy MC method. Finally, the analysis may be affected by the large event weights used. Further investigation, in particular of the systematic uncertainties, requires a data set with much lower event weights, preferably below a value of 1.

If the *GigaZ* running scenario for the ILC, introduced in chapter 2, would be implemented, the resulting $3 \cdot 10^9$ hadronic Z-decays could be used to improve the statistical precision much further. Simply scaling the uncertainty achieved here with the expected number of events, ignoring potential differences in cut and PID efficiencies, results in an uncertainty of only 0.2 %. This is comparable in size to the current uncertainty of the branching fraction of the Z into charm quarks.

15. Summary of Part II

In this part of this thesis an analysis originally devised to measure the branching fractions of the Z boson into light u, d and s quarks in the process $e^+e^- \to q\bar{q}$ at LEP [256] has been adapted for the ILD at the ILC at $\sqrt{s} = 250\,\text{GeV}$. The analysis uses high momentum hadrons with different quark flavour content ($\pi^\pm$, $K^\pm$, $p(\bar{p})$, K^0_S, $\Lambda(\bar{\Lambda})$) to tag jets and events with the different final state quarks. The main difference in the method used here compared to ref. [256] is due to the higher centre-of-mass energy at the ILC. In a large number of events the initial e^+e^--system returns to the Z-resonance by emitting ISR photons. This results in two distinct data samples with different effective centre-of-mass energies, one at the full collision energy and one around the Z-pole. In the former sample the mediator of the process is a mixture of Z and γ. While the beam polarisation of the ILC can be used to disentangle this mixture, this sample was not used here as it is actually the smaller of the two. In the latter sample the emission of the ISR photons results in a strongly boosted event geometry. Since these photons generally are produced outside of the acceptance of the detector, the boost and effective centre-of-mass energy must be reconstructed from the visible part of the event. This can be done using a kinematic fit, which was emulated using MC information in this work.

The major challenge of this analysis is the identification of the tagging hadron species. The long-lived neutral particles K^0_S and $\Lambda(\bar{\Lambda})$ can be reconstructed from their charged decay products. The stable charged hadrons are identified by their specific energy loss. Since no true $\mathrm{d}E/\mathrm{d}x$ information was available in the simulated data, a toy MC method was implemented. Both PID methods were shown to be affected by the higher centre-of-mass energy and the correspondingly higher momenta of the hadrons. For the V^0 the higher momentum results in a relativistic enhancement of their lifetime, allowing large fractions to penetrate the tracking system. These particles are lost for the reconstruction and thus lower the tagging efficiency. For the stable charged hadrons the higher momentum means that the $\mathrm{d}E/\mathrm{d}x$ measurement is performed far in the relativistic rise part of the Bethe-Bloch curve, where the separation between the different particle species is worse than at lower momenta. However, in both cases it has been shown that the performance of the ILD is sufficient to provide efficient separation between the tagging particle species. In comparison with the original analysis performed with the OPAL detector [257] the tagging efficiencies for the two V^0 species were significantly improved and the performance for the stable charged hadrons at least maintained. While this is true for the large ILD model, the reduced outer radius of the TPC in the small ILD model would degrade the tagging efficiency for both groups of particles, as it increases the fraction of V^0 penetrating the tracker and reduces the number of available $\mathrm{d}E/\mathrm{d}x$ samples in the TPC.

The actual measurement of the branching fractions was performed using only the data set around the Z-return peak containing about $1.79 \cdot 10^6$ simulated events. These events

were weighted to the full data set of the complete ILC running scenario corresponding to $73.9 \cdot 10^6$ events, resulting in an average event weight of 41.36. The branching fractions were determined by a χ^2-fit to the number of jets and events tagged by the five hadron species. The fit to the unweighted data reproduces the MC input well within its uncertainties and the fit to the weighted data produces very similar results. The weighted fit results in a relative statistical uncertainty of the down type branching fractions $R'_{\mathrm{d,s}}$ of 1.2 ‰. Compared to the existing measurement at OPAL [257], which used $4.3 \cdot 10^6$ events at the Z-pole and reached a statistical uncertainty of 4.2 ‰, this is an improvement by a factor of 3.5. To benefit from this increased statistical power, the systematic uncertainties must be reduced by the same amount. A first qualitative look suggests that the largest systematic effects identified in the OPAL analysis could be sufficiently improved at the ILD due to the advanced detector performance and the much larger data set available at the ILC.

The result of this analysis may be affected by the large event weights. Therefore it should be validated using a larger data set. This would also allow to investigate and fully quantify the systematic uncertainties. Additionally, the reliance on MC information should be reduced by performing an actual kinematic fit to determine the effective centre-of-mass energy and by using fully simulated $\mathrm{d}E/\mathrm{d}x$ information for the PID process.

Appendix

A. Part I

A.1. GEM Flatness Studies

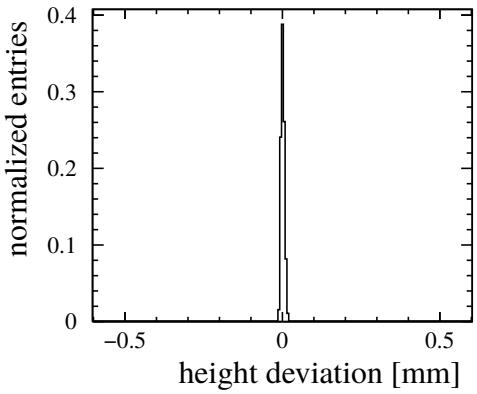

Figure A.1.: Mounting plate height distribution.

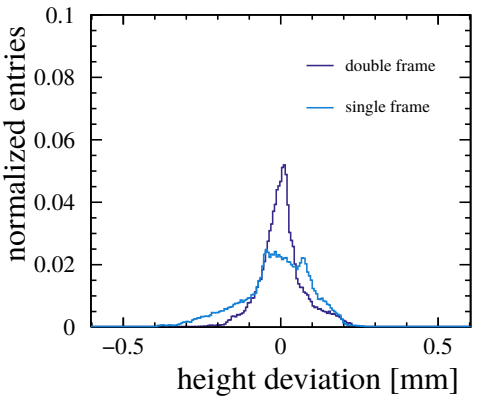

(a) Manually mounted GEM.

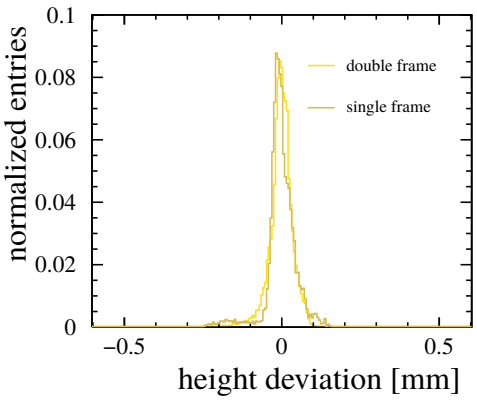

(b) Tool mounted GEM.

Figure A.2.: Comparison of the height deviations in single and double framed GEMs for (a) manually mounted GEMs and (b) GEMs mounted using the new tool.

A.2. Comparison of Beam Test Results

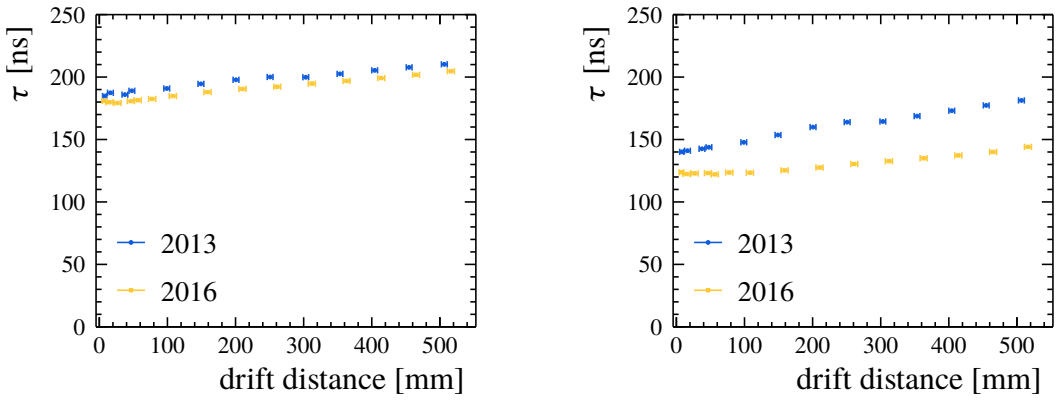

(a) Leading pulses.

(b) Lowest pulses.

Figure A.3.: The rise time τ from a fit of equation (6.1) on page 97 to the average pulse shape from data with $E_{\text{drift}} = 130\,\text{V/cm}$ for (a) the leading pulses with the highest charge and (b) the pulses with the least charge in each hit.

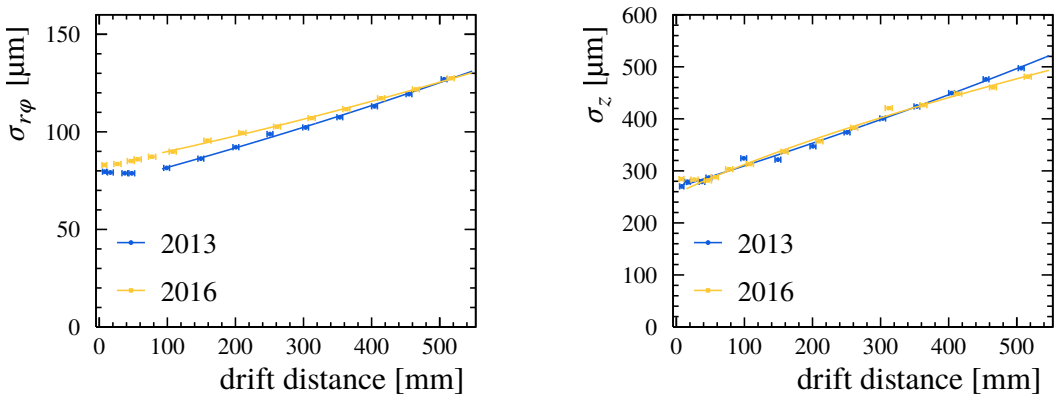

(a) $r\varphi$-resolution.

(b) z-resolution.

Figure A.4.: The point resolution in both data sets for a 130 V/cm drift field at various drift distances in (a) the transverse plane and (b) the drift direction. The solid lines represent fits of equation (8.10) on page 120. The fit results are given in tables 8.3 and 8.4 on page 122.

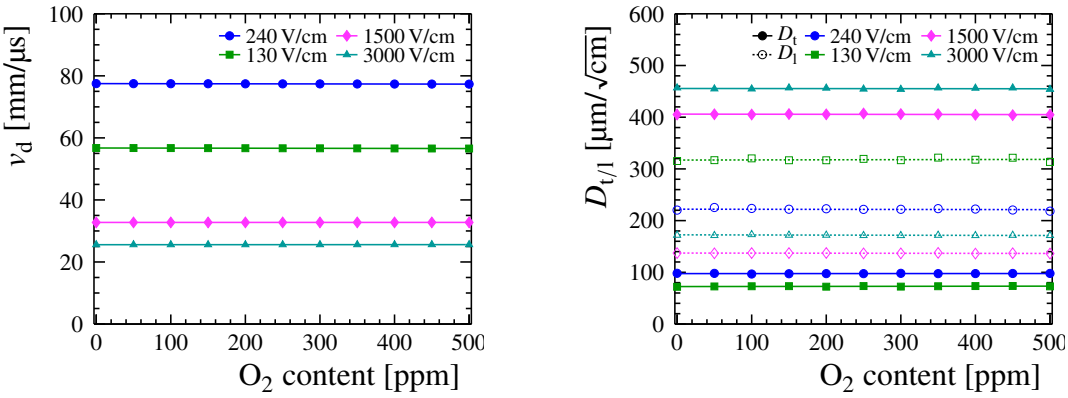

(a) Drift speed. **(b)** Diffusion coefficients.

Figure A.5.: The influence of contamination of the gas with oxygen on (a) the drift speed and (b) the diffusion coefficients. During both beam tests ~60 ppm O_2 were recorded. The lines represent polynomial fits of up to third order to guide the eyes and assess the rate of change.

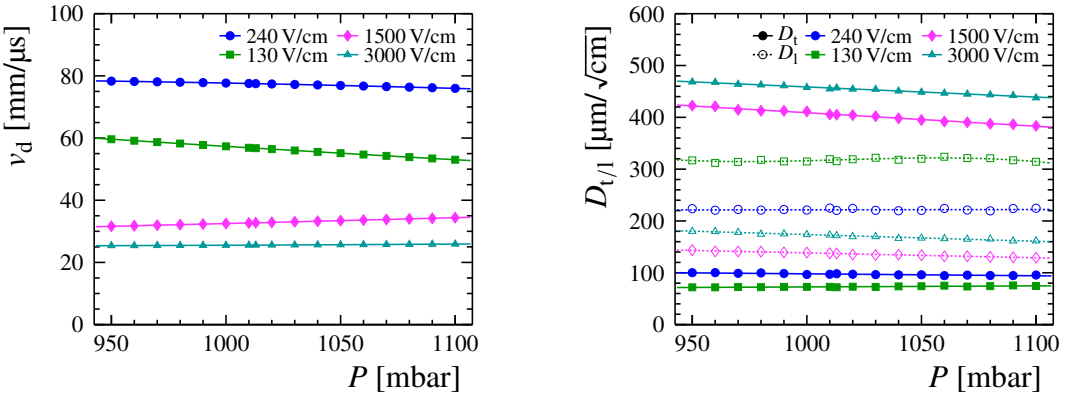

(a) Drift speed. **(b)** Diffusion coefficients.

Figure A.6.: The influence of the gas pressure inside the TPC on (a) the drift speed and (b) the diffusion coefficients. The lines represent polynomial fits of up to third order to guide the eyes and assess the rate of change.

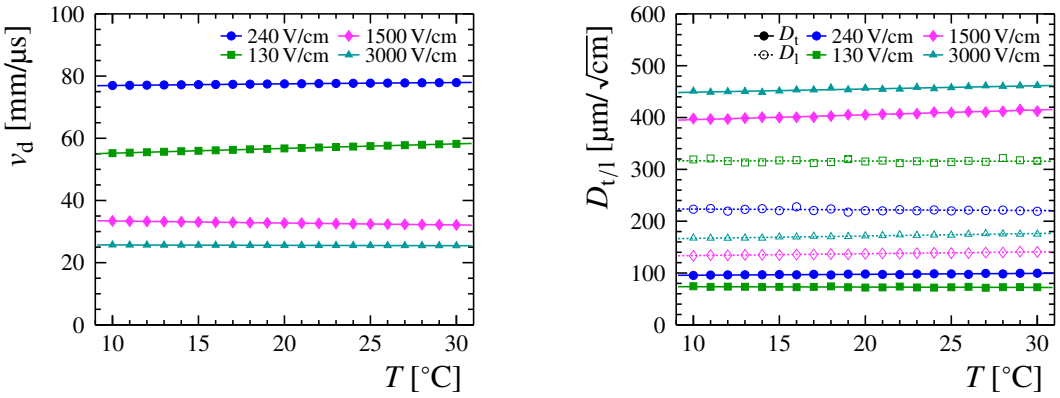

(a) Drift speed.

(b) Diffusion coefficients.

Figure A.7.: The influence of the gas temperature inside the TPC on (a) the drift speed and (b) the diffusion coefficients. The lines represent polynomial fits of up to third order to guide the eyes and assess the rate of change.

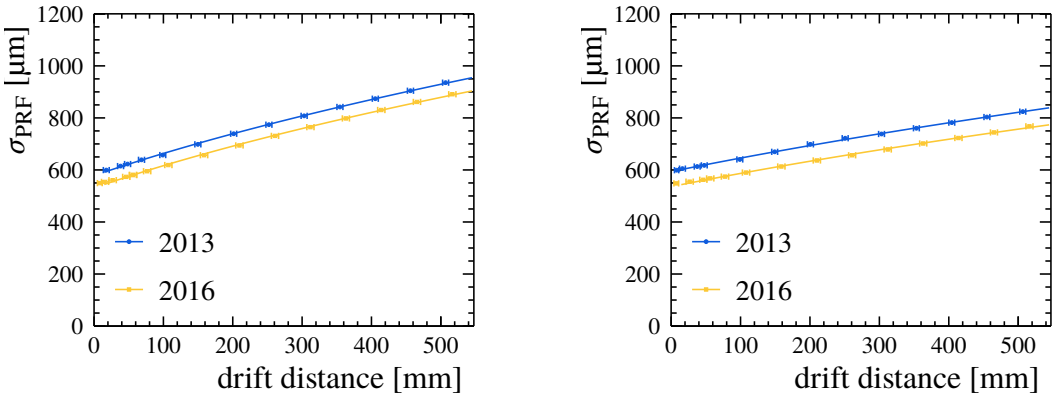

(a) $E_{drift} = 240\,V/cm$.

(b) $E_{drift} = 130\,V/cm$.

Figure A.8.: The measured average width of the PRF in both data sets at various drift distances. The minimum pulse length was reduced for the 2016 data. The solid lines represent fits of equation (8.1) on page 116. The fitted diffusion coefficients are given in table 8.6 on page 131.

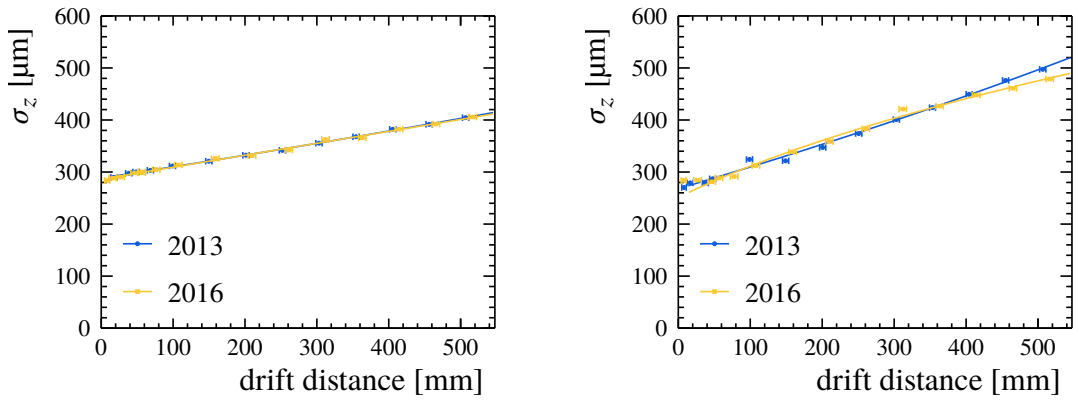

(a) $E_{\text{drift}} = 240\,\text{V/cm}$.

(b) $E_{\text{drift}} = 130\,\text{V/cm}$.

Figure A.9.: The longitudinal point resolution at various drift distances. The minimum pulse length was reduced for the 2016 data The solid lines represent fits of equation (8.10) on page 120. The fit results are given in table 8.7 on page 132.

B. Part II

B.1. Additional Data Reconstruction

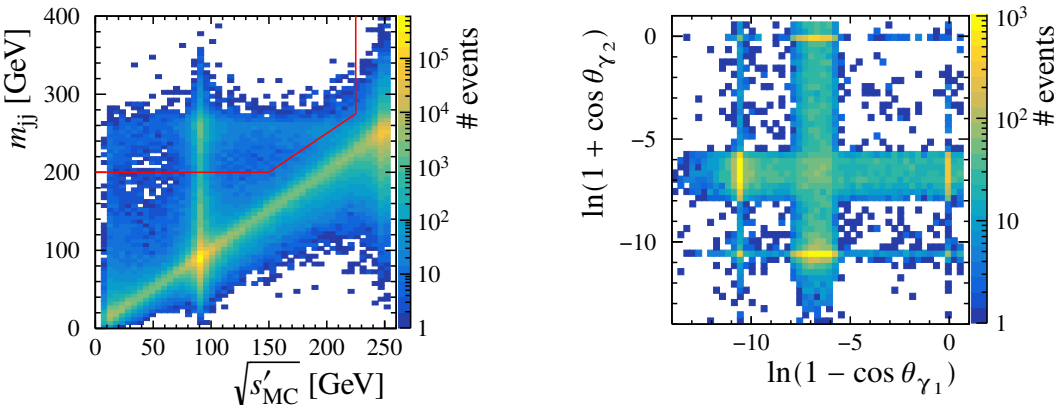

(a) Centre of mass energy comparison.

(b) Polar angle of selected ISR.

Figure B.1.: Some reconstructed ISR photons are not correctly linked to their MC counterparts. (a) These photons are included in the calculation of the invariant di-jet mass, causing the events to migrate to larger m_{jj}. The red line marks the cuts used to select such events. (b) The polar angle distribution for MC ISR photons in the selected events shows that they are primarily directed at $0.9997 > |\cos\theta| > 0.997$ ($1.5° < \theta < 4.6°$), matching the acceptance of the LumiCAL [105].

Table B.1.: The equation and parameters used to calculate the expected energy loss of charged particles [293], where β is the speed of the particle relative to the speed of light and $\gamma = 1/\sqrt{1-\beta^2}$ the relativistic Lorentz factor (see also equation (3.7) on page 35).

$$\left\langle -\frac{\mathrm{d}E}{\mathrm{d}x} \right\rangle = \frac{1}{\beta^2} \cdot \left(\frac{p_0}{2} \cdot \ln\left(p_1 \cdot (\beta\gamma)^2 \cdot Q_{\max} \right) - p_3 \cdot \beta^2 - \frac{p_4 \cdot \beta}{2} \right) \tag{B.1}$$

$$Q_{\max} = p_2 \cdot (\beta\gamma)^2$$

	p_0 $[10^{-2}]$	$p_1 \cdot p_2$	p_3	p_4 $[10^{-4}]$
e	−1.054 232 91	$6.992\,961\,543\,144\,832\,5 \cdot 10^{1}$	−1.764 647 96	−0.083 070 863
μ	7.018 704 74	$1.822\,175\,490\,478 \cdot 10^{14}$	0.444 841 020	3.234 621 27
π	7.276 575 27	$4.032\,284\,759\,595\,497\,3 \cdot 10^{13}$	0.452 784 712	3.715 020 54
K	7.879 450 81	$9.686\,924\,017\,674\,677 \cdot 10^{9}$	0.265 291 325	3.967 002 23
p	7.949 225 64	$3.060\,789\,122\,326\,154\,3 \cdot 10^{9}$	0.232 913 411	3.011 266 98

References

Introduction

[1] C. N. Yang and R. L. Mills. 'Conservation of Isotopic Spin and Isotopic Gauge Invariance'. In: *Phys. Rev.* 96 (1954), 191–195. DOI: 10.1103/PhysRev.96.191.

[2] A. Einstein. 'Zur Elektrodynamik bewegter Körper'. German. In: *Ann. Phys.* 17 (1905), 891.

[3] A. Einstein and M. Grossmann. 'Entwurf einer verallgemeinerten Relativitätstheorie und einer Theorie der Gravitation'. German. In: *Z. Math. Phys.* 62 (1913), 225–261.

[4] P. A. M. Dirac and N. H. D. Bohr. 'The quantum theory of the emission and absorption of radiation'. In: *Proc. R. Soc. Lond.* A 114 (1927), 243–265. DOI: 10.1098/rspa.1927.0039.

[5] E. Fermi. 'Quantum Theory of Radiation'. In: *Rev. Mod. Phys.* 4 (1932), 87–132. DOI: 10.1103/RevModPhys.4.87.

[6] H. Fritzsch and M. Gell-Mann. 'Current Algebra: Quarks and What Else?' In: *Proceedings of the 16th International Conference on High-Energy Physics* (Batavia, Illinois, 6th–13th Sept. 1972). Ed. by J. D. Jackson and A. Roberts. eConf C7209-06V2. 1972, 135–165. arXiv: hep-ph/0208010. URL: https://cds.cern.ch/record/574253.

[7] H. Fritzsch, M. Gell-Mann and H. Leutwyler. 'Advantages of the color octet gluon picture'. In: *Phys. Lett.* B 47 (1973), 365–368. DOI: 10.1016/0370-2693(73)90625-4.

[8] S. L. Glashow. 'Partial-symmetries of weak interactions'. In: *Nucl. Phys.* 22 (1961), 579–588. DOI: 10.1016/0029-5582(61)90469-2.

[9] A. Salam and J. C. Ward. 'On a gauge theory of elementary interactions'. In: *Nuovo Cim.* 19 (1961), 165–170. DOI: 10.1007/BF02812723.

[10] S. Weinberg. 'A Model of Leptons'. In: *Phys. Rev. Lett.* 19 (1967), 1264–1266. DOI: 10.1103/PhysRevLett.19.1264.

[11] F. Englert and R. Brout. 'Broken Symmetry and the Mass of Gauge Vector Mesons'. In: *Phys. Rev. Lett.* 13 (1964), 321–323. DOI: 10.1103/PhysRevLett.13.321.

[12] P. W. Higgs. 'Broken Symmetries and the Masses of Gauge Bosons'. In: *Phys. Rev. Lett.* 13 (1964), 508–509. DOI: 10.1103/PhysRevLett.13.508.

[13] G. S. Guralnik, C. R. Hagen and T. W. B. Kibble. 'Global Conservation Laws and Massless Particles'. In: *Phys. Rev. Lett.* 13 (1964), 585–587. DOI: 10.1103/PhysRevLett.13.585.

[14] P. W. Higgs. 'Spontaneous Symmetry Breakdown without Massless Bosons'. In: *Phys. Rev.* 145 (1966), 1156–1163. DOI: 10.1103/PhysRev.145.1156.

[15] S. N. Bose. 'Plancks Gesetz und Lichtquantenhypothese'. German. In: *Z. Phys.* 26 (1924), 178–181. DOI: 10.1007/BF01327326.

[16] P. A. M. Dirac and R. H. Fowler. 'On the theory of quantum mechanics'. In: *Proc. R. Soc. Lond.* A 112 (1926), 661–677. DOI: 10.1098/rspa.1926.0133.

[17] E. Fermi. 'Zur Quantelung des idealen einatomigen Gases'. German. In: *Z. Phys.* 36 (1926), 902–912. DOI: 10.1007/BF01400221.

[18] Particle Data Group. 'Review of Particle Physics'. In: *Phys. Rev.* D 98 (2018), 030001. DOI: 10.1103/PhysRevD.98.030001.

[19] F. J. Ynduráin. 'Limits on the mass of the gluon'. In: *Phys. Lett.* B 345 (1995), 524–526. DOI: 10.1016/0370-2693(94)01677-5.

[20] P. A. M. Dirac. 'The Quantum Theory of the Electron'. In: *Proc. R. Soc. Lond.* A 117 (1928), 610–624. DOI: 10.1098/rspa.1928.0023.

[21] P. B. Pal. 'Dirac, Majorana, and Weyl fermions'. In: *Am. J. Phys.* 79 (2011), 485–498. DOI: 10.1119/1.3549729.

[22] H. Weyl. 'Gravitation and the Electron'. In: *Proc. Natl. Acad. Sci. U.S.A.* 15 (1929), 323–334. DOI: 10.1073/pnas.15.4.323.

[23] E. Majorana. 'Teoria simmetrica dell'elettrone e del positrone'. Italian. In: *Nuovo Cim.* 14 (1937), 171–184. DOI: 10.1007/BF02961314. 'A symmetric theory of electrons and positrons'. Trans. by L. Maiana. In: *Soryushiron Kenkyu Electronics* 63.3 (1981), 149–162. DOI: 10.24532/soken.63.3_149.

[24] S. Kluth. 'α_S from LEP'. In: *J. Phys.* Conf. Ser. 110 (2008): *The 2007 Europhysics Conference on High Energy Physics 19–25 July 2007, Manchester, England*. Ed. by R. Barlow, 022023. DOI: 10.1088/1742-6596/110/2/022023. arXiv: 0709.0173 [hep-ex].

[25] C. Glasman. 'Precision measurements of α_s at HERA'. In: *J. Phys.* Conf. Ser. 110 (2008): *The 2007 Europhysics Conference on High Energy Physics 19–25 July 2007, Manchester, England*. Ed. by R. Barlow, 022013. DOI: 10.1088/1742-6596/110/2/022013.

[26] ALEPH, DELPHI, L3, OPAL, SLD, LEP Electroweak Working Group, SLD Electroweak Group and SLD Heavy Flavour Group. 'Precision electroweak measurements on the Z resonance'. In: *Phys. Rep.* 427 (2006), 257–454. DOI: 10.1016/j.physrep.2005.12.006. arXiv: hep-ex/0509008.

[27] CDF and D0 Collaborations. 'Combination of CDF and D0 W-Boson mass measurements'. In: *Phys. Rev.* D 88 (2013), 052018. DOI: 10.1103/PhysRevD.88.052018.

[28] ATLAS Collaboration. 'Measurement of the top quark mass in the $t\bar{t} \to$ lepton+jets channel from $\sqrt{s} = 8$ TeV ATLAS data and combination with previous results'. In: *Eur. Phys. J.* C 79 (2019), 290. DOI: 10.1140/epjc/s10052-019-6757-9.

[29] CMS Collaboration. 'Measurement of the top quark mass using proton-proton data at $\sqrt{(s)} = 7$ and 8 TeV'. In: *Phys. Rev.* D 93 (2016), 072004. DOI: 10.1103/PhysRevD.93.072004.

[30] Particle Data Group. *The Review of Particle Physics*. URL: https://pdg.lbl.gov/.

[31] ATLAS Collaboration. *Summary plots from the ATLAS Standard Model physics group*. 2021. URL: https://atlas.web.cern.ch/Atlas/GROUPS/PHYSICS/CombinedSummaryPlots/SM/.

[32] CMS Collaboration. *Summaries of CMS cross section measurements*. 2021. URL: https://twiki.cern.ch/twiki/bin/view/CMSPublic/PhysicsResultsCombined.

[33] Muon $g-2$ Collaboration. 'Measurement of the Positive Muon Anomalous Magnetic Moment to 0.46 ppm'. In: *Phys. Rev. Lett.* 126 (2021), 141801. DOI: 10.1103/PhysRevLett.126.141801.

[34] LHCb Collaboration. 'Branching fraction measurements of the rare $B_s^0 \to \phi\mu^+\mu^-$ and $B_s^0 \to f_2'(1525)\mu^+\mu^-$ decays'. In: *Phys. Rev. Lett.* 127 (2021), 151801. DOI: 10.1103/PhysRevLett.127.151801. arXiv: 2105.14007 [hep-ex].

[35] LHCb Collaboration. *Test of lepton universality in beauty-quark decays*. 2021. arXiv: 2103.11769 [hep-ex].

[36] B. R. Stella and H.-J. Meyer. 'Υ(9.46 GeV) and the gluon discovery (a critical recollection of PLUTO results)'. In: *Eur. Phys. J.* H 36 (2011), 203. DOI: 10.1140/epjh/e2011-10029-3. arXiv: 1008.1869 [hep-ex].

[37] P. Söding. 'On the discovery of the gluon'. In: *Eur. Phys. J.* H 35 (2010), 3–28. DOI: 10.1140/epjh/e2010-00002-5.

[38] M. Gell-Mann. 'Symmetries of Baryons and Mesons'. In: *Phys. Rev.* 125 (1962), 1067–1084. DOI: 10.1103/PhysRev.125.1067.

[39] M. Gell-Mann. 'A schematic model of baryons and mesons'. In: *Phys. Lett.* 8 (1964), 214–215. DOI: 10.1016/S0031-9163(64)92001-3.

[40] H1 and ZEUS Collaborations. *Combination of Measurements of Inclusive Deep Inelastic $e^{\pm}p$ Scattering Cross Sections and QCD Analysis of HERA Data*. 2015. arXiv: 1506.06042 [hep-ex].

[41] D. J. Gross and F. Wilczek. 'Ultraviolet Behavior of Non-Abelian Gauge Theories'. In: *Phys. Rev. Lett.* 30 (1973), 1343–1346. DOI: 10.1103/PhysRevLett.30.1343.

[42] H. D. Politzer. 'Reliable Perturbative Results for Strong Interactions?' In: *Phys. Rev. Lett.* 30 (1973), 1346–1349. DOI: 10.1103/PhysRevLett.30.1346.

[43] I. G. Knowles and G. D. Lafferty. 'Hadronization in Z^0 decay'. In: *J. Phys.* G 23 (1997), 731–789. DOI: 10.1088/0954-3899/23/7/003.

[44] X. Artru and G. Mennessier. 'String model and multiproduction'. In: *Nucl. Phys.* B 70 (1974), 93–115. DOI: 10.1016/0550-3213(74)90360-5.

[45] B. Andersson, G. Gustafson et al. 'Parton fragmentation and string dynamics'. In: *Phys. Rep.* 97 (1983), 31–145. DOI: 10.1016/0370-1573(83)90080-7.

[46] B. R. Webber. 'A QCD model for jet fragmentation including soft gluon interference'. In: *Nucl. Phys.* B 238 (1984), 492–528. DOI: 10.1016/0550-3213(84)90333-X.

[47] SLD Collaboration. 'Measurement of Leading Particle Effects in Decays of Z^0 Bosons into Light Flavors'. In: *Phys. Rev. Lett.* 78 (1997), 3442–3446. DOI: 10.1103/PhysRevLett.78.3442.

[48] J. Goldstone, A. Salam and S. Weinberg. 'Broken Symmetries'. In: *Phys. Rev.* 127 (1962), 965–970. DOI: 10.1103/PhysRev.127.965.

[49] CMS Collaboration. 'Observation of a new boson at a mass of 125 GeV with the CMS experiment at the LHC'. In: *Phys. Lett.* B 716 (2012), 30–61. DOI: 10.1016/j.physletb.2012.08.021.

[50] ATLAS Collaboration. 'Observation of a new particle in the search for the Standard Model Higgs boson with the ATLAS detector at the LHC'. In: *Phys. Lett.* B 716 (2012), 1–29. DOI: 10.1016/j.physletb.2012.08.020.

[51] H. Yukawa, S. Sakata and M. Taketani. 'On the Interaction of Elementary Particles. III'. In: *Proc. Phys.-Math. Soc. Jpn.* 3rd ser. 20 (1938), 319–340. DOI: 10.11429/ppmsj1919.20.0_319.

[52] Z. Maki, M. Nakagawa and S. Sakata. 'Remarks on the Unified Model of Elementary Particles'. In: *Prog. Theor. Phys.* 28 (1962), 870–880. DOI: 10.1143/PTP.28.870.

[53] V. Gribov and B. Pontecorvo. 'Neutrino astronomy and lepton charge'. In: *Phys. Lett.* B 28 (1969), 493–496. DOI: 10.1016/0370-2693(69)90525-5.

[54] B. T. Cleveland, T. Daily et al. 'Measurement of the Solar Electron Neutrino Flux with the Homestake Chlorine Detector'. In: *Astrophys. J.* 496 (1998), 505–526. DOI: 10.1086/305343.

[55] SNO Collaboration. 'Direct Evidence for Neutrino Flavor Transformation from Neutral-Current Interactions in the Sudbury Neutrino Observatory'. In: *Phys. Rev. Lett.* 89 (2002), 011301. DOI: 10.1103/PhysRevLett.89.011301.

[56] Super-Kamiokande Collaboration. 'Evidence for an Oscillatory Signature in Atmospheric Neutrino Oscillations'. In: *Phys. Rev. Lett.* 93 (2004), 101801. DOI: 10.1103/PhysRevLett.93.101801.

[57] Super-Kamiokande Collaboration. 'Evidence for the Appearance of Atmospheric Tau Neutrinos in Super-Kamiokande'. In: *Phys. Rev. Lett.* 110 (2013), 181802. DOI: 10.1103/PhysRevLett.110.181802.

[58] KamLAND Collaboration. 'Measurement of Neutrino Oscillation with KamLAND: Evidence of Spectral Distortion'. In: *Phys. Rev. Lett.* 94 (2005), 081801. DOI: 10.1103/PhysRevLett.94.081801.

[59] T2K Collaboration. 'Measurement of Neutrino Oscillation Parameters from Muon Neutrino Disappearance with an Off-Axis Beam'. In: *Phys. Rev. Lett.* 111 (2013), 211803. DOI: 10.1103/PhysRevLett.111.211803.

[60] OPERA Collaboration. 'Observation of tau neutrino appearance in the CNGS beam with the OPERA experiment'. In: *Prog. Theor. Exp. Phys.* 2014 (2014), 101C01. DOI: 10.1093/ptep/ptu132.

[61] P. Minkowski. '$\mu \to e\gamma$ at a rate of one out of 109 muon decays?' In: *Phys. Lett.* B 67 (1977), 421–428. DOI: 10.1016/0370-2693(77)90435-X.

[62] N. Cabibbo. 'Unitary Symmetry and Leptonic Decays'. In: *Phys. Rev. Lett.* 10 (1963), 531–533. DOI: 10.1103/PhysRevLett.10.531.

[63] M. Kobayashi and T. Maskawa. 'CP-Violation in the Renormalizable Theory of Weak Interaction'. In: *Prog. Theor. Phys.* 49 (1973), 652–657. DOI: 10.1143/PTP.49.652.

[64] V. Trimble. 'Existence and Nature of Dark Matter in the Universe'. In: *Annu. Rev. Astron. Astrophys.* 25 (1987), 425–472. DOI: 10.1146/annurev.aa.25.090187.002233.

[65] B. Carr. 'Baryonic Dark Matter'. In: *Annu. Rev. Astron. Astrophys.* 32 (1994), 531–590. DOI: 10.1146/annurev.aa.32.090194.002531.

[66] T. A. Porter, R. P. Johnson and P. W. Graham. 'Dark Matter Searches with Astroparticle Data'. In: *Annu. Rev. Astron. Astrophys.* 49 (2011), 155–194. DOI: 10.1146/annurev-astro-081710-102528.

[67] J. L. Feng. 'Dark Matter Candidates from Particle Physics and Methods of Detection'. In: *Annu. Rev. Astron. Astrophys.* 48 (2010), 495–545. DOI: 10.1146/annurev-astro-082708-101659.

[68] J. Lesgourgues and S. Pastor. 'Massive neutrinos and cosmology'. In: *Phys. Rep.* 429 (2006), 307–379. DOI: 10.1016/j.physrep.2006.04.001.

[69] S. Hannestad. 'Neutrino physics from precision cosmology'. In: *Prog. Part. Nucl. Phys.* 65 (2010), 185–208. DOI: 10.1016/j.ppnp.2010.07.001.

[70] V. A. Kuzmin, V. A. Rubakov and M. E. Shaposhnikov. 'On anomalous electroweak baryon-number non-conservation in the early universe'. In: *Phys. Lett.* B 155 (1985), 36–42. DOI: 10.1016/0370-2693(85)91028-7.

[71] M. Fukugita and T. Yanagida. 'Barygenesis without grand unification'. In: *Phys. Lett.* B 174 (1986), 45–47. DOI: 10.1016/0370-2693(86)91126-3.

[72] K. G. Wilson. 'Renormalization Group and Strong Interactions'. In: *Phys. Rev.* D 3 (1971), 1818–1846. DOI: 10.1103/PhysRevD.3.1818.

[73] G. 't Hooft. 'Naturalness, Chiral Symmetry, and Spontaneous Chiral Symmetry Breaking'. In: *Recent Developments in Gauge Theories*. Nato Science Series B. Springer Nature, 1980, 135–157.

[74] G. F. Giudice. 'Naturalness after LHC-7 and LHC-8'. In: *Proc. Sci.* 180 (2014): *The European Physical Society Conference on High Energy Physics (EPS-HEP 2013)*. DOI: 10.22323/1.180.0163. arXiv: 1307.7879 [hep-ph].

[75] W. Altmannshofer and P. Stangl. *New Physics in Rare B Decays after Moriond 2021*. 2021. arXiv: 2103.13370 [hep-ph].

[76] W. Altmannshofer, J. Davighi and M. Nardecchia. 'Gauging the accidental symmetries of the standard model, and implications for the flavor anomalies'. In: *Phys. Rev.* D 101 (2020), 015004. DOI: 10.1103/PhysRevD.101.015004. arXiv: 1909.02021 [hep-ph].

[77] A. Celis, J. Fuentes-Martín et al. 'Family nonuniversal Z' models with protected flavor-changing interactions'. In: *Phys. Rev.* D 92 (2015), 015007. DOI: 10.1103/PhysRevD.92.015007. arXiv: 1505.03079 [hep-ph].

[78] A. Angelescu, D. Bečirević et al. *On the single leptoquark solutions to the B-physics anomalies*. 2021. arXiv: 2103.12504 [hep-ph].

[79] C. Cornella, D. A. Faroughy et al. *Reading the footprints of the B-meson flavor anomalies*. 2021. arXiv: 2103.16558 [hep-ph].

[80] W. Altmannshofer, P. S. B. Dev et al. 'Addressing $R_{D^{(*)}}$, $R_{K^{(*)}}$, muon $g-2$ and ANITA anomalies in a minimal R-parity violating supersymmetric framework'. In: *Phys. Rev.* D 102 (2020), 015031. DOI: 10.1103/PhysRevD.102.015031. arXiv: 2002.12910 [hep-ph].

[81] Q.-Y. Hu and L.-L. Huang. 'Explaining $b\to s\ell^+\ell^-$ data by sneutrinos in the R-parity violating MSSM'. In: *Phys. Rev.* D 101 (2020), 035030. DOI: 10.1103/PhysRevD.101.035030. arXiv: 1912.03676 [hep-ph].

[82] D. Bardhan, D. Ghosh and D. Sachdeva. *$R_{K^{(*)}}$ from RPV-SUSY sneutrinos*. 2021. arXiv: 2107.10163 [hep-ph].

[83] Linear Collider Collaboration. *The International Linear Collider*. Technical Design Report. 4 vols. 2013. URL: https://www.linearcollider.org/.
vol. 1: *Executive Summary*. Ed. by T. Behnke, J. E. Brau et al. 2013.
Vol. 2: *Physics*. Ed. by H. Baer, T. Barklow et al. 2013.
Vol. 3.I: *Accelerator. R&D in the Technical Design Phase*. Ed. by C. Adolphsen, M. Barone et al. 2013.
Vol. 3.II: *Accelerator. Baseline Design*. Ed. by C. Adolphsen, M. Barone et al. 2013.
Vol. 4: *Detectors*. Ed. by T. Behnke, J. E. Brau et al. 2013.

[84] Linear Collider Collaboration. *The International Linear Collider Machine Staging Report 2017*. Ed. by L. Evans and S. Michizono. 2017. arXiv: 1711.00568 [physics.acc-ph].

[85] K. Fujii, C. Grojean et al. *Physics Case for the 250 GeV Stage of the International Linear Collider*. 2017. arXiv: 1710.07621 [hep-ex].

[86] P. Bambade, T. Barklow et al. *The International Linear Collider: A Global Project*. 2019. arXiv: 1903.01629 [hep-ex].

[87] ILD Collaboration. *International Large Detector*. Interim Design Report. Ed. by T. Behnke, K. Büsser et al. 2020. arXiv: 2003.01116 [physics.ins-det].

[88] URL: https://ilchome.web.cern.ch/content/images-and-graphics.

[89] Linear Collider Collaboration. *The International Linear Collider*. Technical Design Report. Vol. 3.I: *Accelerator. R&D in the Technical Design Phase*. Ed. by C. Adolphsen, M. Barone et al. 2013. arXiv: 1306.6353 [physics.acc-ph].

[90] Linear Collider Collaboration. *The International Linear Collider*. Technical Design Report. Vol. 3.II: *Accelerator. Baseline Design*. Ed. by C. Adolphsen, M. Barone et al. 2013. arXiv: 1306.6328 [physics.acc-ph].

[91] T. Nishitani, T. Nakanishi et al. 'Highly polarized electrons from GaAs–GaAsP and InGaAs–AlGaAs strained-layer superlattice photocathodes'. In: *J. Appl. Phys.* 97 (2005), 094907. DOI: 10.1063/1.1886888.

[92] TESLA Collaboration. *TESLA. The Superconducting Electron Positron Linear Collider with an Integrated X-Ray Laser Laboratory*. Technical Design Report. Vol. II: *The Accelerator*. Ed. by R. Brinkmann, K. Flöttmann et al. Deutsches Elektronen-Synchrotron, DESY, 2001. URL: https://bib-pubdb1.desy.de/record/352520.

[93] S. Schreiber and B. Faatz. 'The free-electron laser FLASH'. In: *High Power Laser Science and Engineering* 3 (2015), e20. DOI: 10.1017/hpl.2015.16.

[94] R. Abela, A. Aghababyan et al. *XFEL: The European X-Ray Free-Electron Laser*. Technical Design Report. Ed. by M. Altarelli, R. Brinkmann et al. Hamburg: Deutsches Elektronen-Synchrotron DESY, 2006. DOI: 10.3204/DESY_06-097.

[95] D. Reschke, V. Gubarev et al. 'Performance in the vertical test of the 832 nine-cell 1.3 GHz cavities for the European X-ray Free Electron Laser'. In: *Phys. Rev. Accel. Beams* 20 (2017), 042004. DOI: 10.1103/PhysRevAccelBeams.20.042004.

[96] W. Decking, S. Abeghyan et al. 'A MHz-repetition-rate hard X-ray free-electron laser driven by a superconducting linear accelerator'. In: *Nat. Photonics* 14 (2020), 391–397. DOI: 10.1038/s41566-020-0607-z.

[97] S. Boogert, A. F. Hartin et al. 'Polarimeters and energy spectrometers for the ILC Beam Delivery System'. In: *J. Instrum.* 4 (2009), P10015. DOI: 10.1088/1748-0221/4/10/p10015.

[98] R. B. Palmer. 'Energy Scaling, Crab Crossing, and the Pair Problem'. In: *Proceedings of the Summer Study on High-energy Physics in the 1990s* (Snowmass, CO, USA, 27th June–15th July 1988). Ed. by S. Jensen. Singapore: World Scientific, 1989.

[99] G. Burt, P. Ambattu et al. 'Crab cavities for linear colliders'. In: 24th International Linear Accelerator Conference (Victoria, BC, Canada, 29th Sept.–3rd Oct. 2008). Conf. Proc. C0809292. 2008, 830–832. arXiv: 0810.2880 [physics.acc-ph].

[100] K. Yokoya. *Luminosity improvement at 250GeV CM*. ILC Change Request ILC-CR-0016. Linear Collider Collaboration, 2017. URL: https://edmsdirect.desy.de/item/D00000001159725.

[101] K. Yokoya and P. Chen. 'Beam-beam phenomena in linear colliders'. In: *Frontiers of Particle Beams: Intensity Limitations*. Ed. by M. Dienes, M. Month and S. Turner. Vol. 400. Lecture Notes in Physics. Springer, 1992, 415–445. DOI: 10.1007/3-540-55250-2_37.

[102] D. Schulte. 'Beam-Beam Effects in Linear Colliders'. In: *ICFA Beam Dyn. Newsl.* 69 (2016), 237–245. URL: https://cds.cern.ch/record/2264414.

[103] A. Vogel. 'Beam-Induced Backgrounds in Detectors at the ILC'. Doctoral thesis. Universität Hamburg, 2008. DOI: 10.3204/DESY-THESIS-2008-036.

[104] Linear Collider Collaboration. *The International Linear Collider*. Technical Design Report. Vol. 1: *Executive Summary*. Ed. by T. Behnke, J. E. Brau et al. 2013. arXiv: 1306.6327 [physics.acc-ph].

[105] Linear Collider Collaboration. *The International Linear Collider*. Technical Design Report. Vol. 4: *Detectors*. Ed. by T. Behnke, J. E. Brau et al. 2013. arXiv: 1306.6329 [physics.ins-det].

[106] Linear Collider Collaboration. *The International Linear Collider*. Technical Design Report. Vol. 2: *Physics*. Ed. by H. Baer, T. Barklow et al. 2013. arXiv: 1306.6352 [hep-ph].

[107] M. Boronat, J. Fuster et al. 'Jet reconstruction at high-energy electron-positron colliders'. In: *Eur. Phys. J.* C 78 (2018), 144. DOI: 10.1140/epjc/s10052-018-5594-6.

[108] T. Barklow, J. Brau et al. *ILC Operating Scenarios*. 2015. arXiv: 1506.07830 [hep-ex].

[109] R. L. Gluckstern. 'Uncertainties in track momentum and direction, due to multiple scattering and measurement errors'. In: *Nucl. Instrum. Methods* 24 (1963), 381–389. DOI: 10.1016/0029-554X(63)90347-1.

[110] ILD Concept Group. *The International Large Detector*. Letter of Intent. 2010. DOI: 10.2172/975166. arXiv: 1006.3396 [hep-ex].

[111] J. Krüger. 'The Uranium scintillator calorimeter for the ZEUS detector at the electron - proton collider HERA: The Heart of ZEUS'. Habilitation. Universität Hamburg, 1992. URL: https://bib-pubdb1.desy.de/record/309535.

[112] OPAL Collaboration. 'The OPAL detector at LEP'. In: *Nucl. Instrum. Methods Phys. Res.* A 305 (1991), 275–319. DOI: 10.1016/0168-9002(91)90547-4.

[113] F. Cavallari. 'Performance of calorimeters at the LHC'. In: *J. Phys. Conf. Ser.* 293 (2011): *XIV International Conference on Calorimetry in High Energy Physics (CALOR 2010) 10–14 May 2010, Beijing, China*, 012001. DOI: 10.1088/1742-6596/293/1/012001.

[114] M. A. Thomson. 'Particle flow calorimetry and the PandoraPFA algorithm'. In: *Nucl. Instrum. Methods Phys. Res.* A 611 (2009), 25–40. DOI: 10.1016/j.nima.2009.09.009.

[115] J. S. Marshall and M. A. Thomson. 'The Pandora Particle Flow Algorithm'. In: *Proceedings of the International Conference on Calorimetry for the High Energy Frontier* (Paris, France, 22nd–25th Apr. 2013). 2013, 305–315. arXiv: 1308.4537 [physics.ins-det].

[116] C. Adloff, Y. Karyotakis et al. 'Response of the CALICE Si-W electromagnetic calorimeter physics prototype to electrons'. In: *Nucl. Instrum. Methods Phys. Res.* A 608 (2009), 372–383. DOI: 10.1016/j.nima.2009.07.026. arXiv: 0811.2354 [physics.ins-det].

[117] J. Repond, L. Xia et al. 'Construction and response of a highly granular scintillator-based electromagnetic calorimeter'. In: *Nucl. Instrum. Methods Phys. Res.* A 887 (2018), 150–168. DOI: 10.1016/j.nima.2018.01.016. arXiv: 1707.07126 [physics.ins-det].

[118] J. Repond, L. Xia et al. 'Hadronic energy resolution of a combined high granularity scintillator calorimeter system'. In: *J. Instrum.* 13 (2018), P12022. DOI: 10.1088/1748-0221/13/12/p12022. arXiv: 1809.03909 [physics.ins-det].

[119] K. Ackermann, S. Arai et al. *Results from a TPC Prototype for the Linear Collider Tracker with the MWPC and GEM Endplate Technologies*. LC Note LC-DET-2012-066. 2012. URL: https://flc.desy.de/lcnotes.

[120] F. Sauli. 'GEM: A new concept for electron amplification in gas detectors'. In: *Nucl. Instrum. Methods Phys. Res.* A 386 (1997), 531–534. DOI: 10.1016/S0168-9002(96)01172-2.

[121] Y. Giomataris, P. Rebourgeard et al. 'MICROMEGAS: a high-granularity position-sensitive gaseous detector for high particle-flux environments'. In: *Nucl. Instrum. Methods Phys. Res.* A 376 (1996), 29–35. DOI: 10.1016/0168-9002(96)00175-1.

[122] J. Kaminski, Y. Bilevych et al. 'GridPix detectors – introduction and applications'. In: *Nucl. Instrum. Methods Phys. Res.* A 845 (2017): *Proceedings of the Vienna Conference on Instrumentation 2016*. Ed. by G. Badurek, T. Bergauer et al., 233–235. DOI: 10.1016/j.nima.2016.05.134.

Part I

[18] Particle Data Group. 'Review of Particle Physics'. In: *Phys. Rev.* D 98 (2018), 030001. DOI: 10.1103/PhysRevD.98.030001.

[87] ILD Collaboration. *International Large Detector*. Interim Design Report. Ed. by T. Behnke, K. Büsser et al. 2020. arXiv: 2003.01116 [physics.ins-det].

[105] Linear Collider Collaboration. *The International Linear Collider*. Technical Design Report. Vol. 4: *Detectors*. Ed. by T. Behnke, J. E. Brau et al. 2013. arXiv: 1306.6329 [physics.ins-det].

[119] K. Ackermann, S. Arai et al. *Results from a TPC Prototype for the Linear Collider Tracker with the MWPC and GEM Endplate Technologies*. LC Note LC-DET-2012-066. 2012. URL: https://flc.desy.de/lcnotes.

[120] F. Sauli. 'GEM: A new concept for electron amplification in gas detectors'. In: *Nucl. Instrum. Methods Phys. Res.* A 386 (1997), 531–534. DOI: 10.1016/S0168-9002(96)01172-2.

[121] Y. Giomataris, P. Rebourgeard et al. 'MICROMEGAS: a high-granularity position-sensitive gaseous detector for high particle-flux environments'. In: *Nucl. Instrum. Methods Phys. Res.* A 376 (1996), 29–35. DOI: 10.1016/0168-9002(96)00175-1.

[123] O. Schäfer. 'Ein Monitorsystem für Gasbasierte Detektoren am International Linear Collider (ILC)'. German. Diploma thesis. Universität Rostock, 2006.

[124] W. Blum, W. Riegler and L. Rolandi. *Particle Detection with Drift Chambers*. 2nd ed. Particle Acceleration and Detection. Springer, 2008. DOI: 10.1007/978-3-540-76684-1.

[125] F. M. Penning. 'Über Ionisation durch metastabile Atome'. German. In: *Naturwiss.* 15 (1927), 818. DOI: 10.1007/BF01505431.

[126] W. P. Jesse and J. Sadauskis. 'Alpha-Particle Ionization in Mixtures of the Noble Gases'. In: *Phys. Rev.* 88 (1952), 417–418. DOI: 10.1103/PhysRev.88.417.

[127] W. Blum, K. Söchting and U. Stierlin. 'Gas phenomena in spark chambers'. In: *Phys. Rev.* A 10 (1974), 491–498. DOI: 10.1103/PhysRevA.10.491.

[128] M. Inokuti. 'Ionization Yields in Gases under Electron Irradiation'. In: *Radiat. Res.* 64 (1975), 6–22. DOI: 10.2307/3574165.

[129] D. Combecher. 'Measurement of W Values of Low-Energy Electrons in Several Gases'. In: *Radiat. Res.* 84 (1980), 189–218. DOI: 10.2307/3575293.

[130] L. G. Christophorou. *Atomic and molecular radiation physics*. Wiley monographs in chemical physics. London: Wiley, 1971.

[131] H. Bethe. 'Zur Theorie des Durchgangs schneller Korpuskularstrahlen durch Materie'. German. In: *Ann. Phys.* 397 (1930), 325–400. DOI: 10.1002/andp.19303970303.

[132] U. Fano. 'Penetration of Protons, Alpha Particles, and Mesons'. In: *Annu. Rev. Nucl. Sci.* 13 (1963), 1–66. DOI: 10.1146/annurev.ns.13.120163.000245.

[133] E. Fermi. 'The Ionization Loss of Energy in Gases and in Condensed Materials'. In: *Phys. Rev.* 57 (1940), 485–493. DOI: 10.1103/PhysRev.57.485.

[134] H. Bethe. 'Quantenmechanik der Ein- und Zwei-Elektronenprobleme'. German. In: *Handbuch der Physik*. Vol. 24.1: *Quantentheorie*. Ed. by H. Bethe, F. Hund et al. 2nd ed. Springer, 1933. Chap. 3, 273–560. DOI: 10.1007/978-3-642-52619-0_3.

[135] W. Yu. 'Particle identification of the ALICE TPC via dE/dx'. In: *Nucl. Instrum. Methods Phys. Res. A*. Vol. 706: *TRDs for the Third Millenium*. 4th Workshop on Advanced Transition Radiation Detectors for Accelerators and Space Applications (Bari, Italy, 14th–16th Sept. 2011). Ed. by P. Fusco, C. Favuzzi et al. 2013, 55–58. DOI: 10.1016/j.nima.2012.05.022.

[136] F. Lapique and F. Piuz. 'Simulation of the measurement by primary cluster counting of the energy lost by a relativistic ionizing particle in argon'. In: *Nucl. Instrum. Methods* 175 (1980), 297–318. DOI: 10.1016/0029-554X(80)90744-2.

[137] H. Fischle, J. Heintze and B. Schmidt. 'Experimental determination of ionization cluster size distributions in counting gases'. In: *Nucl. Instrum. Methods Phys. Res.* A 301 (1991), 202–214. DOI: 10.1016/0168-9002(91)90460-8.

[138] L. D. Landau. 'On the energy loss of fast particles by ionisation'. In: *J. Phys. (USSR)* 8 (1944), 201–205. Also in: D. Ter Haar, ed. *Collected Papers of L. D. Landau*. Pergamon, 1965. DOI: 10.1016/B978-0-08-010586-4.50061-4. URL: https://www.sciencedirect.com/science/article/pii/B9780080105864500614.

[139] P. V. Vavilov. 'Ionization Losses of High-Energy Heavy Particles'. In: *Sov. Phys. - JETP* 5 (1957), 749.

[140] V. Chechin and V. Ermilova. 'The ionization-loss distribution at very small absorber thickness'. In: *Nucl. Instrum. Methods* 136 (1976), 551–558. DOI: 10.1016/0029-554X(76)90380-3.

[141] V. Ermilova, L. Kotenko and G. Merzon. 'Fluctuations and the most probable values of relativistic charged particle energy loss in thin gas layers'. In: *Nucl. Instrum. Methods* 145 (1977), 555–563. DOI: 10.1016/0029-554X(77)90586-9.

[142] L. G. Christophorou and D. L. McCorkle. 'Experimental evidence for the existence of a Ramsauer–Townsend minimum in liquid CH4 and Ar (Kr and Xe) and in gaseous C_2H_6 and C_3H_8'. In: *Can. J. Chem.* 55 (1977), 1876–1884. DOI: 10.1139/v77-262.

[143] C. Ramsauer. 'Über den Wirkungsquerschnitt der Gasmoleküle gegenüber langsamen Elektronen. I. Fortsetzung'. German. In: *Ann. Phys.* 371 (1922), 546–558. DOI: 10.1002/andp.19223712403.

[144] E. B. Wagner, F. J. Davis and G. S. Hurst. 'Time-of-Flight Investigations of Electron Transport in Some Atomic and Molecular Gases'. In: *J. Chem. Phys.* 47 (1967), 3138–3147. DOI: 10.1063/1.1712365.

[145] J. H. Parker and J. J. Lowke. 'Theory of Electron Diffusion Parallel to Electric Fields. I. Theory'. In: *Phys. Rev.* 181 (1969), 290–301. DOI: 10.1103/PhysRev.181.290.

[146] F. Bloch and N. E. Bradbury. 'On the Mechanism of Unimolecular Electron Capture'. In: *Phys. Rev.* 48 (1935), 689–695. DOI: 10.1103/PhysRev.48.689.

[147] A. Herzenberg. 'Attachment of Slow Electrons to Oxygen Molecules'. In: *J. Chem. Phys.* 51 (1969), 4942–4950. DOI: 10.1063/1.1671887.

[148] B. L. Blaney and G. E. Ewing. 'Van Der Waals Molecules'. In: *Annu. Rev. Phys. Chem.* 27 (1976), 553–584. DOI: 10.1146/annurev.pc.27.100176.003005.

[149] H. Shimamori and H. Hotta. 'Mechanism of thermal electron attachment to O_2: Isotope effect studies with $^{18}O_2$ in rare gases and some hydrocarbons'. In: *J. Chem. Phys.* 81 (1984), 1271–1276. DOI: 10.1063/1.447813.

[150] R. I. Schoen. 'Absorption, Ionization, and Ion-Fragmentation Cross Sections of Hydrocarbon Vapors under Vacuum-Ultraviolet Radiation'. In: *J. Chem. Phys.* 37 (1962), 2032–2041. DOI: 10.1063/1.1733423.

[151] A. Dwuraźny, K. Jeleń and E. Rulikowska Zarbska. 'Inorganic gas mixtures for proportional counters'. In: *Nucl. Instrum. Methods Phys. Res.* 217 (1983), 301–304. DOI: 10.1016/0167-5087(83)90153-9.

[152] A. von Engel. 'Ionization in Gases by Electrons in Electric Fields'. In: *Encyclopedia of Physics / Handbuch der Physik*. Vol. 21: *Electron-Emission Gas Discharges I / Elektronen-Emission Gasentladungen I*. Ed. by S. Flügge. Springer, 1956. Chap. 8, 504–573. DOI: 10.1007/978-3-642-45844-6_8.

[153] W. Legler. 'Zur Statistik der Elektronenlawinen'. German. In: *Z. Phys.* 140 (1955), 221–240. DOI: 10.1007/BF01349380.

[154] W. Legler. 'Die Statistik der Elektronenlawinen in elektronegativen Gasen, bei hohen Feldstärken und bei grosser Gasverstarkung'. German. In: *Z. Naturforschg.* A 16 (1961), 253–261. DOI: 10.1515/zna-1961-0308.

[155] H. Schlumbohm. 'Zur Statistik der Elektronenlawinen im ebenen Feld. III'. German. In: *Z. Phys.* 151 (1958), 563–576. DOI: 10.1007/BF01338427.

[156] G. D. Alkhazov. 'Statistics of electron avalanches and ultimate resolution of proportional counters'. In: *Nucl. Instrum. Methods* 89 (1970), 155–165. DOI: 10.1016/0029-554X(70)90818-9.

[157] W. Shockley. 'Currents to Conductors Induced by a Moving Point Charge'. In: *J. Appl. Phys.* 9 (1938), 635–636. DOI: 10.1063/1.1710367.

[158] S. Ramo. 'Currents Induced by Electron Motion'. In: *Proc. IRE* 27 (1939), 584–585. DOI: 10.1109/JRPROC.1939.228757.

[159] G. Charpak, R. Bouclier et al. 'The use of multiwire proportional counters to select and localize charged particles'. In: *Nucl. Instrum. Methods* 62 (1968), 262–268. DOI: 10.1016/0029-554X(68)90371-6.

[160] J. Alme, Y. Andres et al. 'The ALICE TPC, a large 3-dimensional tracking device with fast readout for ultra-high multiplicity events'. In: *Nucl. Instrum. Methods Phys. Res.* A 622 (2010), 316–367. DOI: 10.1016/j.nima.2010.04.042.

[161] F. Sauli. 'Recent topics on gaseous detectors'. In: *Nucl. Instrum. Methods Phys. Res. A*. Vol. 623. 1st International Conference on Technology and Instrumentation in Particle Physics (Tsukuba, Japan, 12th–17th Mar. 2009). Ed. by H. Iwasaki, T. K. Komatsubara and Y. Sugimoto. 1. 2010, 29–34. DOI: 10.1016/j.nima.2010.02.146.

[162] *Gas Detectors Development Group*. CERN. 2021. URL: https://gdd.web.cern.ch/.

[163] M. Villa, S. D. Pinto et al. 'Progress on large area GEMs'. In: *Nucl. Instrum. Methods Phys. Res. A*. Vol. 628: *VCI 2010*. 12th International Vienna Conference on Instrumentation (Vienna, Austria, 15th–20th Feb. 2010). Ed. by T. Bergauer, J. Hrubec et al. 1. 2011, 182–186. DOI: 10.1016/j.nima.2010.06.312.

[164] Y. Takeuchi, K. Komiya et al. 'Development and properties of 100 mm-square size LTCC-GEM'. In: *J. Phys. Conf. Ser.* Vol. 1498. 6th International Conference on Micro Pattern Gaseous Detectors (La Rochelle, France, 5th–10th May 2019). IOP Publishing, 2020, 012011. DOI: 10.1088/1742-6596/1498/1/012011.

[165] H. Takahashi, Y. Mitsuya et al. 'Development of a glass GEM'. In: *Nucl. Instrum. Methods Phys. Res.* A 724 (2013), 1–4. DOI: 10.1016/j.nima.2013.04.089.

[166] R. Chechik, A. Breskin et al. 'Thick GEM-like hole multipliers: properties and possible applications'. In: *Nucl. Instrum. Methods Phys. Res. A*. Vol. 535. 10th International Vienna Conference on Instrumentation (Vienna, Austria, 16th–21st Feb. 2004). Ed. by M. Jeitler, M. Krammer et al. 1. 2004, 303–308. DOI: 10.1016/j.nima.2004.07.138.

[167] F. Sauli. 'The gas electron multiplier (GEM): Operating principles and applications'. In: *Nucl. Instrum. Methods Phys. Res.* A 805 (2016): *Special Issue in memory of Glenn F. Knoll*. Ed. by D. Wehe, 2–24. DOI: 10.1016/j.nima.2015.07.060.

[168] M. Blatnik, K. Dehmelt et al. 'Performance of a Quintuple-GEM Based RICH Detector Prototype'. In: *IEEE Trans. Nucl. Sci.* 62 (2015), 3256–3264. DOI: 10.1109/TNS.2015.2487999. arXiv: 1501.03530 [physics.ins-det].

[169] K. Zenker. 'Studies of field distortions in a Time Projection Chamber for the International Linear Collider'. Doctoral thesis. Universität Hamburg, 2014. URL: https://bib-pubdb1.desy.de/record/207651.

[170] A. Bondar, A. Buzulutskov et al. 'Study of ion feedback in multi-GEM structures'. In: *Nucl. Instrum. Methods Phys. Res.* A 496 (2003), 325–332. DOI: 10.1016/S0168-9002(02)01763-1.

[171] ALICE Collaboration. *Upgrade of the ALICE Time Projection Chamber*. Technical Design Report. CERN, 2013. URL: https://cds.cern.ch/record/1622286.

[172] *Electronic Substrates Overview. Thin-Film & Thick-Film Ceramic Substrates*. ADS-96R. CoorsTek, Inc., 2017.

[173] *Industrial Laminating Thermosetting Products*. NEMA Standards Publication LI 1-1998 (R2011). National Electrical Manufacturers Association, 2012. URL: https://www.nema.org/Standards/view/Industrial-Laminated-Thermosetting-Products.

[174] *Araldite AY 103-1 / HY 991. Low viscosity two component epoxy adhesive system*. Technical Data Sheet. Switzerland: Huntsman Advanced Materials GmbH, 2004.

[175] M. R. Blom. 'Ageing of the LHCb outer tracker'. MA thesis. Nikhef, Amsterdam, 2009. URL: https://inspirehep.net/record/887134/files/CERN-THESIS-2009-089.pdf.

[176] R. Koopman. 'Ageing of the LHCb Outer Tracker & b - Hadron Production and Decay at $\sqrt{s} = 7$ TeV'. Doctoral thesis. Amsterdam U., 2015. URL: https://www.nikhef.nl/pub/services/biblio/theses_pdf/thesis_R_Koopman.pdf.

[177] *STYCAST 1266 A/B. Two Component, Low Viscosity, Epoxy Encapsulant*. Technical Data Sheet. Emerson & Cuming, 2003.

[178] M. Capeans. 'Aging and materials: lessons for detectors and gas systems'. In: *Nucl. Instrum. Methods Phys. Res.* A 515 (2003): *Proceedings of the International Workshop on Aging Phenomena in Gaseous Detectors*, 73–88. DOI: 10.1016/j.nima.2003.08.134.

[179] *TS9701/TS9702 Microprocessor-Controlled Dispenser*. Techcon Systems, Inc. URL: https://www.adhesivesandsealants.com/doc/ts9701ts9702-microprocessor-controlled-dispen-0001.

[180] *LT Series Technical Data*. Lang GmbH & Co. KG. URL: https://www.lang.de/en/product-overview/automation-systems/linear-axis/lt-series/.

[181] *GT Series Technical Data*. Lang GmbH & Co. KG. URL: https://www.lang.de/en/product-overview/automation-systems/cross-tables/gt-series/.

[182] *LSTEP express*. Lang GmbH & Co. KG. URL: https://www.lang.de/en/product-overview/automation-systems/positioning-system/lstep-express/.

[183] *LabVIEW Website*. National Instruments Corporation. URL: https://www.ni.com/labview.

[184] C. Altunbas, M. Capéans et al. 'Construction, test and commissioning of the triple-gem tracking detector for compass'. In: *Nucl. Instrum. Methods Phys. Res.* A 490 (2002), 177–203. DOI: 10.1016/S0168-9002(02)00910-5.

[185] L. Hallermann. 'Analysis of GEM Properties and Development of a GEM Support Structure for the ILD Time Projection Chamber'. Doctoral thesis. Universität Hamburg, 2010. DOI: 10.3204/DESY-THESIS-2010-015.

[186] P. Schade. *Correction Methods for TPC Operation in Inhomogeneous Magnetic Fields*. LC Note LC-DET-2010-001. 2010. URL: https://flc.desy.de/lcnotes.

[187] P. Schade. 'Development and Construction of a Large TPC Prototype for the ILC and Study of τ Polarisation in $\tilde{\tau}$ Decays with the ILD Detector'. Doctoral thesis. Universität Hamburg, 2009. DOI: 10.3204/DESY-THESIS-2009-040.

[188] T. Krautscheid. 'Simulationen zur Ionenrückdrift in einer Zeit-Projektionskammer am ILC'. German. Diploma thesis. Universität Bonn, 2008.

[189] *Laser Displacement Sensor Technology Book*. KEYENCE CORPORATION. 2008. URL: https://www.keyence.com.

[190] *LK-G Series User's Manual*. KEYENCE CORPORATION. 2016. URL: https://www.keyence.com/products/measure/laser-1d/lk-g3000/models/lk-g10/index.jsp.

[191] J. Gurland and R. C. Tripathi. 'A Simple Approximation for Unbiased Estimation of the Standard Deviation'. In: *Am. Stat.* 25 (1971), 30–32. DOI: 10.2307/2682923.

[192] B. Sobloher. 'Simulationsstudien zu GEM-Folien für die Auslese einer TPC'. German. Diploma thesis. RWTH Aachen, 2002.

[193] T2K ND280 TPC Collaboration. 'Time Projection Chambers for the T2K Near Detectors'. In: *Nucl. Instrum. Methods Phys. Res.* A 637 (2011), 25–46. DOI: 10.1016/j.nima.2011.02.036. arXiv: 1012.0865 [physics.ins-det].

[194] A. Münnich. 'Simulation studies for a high resolution time projection chamber at the international linear collider'. Doctoral thesis. RWTH Aachen, 2007. URL: https://publications.rwth-aachen.de/record/52595.

[195] TESLA Collaboration. *TESLA. The Superconducting Electron Positron Linear Collider with an Integrated X-Ray Laser Laboratory*. Technical Design Report. 6 vols. Deutsches Elektronen-Synchrotron, DESY, 2001. URL: https://flash.desy.de/tesla_technology_collaboration/tesla_documentation/.
vol. I: *Executive Summary*. Ed. by F. Richard, J. R. Schneider et al. 2001.
Vol. II: *The Accelerator*. Ed. by R. Brinkmann, K. Flöttmann et al. 2001.
Vol. III: *Physics at an e^+ e^- Linear Collider*. Ed. by R.-D. Heuer, D. Miller et al. 2001.
Vol. IV: *A Detector for TESLA*. Ed. by T. Behnke, S. Bertolucci et al. 2001.
Vol. V: *The X-RAY Free Electron Laser*. Ed. by G. Materlik and T. Tschentscher. 2001.
Vol. VI: *Appendices*. Ed. by R. Klanner, V. Telnov et al. 2001.

[196] B. Beyer and O. A. Bach. Internal communication. Hamburg: Deutsches Elektronen-Synchrotron, DESY, 2015.

[197] *ANSYS Website*. ANSYS, Inc. URL: https://www.ansys.com.

[198] K. Magnus and H. H. Müller-Slany. *Grundlagen der technischen Mechanik*. German. 7th ed. Leitfäden der angewandten Mathematik und Mechanik. Wiesbaden: Teubner, 2005.

[199] R. Diener, J. Dreyling-Eschweiler et al. 'The DESY II test beam facility'. In: *Nucl. Instrum. Methods Phys. Res.* A 922 (2019), 265–286. DOI: 10.1016/j.nima.2018.11.133. arXiv: 1807.09328 [physics.ins-det].

[200] A. Yamamoto, K. Anraku et al. 'Balloon-borne experiment with a superconducting solenoidal magnet spectrometer'. In: *Adv. Space Res.* 14 (1994), 75–87. DOI: 10.1016/0273-1177(94)90071-X.

[201] J. Alozy, F. Bergsma, F. Formenti et al. *First Version of the PCMAG Field Map*. Eudet-Memo 2007-51. 2007. URL: https://www.eudet.org/e26/e28/e182/e599/eudet-memo-2007-51.pdf.

[202] C. Grefe. 'Magnetic Field Map for a Large TPC Prototype'. Diploma thesis. Hamburg: Universität Hamburg, 2008. DOI: 10.3204/DESY-THESIS-2008-052.

[203] O. Schäfer. *A Slow Control System for R&D Studies on TPCs*. LC Note LC-DET-2008-005. 2008. URL: https://flc.desy.de/lcnotes.

[204] S. Goloborodko, G. Grygiel et al. 'DOOCS: an Object Oriented Control System as the Integrating Part for the TTF Linac'. In: International Conference on Accelerator and Large Experimental Physics Control Systems (Beijing, China, 3rd–7th Nov. 1997). 1997.

[205] *DOOCS. The Distributed Object-Oriented Control System Framework*. Deutsches Elektronen-Synchrotron, DESY. URL: https://doocs-web.desy.de/index.html.

[206] *MKS Type 1179A and 2179A Mass Flow Controller and Type 179A Mass Flow Meter Operation Manual*. MKS Instruments, Inc. 1999. URL: https://www.mksinst.com.

[207] *Dew Point Instrument DP3-D-SH*. formerly MBW Elektronik AG. MBW Calibration AG. URL: https://www.mbw.ch.

[208] *XLT-12-123 PPM Oxygen Sensor-Replacment for A2C, OX2 and T2*. Analytical Industries Inc. URL: https://aii1.com.

[209] FuG Elektronik GmbH. URL: https://www.fug-elektronik.de.

[210] *Mod. SY2527 Universal Multichannel Power Supply System*. User's Manual. CAEN S.p.A. 2002. URL: https://www.caen.it.

[211] *Mod. A1732-A1832 High Voltage Boards*. User's Manual. Version 7. CAEN S.p.A. 2010. URL: https://www.caen.it.

[212] LCTPC Collaboration. 'A Time projection chamber with GEM-Based readout'. In: *Nucl. Instrum. Methods Phys. Res.* A 856 (2017), 109–118. DOI: 10.1016/j.nima.2016.11.002. arXiv: 1604.00935 [physics.ins-det].

[213] T. Behnke, K. Dehmelt et al. 'A lightweight field cage for a large TPC prototype for the ILC'. In: *J. Instrum.* 5 (2010), 10011. DOI: 10.1088/1748-0221/5/10/P10011.

[214] D. Peterson. *Development of a Low-Material TPC Endplate for ILD*. LC Note LC-DET-2012-072. 2012. URL: https://flc.desy.de/lcnotes.

[215] L. Musa, J. Baechler et al. 'The ALICE TPC Front End Electronics'. In: *Conference Record of the IEEE Nuclear Science Symposium* (Portland, OR, USA, 19th Oct. 2003–25th Oct. 2013). Vol. 5. IEEE, 2004, 3647–3651. DOI: 10.1109/NSSMIC.2003.1352697.

[216] *Detector R&D towards the International Linear Collider*. EUDET. URL: https://www.eudet.org.

[217] V. Hedberg, L. Jönsson et al. *Development of the Readout System for a TPC at the Future Linear Collider*. LC Note LC-DET-2012-080. 2012. URL: https://flc.desy.de/lcnotes.

[218] R. Esteve Bosch, A. Jimenez de Parga et al. 'The ALTRO chip: A 16-channel A/D converter and digital processor for gas detectors'. In: *IEEE Trans. Nucl. Sci.* 50 (2003), 2460–2469. DOI: 10.1109/TNS.2003.820629.

[219] L. Jönsson and U. Mjörnmark. *Front-end electronics and data acquisition for the LCTPC*. Eudet-Memo 2007-53. 2007. URL: https://www.eudet.org/e26/e28/e182/e605/eudet-memo-2007-53.pdf.

[220] A. Oskarsson, K. Dehmelt et al. *A General Purpose Electronic readout system for tests of Time Projection Chambers, equipped with different avalanche multiplication systems*. Eudet-Memo 2008-49. 2008. URL: https://www.eudet.org/e26/e28/e615/e830/eudet-memo-2008-49.pdf.

[221] C. G. Gutierrez, R. Campagnolo et al. 'The ALICE TPC Readout Control Unit'. In: *Conference Record of the IEEE Nuclear Science Symposium* (Fajardo, Puerto Rico, 23rd–29th Oct. 2005). Vol. 1. IEEE, 2006, 575–579. DOI: 10.1109/NSSMIC.2005.1596317.

[222] T2K Collaboration. 'The T2K experiment'. In: *Nucl. Instrum. Methods Phys. Res.* A 659 (2011), 106–135. DOI: 10.1016/j.nima.2011.06.067.

[223] F. J. Müller. 'Development of a Triple GEM Readout Module for a Time Projection Chamber & Measurement Accuracies of Hadronic Higgs Branching Fractions in $\nu\nu$H at a 350 GeV ILC'. Doctoral thesis. Universität Hamburg, 2016. DOI: 10.3204/PUBDB-2016-02659.

[224] T. Behnke and F. Gaede. 'Software for the international linear collider: Simulation and reconstruction frameworks'. In: *Pramana – J. Phys.* 69 (2007), 1089–1092. DOI: 10.1007/s12043-007-0233-z.

[225] *ILC Software Website*. Deutsches Elektronen-Synchrotron, DESY. URL: https://ilcsoft.desy.de.

[226] S. Aplin, J. Engels et al. 'LCIO: A persistency framework and event data model for HEP'. In: *Conference Record of the 2012 IEEE Nuclear Science Symposium and Medical Imaging Conference* (Anaheim, California, 29th Oct.–3rd Nov. 2012). 2013, 2075–2079. DOI: 10.1109/NSSMIC.2012.6551478.

[227] *Homepage of the Gear toolkit*. Deutsches Elektronen-Synchrotron, DESY. URL: https://ilcsoft.desy.de/portal/software_packages/gear/.

[228] F. Gaede. 'Marlin and LCCD: Software tools for the ILC'. In: *Nucl. Instrum. Methods Phys. Res.* A 559 (2006), 177–180. DOI: 10.1016/j.nima.2005.11.138.

[229] J. Abernathy, K. Dehmelt et al. *MarlinTPC: A Marlin based common TPC software framework for the LC-TPC Collaboration.* LC Note LC-TOOL-2007-001. 2007. URL: https://bib-pubdb1.desy.de/record/83142.

[230] I. Heinze. 'Development of a Hough Transformation Track Finder for Time Projection Chambers'. Doctoral thesis. Universität Hamburg, 2013. DOI: 10.3204/DESY-THESIS-2013-055.

[231] T. Krämer. *Track Parameters in LCIO*. LC Note LC-DET-2006-004. 2006. URL: https://bib-pubdb1.desy.de/record/81214.

[232] URL: https://svnsrv.desy.de/desy/marlintpc/branches/malekp/final-thesis-version.

[233] S. F. Biagi. 'Monte Carlo simulation of electron drift and diffusion in counting gases under the influence of electric and magnetic fields'. In: *Nucl. Instrum. Methods Phys. Res.* A 421 (1999), 234–240. DOI: 10.1016/S0168-9002(98)01233-9.

[234] R. Diener. 'Study of Reconstruction Methods for a Time Projection Chamber with GEM Gas Amplification System'. Diploma thesis. Universität Hamburg, 2006. DOI: 10.3204/DESY-THESIS-2006-040.

[235] C. Kleinwort. *A Track Finding Method for a TPC Based on fast Hough Transformation*. LC Note LC-TOOL-2014-006. 2014. URL: https://bib-pubdb1.desy.de/record/193046.

[236] C. Kleinwort. *A Track Finding Method for a TPC Based on Triplet Chains*. LC Note LC-TOOL-2014-004. 2014. URL: https://bib-pubdb1.desy.de/record/193045.

[237] R. Frühwirth. 'Application of Kalman filtering to track and vertex fitting'. In: *Nucl. Instrum. Methods Phys. Res.* A 262 (1987), 444–450. DOI: 10.1016/0168-9002(87)90887-4.

[238] F. Gaede, S. Aplin et al. 'Track reconstruction at the ILC: the ILD tracking software'. In: *J. Phys.* Conf. Ser. 20th International Conference on Computing in High Energy and Nuclear Physics (Amsterdam, The Netherlands, 14th–18th Oct. 2013). Vol. 513.2. IOP Publishing, 2014, 022011. DOI: 10.1088/1742-6596/513/2/022011.

[239] V. Blobel. 'A new fast track-fit algorithm based on broken lines'. In: *Nucl. Instrum. Methods Phys. Res.* A 566 (2006), 14–17. DOI: 10.1016/j.nima.2006.05.156.

[240] C. Kleinwort. 'General Broken Lines as advanced track fitting method'. In: *Nucl. Instrum. Methods Phys. Res.* A 673 (2012), 107–110. DOI: 10.1016/j.nima.2012.01.024. arXiv: 1201.4320 [physics.ins-det].

[241] V. Karimäki. 'Effective circle fitting for particle trajectories'. In: *Nucl. Instrum. Methods Phys. Res.* A 305 (1991), 187–191. DOI: 10.1016/0168-9002(91)90533-V.

[242] R. Yonamine. 'Measuring the top Yukawa coupling at the ILC at $\sqrt{s}$ = 500 GeV and R&D for the ILD-TPC'. Doctoral thesis. The Graduate University for Advanced Studies, 2012.

[243] R. Yonamine, K. Fujii et al. 'Spatial resolutions of GEM TPC. A novel theoretical formula and its comparison to latest beam test data'. In: *J. Instrum.* 9 (2014), C03002. DOI: 10.1088/1748-0221/9/03/c03002.

[244] *Hamburger Luftmessnetz*. German. Behörde für Gesundheit und Verbraucherschutz Hamburg. URL: https://luft.hamburg.de.

[245] D. Jeanne, P. Lazeyras et al. 'High energy particle identification using multilayer proportional counters'. In: *Nucl. Instrum. Methods* 111 (1973), 287–300. DOI: 10.1016/0029-554X(73)90077-3.

[246] M. Hauschild, R.-D. Heuer et al. 'Particle identification with the OPAL jet chamber'. In: *Nucl. Instrum. Methods Phys. Res.* A 314 (1992), 74–85. DOI: 10.1016/0168-9002(92)90501-T.

[247] C. Kleinwort. *Energy loss measurement with the H1 Central Jet Chamber*. H1 note H1-08/08-630. internal. 2008.

[248] H. Breuker, M. Fischer et al. ‘Particle identification with the OPAL jet chamber in the region of the relativistic rise’. In: *Nucl. Instrum. Methods Phys. Res.* A 260 (1987), 329–342. DOI: 10.1016/0168-9002(87)90097-0.

[249] ALEPH Collaboration. ‘ALEPH: A detector for electron-positron annihilations at LEP’. In: *Nucl. Instrum. Methods Phys. Res.* A 294 (1990), 121–178. DOI: 10.1016/0168-9002(90)91831-U.

[250] ALEPH Collaboration. *The ALEPH handbook: 1989*. Ed. by W. Blum. Geneva, Switzerland: CERN, 1989. URL: https://cds.cern.ch/record/227125.

[251] DELPHI Collaboration. ‘Performance of the HPC calorimeter in DELPHI’. In: *IEEE Trans. Nucl. Sci.* 42 (1995), 491–498. DOI: 10.1109/23.467923.

[252] NA49 Collaboration. ‘The NA49 large acceptance hadron detector’. In: *Nucl. Instrum. Methods Phys. Res.* A 430 (1999), 210–244. DOI: 10.1016/S0168-9002(99)00239-9.

[253] W. W. M. Allison and J. H. Cobb. ‘Relativistic Charged Particle Identification by Energy Loss’. In: *Annu. Rev. Nucl. Part. Sci.* 30 (1980), 253–298. DOI: 10.1146/annurev.ns.30.120180.001345.

[254] A. H. Walenta. ‘The Time Expansion Chamber and Single Ionization Cluster Measurement’. In: *IEEE Trans. Nucl. Sci.* 26 (1979), 73–80. DOI: 10.1109/TNS.1979.4329616.

[255] A. H. Walenta, J. Fischer et al. ‘Measurement of the ionization loss in the region of relativistic rise for noble and molecular gases’. In: *Nucl. Instrum. Methods* 161 (1979), 45–58. DOI: 10.1016/0029-554X(79)90360-4.

Part II

[18] Particle Data Group. 'Review of Particle Physics'. In: *Phys. Rev.* D 98 (2018), 030001. DOI: 10.1103/PhysRevD.98.030001.

[47] SLD Collaboration. 'Measurement of Leading Particle Effects in Decays of Z^0 Bosons into Light Flavors'. In: *Phys. Rev. Lett.* 78 (1997), 3442–3446. DOI: 10.1103/PhysRevLett.78.3442.

[84] Linear Collider Collaboration. *The International Linear Collider Machine Staging Report 2017*. Ed. by L. Evans and S. Michizono. 2017. arXiv: 1711.00568 [physics.acc-ph].

[87] ILD Collaboration. *International Large Detector*. Interim Design Report. Ed. by T. Behnke, K. Büsser et al. 2020. arXiv: 2003.01116 [physics.ins-det].

[90] Linear Collider Collaboration. *The International Linear Collider*. Technical Design Report. Vol. 3.II: *Accelerator. Baseline Design*. Ed. by C. Adolphsen, M. Barone et al. 2013. arXiv: 1306.6328 [physics.acc-ph].

[105] Linear Collider Collaboration. *The International Linear Collider*. Technical Design Report. Vol. 4: *Detectors*. Ed. by T. Behnke, J. E. Brau et al. 2013. arXiv: 1306.6329 [physics.ins-det].

[114] M. A. Thomson. 'Particle flow calorimetry and the PandoraPFA algorithm'. In: *Nucl. Instrum. Methods Phys. Res.* A 611 (2009), 25–40. DOI: 10.1016/j.nima.2009.09.009.

[115] J. S. Marshall and M. A. Thomson. 'The Pandora Particle Flow Algorithm'. In: *Proceedings of the International Conference on Calorimetry for the High Energy Frontier* (Paris, France, 22nd–25th Apr. 2013). 2013, 305–315. arXiv: 1308.4537 [physics.ins-det].

[124] W. Blum, W. Riegler and L. Rolandi. *Particle Detection with Drift Chambers*. 2nd ed. Particle Acceleration and Detection. Springer, 2008. DOI: 10.1007/978-3-540-76684-1.

[224] T. Behnke and F. Gaede. 'Software for the international linear collider: Simulation and reconstruction frameworks'. In: *Pramana – J. Phys.* 69 (2007), 1089–1092. DOI: 10.1007/s12043-007-0233-z.

[225] *ILC Software Website*. Deutsches Elektronen-Synchrotron, DESY. URL: https://ilcsoft.desy.de.

[228] F. Gaede. 'Marlin and LCCD: Software tools for the ILC'. In: *Nucl. Instrum. Methods Phys. Res.* A 559 (2006), 177–180. DOI: 10.1016/j.nima.2005.11.138.

[256] J. Letts and P. Mättig. 'A new method to determine the electroweak couplings of individual light flavours at LEP'. In: *Z. Phys.* C 73 (1997), 217–228. DOI: 10.1007/s002880050311.

[257] OPAL Collaboration. 'Measurement of the Branching Fractions and Forward-Backward Asymmetries of the Z^0 into Light Quarks'. In: *Z. Phys.* C 76 (1997), 387–400. DOI: 10.1007/s002880050563. arXiv: hep-ex/9707019.

[258] S. Bethke. 'QCD studies at LEP'. In: *Physics Reports* 403-404 (2004), 203–220. DOI: 10.1016/j.physrep.2004.08.014.

[259] SLD Collaboration. 'Improved test of the flavor independence of strong interactions'. In: *Phys. Rev.* D 59 (1998), 012002. DOI: 10.1103/PhysRevD.59.012002.

[260] OPAL Collaboration. 'A test of the flavour independence of the strong interaction for five flavours'. In: *Z. Phys.* C 60 (1993), 397–420. DOI: 10.1007/BF01560038.

[261] OPAL Collaboration. 'Leading Particle Production in Light Flavour Jets'. In: *Eur. Phys. J.* C 16 (2000), 407–421. DOI: 10.1007/s100520000406. arXiv: hep-ex/0001054.

[262] T. Suehara and T. Tanabe. 'LCFIPlus: A framework for jet analysis in linear collider studies'. In: *Nucl. Instrum. Methods Phys. Res.* A 808 (2016), 109–116. DOI: 10.1016/j.nima.2015.11.054.

[263] OPAL Collaboration. 'Measurement of $\Gamma(Z^0 \to b\bar{b})/\Gamma(Z^0 \to \text{hadrons})$ using a double tagging method'. In: *Z. Phys.* C 65 (1995), 17–30. DOI: 10.1007/BF01571301.

[264] P. Kesten, C. Akerlof et al. 'Comparison of light quark and charm quark fragmentation'. In: *Phys. Lett.* B 161 (1985), 412–416. DOI: 10.1016/0370-2693(85)90789-0.

[265] M. Schmelling. 'QCD results from the study of hadronic Z-decays'. In: *Physica Scripta* 51 (1995), 683–713. DOI: 10.1088/0031-8949/51/6/004.

[266] G. D. Lafferty, P. I. Reeves and M. R. Whalley. 'A compilation of inclusive particle production data in e^+e^--annihilation'. In: *J. Phys.* G 21 (1995), 1–151. DOI: 10.1088/0954-3899/21/12a/001.

[267] W. Kilian, T. Ohl and J. Reuter. 'WHIZARD—simulating multi-particle processes at LHC and ILC'. In: *Eur. Phys. J.* C 71 (2011), 1742. DOI: 10.1140/epjc/s10052-011-1742-y. arXiv: 0708.4233 [hep-ph].

[268] W. Kilian, J. Reuter and T. Ohl. *The WHIZARD Event Generator Website*. URL: https://whizard.hepforge.org.

[269] M. Moretti, T. Ohl and J. Reuter. *O'Mega: An Optimizing Matrix Element Generator*. 2001. arXiv: hep-ph/0102195 [hep-ph].

[270] T. Sjöstrand, S. Mrenna and P. Skands. 'PYTHIA 6.4 physics and manual'. In: *J. High Energy Phys.* 05 (2006), 026. DOI: 10.1088/1126-6708/2006/05/026. arXiv: hep-ph/0603175 [hep-ph].

[271] T. Sjöstrand, S. Mrenna and P. Skands. *PYTHIA 6 Website*. URL: https://pythia.org/pythia6/.

[272] A. Böhrer. 'Inclusive particle production in hadronic decays of the Z boson at LEP I'. In: *Phys. Rep.* 291 (1997), 107–217. DOI: 10.1016/S0370-1573(97)00015-X.

[273] P. M. de Freitas and H. Videau. *Detector simulation with MOKKA / GEANT4: Present and future*. LC Note LC-TOOL-2003-010. 2003. URL: https://flc.desy.de/lcnotes.

[274] F. Gaede. 'Mokka/Marlin framework'. In: Joint ACFA Physics and Detector Workshop and GDE meeting on the International Linear Collider (Sendai, Japan, 3rd–6th Mar. 2008). 2008. URL: https://agenda.linearcollider.org/event/2432/contributions/7006/.

[275] S. Agostinelli, J. Allison et al. 'GEANT4—a simulation toolkit'. In: *Nucl. Instrum. Methods Phys. Res.* A 506 (2003), 250–303. DOI: 10.1016/S0168-9002(03)01368-8.

[276] J. Allison, K. Amako et al. 'Geant4 developments and applications'. In: *IEEE Trans. Nucl. Sci.* 53 (2006), 270–278. DOI: 10.1109/TNS.2006.869826.

[277] F. Gaede, T. Behnke et al. 'LCIO: A Persistency framework for linear collider simulation studies'. In: *Proceedings of the 13th International Conference on Computing in High-Energy and Nuclear Physics* (La Jolla, California, 24th–28th Mar. 2003). eConf C0303241. 2003. arXiv: physics/0306114 [physics].

[278] T. Behnke, G. A. Blair et al. *Performance study of the proposed TESLA detector using a realistic track reconstruction package*. LC Note LC-DET-2001-029. 2001. URL: https://flc.desy.de/lcnotes.

[279] A. Raspereza, X. Chen and A. Frey. 'LDC Tracking Package'. In: *Proceedings of the 2007 International Linear Collider Workshop* (Hamburg, Germany, 30th May–3rd June 2007). eConf C0705302. URL: https://www.slac.stanford.edu/econf/C0705302/index.htm.

[280] F. A. Berends, R. Kleiss and S. Jadach. 'Radiative corrections to muon pair and quark pair production in electron-positron collisions in the Z_0 region'. In: *Nucl. Phys.* B 202 (1982), 63–88. DOI: 10.1016/0550-3213(82)90221-8.

[281] F. A. Berends, R. Kleiss and S. Jadach. 'Monte Carlo simulation of radiative corrections to the processes $e^+e^-\to\mu^+\mu^-$ and $e^+e^-\to\bar{q}q$ in the Z_0 region'. In: *Comput. Phys. Commun.* 29 (1983), 185–200. DOI: 10.1016/0010-4655(83)90073-5.

[282] G. Moortgat-Pick. 'Impact of polarized e^- and e^+ beams at a future Linear Collider and a Z-factory'. In: *J. Phys.* Conf. Ser. 295 (2011): *19th International Spin Physics Symposium (SPIN2010) 27 September–2 October, 2010, Jülich, Germany*, 012159. DOI: 10.1088/1742-6596/295/1/012159.

[283] *Generator samples for the DBD production*. URL: https://ilcsoft.desy.de/dbd/generated/.

[284] M. Takahiro. *Photon Energy Calibration using $e^+e^- \to \gamma Z$ at the ILC*. ILD Note ILD-PHYS-PUB-2019-006. 2020. URL: https://confluence.desy.de/display/ILD/ILD+notes.

[285] T. Mizuno. 'Jet energy calibration using $e^+e^- \to \gamma Z$ process at the ILC'. In: ILC Workshop on Potential Experiments (Virtual Conference, 26th–29th Oct. 2021). 2021. URL: https://agenda.linearcollider.org/event/9211/contributions/49458/.

[286] T. Mizuno. 'Photon energy calibration using e+e- to gamma Z process at the ILC'. In: International Workshop on Future Linear Colliders (Sendai, Japan, 28th Oct.–1st Nov. 2019). 2019. URL: https://agenda.linearcollider.org/event/8217/contributions/44772/.

[287] M. Beckmann, B. List and J. List. 'Treatment of photon radiation in kinematic fits at future e^+e^- colliders'. In: *Nucl. Instrum. Methods Phys. Res.* A 624 (2010), 184–191. DOI: 10.1016/j.nima.2010.08.107.

[288] M. Beckmann. 'Improving the pair separation of WW/ZZ at the ILC by consideration of photon radiation in kinematic fits'. Diploma thesis. Leibniz Universität Hannover, 2010. DOI: 10.3204/DESY-THESIS-2010-014.

[289] Y. Radkhorrami and J. List. 'Conceptual aspects for the improvement of the reconstruction of *b*- and *c*-jets at e^+e^- Higgs Factories with ParticleFlow detectors'. In: International Workshop on Future Linear Colliders (Geneva, Switzerland, 15th–18th Mar. 2021). Based on the talk "Reconstruction of b- and c-jets at e+e– Higgs Factories with ParticleFlow detectors". 2021. DOI: 10.3204/PUBDB-2021-02274. arXiv: 2105.08480 [hep-ex].

[290] M. Berggren. personal communication. Deutsches Elektronen-Synchrotron, DESY, 2020.

[291] M. Berggren. *Fix of the wrong xyz for hits in LCal*. 2015. URL: https://github.com/iLCSoft/MarlinReco/commit/484646583978660ffea3c783c6cfc85877b7a75d.

[292] S. Brandt, C. Peyrou et al. 'The principal axis of jets — an attempt to analyse high-energy collisions as two-body processes'. In: *Phys. Lett.* 12 (1964), 57–61. DOI: 10.1016/0031-9163(64)91176-X.

[293] R. Ete. *[WIP] PIDLikelihood: new dEdX parameters*. ILDConfig Pull Request #97. 2019. URL: https://github.com/iLCSoft/ILDConfig/pull/97.

[294] OPAL Collaboration. 'The production of neutral kaons in Z0 decays and their Bose-Einstein correlations'. In: *Z. Phys.* C 67 (1995), 389–401. DOI: 10.1007/BF01624582.

[295] A. Irles, R. Pöschl and F. Richard. 'Production and measurement of $e^+e^- \to c\bar{c}$ signatures at the 250 GeV ILC'. In: *Proceedings of the International Workshop on Future Linear Colliders* (Sendai, Japan, 28th Oct.–1st Nov. 2019). 2020. arXiv: 2002.05805 [hep-ex].

Acknowledgements

I would not have been able to write this thesis without the help of many people and I want to take the opportunity to acknowledge their contributions to my work.

Foremost I want to thank Ties Behnke for giving me the opportunity to work on this interesting topic and for his advise and ideas that helped to guide my work. I also want to express my gratitude to Erika Garutti for agreeing to be my second referee, as well as the other members of my review committee.

I want to thank Jenny List and Ralf Diener for their supervision, help and advise in the different stages of my work. I am especially grateful for their thorough proofreading of this thesis.

Particular thanks go to Ralf for sharing his endless optimism during the various setbacks and delays of my test-beam campaign. Furthermore I am grateful to him and Felix Müller for their indispensable help in organising and planing the test-beam measurements. I also want to thank them and all other members of the TPC group for making the test beam a success by helping in the preparation and by taking shifts in the control room. I want to acknowledge Uwe Krämer, who supported me greatly in the assembly of the readout modules.

The hardware part of my thesis would not have been possible without the support by the technical department of the FLC group. Here I want to thank Bernd Beyer for his great work on the GEM mounting tool, Volker Prahl and Ole Bach for making sure that the drawings and the parts of the readout modules were in order and again Ole for providing the mechanical simulations of the ceramic frames.

Kudos to all my colleagues in the FLC group for creating a friendly and enjoyable working environment. In particular I want to thank my office mates Uli Einhaus and Oliver Schäfer, but also many others, for the many interesting discussions, about our work and broader physics topics as well as the world in general. I am particularly grateful to Uli, who became a good friend and played a great part in making my time in Hamburg about more than just work.

Last but decidedly not least I want to thank my family, in particular my parents and my sister, who supported me all the way.

This material is based upon work supported by the National Science Foundation of the U.S.A. under Grant No. 0935316 and was supported by the Japan Society for the Promotion of Science (JSPS) KAKENHI Grant No. 23000002. The research leading to these results has received funding from the European Commission under the 6th Framework Programme "Structuring the European Research Area", contract No. RII3-026126, and under the FP7 Research Infrastructures project AIDA, grant agreement No. 262025. Special thanks go to Y. Makida, M. Kawai, K. Kasami and O. Araoka of the KEK IPNS cryogenic group, and A. Yamamoto of the KEK cryogenic centre for their support in the configuration and installation of the superconducting PCMAG solenoid. The measurements leading to these results have been performed at the Test Beam Facility at DESY Hamburg (Germany), a member of the Helmholtz Association. The contributions to the experiment by the University of Lund, KEK, Nikhef and CEA are gratefully acknowledged.

Eidesstattliche Versicherung / Declaration on Oath

Hiermit versichere ich an Eides statt, die vorliegende Dissertationsschrift selbst verfasst und keine anderen als die angegebenen Hilfsmittel und Quellen benutzt zu haben.

Hamburg, den 24. Mai 2022

Paul Malek